NOTE TO USERS

Page(s) missing in number only; text follows. Page(s) were scanned as received.

II

This reproduction is the best copy available.

UMI®

RICE UNIVERSITY

DYNAMIC ASPECTS OF EMULSION STABILITY

by

ALEJANDRO A. PEÑA

A THESIS SUBMITTED
IN PARTIAL FULFILLMENT OF THE
REQUIREMENTS FOR THE DEGREE

DOCTOR OF PHILOSOPHY

APPROVED, THESIS COMMITTEE:

Clarence A. Miller, Louis Calder Professor
Chemical Engineering, Co-chair

George J. Hirasaki, A. J. Hartsook Professor
Chemical Engineering, Co-chair

Mason Tomson, Professor
Civil and Environmental Engineering

Matteo Pasquali, Assistant Professor
Chemical Engineering

Norman E. Byrne, OndeoNalco Energy Services

Michael Poindexter, OndeoNalco Energy Services

HOUSTON, TEXAS
AUGUST, 2003

UMI Number: 3122521

INFORMATION TO USERS

The quality of this reproduction is dependent upon the quality of the copy submitted. Broken or indistinct print, colored or poor quality illustrations and photographs, print bleed-through, substandard margins, and improper alignment can adversely affect reproduction.

In the unlikely event that the author did not send a complete manuscript and there are missing pages, these will be noted. Also, if unauthorized copyright material had to be removed, a note will indicate the deletion.

UMI®

UMI Microform 3122521

Copyright 2004 by ProQuest Information and Learning Company.

All rights reserved. This microform edition is protected against unauthorized copying under Title 17, United States Code.

ProQuest Information and Learning Company
300 North Zeeb Road
P.O. Box 1346
Ann Arbor, MI 48106-1346

Abstract

DYNAMIC ASPECTS OF EMULSION STABILITY

by

ALEJANDRO A. PEÑA

This dissertation encompasses novel theoretical, experimental and computational advances in the understanding of the transient behavior of emulsions undergoing phase separation. Firstly, the kinetics of dissolution of single drops of pure hydrocarbons and their mixtures in aqueous solutions of a nonionic surfactant ($C_{12}E_8$) was studied theoretically and experimentally. At moderate surfactant concentrations, both interfacial resistance to mass transfer and diffusion of micelles carrying solubilized oil dictated the solubilization rates. At high surfactant concentrations, the onset of spontaneously generated convection in the aqueous phase was observed. In such cases, convection aided mass transport in the bulk phase and reduced the diffusional resistance, thus leaving interfacial resistance as rate-controlling. Data suggest that the adsorption/fusion of micelles at the interfaces was the elementary molecular step within the kinetic mechanism that dictated the interfacial resistance to mass transport. Experimental results for the solubilization of single droplets were correlated without adjustable parameters with a plausible mass transfer model in agreement with such mechanism. This model was extended to polydisperse emulsions of hydrocarbons in nonionic surfactant solutions, and it was successfully applied to correlate data from experiments on solubilization in emulsions, Ostwald ripening and compositional ripening.

In addition, a new experimental technique based on nuclear magnetic resonance (NMR) was developed to characterize emulsions. The contributions of this work include a novel theory to interpret results from NMR restricted diffusion experiments and an

original procedure that couples diffusion measurements with transverse relaxation rate experiments to determine drop size distributions with arbitrary shape, the water/oil ratio of the emulsion and the rate of decay of magnetization at the interfaces, i.e., the surface relaxivity. It is shown that the procedure also allows identification of whether the dispersion is oil-in-water (O/W) or water-in-oil (W/O) in a straightforward manner and is suitable to evaluate changes in drop size distributions in time steps of approximately five minutes without manipulation or destruction of the sample.

Finally, the effect of chemicals of known structure and composition (alkylphenol polyalkoxylated resins and polyurethanes) on the stability and properties of brine-in-crude-oil emulsions was assessed experimentally. The relative rates of water separation and changes of the drop size distributions in time were characterized via bottle tests, interfacial tension experiments, rheometry and nuclear magnetic resonance. The phenolic resins promoted coalescence of droplets. Optimum performance was obtained with resins exhibiting intermediate hydrophilicity, in a manner consistent with the optimum formulation for formation of microemulsions in conventional oil-water-surfactant systems. In contrast, polyurethanes promoted aggregation and slow coalescence. The performance of polyurethanes improved with increase of molecular weight. Phenolic resins and polyurethanes acted synergistically when added simultaneously, rendering water separation rates significantly higher than those observed when they were used individually. Polyurethanes aided phase separation at moderate concentrations (ca. 200 ppm), but they retarded coalescence when added at significantly higher concentrations. Plausible molecular mechanisms for demulsification by chemical means that are consistent with these findings are proposed and discussed.

Acknowledgements

I wish to express my sincere thankfulness and appreciation to the following persons and organizations:

Dr. Clarence Miller for his many words of wisdom as thesis co-advisor, mentor and friend during my tenure at Rice University.

Dr. George Hirasaki for serving as my thesis co-advisor and for his support and guidance throughout these years.

Dr. Matteo Pasquali for serving in my thesis committee, and for many enlightening discussions on emulsion rheology.

Dr. Mason Tomson, Dr. Norman E. Byrne and Dr. Michael Poindexter for serving in my thesis committee.

The J. W. Fulbright Program, the Lodieska Stockbridge Vaughan fellowship, OndeoNalco Energy Services and an industrial consortium (Schlumberger, Arco, Baker Atlas, Chevron, Deepstar, Exxon, GRI, Halliburton/NUMAR, Kerr McGee, Marathon, Mobil, Norsk Hydro, Phillips, PTS, Saga and Shell) for financial support.

Mr. Mark Flaum and Dr. John Shafer for their assistance with NMR measurements, and for useful suggestions to my research on NMR characterization of emulsions.

Very specially, my family for their encouragement and unconditional support.

Table of Contents

Abstract iii
Acknowledgements v
Table of Contents vi
List of Tables ix
List of Figures x

Chapter 1. Basic concepts on emulsions and emulsion stability 1
1.1. Basic definitions 1
1.2. Properties of emulsions 3
1.2.1. Emulsion morphology 3
1.2.2. Drop size distribution and mean drop sizes 4
1.2.3. Shear viscosity 7
1.2.4. Emulsion stability 10
1.2.4.1. Sedimentation and Creaming 11
1.2.4.2. Aggregation 14
1.2.4.3. Coalescence 22
1.3. References 31

Chapter 2. Destabilization of emulsions via mass transfer 34
2.1. Introduction 34
2.2. Theory 38
2.2.1. Solubilization of individual droplets 38
2.2.2. Mixed kinetics with convection 48
2.2.3. Mass transfer in emulsions 53
2.2.4. LSW theory for interface-controlled Ostwald ripening in emulsions 58
2.3. Computational procedures 61
2.4. Materials and Methods 62
2.5. Results and discussion 64
2.5.1. Equilibrium solubilization capacity and interfacial tension measurements 64
2.5.2. Solubilization tests for individual drops 67
2.5.3. Mass transfer in emulsions 88
2.5.3.1. Case Study 1: Solubilization 88

2.5.3.2. Case Study 2: Ostwald Ripening 94
2.5.3.3. Case Study 3: Compositional Ripening 100
2.5.4. Effect of surfactant concentration on the solubilization kinetics of alkanes in nonionic surfactant solutions 111
2.6. References 129

Chapter 3. Enhanced Characterization of Oilfield Emulsions via NMR Diffusion and Transverse Relaxation Experiments 134
3.1 Introduction 134
3.2. CPMG experiment: basic theory and interpretation 136
3.2.1. Description of the test 136
3.2.2. Determination of drop sizes in emulsions via CPMG 137
3.2.3. Range of drop sizes that can be resolved via CPMG 139
3.2.4. Determination of the water/oil composition in emulsions 142
3.3. PGSE experiment: basic theory and interpretation 143
3.3.1. Description of the test 143
3.3.2. Determination of drop sizes in emulsions via PGSE 145
3.3.3. A novel theory to resolve PGSE data in the time domain 151
3.3.4. Range of drop sizes that can be resolved via PGSE 154
3.4. Combined CPMG-PGSE method 156
3.4.1. Advantages and limitations of the CPMG experiment 156
3.4.2. Advantages and limitations of the PGSE experiment 157
3.4.3. Combining experimental data from both methods 158
3.5. Computational procedures 161
3.6. Experimental 163
3.7. Results and Discussion 164
3.7.1. Properties of the pure fluids 164
3.7.2. Validation of Eq. [3.32] 168
3.7.3. The combined CPMG-PGSE method in practice 175
3.7.4. Morphology of the emulsion 185
3.7.5. Oil/water composition 187
3.7.6. Surface relaxivities 189
3.8. References 193

Chapter 4. Destabilization of emulsions via aggregation, sedimentation and coalescence **198**

4.1. Introduction 198

4.2. Oilfield emulsions and chemical demulsification: a literature review 199

4.2.1. Surface-active materials in crude oils: asphaltenes, resins and naphtenates 199

4.2.2. Stabilizing mechanism for water-in-crude oil emulsions 204

4.2.3. Chemical demulsification 207

4.2.4. Effect of demulsifiers on interfacial properties of water/crude oil systems 210

4.2.5. On the relationship between chemical structure of demulsifiers and efficiency of emulsion breakup 217

4.3. Materials and Methods 219

4.4. Results and Discussion 224

4.4.1. Performance of polyoxyalkylenated alkylphenolformaldehide resins 224

4.4.2. Performance of cross-linked polyurethanes 234

4.4.3. Synergistic action and overdosage effects 238

4.4.4. NMR characterization of emulsions undergoing phase separation 243

4.5. On the mechanism of chemical demulsification 254

4.6. References 258

Chapter 5. Conclusions and Future Work **262**

5.1. Conclusions 262

5.1.1. Destabilization of emulsions via mass transfer 262

5.1.2. NMR Characterization of emulsions 264

5.1.3. Destabilization of emulsions via aggregation, sedimentation and coalescence 265

5.2. Future Work 266

Appendix A. Usage of the log-normal p.d.f. to describe drop size distributions in emulsions **269**

Appendix B. Analyses of crude oils **276**

Appendix C. Equations for NMR characterization of emulsions **277**

Appendix D. MATLAB code used to process NMR CPMG/PGSE data **282**

List of Tables

Table 1.1. Mean drop sizes used to characterize emulsions 6

Table 2.1. Molecular and micellar equilibrium solubilization capacities of alkanes in aqueous solutions of $C_{12}E_8$ 66

Table 2.2. Mass transfer coefficients k^o (mol m^{-2} s^{-1}) for pure alkanes in $C_{12}E_8$ (2.5 wt.%) 69

Table 2.3. Interfacial resistance $\Re_I^o = c_{sat}^o / k^o$ (s/m) for alkanes in $C_{12}E_8$ (2.5 wt.%) 69

Table 2.4. Parameters used in the simulations for case study 1 90

Table 2.5. Parameters used in the simulations for case study 2 96

Table 2.6. Parameters used in the simulations for case study 3 102

Table 3.1. Summary of surface relaxivities measured in this study 190

Table A-1. Values of β_{ij} for the expression $d_j = d_i e^{\beta_{ij}\sigma_g^2}$ 274

Table B.1. Analyses of crude oils 276

List of Figures

Figure 1.1. Common emulsion morphologies 2

Figure 1.2. Drop size distributions commonly found in emulsions 5

Figure 1.3. Destabilizing mechanisms in emulsions 11

Figure 1.4. Energy of interaction between two spherical particles, as calculated from the DLVO theory. Parameters: droplet radius a = 3 μm, Hamaker constant A = 10^{-20} J, surface potential ψ_0 = 60 mV, Debye length $1/\kappa$ = 3 nm (c_0 = 10 mM) and T = 25 °C 17

Figure 1.5. Sketch of interaction energies between two droplets stabilized by polymers 20

Figure 1.6. Transient behavior of a thin liquid film. The arrow indicates the direction in which the interface is displaced. The inserted drawing illustrates the section of the interface that is shown. The time lapse between initial and final positions is 37s. r_0 = 1 mm. h_0 = 160 nm. s = 0.5. σ = 72 mN/m. Interaction forces have been neglected in these calculations 25

Figure 1.7. Upper view of interference patterns observed in the drainage of a thin film of a toluene diluted bitumen film in water. (a) drainage is axisymmetrical when the dimple is formed; (b) an instability develops and the drainage takes place asymmetrically; (c) an equilibrium gray film is obtained at the end. The film remained stable over one hour before break-up 25

Figure 1.8. (a) Interferogram showing the stepwise thinning of a film of aqueous nonionic micellar solution; (b) Schematic plot of the disjoining pressure Π vs. film thickness h. The equilibrium states of the liquid film correspond to $\Pi = \Delta P$, where ΔP is the pressure difference across the film. 28

Figure 1.9. Time-dependent behavior of the concentration of single drops (n_1) and doublets (n_2) in a 5 vol. % O/W emulsion undergoing aggregation and coalescence. (a) fast aggregation, slow coalescence. (b) slow aggregation, fast coalescence. Parameters: T = 298 K, η = 1 mPa.s, a = 1 μm, (τ_{Sm} = 1.7 s) (a) U_{min} = -45kT (τ_d = 0.1 s), τ_c = 10 s (b) U_{min} = -40kT (τ_d = 19.5 s), τ_c = 0.01 s 30

Figure 2.1. Schematic representations showing the transient behavior of drops sizes in emulsions undergoing mass transfer. (a) Solubilization of drops in an undersaturated surfactant solution: as time proceeds, a reduction in the sizes of the droplets is expected; (b) Ostwald ripening: drops with radii $a(t)$ greater than a critical size $a_C(t)$ grow, while those with $a(t) < a_C(t)$ shrink; (c) compositional ripening in a mixed emulsion containing two drop types, with one of them (white circles) being insoluble in the surfactant solution: the latter grow at the expense of the solubilization of drops containing a soluble solute (black circles) 35

Figure 2.2. Basic configuration of the water-oil interfacial region showing the quasi-steady interface-controlled concentration profile of a solute being transferred from drop to solution 39

Figure 2.3. Plots of the asymptotic solutions for the number-based drop size distribution of emulsions undergoing Ostwald ripening 60

Figure 2.4. Light transmittance of aqueous $C_{12}E_8$ (2.5 wt.%) titrated with n-decane and n-undecane at room temperature. Triangles: Data obtained for n-decane allowing 4 hours between additions. Dots: Data obtained for n-decane allowing 10 hours between additions. Circles: Data for n-undecane allowing 10 hours between additions. The onset of a permanent turbidity indicates the solubility limit..... 65

Figure 2.5. Solubilization of several drops of linear alkanes in oil-free solutions of $C_{12}E_8$ (2.5 wt. %) in water ($\theta^o = 0$) at two different temperatures 68

Figure 2.6. Solubilization of several drops of n-decane in an oil-free solution of $C_{12}E_8$ (2.5 wt. %) in water ($\theta^o = 0$) at room temperature. Solid lines: linear fit of the data with Eq. [2.69]. Dashed line: predicted trend assuming mass transport controlled by micellar diffusion (Eq. [2.70]). Experimental error is shown in the last datum for the drop with largest initial radius 70

Figure 2.7. Solubilization of a drop of n-decane in aqueous $C_{12}E_8$ (2.5 wt. %) partially saturated with n-decane ($\theta^o = 0.50$). Solid line: predicted trend assuming interfacial resistance as limiting (Eq. [2.69]). Dashed line: predicted trend when micellar diffusion is limiting (Eq. [2.70]) 71

Figure 2.8. Solubilization of mixed drops of n-decane and squalane in an oil-free solution of $C_{12}E_8$ (2.5 wt. %) in water ($\theta^o = 0$) at 23 °C. Solid lines: predicted trends assuming mass transport controlled by interfacial resistance (Eq. [2.8]). Dashed lines: predicted trends assuming mass transport controlled by micellar diffusion (Eq. [2.11]). Dotted lines: predicted limiting sizes, determined from the condition $x = \theta^o$. x_0 is the molar fraction of n-decane in the drop at $t = 0$ 74

Figure 2.9. Swelling of drops of squalane in aqueous $C_{12}E_8$ (2.5 wt. %) partially saturated with n-decane at 23°C. Solid lines: predicted trends assuming interfacial phenomena as limiting (Eq. [2.8]). Dashed lines: predicted trends assuming micellar diffusion as limiting (Eq. [2.11]). Dotted lines: Predicted radii at equilibrium, determined from the condition $x = \theta^o$ 76

Figure 2.10. Solubilization of mixed drops of n-octane and squalane in an oil-free solution of $C_{12}E_8$ (2.5 wt. %) in water ($\theta^o = 0$) at 30.9 °C. Solid lines: predicted trends assuming mass transport controlled by interfacial resistance and $a_j = x_j$. Dashed lines: predicted trends assuming mass transport controlled by interfacial resistance and $a_j = \phi_j$ 77

Figure 2.11. Measured activities ($a_j = c_{sat,j} / c^o_{sat,j}$) of individual components in n-octane/n-undecane and n-decane/n-undecane mixtures in contact with a solution of $C_{12}E_8$ (2.5 wt.%) at 30.9°C 79

Figure 2.12. (a) Molar solubilization ratio, and (b) composition of oil and micellar phases in equilibrium for the n-decane/n-undecane system in solutions of $C_{12}E_8$ (2.5 wt.%) at 30.9 °C 79

Figure 2.13. Solubilization of mixed drops of n-octane and n-undecane in an oil-free solution of $C_{12}E_8$ (2.5 wt. %) in water ($\theta^o = 0$) at 30.9 °C. Solid

lines: predicted trends assuming mass transport controlled by interfacial resistance and $\mathbf{a}_j = x_j$. Dashed lines: predicted trends assuming mass transport controlled by interfacial resistance with the experimental activities reported in Figure 2.12 81

Figure 2.14. Experimental values for the initial and final rates of decay of drop radius of mixed drops of n-octane and n-undecane in an oil-free solution of $C_{12}E_8$ (2.5 wt. %) in water (θ^o = 0) at 30.9 °C 82

Figure 2.15. Predicted trends for the molar composition $x_1/(x_1+x_2)$ of the oil drops and surfactant solutions for the solubilization of mixtures of n-octane (1) / n-undecane (2) in $C_{12}E_8$ (2.5 wt.%) at 30.9 °C 84

Figure 2.16. Solubilization of mixed drops of n-decane and n-undecane in oil-free solutions of $C_{12}E_8$ (2.5 wt. %) in water (θ = 0) at 30.9 °C. Dots: Experimental data. Solid lines: Predictions from multicomponent mass transfer model assuming interface-controlled mass transfer. Dash-dot lines, Predictions assuming that the initial solubilization rate remains constant 85

Figure 2.17. Predicted trends for the molar composition $x_1/(x_1+x_2)$ of the oil drops and surfactant solutions for the solubilization of mixtures of n-decane (1) / n-undecane (2) in $C_{12}E_8$ (2.5 wt.%) at 30.9 °C 86

Figure 2.18. *Case study 1:* [(a)] Experimental data and [(b), (c)] simulation results for the transient volume (b) and number (c) drop size distribution of the emulsion 89

Figure 2.19. *Case study 1:* Numerical results for the transient behavior of the transient mean and Sauter drop sizes 91

Figure 2.20. *Case study 1:* Experimental and numerical results for the concentration of oil present as droplets in the emulsion 92

Figure 2.21. *Case study 1:* Effect of the selection of the time step $\Delta\tau$ on the numerical response of the proposed algorithm for case study 1 94

Figure 2.22. *Case study 2:* Experimental and numerical results for the transient behavior of the mean drop size. Top: plot of a^2 vs. time. Bottom: plot of a^3 vs. time. Black dots: experimental data. Solid lines: Linear fits at long ripening times. Dashed lines: Results from numerical simulations 95

Figure 2.23. *Case study 2:* Validation of the extension of the LSW theory for interface-controlled Ostwald ripening via numerical simulations. Top: Transient behavior of the drop size distribution. Botton: correlation between the mean size $\overline{a}$ and the critical radius a_C 100

Figure 2.24. *Case study 3:* Drop size distributions of the initial emulsions before mixing them. Solid bars and lines: Experimental data. Dashed lines: Numerical fit using the log-normal p.d.f. 101

Figure 2.25. *Case study 3:* Transient behavior of the drop size distribution for the mixed emulsion. Solid bars and lines: Experimental data. Dashed lines: Results from numerical simulations 103

Figure 2.26. *Case study 3:* Transient behavior of the volume-weighted mean drop sizes of the two drop types present in the mixed emulsion. Dots: Experimental data. Solid lines: Numerical simulations with interface-

controlled mass transfer model taking into account polydispersity in drop sizes. Dashed lines: Numerical simulations with interface-controlled mass transfer model neglecting polydispersity in drop sizes (Eq. [2.80]). Dash-and-dot lines: Numerical simulations with diffusion-controlled mass transfer model neglecting polydispersity in drop sizes (Eq. [2.82]) 106

Figure 2.27. *Case study 3:* Numerical results for the time-dependent behavior of the number-based drop size distributions of the two drop types present in the mixed emulsion 109

Figure 2.28. *Case study 3:* Transient behavior of the concentration of n-decane in the surfactant solution, expressed in dimensionless form $\theta^o = c_B / c^o_{sat}$ 110

Figure 2.29. Solubilization of drops of n-octane in oil-free aqueous solutions of $C_{12}E_8$ at several surfactant concentrations. All experiments were performed at 30.9 ± 0.1 °C. Symbols, experimental data. Solid lines, linear fit of the data (only first six points for the data for experiments at 0.25 wt.% and 0.5 wt.% $C_{12}E_8$). The slopes that are reported correspond to the solid lines. Dash-dot lines, predicted trend assuming micellar diffusion as rate-controlling. Dashed lines, predicted trends assuming mixed kinetics and considering spontaneously-generated convection as the surfactant concentration is increased. $C_{12}E_8$ concentration: 1.00 wt.% = 18.60 mol/m^3 112

Figure 2.30. Solubilization of a drop of n-octane in a 0.25 wt.% aqueous solutions of $C_{12}E_8$ in the presence of polystyrene particles at 30.9 ± 0.1 °C. The comparison between frames (a) and (b) illustrates that particles practically did not change their position. The time difference between both frames is 14.3 s. The arrow indicates the axial direction of the cylindrical capillary in which the drop was injected. The apparent slight elongation of the drop in the direction normal to such axis is an optical effect due to the curvature of the capillary. Measurements are performed in the axial direction to avoid that such effect influences the reported drop sizes and particle velocities 116

Figure 2.31. Solubilization of a drop of n-octane in a 2.50 wt.% aqueous solutions of $C_{12}E_8$ in the presence of polystyrene particles at 30.9 ± 0.1 °C. The comparison between frames (a) and (b) illustrates that particles displaced away from the drop in the radial direction. The time difference between both frames is 0.4 s 117

Figure 2.32. Schematic representation of the flow pattern that was observed at the onset of spontaneously-generated convection. Dashed lines, streamlines; arrowheads indicate direction of flow in the plane of observation 118

Figure 2.33. Effect of surfactant concentration, drop size and solubilized oil on the velocity of PS particles present in solubilization experiments 119

Figure 2.34. Effect of surfactant concentration, drop size and solubilized oil on the velocity of PS particles present in solubilization experiments 122

Figure 2.35. Effect of surfactant concentration on K, Pe_u, ℓ and $\Re_I/(\Re_I + \Re_B)$ for the solubilization of n-octane in $C_{12}E_8$ aqueous solutions at 30.9 °C. 123

Figure 2.36. Schematic representation of plausible molecular mechanisms able to dictate interfacial resistance to mass transport. (a) Complete (white

arrows) or partial (black arrows) adsorption of micelles, followed by emission/desorption; (b) molecular transport of solute, followed by irreversible incorporation in micelles 124

Figure 3.1. Sequence of events in a CPMG experiment 136

Figure 3.2. Sequence of events in a PGSE experiment 143

Figure 3.3. T_2 distributions of the oils used in this study 165

Figure 3.4. PGSE data for water and crude oils MP6 and SHU 166

Figure 3.5. PGSE results for mixtures of water and SHU at several water-oil compositions. No parameters have been adjusted in the calculations and the comparison with the experimental data is absolute 168

Figure 3.6. PGSE results for a mixture of water (50 vol.%) and SHU contacted as bulk fluid, not emulsified. Measurements were performed at different values of g 169

Figure 3.7. PGSE results for mixtures of water (50 vol.%) and MP6 (○), SHU (□) and PBB (Δ) contacted as bulk fluids, not emulsified 171

Figure 3.8. Effect of the transverse magnetization of the continuous phase on the PGSE response of mixtures of water and MP6, contacted as bulk fluids and emulsified. The features of the plot are explained in the text. (a) Mixtures with ϕ_W = 0.05; (b) mixtures with ϕ_W = 0.10 172

Figure 3.9. T_2 distribution of mixtures of water (30 vol.%) and SHU, contacted as bulk fluids and emulsified 176

Figure 3.10. PGSE data for fresh (t = 0) and aged (t = 48 h) emulsions of water (30 vol.%) in SHU 177

Figure 3.11. NMR results for the drop size distribution of fresh (t = 0) and aged (t = 48 h) emulsions of water (30 vol.%) in SHU 178

Figure 3.12. Drop size distribution of the fresh emulsion: Comparison of NMR and microphotography results. (a) Volume-weighted distribution; (b) number-based distribution 180

Figure 3.13. T_2 distribution of a blend of two emulsions of water (30 vol.%) in SHU 182

Figure 3.14. PGSE data for the blend of two emulsions of water (30 vol.%) in SHU 184

Figure 3.15. Drop size distribution of the blend of two emulsions of water (30 vol.%) in SHU: Comparison between NMR and microphotography results. (a) Volume-weighted distribution; (b) number-based distribution 186

Figure 3.16. T_2 distribution of a bimodal emulsion of water (30 vol.%) in PBB 160

Figure 3.17. PGSE data of a bimodal emulsion of water (30 vol.%) in PBB 186

Figure 3.18. Volume-weighted and number-based drop size distribution of a bimodal 187

Figure 3.19. Determination of water composition via CPMG. (a) T_2 distribution of selected emulsions of water in SHU. Data were normalized with respect to the oil signal; (b) comparison between actual and NMR-measured water contents 188

Figure 3.20. Simulated attenuation profiles at two different surface relaxations for a hypothetical W/O model emulsion at 25 °C 191

Figure 4.1. Hypothetical structure of an asphaltene molecule 200

Figure 4.2. Proposed structure for asphaltenes in Athabasca bitumen 201

Figure 4.3. (a) Asphaltene aggregate [10, 11]. L_a = diameter of aromatic sheet; d_m = spacing between aromatic sheets; d_γ = spacing between aliphatic side-chains; L = Characteristic length of aromatic cluster. (b) resin-solubilized asphaltene colloid. 202

Figure 4.4. Chemical structure of some naphthenic acids present in crude oils from Angola and the North Sea. 203

Figure 4.5. Stepwise drainage of an oil film stabilized by asphaltenes (7 vol.%) 206

Figure 4.6. Evolution in the chemistry and average dosage of demulsifiers 208

Figure 4.7. Π-A isotherms for (a) asphaltene/resins mixtures at the air/water interface; (b) asphaltene/demulsifier (G) mixtures at the air/water interface; (c) asphaltene/resins mixtures at the oil/water interface; (d) asphaltene/demulsifier mixtures at the oil/water interface 215

Figure 4.8. Langmuir-Blodgett films of asphaltenes, asphaltenes + resins and asphaltenes + high molecular weight demulsifier (G) at the water/air interface, studied by means of atomic force microscopy (AFM). Resins and demulsifier modify the structure of the asphaltene film in a similar fashion 216

Figure 4.9. Plausible structures of the chemicals used in demulsification experiments. (a) EO/PO alkylphenolformaldehyde resins (PR_X); (b) cross-linked polyurethanes PU_Y, showing the basic groups for linear (1) and crossed (2,3) linking 221

Figure 4.10. (a) Dimension of the mixer used in the preparation of water-in-oil emulsions; (b) experimental setting for the formation of emulsions for bottle tests; (c) experimental setting for the formation of emulsions for viscosity tests 222

Figure 4.11. Bottle test results for an untreated emulsions (squares) and for and emulsion treated with the phenolic resin PR_3 (filled circles). The inserted pictures show the appearance of the bottles at the beginning and end of the test when the resin PR_3 was used. 225

Figure 4.12. Effect of EO/PO content and temperature on the performance of the phenolic resins in bottle tests 226

Figure 4.13. Appearance of the bottles used in the experiment reported in Figure 4.12 at 30 °C, five months after the beginning of the test. The acronym PR_X indicates the phenolic resin that was dosed in each case (240 ppm) 229

Figure 4.14. Effect of EO/PO content on the equilibrium interfacial tensions of emulsions treated with phenolic resins (filled circles). The times required in bottle tests to decant 50 % of the brine initially present in the emulsion are also plotted (triangles) 230

Figure 4.15. (a) Schematic representation of the events that take place in a viscosity test; (b) transient viscosity of an untreated emulsion (open circles) and of an emulsion treated with the phenolic resin PR_3. The

viscosity of the crude oil SHU that is reported in Appendix B is also shown for comparison 232

Figure 4.16. Effect of the EO/PO content of the phenolic resins on the transient behavior of the shear viscosity 233

Figure 4.17. Appearance of the samples used in the bottle tests with the cross-linked polyurethanes PU_Y (240 ppm), five months after the beginning of the test 235

Figure 4.18. Effect of the molecular weight of the polyurethanes on the transient behavior of the shear viscosity 235

Figure 4.19. (a) schematic representation of droplets sedimenting individually (the lengths of the arrows are proportional to d^2); (b) the same droplets sedimenting in a single aggregate. Group sedimentation enhances the overall sedimentation rate 236

Figure 4.20. Effect of the molecular weight of the cross-linked polyurethane (200 ppm) on the transient amount of water separated in bottle tests, when dosed along with the phenolic resin PR_3 (40 ppm); (b) appearance of the samples one week after the beginning of the test 237

Figure 4.21. Effect of the molecular weight of the cross-linked polyurethane on the equilibrium interfacial tensions of emulsions treated with PU_Y (200 ppm) and 40 ppm of phenolic resin PR_3 (filled circles). The times required in bottle tests to decant 50 % of the brine initially present in the emulsion are also plotted (triangles) 238

Figure 4.22. Results from a bottle test designed to screen the synergistic performance of phenolic resins and cross-linked polyurethanes; (b) appearance of the samples one day after the beginning of the test 239

Figure 4.23. Results from a bottle test designed to screen overdosage effects when using phenolic resins and cross-linked polyurethanes; (b) appearance of the samples one day after the beginning of the test 241

Figure 4.24. Results from bottle tests for emulsions treated with the phenolic resin PR_4 with (filled circles) and without (open circles) polyurethane PU_3. The arrows illustrate synergistic and inhibiting effects on the performance 242

Figure 4.25. T_2 distribution of the emulsion used to follow-up the performance of demulsifiers via NMR. The inserted plot shows results from NMR-PGSE experiments for the same emulsion 243

Figure 4.26. Evolution of the T_2 distribution of the water phase for an emulsion treated with 240 ppm of the phenolic resin PR_3. The distribution of the oil phase has been omitted to simplify the interpretation of the plot 245

Figure 4.27. (a) Time-dependent drop size distribution of the emulsion treated with 240 ppm of phenolic resin PR_3; (b) transient behavior of the Sauter mean diameter d_{AV} (filled circles) and polydispersity (open circles) of the emulsion. The convention used to calculate the lower and upper limits shown in open circles is provided in the text 247

Figure 4.28. T_2 distributions of the oil and water phases that were separated by decantation from the emulsion treated with 240 ppm of phenolic resin PR_3, one week after the beginning of the experiment. The inserted

plot shows the estimated drop size distribution for the droplets that remained dispersed in the oil phase 248

Figure 4.29. Evolution of the T_2 distribution of the water phase for an emulsion treated with 240 ppm of the cross-linked polyurethane PU_3. The distribution of the oil phase has been omitted to simplify the interpretation of the plot 249

Figure 4.30. (a) Time-dependent drop size distribution of the emulsion treated with 240 ppm of cross-linked polyurethane PU_3; (b) transient behavior of the Sauter mean diameter d_{AV} (filled circles) and polydispersity (open circles) of the emulsion. The convention used to calculate the lower and upper limits shown in open circles is provided in the text 250

Figure 4.31. T_2 distributions of selected regions of the emulsion treated with 240 ppm of cross-linked polyurethane PU_3, one week after the beginning of the experiment 252

Figure 4.32. (a) Plausible conformation of indigenous materials (asphaltenes/asphaltene-resin aggregates), phenolic resin and cross-linked polyurethane molecules at the water-oil interface when two water drops approach each other and the formation of a "hole" takes place; (b) schematic representation of the hole, showing the region of near-zero interfacial curvature 256

Figure A.1. Calculated log-normal size distributions as a function of the scale used to plot particle size, using d_{gN} = 10 μm and σ_g = 1. Solid lines: number-based distributions. Dashed lines: corresponding volume-weighted distributions 270

Figure C.1. Plot of the three first intensities I_0, I_1 and I_2 of the magnetization of an isotropic fluid confined in a sphere. In the "fast diffusion" mode, the first intensity I_0 dominates 278

Figure D.1. Files required to process NMR CPMG/PGSE data with Matlab and tree organization of files and sub-directories, as required for execution 282

Figure D.2. Schematic representation of the ordering required for input files containing CPMG data 283

Figure D.3. Schematic representation of the ordering required for input files containing PGSE data 283

Figure D.4. Flowchart summarizing the algorithm of the Matlab code 285

Figure D.5. Key to run the Matlab code for Example 1 287

Figure D.6. Plot generated by the code for the T_2 distribution (blue) and the corresponding cumulative curve (red) for Example 1 288

Figure D.7. Report generated for the code for Example 1 288

Figure D.8. Key to run the Matlab code for Example 2 290

Figure D.9. Plot generated by the code for the T_2 distribution (blue) and the corresponding cumulative curve (red) for Example 2 292

Figure D.10. Plot generated by the code for the attenuation profile for Example 2. Circles, synthetic data; solid line, best fit to the data using the model reported in Chapter 3 292

Figure D.11. Plot generated by the code for the volume-weighted drop size distribution for Example 2. Circles, synthetic data from CPMG; stars, cumulative distribution for the synthetic data; red dashed line, best fit using the bimodal Weibull distribution; blue dashed line, best fit using the lognormal distribution; red solid line; best fit to the cumulative distribution using the bimodal Weibull distribution; blue solid line; best fit to the cumulative distribution using the lognormal distribution; dash-dot line, d_{MAX} as calculated from Eq. [3.12] 293

Figure D.12. Key to run the Matlab code for Example 3 295

Figure D.13. Plot generated by the code for the T_2 distribution (blue) and the corresponding cumulative curve (red) for Example 3. Solid lines, original dataset; dashed lines, edited CPMG dataset after discarding the contribution of bulk water 296

Figure D.14. Plot generated by the code for the volume-weighted drop size distribution for Example 3, without reprocessing. The description of the features of Figure D.9 given in the caption of such also applies in this case 297

Figure D.15. Plot generated by the code for the volume-weighted drop size distribution for Example 3, after reprocessing 297

Chapter 1
Basic concepts on emulsions and emulsion stability

This chapter summarizes conventional knowledge on emulsions and emulsion stability and it is mainly intended for readers that are not familiar with these matters. The specialized reader may skip it and proceed directly to Chapter 2.

1.1. BASIC DEFINITIONS

An emulsion is a relatively stable dispersion of a liquid within another liquid with which it exhibits limited miscibility. The relative stability referred to above is conferred by the presence of agents at the interfaces able to delay the spontaneous tendency of the liquids to separate. Such agents are most commonly molecules with polar and non-polar chemical groups in their structure – usually referred to as *surfactants*- or finely divided solids. The dispersed phase is commonly present in an emulsion in the form of spherical drops. If the volume fraction of such phase (ϕ) is above a critical random close-packing threshold ϕ_m (ϕ_m ranges between 0.64 (random packing) [1] and 0.74 (ordered packing) [2] for spheres with identical size), droplets are compressed against each other, the interfaces are deformed and the emulsion adopts a foam-like structure.

In general, emulsions contain a polar and a non-polar liquid phase. The former is usually water or a solution of electrolytes, polymers or other chemicals in water, and it is termed the *water* (W) phase. The latter refers to liquids such as hydrocarbons, triglycerides and silicone fluids, among others, and it is commonly named the *oil* (O) phase. Molecules exhibiting both non-polar (hydro- or fluorocarbon chains, naphthenic or aromatic rings) and polar groups (structures with heteroatoms O, S and N) might be present as small fractions of these phases. Only in very few cases (i.e., long-chain

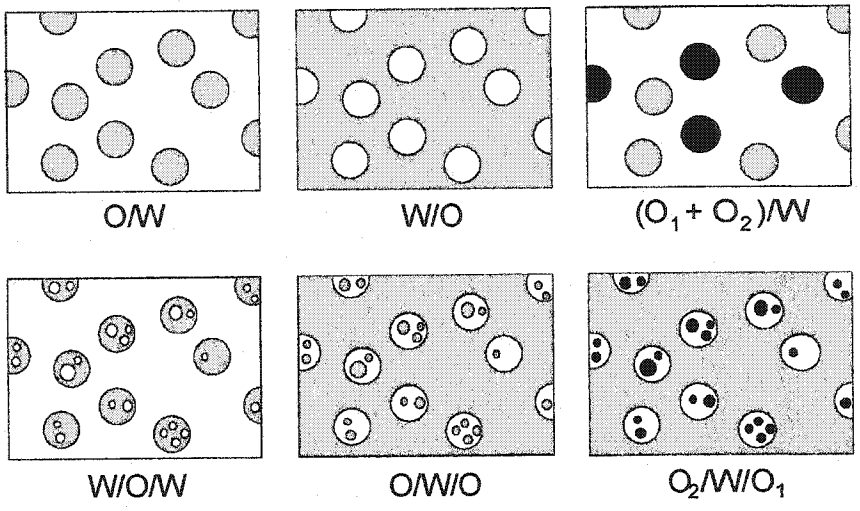


Figure 1.1. Common emulsion morphologies.

alcohols and fluorinated amines and ethers being the oil phase in the so-called fluorocarbon emulsions [3]) do they fully constitute one of the phases in the emulsion.

An emulsion can be classified according to different criteria, the most important being the morphology or spatial arrangement of the phases (Figure 1.1). The two most common types are emulsions of water dispersed in oil (W/O) and oil dispersed in water (O/W). For W/O emulsions, water is considered the *dispersed* or *internal* phase, and oil is the *continuous* or *external* phase, and conversely for the O/W type. More complex morphologies such as mixed emulsions in which more than one dispersed phase is present [$(O_1 + O_2)/W$ or $(W_1 + W_2)/O$] and multiple emulsions, say W/O/W (in which a water phase is dispersed within the droplets of the oil phase, and the latter in another aqueous phase) and conversely O/W/O are also relevant in some cases.

Finally, the process through which an emulsion is formed is called *emulsification*. Emulsification can be induced by the action of devices such as a turbine blender, an

ultrasonicator, or by the flow of the two phases through a membrane, static mixer or porous media. Emulsification can also take place spontaneously when the phases are contacted [4]. In this case, selective mass transfer of some of the components present in one phase into the other provides the energy needed to create the dispersion. Spontaneous emulsification can also occur, for example, by chemical reactions [5] or by the nucleation of one phase in another due to a reduction in temperature.

1.2. PROPERTIES OF EMULSIONS

1.2.1. Emulsion morphology

The morphology (W/O, O/W or multiple) is the most basic characteristic of an emulsion. There are qualitative procedures that can be used to discern emulsion type. These are based on the observation of a physical phenomenon that depends on the prevailing polarity in the continuous phase, such as contacting a drop of the emulsion with water or oil and observing whether the external phase is miscible or not with it. However, results from such tests are sometimes ambiguous and do not allow to discern between simple and multiple emulsions.

The type of emulsion can also be determined by measuring its electrical conductivity. Very commonly, the aqueous phase in an emulsion contains electrolytes and therefore a significant conductivity should be observed (of order several milli Siemens per centimeter, mS/cm) for those dispersions with water as external phase. On the contrary, in most cases non-polar liquids exhibit very low electrical conductivity (of order a few μS/cm), and so would emulsions with oil as external phase. Conductivity measurements can also be used to characterize W/O/W emulsions and to determine the fraction of the continuous aqueous phase that is dispersed within the oil droplets [6, 7].

1.2.2. Drop size distribution and mean drop sizes

In practice, drops in emulsions always exhibit finite polydispersity in their sizes, which usually range between 0.1 μm and 1 mm. The corresponding drop size distribution is a statistical inventory of the disaggregation of the dispersed phase. It is valuable information because the sizes of the droplets affect other properties of the emulsion such as its stability and rheology as discussed later.

Several experimental methods have been used to determine drop sizes in emulsions, including microscopy, photomicrography, videomicroscopy, light scattering, Coulter counting, turbidimetry, nuclear magnetic resonance (NMR) and acoustics among others [8].

Whereas the collection of sizes in an emulsion is discrete, the number of drops is usually large enough to allow describing its size distribution with a continuous mathematical expression, most commonly a probability distribution function (p.d.f.) taken from statistics. It is often found that the so-called log-normal distribution function,

$$p(a) = \frac{1}{2a\sqrt{2\pi}\sigma_g} e^{\frac{(\ln 2a - \ln d_g)^2}{2\sigma_g^2}}, \qquad [1.1]$$

describes well drop sizes in emulsions [9], and indeed, mathematical studies on solid grinding [10] and emulsification with turbulent stirring [11] report that breakup sequences of drops or solid fragments lead to such distribution. In this expression, a is the droplet radius, d_g is the geometric mean drop size and σ_g is the geometric standard deviation or width of the distribution. In general, a log-normal unimodal drop size distribution can be expected for emulsions made in closed vessels when agitation is turbulent and isotropic. In other cases, such as emulsion mixtures (which may exhibit multimodal distributions)

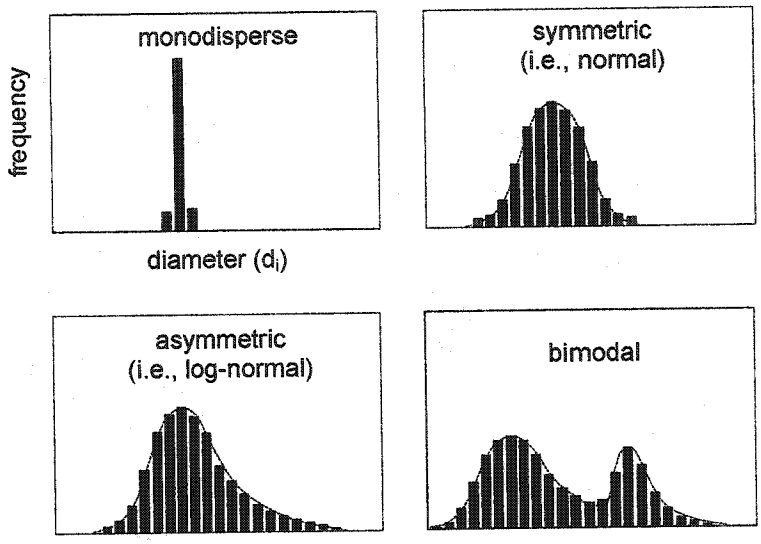


Figure 1.2. Drop size distributions commonly found in emulsions.

or anisotropic agitation (i.e., emulsification of liquids with strongly dissimilar viscosity in closed vessels), log-normality is not observed (Figure 1.2). In such cases, an alternative distribution function must be adopted empirically. A description of the usage of the log-normal probability distribution function to account for the drop size distribution of emulsions is given in Appendix A.

The mean drop size is the most commonly reported characteristic of an emulsion. There are several bases on which an average size can be calculated, as shown in Table 1.1, and each of them is physically meaningful. For example, the volume mean d_{NV} corresponds to the size of a monodisperse collection of drops with same number N_0 and overall dispersed volume V_0 present in the original emulsion. Likewise, the Sauter mean diameter d_{AV} is the size of a drop with the same volume-to-surface ratio of the entire population. Therefore, if for a given emulsion V_0 is known, N_0 and A_0 can be readily calculated as follows:

Table 1.1. Mean drop sizes used to characterize emulsions [12]. In these equations, $d = 2a$.

Descriptive name (alternative found in literature)	*Symbol (alternative)*	*Discrete distribution*	*Continuous distribution*[a]
Number-length mean (arithmetic mean)	d_{NL} (d_{av})	$\frac{\sum d\Delta N}{\sum \Delta N}$	$2\frac{\int ap(a)\,\mathrm{d}a}{\int p(a)\,\mathrm{d}a}$
Number-surface mean (surface mean)	d_{NA} (d_S)	$\left(\frac{\sum d^2\Delta N}{\sum \Delta N}\right)^{1/2}$	$2\left(\frac{\int a^2 p(a)\,\mathrm{d}a}{\int p(a)\,\mathrm{d}a}\right)^{1/2}$
Number-volume mean (volume mean)	d_{NV} (d_V)	$\left(\frac{\sum d^3\Delta N}{\sum \Delta N}\right)^{1/3}$	$2\left(\frac{\int a^3 p(a)\,\mathrm{d}a}{\int p(a)\,\mathrm{d}a}\right)^{1/3}$
Length-surface mean (linear mean, length diameter mean)	d_{LA} (d_{21})	$\frac{\sum d^2\Delta N}{\sum d\Delta N}$	$2\frac{\int a^2 p(a)\,\mathrm{d}a}{\int ap(a)\,\mathrm{d}a}$
Length-volume mean (volume-diameter mean)	d_{LV} (d_{31})	$\left(\frac{\sum d^3\Delta N}{\sum d\Delta N}\right)^{1/2}$	$2\left(\frac{\int a^3 p(a)\,\mathrm{d}a}{\int ap(a)\,\mathrm{d}a}\right)^{1/2}$
Surface-volume mean (Sauter mean diameter, surface mean)	d_{AV} (d_{32})	$\frac{\sum d^3\Delta N}{\sum d^2\Delta N}$	$2\frac{\int a^3 p(a)\,\mathrm{d}a}{\int a^2 p(a)\,\mathrm{d}a}$
Volume-(or weight-) moment mean [De Brouckere mean size, volume-(or weight-) mean]	d_{VM} or d_{WM} (d_{43})	$\frac{\sum d^4\Delta N}{\sum d^3\Delta N}$	$2\frac{\int a^4 p(a)\,\mathrm{d}a}{\int a^3 p(a)\,\mathrm{d}a}$

[a] Expressions for continuous distribution functions are obtained from their corresponding discrete definition in the limit of classes of drop sizes Δx infinitesimally small, with $x = d$, ln$d$ or log$d$ according to the selected size scale. For example, for d_{AV}:

$$d_{AV} = \lim_{\Delta x \to 0} \frac{\sum_{k=1}^{\infty} \overline{d}_k^3 \Delta N}{\sum_{k=1}^{\infty} \overline{d}_k^2 \Delta N} = \lim_{\Delta x \to 0} \frac{\sum d^3 \Delta N}{\sum d^2 \Delta N} = \frac{\int d^3\,\mathrm{d}N}{\int d^2\,\mathrm{d}N} = 2\frac{\int a^3\,\mathrm{d}a}{\int a^2\,\mathrm{d}a}$$

where $\overline{d}_k$ is calculated as the arithmetic average of the lower and upper limits of the abscissas for class k.

$$\frac{V_0}{N_0} = \lim_{\Delta x \to 0} \frac{\sum \frac{\pi}{6} d^3 \Delta N}{\sum \Delta N} = \frac{\pi}{6} d_{NV}^3 \quad \text{hence} \quad N_0 = \frac{6V_0}{\pi d_{NV}^3} \qquad [1.2]$$

$$\frac{V_0}{A_0} = \lim_{\Delta x \to 0} \frac{\sum \frac{\pi}{6} d^3 \Delta N}{\sum \pi d^2 \Delta N} = \frac{1}{6} d_{AV} \quad \text{hence} \quad A_0 = \frac{6V_0}{d_{AV}} \qquad [1.3]$$

Also, the property of the emulsion of primary interest should be considered to determine which averages of those listed in Table 1.1 are relevant in specific cases. For example, surfactant adsorption at the water-oil interfaces depends on the available interfacial area and therefore d_{AV} is more significant in this case. Numerical examples that illustrate how to use Eqs. [1.2] and [1.3], and the expressions summarized in Table 1.1. are provided at the end of Appendix A.

1.2.3. Shear viscosity

This section summarizes concepts on emulsion rheology that are relevant to this project. More exhaustive reviews, particularly on the elastic behavior of these dispersed systems, can be found elsewhere [13].

The definition of apparent shear viscosity of an emulsion η is analogous to that of pure fluids as given by Newton's law, i.e., η is the proportionality coefficient between stress (τ_{ji}) and rate of strain (also shear rate, $\dot{\gamma}_{ij}$), $\eta = \tau_{ji}/\dot{\gamma}_{ij}$. The term "apparent" comes from the fact that in general, emulsions are shear-thinning fluids, this is, η is not constant but diminishes as the shear rate increases due to the ability of the droplets to deform.

Other factors affecting the shear viscosity of an emulsion are, in order of relevance, the viscosity of the continuous phase (η_C), the dispersed phase content (ϕ), and the mean size and size distribution of droplets.

The viscosity of emulsions is usually correlated as proportional to the viscosity of the continuous phase, and that is why in practice it is very common to report the effect of a given variable upon the relative viscosity, which is defined as $\eta_r = \eta / \eta_C$.

The viscosity increases with the dispersed phase content due to interactions among droplets. Several correlations have been reported in the literature to account for this effect. The first of these correlations was proposed by Einstein for very dilute colloidal dispersions (say $\phi < 0.02$) from hydrodynamic considerations on suspensions of hard spheres:

$$\eta = \eta_C (1 + K\phi) \qquad [1.4]$$

$K = 1$ was reported in the original reference [14], and it was corrected to $K = 2.5$ a few years later [15]. Several experiments with diluted dispersions have confirmed the validity of Eq. [1.4] with $K = 2.5$ [16]. For emulsions with higher dispersed phase content, Eq. [1.4] underpredicts the observed viscosity. Several correlations have been proposed to overcome this issue. For example, the semi-empirical equation of Pal and Rhodes [17],

$$\eta = \eta_C \left(1 + \frac{\phi / \phi_{100}}{1.187 - \phi / \phi_{100}} \right)^{2.49} \qquad [1.5]$$

seems to correlate well the viscosity of emulsions below close-packing. In Eq. [1.5], ϕ_{100} stands for the dispersed phase content at which $\eta/\eta_C = 100$ and must be determined experimentally.

Another important variable to consider is the mean drop size [18]. Friction between droplets is related to the interfacial area and therefore an increase in viscosity should be expected when the surface-to-volume ratio of the dispersed phase increases. As shown in Eq. [1.3], such ratio is inversely proportional to the Sauter mean size d_{AV} and therefore

an emulsion with smaller mean drop size should exhibit higher apparent viscosity than another with higher d_{AV}. The reciprocal effect is also important: when the viscosity of the emulsion is high and emulsification is carried out by stirring, shearing is more efficient and the break-up and formation of smaller drops is favored.

There are a few expressions that account for the relationship between η and mean drop size. Empirical correlations of the form:

$$\eta \propto 1/d_m \qquad [1.6]$$

have been proposed [19], where d_m is a given mean size of the emulsion. Similarly, the following correlation for monodisperse suspensions of solids in liquids has been suggested as valid for emulsions [20]:

$$\frac{\eta}{\eta_{REF}} = \left(\frac{d_{m,REF}}{d_m} \right)^B \qquad [1.7]$$

where $B > 0$ is a constant and η_{REF} and $d_{m,REF}$ are data obtained at a reference condition. No general correlations for the constants that appear in these expressions have been published, mainly because there are many other factors affecting the observed η and because the criterion to determine d_m is not unique as noted above.

Regarding the effect of drop size distribution, in general it is observed that a monodisperse emulsion is more viscous than a polydisperse emulsion with similar mean drop size, probably because in the latter small drops can flow through the voids between large droplets in contact. This explains why mixtures of two monodisperse emulsions with different particle sizes but the same dispersed phase content usually exhibit viscosities that are lower than those of the original emulsions [21, 22].

Finally, Pal [23] has considered simultaneously the effect of dispersed phase content, shear rate, time, viscosity of the phases, density of the phases, mean particle size and polydispersity of sizes to correlate emulsion viscosity data of dilute and concentrated emulsions. Whereas the final expressions for η seem to provide some generality to the analysis, they require up to three empirical parameters that must be determined experimentally.

1.2.4. Emulsion stability

Phase separation in emulsions is imposed by thermodynamics because as the oil and water form two continuous phases while they separate, the interfacial area and therefore the free energy of the dispersion are reduced. As a consequence, the characteristics of the emulsion (drop size distribution, mean drop size and other properties) cannot remain unchanged in time. Therefore, the stability of an emulsion refers to the ability of the dispersion to preserve its properties within a given timeframe as mentioned earlier.

Figure 1.3 illustrates several physical instabilities that lead to phase separation in emulsions. *Gravitational separation* or *creaming* takes place when the two liquids exhibit different densities. *Aggregation* occurs when droplets stay very close to one another for far longer time than if there were no attractive forces acting between them [24]. *Coalescence* takes place when the thin film of continuous phase between two drops breaks and they fuse rapidly to form a single droplet.

Figure 1.3 also shows mass-transfer processes that can take place in emulsions if at least one solute can be transferred across the continuous phase. If the concentration of solute in the external phase is below the saturation limit, *solubilization* takes place and drop sizes diminish. If the continuous phase is slightly supersaturated in the solute,

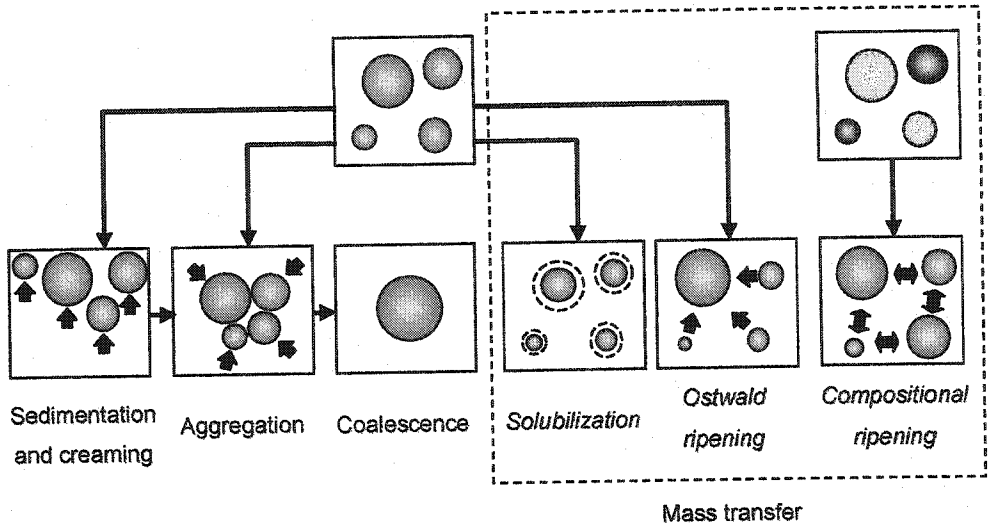


Figure 1.3. Destabilizing mechanisms in emulsions.

Ostwald ripening occurs. In this case, large drops grow at the expense of those smaller because the chemical potential of the solute is higher in drops with greater interfacial curvature. Emulsions with droplets of different composition may undergo *compositional ripening*, or exchange of matter due to differences in concentration between drops.

In what follows, classic theory on sedimentation and creaming, aggregation and coalescence is presented. Novel contributions to the understanding of the destabilization of emulsions via mass transfer are presented in Chapter 2.

1.2.4.1. Sedimentation and Creaming

Sedimentation takes place due to differences in density between the continuous phase (fluid) and the dispersed phase (fluid or solid). The well-known Stokes expression for the terminal velocity v_S of a spherical, rigid particle of diameter d and density ρ_D in a Newtonian fluid with viscosity η_C and density ρ_C:

$$v_S = \frac{g\Delta\rho d^2}{18\eta_C} \qquad [1.8]$$

is commonly used to calculate sedimentation rates. In this expression, g is the acceleration either due to gravity ($g \approx 9.81$ m/s^2) or to centrifugation ($g = L\omega^2$, with L being the effective radius of the centrifuge and ω the angular velocity) and $\Delta\rho = \rho_D - \rho_C$. The term *sedimentation* is used if the particles are displaced in the direction in which gravity acts ($\Delta\rho > 0$). Otherwise ($\Delta\rho < 0$), the process is referred to as *creaming*. The former applies to most W/O emulsions and solid dispersions, whereas the latter applies to most O/W emulsions and bubbles dispersed in liquids.

According to Eq. [1.8], sedimentation of a water drop with d = 1 μm in a W/O emulsion with $\Delta\rho$ = 200 Kg/m^3, η_C = 100 mPa.s, η_D = 1 mPa.s under gravity would take place at a rate of approximately 0.1 mm/day. In contrast, oil drops with d = 1 μm in an O/W emulsion of the same liquids ($\Delta\rho$ = -200 Kg/m^3, η_C = 1 mPa.s, η_D = 100 mPa.s) would cream at a rate of 1 cm/day, i.e., one hundred times faster. Furthermore, the droplets in the O/W emulsions should have a drop diameter d = 0.3 μm to exhibit the same separation rate than that of the referred W/O emulsion. These simple calculations are useful to understand the common practices of increasing the viscosity of the external phase and reducing the drop sizes to the minimum value that can be attained with the available emulsification process to enhance emulsion stability.

The expression given for v_S is derived based on a number of assumptions that are not always satisfied [24]. In particular, it applies to very dilute dispersions. If the volume fraction of the dispersed phase ϕ is significant (say $\phi > 0.01$), so-called hindered sedimentation takes place. In general, the effect of ϕ is to reduce the sedimentation rate

due to hydrodynamic interactions among particles. This is seen in expressions such that of Batchelor [25] for $\phi << 0.1$:

$$\frac{v_{S,H}}{v_S} = 1 - 6.55\phi \qquad [1.9]$$

where $v_{S,H}$ is the hindered sedimentation rate, or that of Richardson and Zaki [26]:

$$\frac{v_{S,H}}{v_S} = (1-\phi)^n \qquad [1.10]$$

where n is an empirical constant, and should be n = 6.55 in the limit of low ϕ according to Eq. [1.9]. However, it has been observed in some emulsions and dispersions of glass spheres that the sedimentation rate may show a slight increase with the dispersed phase content over narrow ranges of ϕ, possibly due to group sedimentation [24]. This is, if two drops or particles sediment close to each other –particularly one behind the other-during finite periods of time, the joint resistance to sediment would be smaller than if they were separated.

To obtain Equation [1.8] it is also assumed that the particles are monodisperse. For diluted dispersions, this effect can be taken into account by replacing d^2 in Eq. [1.8] by the following average:

$$d_{53}^2 = \frac{\sum N_i d_i^5}{\sum N_i d_i^3} \qquad [1.11]$$

and in general it is expected that an increase in the polydispersity of drop sizes would diminish the overall sedimentation rate. For example, it has been reported [24] that for polydisperse emulsions for which $\phi \leq 0.1$, Eq. [1.10] described well the observed rate

with n = 8.6 instead of the value n = 6.55 that is expected for monodisperse systems as noted above.

In addition, Eq. [1.8] is derived assuming that the colloidal interactions between droplets are negligible. When repulsive forces dominate (i.e., electrostatic interaction among drops on O/W emulsions stabilized with anionic surfactants), sedimentation is slower, probably because group sedimentation is not favored [27]. On the other hand, if attractive forces prevail and irreversible aggregation takes place, the sedimentation rate can be increased significantly. This has been considered for monodisperse droplets which aggregate forming fractals [24]. In this case the sedimentation velocity would be given by:

$$\frac{v_{Agregg}}{v_S} \approx 1.8 N_f^{\left(1-1/D_f\right)} \qquad [1.12]$$

where D_f is the fractal dimensionality, N_f is the characteristic number of drops per aggregate and v_S is the Stokes velocity of a single drop, as given by Eq. [1.8]. An enhancement factor of 5 for the sedimentation velocity is obtained from Eq. [1.12] when plausible values for N_f and D_f are assumed (i.e., clusters of 10 drops for which D_f = 1.5).

1.2.4.2. Aggregation

From a thermodynamic standpoint, aggregation of particles in colloidal systems and droplets in emulsions takes place as a result of the interplay between attractive and repulsive interactions. The approach that is most often referred in emulsion literature to explain such interplay is the so-called DLVO theory, developed independently by Derjaguin and Landau [28] in Russia and Verwey and Overbeek [29] in the Netherlands. This theory considers the acting force between two close particles as the result of long-

range London-van der Waals attractive forces and repulsive electrostatic forces that arise due to the overlap of electrical double layers of two charged surfaces. Let us consider these forces for the case of two spherical particles of radius a and center-center separation distance H. Hamaker [30] derived an expression for the London-van der Waals attraction for this case by integrating the interaction energy dU_A over the total volumes of the two particles to obtain:

$$U_A = -\frac{A}{6}\left[\frac{2a^2}{h^2+4ah} + \frac{2a^2}{h^2+4ah+4a^2} + \ln\left(\frac{a^2+4ah}{h^2+4ah+4a^2}\right)\right]; \quad h = H - 2a \quad [1.13]$$

where h is the minimum distance between the two approaching surfaces. Eq. [1.13] can be simplified to

$$U_A = -\frac{Aa}{12h} \quad [1.14]$$

if $h << a$. In these expressions, A is the so-called Hamaker constant, which usually has values between 1 and 1.5 x kT (k = 1.38 × 10^{-23} J/K is the Boltzmann's constant). Eq. [1.13] was derived for particles in vacuum. Such expression still holds for particles suspended in another material, but A is now and effective Hamaker constant, usually calculated as $A_{eff} \sim (A_{11}^{1/2} - A_{22}^{1/2})^2$, where A_{11} and A_{22} correspond to the constants of the two materials.

On the other hand, the electrostatic interaction energy U_E for two approaching spheres exhibiting electrical double layers cannot be resolved analytically, and only approximate expressions have been provided, such as [31],

$$U_E = \frac{64\pi a c_0 N_A kT \Psi_0^2}{\kappa^2}\exp(-\kappa h) \quad [1.15]$$

where c_0 is the bulk concentration of the ionic specie, N_A is the Avogadro's number (6.02 x 10^{23} mol^{-1}), $\aleph_0 = \tanh(ze_0\psi_0 / 4kT)$ with z being the magnitude of the ion valence, e_0 the electronic charge (1.60 x 10^{-19} C), κ^{-1} the so-called Debye length -which is a measure of the electrical double layer thickness- and ψ_0 the electrical potential at the interfaces. Eq. [1.15] is valid whenever the radius is much larger than the Debye length, i.e., $\kappa a >> 1$. The reader is referred to the literature [16, 31] for a more detailed discussion on electric double layer theory.

The overall interaction energy U is given by the sum of U_A and U_E. Figure 1.4 shows a typical profile for U that can be calculated accordingly. At very narrow separations ($h \rightarrow 0$), attractive forces dominate and particles are expected to aggregate irreversibly. This case is usually referred to as *coagulation*. When a secondary energy minimum appears at a finite separation, particles may form aggregates that can be redispersed with relative ease. This kind of aggregation might be considered reversible, and it is usually termed *flocculation*. Whereas the distinction between coagulation and flocculation seems clear under this approach, it has been noted [24] that in practice it is difficult to differentiate one case from the other. Therefore the general term aggregation is suggested to describe either phenomenon.

The overall interaction energy profile depicted in Figure 1.4 is also useful to understand the kinetics of aggregation. If $U_{max} = 0$, there is no energy barrier to prevent the two surfaces from approaching each other. In this case, so-called *fast* aggregation takes place. On the other hand, if $U_{max} > 0$, an energy barrier must be overcome to achieve irreversible aggregation. This process is usually referred to as *slow* aggregation.

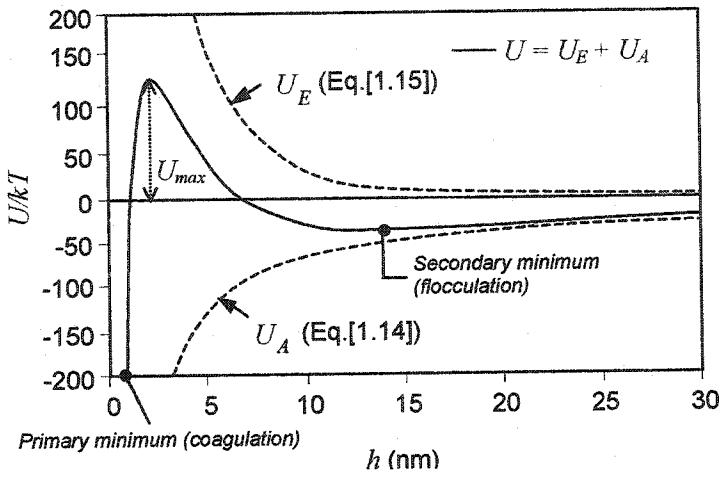


Figure 1.4. Energy of interaction between two spherical particles, as calculated from the DLVO theory. Parameters: droplet radius a = 3 μm, Hamaker constant A = 10^{-20} J, surface potential ψ_0 = 60 mV, Debye length 1/κ = 3 nm (c_0 = 10 mM) and T = 25 °C.

The simplest model for fast aggregation is that of Smoluchowski [32], who considered the particles as equally sized hard spheres that adhere irreversibly on contact but do not interact otherwise. If the displacement of the particles is dominated solely by Brownian diffusion, the process is referred to as *perikinetic* aggregation and the rate of change of the number of particles per unit volume N is given by:

$$-\frac{dN}{dt} = k_P N^2 = (8\pi Da)N^2 = \left(\frac{4kT}{3\eta}\right)N^2 \quad \text{whence} \quad N(t) = \frac{N_0}{1 + k_P N_0 t} \qquad [1.16]$$

where D is the diffusion coefficient of the particles, η is the viscosity of the continuous phase and N_0 is the initial number concentration of particles in solution. In writing equivalent expressions for the perikinetic rate constant k_P ($k_P = 8\pi Da = 4kT/3\eta$), the Stokes-Einstein equation for D ($D = kT/6\pi\eta a$) is assumed as valid.

On the other hand, if non-Brownian forces govern the displacement of the particles, aggregation is termed as *orthokinetic*. The simplest case is that in which particles encounter each other due to a velocity gradient G. In such a case, the rate $-dN/dt$ is [32]:

$$-\frac{dN}{dt} = \mathrm{k_O}\, N^2 = \left(\frac{8}{3}a^3 G\right)N^2 \quad \text{whence} \quad N(t) = \frac{N_0}{1+\mathrm{k_O}\, N_0 t} \qquad [1.17]$$

with k_O being the orthokinetic rate constant. Therefore, if Eqs. [1.16] and [1.17] apply, say for water at room temperature, the ratio $k_O/k_P \sim 0.5a^3G$ (a in μm, G in s^{-1}). This means that if a small velocity gradient arises from convection currents due to, say, small temperature fluctuations ($G \sim 0.1$ s^{-1}), perikinetic aggregation would be more significant for smaller particles ($a < 2$ μm) and orthokinetic aggregation would dominate otherwise ($a > 5$ μm). However, this is a very simplified model that does not take into account effects such as hydrodynamic and colloidal interactions, polydispersity in the sizes of the particles, sedimentation, and presence of other surfaces (gas/liquid, solid/liquid), among others [24].

The most widely accepted treatment of slow aggregation ($U_{max} > 0$) is that of Fuchs [33], who considered interactions in addition to Brownian forces to model the displacement of particles, and arrived at the following expression for $-dN/dt$:

$$-\frac{dN}{dt} = \frac{\mathrm{k_P}}{W}N^2 \qquad [1.18]$$

Here, k_P is the perikinetic rate as given above and W is the so-called stability ratio:

$$W = 2a\int_{2a}^{\infty}\exp\left(\frac{U}{kT}\right)\frac{dH}{H^2} \approx \frac{2\pi^{1/2}a}{H_{\max}^2 p}\exp\left(\frac{U_{\max}}{kT}\right) \;;\; p^2 = -\frac{\left(\partial^2 U/\partial H^2\right)_{H=H_{\max}}}{2kT} \qquad [1.19]$$

where H is as defined above. The approximate expression for W holds if p can be considered constant. If so, the ratio k_P/W is proportional to $\exp(-U_{max}/kT)$, i.e., the kinetic rate constant adopts the form of an Arrhenius-type expression. Clearly, an increase in U_{max} implies a reduction of the rate at which particles or droplets aggregate, as might be expected.

Whereas the DLVO theory as discussed above provides an elegant framework to understand the role of inter-particle interactions on aggregation and emulsion stability, it is strictly valid in a reduced number of practical cases, particularly when emulsions are of the O/W type and are stabilized by small-molecule ionic surfactants [24]. An important extension of the theory aims at accounting for the *steric repulsion* mechanism, in which the molecules adsorbed at the interfaces are voluminous and provide a physical barrier against flocculation and coalescence. In this case, an additional contribution to U due to steric repulsion, U_S, must be considered, i.e.,

$$U = U_A + U_E + U_S . \qquad [1.20]$$

U_A and U_E are affected by the presence of the adsorbed molecules at the interfaces. For the case of U_A, the adsorbed layer can be considered as a third material present in the system, in addition to the solvent and the dispersed phase, and therefore a third Hamaker constant must be included in the theoretical analysis [34]. Clearly, the attractive London-van der Waals force will increase or decrease if the value of the Hamaker constant for the adsorbed layer is respectively greater or smaller than those of the phases present in the dispersion. Regarding U_E, the adsorbed layer commonly imposes a redistribution of the ions in the electrical double layer and a change of the surface charge density. The net influence of the presence of macromolecules on U_E is

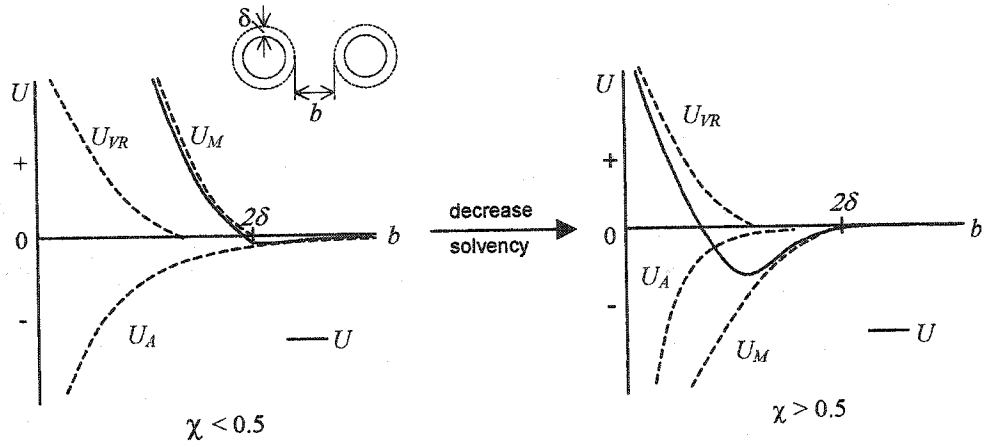


Figure 1.5. Sketch of interaction energies between two droplets stabilized by polymers.

specific to the nature of the adsorbing species and of the ionic species present, and a satisfactory theory to account in full for these effects is as yet not available.

In it simpler form, U_S is defined by two contributions, (a) a repulsive energy due to volume restrictions U_{VR}, and (b) an energy of mixing U_M, associated with the osmotic pressure that arises when the overlapping region of two approaching interfaces stabilized by macromolecules is depleted of solvent molecules [35].

Figure 1.5 shows a schematic representation of the interaction forces that arise when particles or droplets are stabilized by adsorbed polymeric species, modeled here as hard spheres surrounded by soft layers of thickness δ. It is first noticed that the electrostatic interaction U_E has been neglected. This is a valid assumption for drops in O/W emulsions stabilized with nonionic surfactants such as alkyl polyethylene oxides, or for emulsions in general that are stabilized with non-electrolitic homopolymers and copolymers of polyethylene oxide (PEO), polypropylene oxide (PPO), polyvinyl alcohol (PVA), polyacrylamide (PAM) and polystyrene (PS) among others. Second, it is seen

that U_M starts at a higher distance b than U_{VR}. This is due to the fact that osmotic effects arise as soon as the polymeric chains overlap, whereas some degree of deformation is needed to make the volumetric repulsion significant. Also, by comparing Figures 1.4 and 1.5 it is seen that the primary minimum that was associated with coagulation is no longer present, because in this case at short distances the volumetric repulsion easily overcomes the attractive forces due to London-van der Waals interactions.

More importantly, it is noted that the solvency has a significant effect on the overall interaction energy because it strongly affects the energy of mixing U_M. For the case of polymers, U_M is repulsive (positive) if the continuous phase is a good solvent for the stabilizing moiety of the adsorbed (macro)molecule, and it is attractive (negative) otherwise. By good solvent is meant that the continuous phase is better than a θ-solvent, i.e., that $\chi < 0.5$, χ being the well-known Flory-Huggins interaction parameter. It is seen that a decrease in solvency leads to the appearance of a deeper energy minimum.

Another contribution to the overall energy of interaction arises in the presence of non-adsorbing macromolecules in the bulk phase, due to a phenomenon referred to as *depletion interaction*. This effect favors aggregation because the adsorbed stabilizing layers tend to compress against each other in order to reduce the volume from which the non-adsorbing species are depleted and thus reduce the osmotic pressure. The mechanism has been remarked as important not only for polymers, but also for small particles and micelles in solutions where the surfactant concentration is as low as 1 percent above the cmc [24].

In light of these and other considerations [35], aggregation in emulsions stabilized with macromolecules is disfavored if (a) the stabilizing agent is well soluble in the continuous phase; (b) the polymer is well anchored at the water-oil interfaces; (c) the

adsorbed layer is sufficiently thick as to make the depth of the energy minimum small or negligible; (d) the concentration of adsorbing macromolecules suffices to completely cover the water/oil interfaces. Otherwise, some molecules would tend to adsorb at more than one interface and the so-called *bridging flocculation* would take place; (e) the concentration of non-adsorbing species is low to reduce the effect of depletion interaction.

1.2.4.3. Coalescence

Coalescence accounts for the rupture of the thin film of continuous phase that separates two nearby droplets.

Many theoretical and experimental efforts have been devoted to the understanding of the formation and thinning of a flat film between drops. However, it has been suggested [24] that in many practical cases a flat film is not developed because droplets remain spherical. The stability of very small films bounded by curved interfaces has to be considered from a different standpoint since the theories for drainage in flat films that are discussed later no longer apply in such cases. This refers to drops for which the internal Laplace pressure P_L significantly exceeds any external stress τ_{ext} exerted upon the doublet of drops, i.e.,

$$We = \frac{\tau_{ext}}{P_L} << 1 \qquad [1.21]$$

where We stands for a Weber number. It can be calculated that for drops below 5 μm in diameter exhibiting a relatively low interfacial tension ($\sigma \sim 1$ mN/m), $P_L = 2\sigma/a > 10^3$ Pa, whereas the τ_{ext} that is imposed by interactions among drops and/or external shearing or

buoyancy is about 10^2 Pa or less, whence We << 1 is satisfied. In this case, the following stability criterion has been suggested by Walstra [24]:

$$\frac{d^2U(h)}{dh^2} - \frac{dU(h)}{hdh} > -C\frac{\sigma}{a^2} \qquad [1.22]$$

based on a previous analysis by Vrij [36] (see Eq. [1.25]) on the coalescence of drops caused by the development of varicose capillary waves at the approaching interfaces, which eventually touch each other and initiate the rupture of the film [37]. In Eq. [1.22] $U(h)$ is the interaction energy between drops when the thickness of the film is h, and C > 0 is a constant. If the interaction energy U is calculated from the DLVO theory as before, it follows from Eq. [1.22] that coalescence would only take place if the drops get close enough as to reach the primary minimum (Figure 1.4). If so, the coalescence rate would be determined, among other factors, by the probability of overcoming U_{max}. For the case of emulsions stabilized by polymers, which do not exhibit such minimum (Figure 1.5), Eq. [1.22] suggests that coalescence of small drops would never take place. This is perhaps why some emulsions, particularly those stabilized with high molecular mass polymers and proteins, are regarded as kinetically stable [38]. But if drops are in contact long enough, for example after creaming, the adsorbed polymer layers could rearrange, possibly (but not certainly) leading to coalescence.

When We >> 1, large flat films are expected to develop. Deformation is favored in this case by large drop sizes and low interfacial tensions, i.e. by a reduction in P_L. Also, imposing large external force fields such as high-speed centrifugation induces the formation of flat films, since τ_{ext} increases appreciably. In this case, coalescence is preceded by the drainage of the liquid present in the film. The latter phenomenon has been modeled using hydrodynamic theory. Most theoretical approaches are sophistications of the analysis introduced by Reynolds [39] for the symmetrical drainage

of a film of Newtonian liquid with viscosity η that is confined between two flat disks of radii r and separated by a distance h, and for which $h/r << 1$. By solving the continuity equation and the equation of motion with suitable boundary conditions, the following expression for the rate of thinning of the film $-dh/dt$ is obtained

$$-\frac{dh}{dt} = \frac{2}{3}\frac{r\Delta P}{\eta}\left(\frac{h}{r}\right)^3 \qquad [1.23]$$

where ΔP is the difference in pressure across the disk. Eq. [1.23] shows that the rate dh/dt decays as the film thins symmetrically, as has been observed experimentally [40].

Reynolds' theory has been extended for fluid-fluid interfaces. Numerical results from more general models often indicate that drainage is accompanied by the formation of a dimple due to normal stresses acting upon the interfaces. Figure 1.6 shows calculations for the thinning of a film between two bubbles or droplets using a model reported by Joye *et al.* [41, 42].

Drainage of the dimple that forms in films between fluid-fluid interfaces has been observed to occur symmetrically [41] as referred above (Figure 1.7, left), but also asymmetrically (Figure 1.7, center) both in foam [42] and emulsion [40] film experiments. The prevailing drainage mode has a significant effect on the stability of the film and therefore on the characteristic time for coalescence, because asymmetrical drainage takes place much faster than axisymmetrical drainage. A stability criterion has been proposed for the case of foams stabilized by surfactants to discern which drainage mode would take place in a given system [42]:

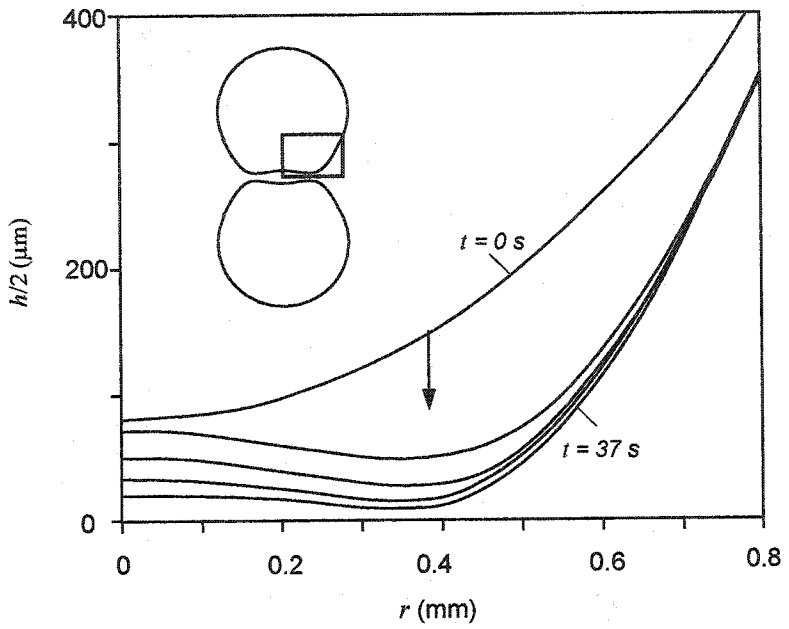


Figure 1.6. Transient behavior of a thin liquid film. The arrow indicates the direction in which the interface is displaced. The inserted drawing illustrates the section of the interface that is shown. The time lapse between initial and final positions is 37s. r_0 = 1 mm. h_0 = 160 nm. s = 0.5. σ = 72 mN/m. Interaction forces have been neglected in these calculations.

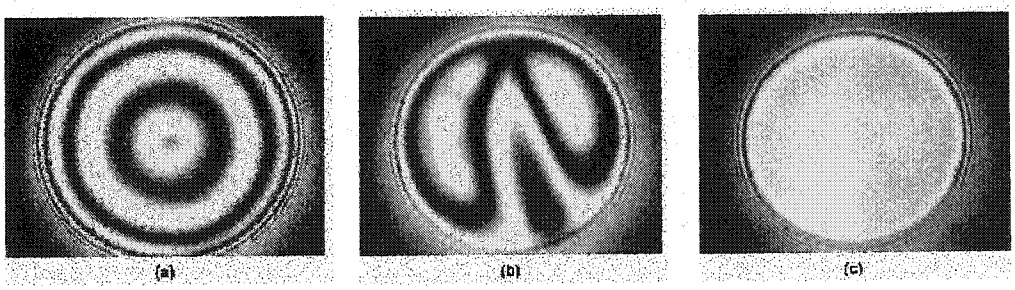


Figure 1.7. Upper view of interference patterns observed in the drainage of a thin film of a toluene diluted bitumen film in water. (a) drainage is axisymmetrical when the dimple is formed; (b) an instability develops and the drainage takes place asymmetrically; (c) an equilibrium gray film is obtained at the end. The film remained stable over one hour before break-up [40].

$$\left[\frac{D_S\eta_S\sigma}{\left(-\partial P^{SS}/\partial x\right)^2}+\frac{\sigma h_0\eta_S\Gamma_{eq}\alpha}{6\eta\left(-\partial P^{SS}/\partial x\right)^2}\right]\left(\frac{2\pi}{\lambda_y}\right)^6+$$
$$+\left[\frac{\sigma D_S\eta_S\left(\eta_d+\eta_S\right)h_0}{6\eta\left(-\partial P^{SS}/\partial x\right)^2}\right]\left(\frac{2\pi}{\lambda_y}\right)^8\begin{cases}>1, & stable\\ =1, & metastable\\ <1, & unstable\end{cases} \qquad [1.24]$$

By *stable* is meant that the drainage takes place symmetrically and vice versa. In Eq. [1.24], η_S and η_d are the surface shear and surface dilational viscosities ($kg.s^{-1}$), D_S is the surface diffusivity of the surfactant ($m^2.s^{-1}$), h_0 is the uniform thickness of the steady-state solution for the film, λ_y is the characteristic length of the perturbations in the direction transverse to the flow (m), Γ_{eq} is the equilibrium surfactant concentration at the surface and at rest ($kg.m^{-2}$) and $-\partial P^{SS}/\partial x$ is the pressure gradient along the direction of the flow at steady state, i.e., prior to imposing the perturbation. Experimental results for the drainage of foam films stabilized with sodium dodecyl sulfate (SDS) and a SDS/1-dodecanol mixture at several concentrations showed good agreement with the predictions of Eq. [1.24]. Moreover, it was found that the stability of the film increased when the surface shear viscosity was higher, a fact that has been noted in other independent experimental studies [43, 44] (See section 4.1.4.3).

The last stage of the drainage is in many cases the formation of a stable flat thin film (Figure 1.7, right). The equilibrium thickness of the film is determined in this case by the interaction energies considered above, which become significant when compared to hydrodynamic forces whenever the film thins to about 100 nm [41]. If the electrostatic repulsion is strong enough as to balance van der Waals attraction and the capillary pressure, the film is referred to as *common black film* (h ~ 20-30 nm). If the electrostatic repulsion is weak and short range repulsive forces dominate instead, the film is very thin

(h ~ 5-10 nm) and is referred to as *Newton black film*. Vrij [36] proposed a stability criterion for such films in the presence of destabilizing capillary waves,

$$\frac{d^2U(h)}{dh^2} > -\frac{2\pi^2\sigma}{r^2} \qquad [1.25]$$

where U is the overall interaction energy as before and r is the radius of the film. Eq. [1.25] indicates that film rupture is more likely to occur in large films exhibiting low interfacial tensions.

In other cases, materials present within the film determine the equilibrium thickness. The thinning process is referred to in this case as *stepwise drainage*. In this mechanism, isotropic structures in the 10-100 nm range, including micelles, finely divided solids or macromolecules such as proteins, protein aggregates and asphaltene/resins are present in the film as microlayers, and they are disrupted discontinuously as time proceeds until equilibrium is reached. Figure 1.8(a) shows results from reflected light interferometry for the thinning of a water film in oil containing a nonionic surfactant (ethoxylated alcohol) [45]. The discontinuities in the curve correspond to transitions in which one layer of micelles is eliminated at a time. It has been shown that microlayering is a universal phenomenon that differs from the common/Newton black film mechanism referred to above [46]. In this case, the DLVO approach is no longer valid because the distances between interfaces are usually high enough due to the presence of the microstructures as to make the van der Waals attractive forces negligible. It has been shown by Wasan and co-workers [47] and by Ivanov and co-workers [37] that ordered microstructures within the film impose an oscillatory force able to stabilize the film (Figure 1.8(b)). Oscillatory disjoining pressure isotherms have also been reported by Bergeron and Radke [48] for foam films stabilized with sodium dodecyl sulfate above the critical micelle concentration.

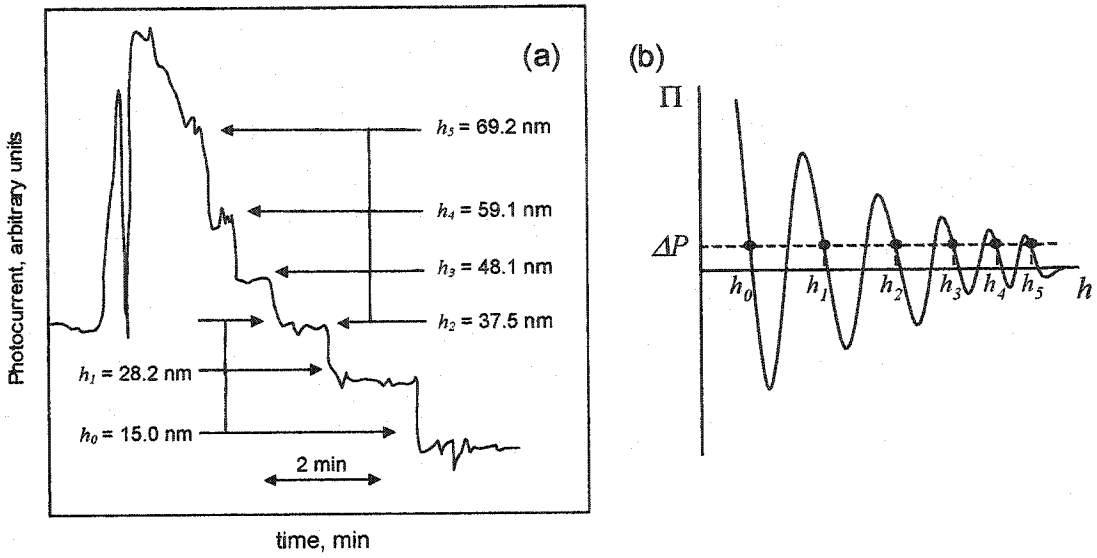


Figure 1.8. (a) Interferogram showing the stepwise thinning of a film of aqueous nonionic micellar solution (Adapted from Ref. [45]); (b) Schematic plot of the disjoining pressure Π vs. film thickness h. The equilibrium states of the liquid film correspond to $\Pi = \Delta P$, where ΔP is the pressure difference across the film [37].

So far we have considered the conditions under which a flat film is/is not expected to form, and the stability criteria for the drainage and break-up of the film in either case. It remains to review the kinetics of coalescence, i.e., the rates at which the number of droplets diminishes in time. The models available in literature, such as those by van den Tempel [49], Borwankar et al. [50] and Danov et al. [51] are in essence extensions of the aggregation model described in Section 1.2.4.2, and they rely on a number of empirical rate constants that are determined for particular experimental systems as fitting parameters. A recent, more comprehensive model by Dukhin and Sjöblom [38, 52] for dilute O/W emulsions combines aggregation, dissagregation and coalescence and refers the relative kinetic rates as the inverse of characteristic times for each event. The model is defined by two coupled ordinary differential equations, the first one standing for the rate of change in the (dimensionless) number of doublets $n_2 = N_2/N_{1,0}$,

$$\frac{dn_2}{dt} = \frac{n_1^2}{\tau_{Sm}} - n_2\left(\frac{1}{\tau_d} + \frac{1}{\tau_c}\right) \qquad [1.26]$$

and the second accounting for the decrease in droplet concentration due to coalescence,

$$\frac{d}{dt}\left(n_1 + 2n_2\right) = -\frac{n_2}{\tau_c} \text{ whence } \frac{dn_1}{dt} = n_2\left(\frac{1}{\tau_c} + \frac{2}{\tau_d}\right) - 2\frac{n_1^2}{\tau_{Sm}} \qquad [1.27]$$

subject to the following initial conditions:

$$n_1\big|_{t=0} = 1; \quad n_2\big|_{t=0} = 0; \quad \left.\frac{dn_2}{dt}\right|_{t=0} = \frac{1}{\tau_{Sm}} \qquad [1.28]$$

In these expressions, $n_1 = N_1/N_{1,0}$ is the dimensionless number concentration of individual drops, τ_{Sm} is the Smoluchowski time or average time between collisions of droplets, and is given by,

$$\tau_{Sm} = \left(k_P\, N_{1,0}\right)^{-1} \qquad [1.29]$$

where k_P is the perikinetic aggregation constant defined by Eq. [1.16], τ_d is the characteristic time for the dissagregation of doublets and τ_c is the characteristic coagulation time. For doublets of charged droplets, the following expression for τ_d has been proposed:

$$\tau_d = \frac{6\pi\eta a^3}{kT}\exp\left(-\frac{U_{\min}}{kT}\right) \qquad [1.30]$$

where $U_{\min}$ is the depth of the interaction energy minimum as obtained with the DLVO theory. An analytical expression for τ_c is yet to be proposed.

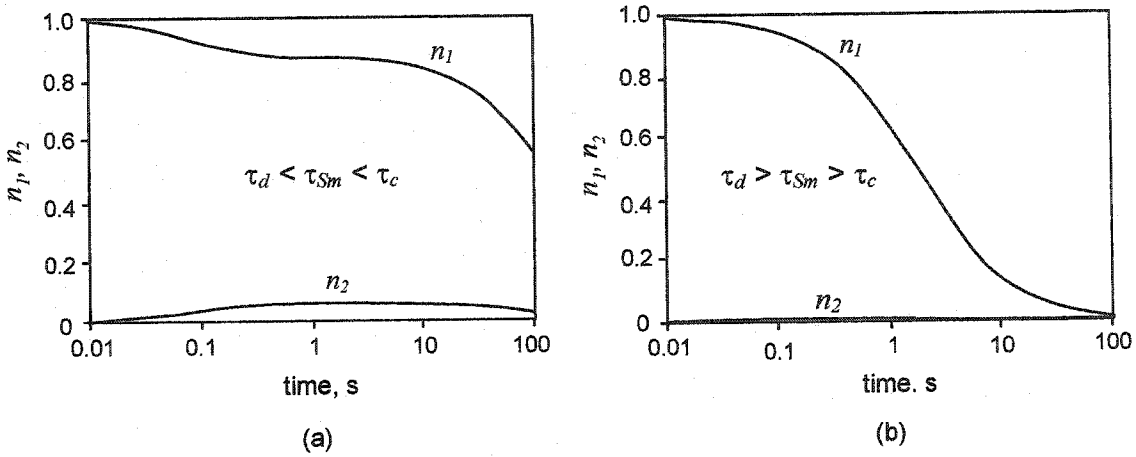


Figure 1.9. Time-dependent behavior of the concentration of single drops (n_1) and doublets (n_2) in a 5 vol. % O/W emulsion undergoing aggregation and coalescence. (a) fast aggregation, slow coalescence. (b) slow aggregation, fast coalescence. Parameters: T = 298 K, η = 1 mPa.s, a = 1 μm, (τ_{Sm} = 1.7 s) (a) U_{min} = -45kT (τ_d = 0.1 s), τ_c = 10 s (b) U_{min} = -40kT (τ_d = 19.5 s), τ_c = 0.01 s.

Figure 1.9 shows numerical results from Eqs. [1.26]-[1.30] for the transient behavior of the concentration of individual droplets (n_1) and doublets (n_2) for slow and fast coalescence regimes. The observed trends are physically meaningful (i.e., the decay of n_1 takes place much faster in the fast coalescence regime at comparable conditions), but it is clear that the model is a simplification of the actual coalescence process. For example, the effect of polydispersity in drop sizes, and the change in size of drops once coalescence takes place is not considered. This suggests that τ_d is not constant, but that it is shifted towards higher values as coalescence proceeds (see Eq. [1.30]). Also, the formation of flocculates (i.e., triplets and aggregates with higher number of drops) is neglected. The effect of creaming, which might lead to a distribution of characteristic times –shorter values in the creamed layer and longer values for drops still dispersed in the more dilute regions of the emulsion- is not considered either.

1.3. REFERENCES

1. J.G. Berryman, Random close packing of hard spheres and disks, *Phys. Rev. A*, **27** (1983) *1053-1061*
2. W. Ostwald, Beiträge zur kenntnis der emulsionen, *Kolloid-Z.*, **6** (1910) *103-109*
3. A.S. Kabalnov and E.D. Shchukin, Ostwald ripening theory: applications to fluorocarbon emulsion stability, *Adv. Colloid Interface Sci.*, **38** (1992) *69-97*
4. C.A. Miller, Spontaneous emulsification produced by diffusion - a review, *Colloids and Surfaces*, **29** (1988) *89-102*
5. T. Nishimi and C.A. Miller, Spontaneous emulsification produced by chemical reactions, *J. Colloid Interface Sci.*, **237** (2001) *259-266*
6. G.J. Vaessen, "Predicting catastrophic phase inversion in emulsions". PhD Thesis. Eindhoven University of Technology. Eindhoven, The Netherlands, 1996.
7. J.L. Salager, M. Miñana-Pérez, M. Pérez-Sánchez, M. Ramírez-Gouveia, and C. Rojas, Surfactant-oil-water systems near the affinity inversion. 3. The two kinds of emulsion inversion, *J. Disp. Sci. Technol.*, **4** (1983) *313-329*
8. Ø. Sæther, Video-enhanced microscopy investgation of emulsion droplets and size distributions, in "Encyclopedic Handbook of Emulsion Technology", J. Sjöblom, Editor. Marcel Dekker, Inc., New York, 2001, pp. 349-360.
9. P. Sherman, "Emulsion Science", Academic Press, London, 1968.
10. B. Epstein, Logarithmico-normal distribution in breakage of solids, *Ind. Eng. Chem.*, **40** (1948) *2289-2290*
11. J. Lachaise, B. Mendiboure, C. Dicharry, G. Marion, M. Bourrel, P. Cheneviere, and J.L. Salager, A simulation of emulsification by turbulent stirring, *Colloids Surf. A: Phys. Chem. Eng. Aspects*, **94** (1995) *189-195*
12. C. Orr, Emulsion droplet size data, in "Encyclopedia of Emulsion Technology", P. Becher, Editor. Volume 1. Chapter 6. Marcel Dekker, New York, 1983.
13. R.G. Larson, "The structure and rheology of complex fluids", Oxford University Press, New York, 1999.
14. A. Einstein, Eine neue bestimmung der moleküldimensionen, *Ann. Physik*, **19** (1906) *289-306*
15. A. Einstein, Berichtigung zu meiner arbeit: "Eine neue bestimmung der moleküldimensionen", *Ann. Physik*, **34** (1911) *591-592*
16. P.C. Hiemenz, "Principles of colloid and surface chemistry", Marcel Dekker, Inc., New York, 1986.
17. R. Pal and E. Rhodes, Viscosity-concentration relationships for emulsions, *J. Rheol.*, **33** (1989) *1021-1045*
18. R. Pal, Effect of droplet size on the rheology of emulsions, *AIChE J.*, **42** (1996) *3181-3190*
19. P. Becher, "Emulsions. Theory and Practice", Oxford University Press, New York, 2001.
20. J.L. Salager, Emulsion properties an related know-how to attain them, in "Pharmaceutical Emulsions and Suspensions", F. Nielloud and G. Marti-Mestres, Editors. Marcel Dekker, Inc., New York, 1998.

21. M. Ramírez, "Influence of particle size distribution on the properties of emulsions and emulsion mixtures" (In Spanish). FIRP Laboratory. Technical Report 9210. Universidad de Los Andes, Mérida, Venezuela, 1992.

22. R. Pal, Viscosity and storage/loss moduli for mixtures of fine and coarse emulsions, *Chem. Eng. J.*, **67** (1997) *37-44*

23. R. Pal, A novel method to correlate emulsion viscosity data, *Colloids Surf. A: Phys. Chem. Eng. Asp.*, **137** (1998) *275-286*

24. P. Walstra, Emulsion stability, in "Encyclopedia of Emulsion Technology", P. Becher, Editor. Vol. 4. Marcel Dekker, Inc., New York, 1990, pp. 1-62.

25. G.K. Batchelor, Sedimentation in a dilute dispersion of spheres, *J. Fluid Mech.*, **52** (1972) *245-268*

26. J.F. Richardson and W.N. Zaki, Sedimentation and fluidisation: Part I, *Trans. Inst. Chem. Eng.*, **32** (1954) *35-53*

27. E. Dickinson, Sedimentation of interacting colloidal particles, *J. Colloid Interface Sci.*, **73** (1980) *578-581*

28. B.V. Derjaguin and L. Landau, *Acta Physicochem. URSS*, **14** (1941) *633*

29. E.J.W. Verwey and J.T.G. Overbeek, "Theory of the Stability of Lyophobic Colloids", Elsevier, Amsterdam, 1948.

30. H.C. Hamaker, The London-van der Waals attraction between spherical particles, *Physica*, **4** (1937) *1058-1072*

31. C.A. Miller and P. Neogi, "Interfacial Phenomena: Equilibrium and Dynamic Effects", Marcel Dekker, Inc., New York, 1985.

32. M.V. Smoluchowski, Versuch einer mathematischen theorie der koagulationskinetik kolloider lösungen, *Z. Phys. Chem.*, **92** (1918) *129-168*

33. N. Fuchs, Über die stabilität und aufladung der aerosole, *Z. Physik*, **89** (1934) *736-743*

34. M.J. Vold, The effect of adsoprtion on the van der Waals interaction of spherical colloidal particles, *J. Colloid Sci.*, **16** (1961) *1-12*

35. T.F. Tadros and B. Vincent, Emulsion stability, in "Encyclopedia of Emulsion Technology", P. Becher, Editor. Chapter 1. Marcel Dekker, Inc., New York, 1983, pp. 129-284.

36. A. Vrij, Posible mechanism for the spontaneous rupture of thin free liquid films, *Disc. Faraday Soc.*, **42** (1966) *23-33*

37. K.D. Danov, P.A. Kralchevsky, and I. Ivanov, Dynamic processes in surfactant-stabilized emulsions, in "Handbook of Emulsion Technology", J. Sjöblom, Marcel Dekker, Inc., New York, 2001, pp. 621-659.

38. S. Dukhin, Ø. Sæther, and J. Sjöblom, Coupling of coalescence and flocculation in dilute O/W emulsions, in "Encyclopedic Handboook of Emulsion Technology", J. Sjöblom, Editor, Marcel Dekker, New York, 2001, pp. 71-94.

39. O. Reynolds, On the theory of lubrication and its application to Mr. Beauchamp Tower's experiments, including an experimental determination of the viscosity of olive oil, *Philos. Trans. R. Soc. London*, **177** (1886) *157-234*

40. K. Khristov, S.D. Taylor, J. Czarnecki, and J. Masliyah, Thin Liquid Film Technique - applications to water-oil-water bitumen emulsion films, *Colloids Surf. A.: Phys. Chem. Eng. Aspects*, **174** (2000) *183-196*

41. J.-L. Joye, C.A. Miller, and G.J. Hirasaki, Dimple Formation and Behavior during Axisymmetrical Foam Film Drainage, *Langmuir*, **8** (1992) *3083-3092*

42. J.-L. Joye, G.J. Hirasaki, and C.A. Miller, Asymmetric Drainage in Foam Films, *Langmuir*, **10** (1994) *3174-3179*

43. E. Dickinson, B.S. Murray, and G.J. Stainsby, Coalescence stability of emulsion-sized droplets at a planar oil-water interface and the relationship to protein film surface rheology, *J. Chem. Soc., Faraday Trans. 1*, **84** (1988) *871-883*

44. P. Becher, Water-in-oil emulsions, in "Interfacial Phenomena in Apolar Media", H.F. Eicke and G.D. Parfitt, Editors, Marcel Dekker, Inc., New York, 1987, pp. 257-280.

45. D.T. Wasan, Foam and emulsion stability: interfacial rheology and thin liquid film phenomena, in "Emulsions, foams and thin films", K.L. Mittal and P. Kumar, Editors, Marcel Dekker, Inc., New York, 2000.

46. D.T. Wasan and A.D. Nikolov, Structure and stability of emulsions, in "Encyclopedic Handbook of Emulsion Technology", J. Sjöblom, Editor, Marcel Dekker, Inc., New York, 2001, pp. 59-70.

47. P.J. Breen, D.T. Wasan, Y.H. Kim, A.D. Nikolov, and C.S. Shetty, Emulsions and emulsion stability, in "Emulsions and Emulsion Stability", J. Sjöblom, Marcel Dekker, Inc., New York, 1996, pp. 237-285.

48. V. Bergeron and C.J. Radke, Equilibrium measurements of oscillatory disjoining pressures in aqueous foam films, *Langmuir*, **8** (1992) *3020-3026*

49. M. van den Tempel, Stability of oil-in-water emulsions I. The electrical double layer at the water-oil interface, *Rec. Trav. Chim. Pays-Bas*, **72** (1953) *419-432*

50. R. Borwankar, L. Lobo, and D.T. Wasan, Emulsion stability - kinetics of flocculation and coalescence, *Colloids Surfaces*, **69** (1992) *135-146*

51. K.D. Danov, I. Ivanov, T. Gurkov, and R. Borwankar, Kinetic model for the simultaneous processes of flocculation and coalescence in emulsion systems, *J. Colloid Interface Sci.*, **167** (1994) *8-17*

52. S.S. Dukhin and J. Sjöblom, Fragmentation of primary flocs in emulsions and the subsequent reduction of coalescence, *J. Disp. Sci. Technol.*, **19** (1998) *311-327*

Chapter 2

Destabilization of emulsions via mass transfer

*Solubilization, Ostwald ripening and compositional ripening in emulsions of hydrocarbons dispersed in nonionic surfactant solutions**

2.1. INTRODUCTION

The role of mass transport on emulsion stability has been the subject of a number of research efforts that may seem unrelated in many cases. Firstly, some investigations [1, 2] report experiments on the solubilization of oil droplets in micellar aqueous surfactant solutions when the concentration of the transferred oil in the bulk phase is below the saturation limit (hereafter referred to as the equilibrium solubilization capacity). It might be expected that droplet sizes would diminish because oil is transferred from drops to solution (Figure 2.1, top), but these studies indicate that the mean size does not change appreciably in time or even increases in some cases. An explanation for these counterintuitive observations is provided in this chapter.

Secondly, several studies [3-9] have dealt with the so-called Ostwald ripening (Figure 2.1, middle), a phenomenon in which bigger drops grow at the expense of smaller drops due to the well-known Kelvin effect [10]. In contrast to the solubilization studies referred to earlier, Ostwald ripening takes place when the bulk phase is slightly supersaturated in the solute that is being transferred. The so-called LSW theory, often used to analyze Ostwald ripening data, was developed by Lifshitz and Slyozov [11] and Wagner [12] to model precipitation from supersaturated solutions.

---

* Published in part in Peña, A. A. and Miller, C. A. *Journal of Colloid and Interface Science.* **244** (2001) *154-163* and Peña, A. A. and Miller, C. A. *Industrial & Engineering Chemistry Research.* **41** (2002) *6284-6296*

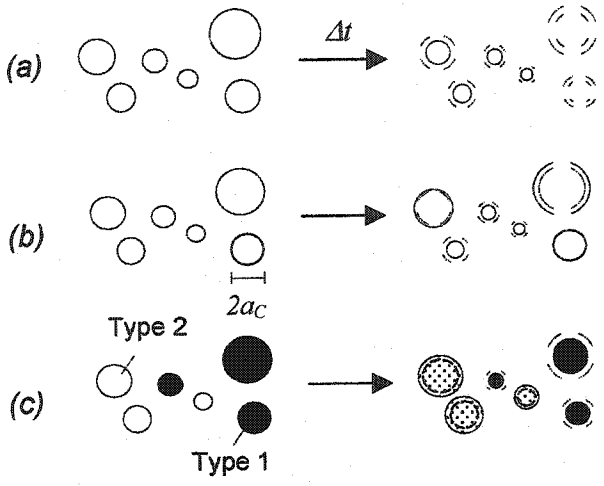


Figure 2.1. Schematic representations showing the transient behavior of drops sizes in emulsions undergoing mass transfer. (a) Solubilization of drops in an undersaturated surfactant solution: as time proceeds, a reduction in the sizes of the droplets is expected; (b) Ostwald ripening: drops with radii $a(t)$ greater than a critical size $a_C(t)$ grow, while those with $a(t) < a_C(t)$ shrink; (c) compositional ripening in a mixed emulsion containing two drop types, with one of them (white circles) being insoluble in the surfactant solution: the latter grow at the expense of the solubilization of drops containing a soluble solute (black circles).

Finally, when more than one solute is present in the emulsion, differences in concentration among droplets drive mass exchange and induce changes in their sizes [13-15] (Figure 2.1, bottom). This phenomenon, which has been referred to as compositional ripening [2], is frequently regarded as a particular case of Ostwald ripening [8, 16]. However, this generalization is inadequate because in the case of compositional ripening mass transfer is not dictated by differences in drop sizes.

In all these cases, it is necessary to dissolve the transferred materials in the continuous phase, and therefore the kinetics of dissolution play a key role in determining the transient characteristics of ripening emulsions. Dissolution in water/oil/surfactant systems takes place through mechanisms that occur at the molecular level. Kinetic studies aim at determining the limiting step(s) within such mechanisms that dictate mass

transfer rates and transient behavior. Most kinetic studies have been interpreted in terms of (a) the diffusion of the transferred solutes in the bulk as individual molecules [13, 17] or incorporated in micellar aggregates [14, 15]; (b) the interfacial resistance to mass transfer, which may refer to transport across a surfactant monolayer or some other physical barrier when molecular dissolution prevails [18-20] or to the adsorption and emission of micelles that act as carriers for the transported compounds [21-31]; or (c) the molecular diffusion of the solute in the continuous phase and subsequent capturing by surfactant micelles [32, 33].

This chapter reports experimental data for the kinetics of dissolution of single drops of hydrocarbons (pure C_8-C_{11} linear alkanes, octane/undecane, decane/undecane, octane/squalane and decane/squalane mixtures) in aqueous solutions containing a nonionic surfactant ($C_{12}E_8$) at concentrations well above the *cmc*. Results for the solubilization of octane drops indicated that at low surfactant concentrations (0.25 - 0.50 wt.%) both interfacial resistance to mass transfer and diffusion of micelles carrying solubilized oil significantly influenced the solubilization rate. When the surfactant concentration was increased (1.0 - 3.75 wt.%), spontaneously generated convection in the aqueous phase and Rybczynski-Hadamard circulation within the drops were observed. It is demonstrated that in such cases convection aided mass transport in the bulk phase and reduced the diffusional resistance, thus making interfacial resistance rate-controlling. The interfacial mass transfer coefficient was proportional to the first power of the surfactant concentration, which suggests that the adsorption/fusion and desorption/emission of micelles carrying oil molecules was the elementary molecular step within the kinetic mechanism that dictated the rates of solubilization. Significant spontaneously-generated convection was also observed in the solubilization of

undecane in aqueous $C_{12}E_8$ (2.5 wt.%). All experiments for hydrocarbon mixtures were performed in $C_{12}E_8$ 2.5 wt.% solutions, and the results were successfully correlated without adjustable parameters with a plausible mass transfer model that assumes interfacial resistance as rate-controlling.

The above-mentioned model was extended to account for mass-transfer kinetics in polydisperse emulsions and emulsion mixtures. The model was applied to simulate experiments reported in the literature for mass transport in emulsions of hydrocarbons in nonionic surfactant solutions. Three case studies representative of the processes depicted in Figure 2.1 are presented and discussed. In doing so, we aim at showing that these diverse phenomena can be accounted for with a single theoretical model.

2.2. THEORY

Two different approaches are commonly followed in the theoretical and experimental evaluation of mass transfer in emulsions. The first one relies on the measurement of solubilization rates of individual drops, usually oil in aqueous solution. The second approach consists of following –both theoretically and experimentally- the size of droplets in emulsions, assuming that the effects of destabilizing mechanisms different from mass transport are negligible or at least secondary.

2.2.1. Solubilization of individual droplets

The dissolution of individual drops in micellar solutions is usually followed through optical methods such as microphotography [21] or videomicroscopy [34, 35]. The change in geometry can be related to the molar solubilization rate (J). For a spherical

drop of radius a that is either pure or that contains only one mobile solute, J can be defined as:

$$J \equiv -\frac{1}{A}\frac{dn}{dt} = \frac{1}{v}\left(-\frac{da}{dt}\right) \qquad [2.1]$$

Here n is the number of moles of solute in the drop, A is the interfacial area and v is the molar volume of the solute. Let c^{o}_{sat} be the equilibrium solubilization capacity of the pure solute in the bulk phase when contacted across a flat interface. Solubilization across an interface with finite curvature radius a is driven by the difference between the local solubilization capacity at the interface c_I -which may differ from c^{o}_{sat} due to composition and curvature as explained later-, and the concentration of solute in the bulk solution away from the interface, c_B (Figure 2.2). Let c^* be the concentration of solute at a position near the droplet-bulk solution interface such that:

$$J = J_I = \frac{c_I - c^*}{\Re_I}; \quad J = J_B = \frac{c^* - c_B}{\Re_B}, \text{ whence } J = \frac{c_I - c_B}{\Re_I + \Re_B} \qquad [2.2]$$

Here, $\Re_I$ accounts for the resistance to mass transport at the interface, and $\Re_B$ quantifies the resistance to mass transport in the bulk phase. Eq. [2.2] implies no accumulation of solute in the interfacial region. The concentrations defined above refer to moles of solute dissolved either as individual molecules or within micellar aggregates per unit volume of solution. The theory is further developed on this basis, and applied to the case in which molecular solubility is significantly smaller than the solubility in the micellar solution. It can be extended to account for simultaneous micellar (M) and molecular (m) solubilization since $J = J_{I,M} + J_{I,m} = J_{B,M} + J_{B,m}$, with J_I and J_B given by

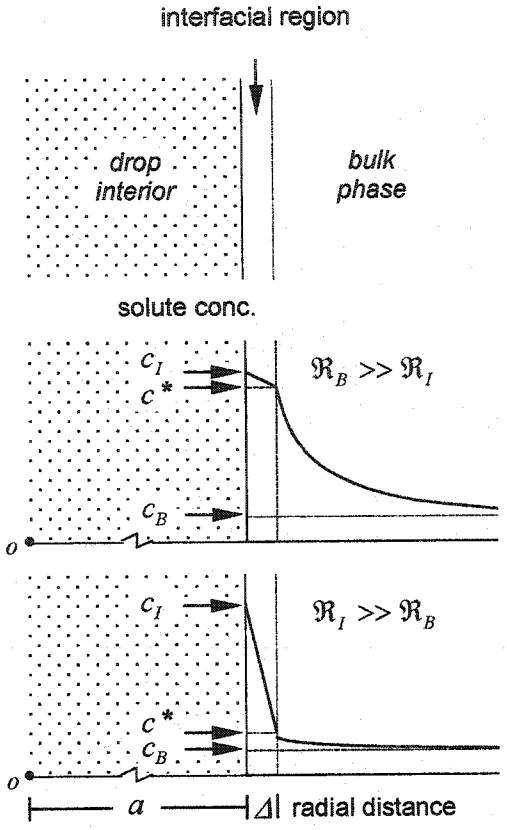


Figure 2.2. Basic configuration of the water-oil interfacial region showing the quasi-steady interface-controlled concentration profile of a solute being transferred from drop to solution.

Eq. [2.2] with the corresponding micellar and molecular concentrations of solute and resistances.

If bulk diffusion controls mass transport between a spherical droplet and the bulk solution in which it is suspended (Figure 2.2, middle), J is dictated by:

$$J = \frac{D}{a+\Delta}\left(c^* - c_B\right) \cong \frac{D}{a}\left(c_I - c_B\right), \text{ whence } \frac{da}{dt} = \frac{Dvc^o_{sat}}{a}\left(\frac{c_B}{c^o_{sat}} - \frac{c_I}{c^o_{sat}}\right) \qquad [2.3]$$

D is the diffusion coefficient and Δ is discussed later. The expression for J on the left hand side is obtained from a quasi-steady approximation of the solution of the diffusion

equation in the bulk phase region, as presented by Smoluchowski [36]. It assumes no interfacial barrier to mass transport and neglects hydrodynamic effects. This expression suggests that the drop size significantly affects the solubilization rate. It is a particular case of Eq. [2.2] for which $\Re_B >> \Re_I$, with

$$\frac{1}{\Re_B} = \frac{D}{a} \qquad [2.4]$$

and local equilibrium at the interface ($c_I \sim c^*$). Eq. [2.3] has been used previously to model mass transport in emulsions [13-15, 18-20, 37]. It is strictly valid for infinitely dilute emulsions with negligible hydrodynamic effects.

A case study of interface-controlled mass transfer kinetics is the dissolution of individual drops of pure non-polar oils in aqueous nonionic surfactant solutions when $c_B/c^o_{sat} \sim 0$ and $c_I/c^o_{sat} \sim 1$, for which it was found that a decays linearly in time at a rate that is proportional to c_S, the surfactant concentration available to form micelles [21, 22, 25]. In these experiments, c_S is greater than the *cmc* and solubilization of oil in micelles at the interfaces is thought to play a key role in the kinetic mechanism. Eq. [2.2] properly accounts for these features since in this case, $\Re_I >> \Re_B$ and also $c^* \sim c_B$ because diffusion is not limiting (Figure 2.2, bottom). If so:

$$J \cong \frac{c_I - c_B}{\Re_I} \text{ , whence } \frac{da}{dt} = k^o v \left(\frac{c_B}{c^o_{sat}} - \frac{c_I}{c^o_{sat}} \right) \qquad [2.5]$$

$k^o \equiv c^o_{sat}/\Re_I$ is a specific solubilization rate constant with units of mol·(length)$^{-2}$·(time)$^{-1}$, The superscript ° indicates that the designated quantity refers to the pure solute. Eq. [2.5] is the proposed counterpart to Eq. [2.3] for the case in which interfacial resistance to mass transport dictates the transient size of spherical droplets.

The interfacial resistance to mass transfer, $\Re_I$, can be interpreted in different ways. For example, if it is assumed that solubilization at the interface is retarded by the transport of solute through an interfacial region of thickness Δ (Figure 2.2), the diffusion equation may be solved for such region to find $\Re_I = \Delta/D_I$, *with* D_I being an "effective" diffusion coefficient. On the other hand, if events like the adsorption and desorption of micelles at the interface dictate mass transport kinetics, $\Re_I$ most likely depends on the characteristic timescales of such events, Δ may be comparable to the size of the micelles as suggested by Carroll [21], and convection should not have significant influence on the dissolution rates. The mechanisms through which surfactant molecules are transferred from micelles in the bulk phase to the interface and solute from the dispersed phase to micelles -and vice versa- have been considered previously [21, 27, 38, 39] and are discussed in detail later. It suffices to say here that the experiments referred to above suggest that if micellar adsorption/desorption are limiting, $\Re_I$ is constant throughout the solubilization tests and thus independent of the droplet size.

When local equilibrium between the drop interior and the interface is achieved, the concentration of solute at the interface c_I differs from the equilibrium solubilization capacity c^o_{sat} by a factor that includes the difference in chemical potential due to curvature and composition. For an ideal mixture in the drop, these quantities are related for a given solute by [14]:

$$\frac{c_I}{c^o_{sat}} = \exp\left(\frac{\Delta\mu}{RT}\right) \quad \text{where} \quad \Delta\mu = \mu(x,a) - \mu^0 = RT \ln x + \frac{2\sigma v}{a} \qquad [2.6]$$

and thus $c_I / c^o_{sat} = x \cdot \exp(2\sigma v / RTa)$. Here, σ is the water-oil interfacial tension and $\mu(x, a)$ and μ^o are the chemical potentials of the solute in a drop of size a and molar composition

x, and of pure solute in contact with the same bulk solution across a flat interface, respectively.

Eqs. [2.3], [2.5] and [2.6] can be combined to predict the drop size evolution in a number of particular cases. It is relevant for this work to consider the solubilization of drops of a binary mixture of oils in aqueous surfactant solution, with one of the oils being insoluble in the aqueous phase and the other oil exhibiting limited but measurable solubility in the aqueous solution. The concentration of the soluble oil in the aqueous phase at the beginning of the test is $\theta^o \equiv c_B / c^o_{sat}$. Two additional assumptions are made. First, it is said that θ^o remains constant during the solubilization test. Second, it is assumed that the contribution of the drop curvature to the chemical potential in Eq. [2.6] is negligible, i.e., $\exp(2\sigma v / \mathrm{R}Ta) \cong 1$. The first assumption seems plausible for a typical single-drop solubilization experiment, since the volumes of surfactant solution and oil commonly differ by more than a million-fold. It will be shown that the second assumption is valid for all mass transfer processes discussed in this chapter, with the notable exception of Ostwald ripening. When these assumptions are valid, both Eq. [2.3] and Eq. [2.5] become ordinary differential equations in a that can be solved explicitly when combined with a suitable expression for x, which is readily obtained from a mass balance in the drop:

$$x = \frac{r^3 - \phi}{r^3 - \phi(1-\delta)}, \quad \text{where} \quad r = \frac{a}{a_0}; \ \phi = \frac{1-x_0}{1-x_0(1-\delta)}; \ \delta = \frac{v_m}{v_i} \qquad [2.7]$$

The parameters a_0, x_0 and ϕ are the initial values for the drop radius, molar fraction of the soluble oil and volume fraction of the immobile oil in the drop, and v_m and v_i are the molar volumes of the mobile and immobile oil, respectively.

For the case in which mass transfer at the interface is regarded as limiting, Eq. [2.5] becomes

$$dr/d\tau = \theta^o - x \qquad [2.8]$$

with the dimensionless time τ defined as $\tau = (k^o v_m/a_0)\ t$. The following expressions are obtained by substituting [2.7] in [2.8] and integrating:

$$\tau = \frac{1}{1-\theta^o}\cdot\left[1-r+\frac{\delta\kappa}{6\left(1-\theta^o+\delta\theta^o\right)}\left(B-C\right)\right] \quad \text{if} \quad 0 \le \theta^o < 1 \qquad [2.9]$$

$$\tau = \frac{1-\delta}{\delta}\cdot\left[1-r-\frac{1}{4(1-\delta)\phi}\left(1-r^4\right)\right] \qquad \text{if} \quad \theta^o = 1 \qquad [2.10]$$

On the other hand, if diffusion dictates the time-dependent behavior of droplet size, Eq. [2.3] becomes

$$dr/d\tau' = (\theta^o - x)/r \qquad [2.11]$$

τ' being defined for this case as $\tau' = \left(Dc^o_{sat} v_m/a_0^2\right)t$. Therefore:

$$\tau' = \frac{1}{1-\theta^o}\cdot\left[\frac{1}{2}\left(1-r^2\right)+\frac{\delta\phi}{6\left(1-\theta^o\right)\kappa}\left(B+C\right)\right] \quad \text{if} \quad 0 \le \theta^o < 1 \qquad [2.12]$$

$$\tau' = \frac{1-\delta}{\delta}\cdot\left[\frac{1}{2}\left(1-r^2\right)-\frac{1}{5(1-\delta)\phi}\left(1-r^5\right)\right] \qquad \text{if} \quad \theta^o = 1 \qquad [2.13]$$

The parameters κ, B and C are given by:

$$\kappa \equiv \left[\phi\left(1+\delta\frac{\theta^o}{1-\theta^o}\right)\right]^{1/3} \ ; \ B = ln\left[\frac{(1-\kappa)^3}{(r-\kappa)^3}\cdot\frac{r^3-\kappa^3}{1-\kappa^3}\right] \ ; \ C = 2\sqrt{3}\,tan^{-1}\left[\frac{2\sqrt{3}\kappa(1-r)}{\kappa(1+r+2\kappa)+2r}\right] \qquad [2.14]$$

It can be shown that Eqs. [2.9] and [2.12] reduce to Eqs. [2.10] and [2.13] respectively in the limit $\theta^o \rightarrow 1$. For either mechanism, the relationship between dimensionless drop radius r and time τ or τ' that corresponds to a given set of experimental conditions is determined by computing the parameters δ, ϕ and κ, and then evaluating either τ or τ' at a given θ^o for arbitrary but meaningful values of r. That is, if the initial molar fraction of mobile oil exceeds the relative saturation of the surfactant solution ($x_0 > \theta^o$), then this oil will be transferred from the drop to the aqueous bulk phase, and therefore the radius of the droplet will *diminish* ($r \leq 1$). Analogously, the drop will *grow* ($r \geq 1$) whenever the relative saturation of the solution exceeds x_0. Clearly, $x_0 = \theta^o$ corresponds to the equilibrium condition for the system, from which the limiting drop size can be calculated.

A more general case for solubilization of individual droplets is that of a multi-component system in which an arbitrary number of species exhibits measurable solubility in the surfactant solution. Let us consider the case in which interfacial resistance to mass transfer limits mass transport kinetics, with some of the constraints stated above, namely: negligible effect of interfacial curvature on the concentration of all species at the interface and negligible change in concentration of all the solutes in the bulk phase.

Eqs. [2.1] and [2.5] can be extended to account for the number of moles of any individual component j in the mixture of solutes present in the drop as follows:

$$\frac{dn_j}{dt} = 4\pi a^2 k_j \left(\frac{c_{B,j}}{c_{sat,j}} - \frac{c_{I,j}}{c_{sat,j}} \right). \qquad [2.15]$$

In this case k, c_B, c_I and c_{sat} are referred to solute j. For example, $c_{sat,j}$ refers to the concentration of species j when the aqueous solution is in equilibrium with the oil drop, and it can be related to $c^o_{sat,j}$ by Raoult's law. That is:

$$c_{sat,j} = c^o_{sat,j}\,\mathbf{a}_j \qquad [2.16]$$

where $\mathbf{a}_j$ is the activity of solute j in the mixture, and it can be determined experimentally or calculated with the aid of thermodynamics of micellar solubilization [40]. In either case, the outcome would be a function of the form:

$$\mathbf{a}_j = \mathbf{a}_j(\underline{x},T) \therefore \underline{x} = \{x_1, x_2, ..., x_j, ...x_m\};\ \lim_{x_j \to 0}(\mathbf{a}_j) = 0; \lim_{x_j \to 1}(\mathbf{a}_j) = 1. \qquad [2.17]$$

If the mixture in the drop is considered ideal,

$$\mathbf{a}_j = x_j \qquad [2.18]$$

For small deviations from ideal behavior, the first-order correction of the Flory-Huggins theory [41] can be assumed as valid:

$$\mathbf{a}_j = \phi_j. \qquad [2.19]$$

where ϕ_j is the volume fraction of solute j in the drop.

The specific solubilization rate k_j should be expected to depend on the composition of the drop because different species are transferred across the interfaces. The specific mass transfer rate of the pure oil j was defined previously as:

$$k^o_j = \frac{c^o_{sat,j}}{\Re^o_{I,j}} \qquad [2.20]$$

with the superscript ° indicating that the designated quantity is referred to the solute j pure. An analogous definition holds for the rate k_j:

$$k_j = \frac{c_{sat,j}}{\Re_{I,j}} \qquad [2.21]$$

The relationship between the variables shown in Eqs. [2.20] and [2.21] is:

$$\lim_{x_j \to 1} \left\{ k_j, c_{sat,j}, \Re_{I,j} \right\} = \left\{ k_j^o, c_{sat,j}^o, \Re_{I,j}^o \right\}$$

Let us assume for solutes with similar chemical structure that the interfacial resistance to transfer of a given component j does not depend significantly on composition, i.e., $\Re_{I,j} \sim \Re_{I,j}^o$. This assumption is plausible for micelle-mediated solubilization processes in which the rate of adsorption of micelles is rate limiting, as discussed later. If so, Eqs. [2.16], [2.20] and [2.21] can be combined to render:

$$k_j = k_j^o \mathbf{a}_j \qquad [2.22]$$

Also, the relationship between the interfacial area and the moles of the m components in the mixture is given by:

$$V = \frac{4}{3}\pi a^3 = \sum_l n_l v_l \;\therefore l \in \{1,2,\ldots,m\} \;\Rightarrow\; 4\pi a^2 = (36\pi)^{1/3}\left(\sum_l n_l v_l\right)^{2/3} \qquad [2.23]$$

Finally, the pressure jump across the interface is neglected as before and therefore,

$$\frac{c_{I,j}}{c_{sat,j}} = \frac{c_{sat,j}\,\mathbf{exp}(2\sigma v_j / \mathrm{R}Ta)}{c_{sat,j}} \cong 1 \qquad [2.24]$$

Eqs. [2.22]-[2.24] can be substituted into Eq. [2.15] to obtain an ordinary differential equation for the component j in terms of the moles of the m components of the mixture:

$$\frac{dn_j}{dt} = 4\pi a^2 k_j^o \, \mathbf{a}_j \left(c_{B,j}/c_{sat,j} - 1\right) = \\ = (36\pi)^{1/3} k_j^o \left(\sum_l n_l v_l\right)^{2/3} \left(\theta_j^o - \mathbf{a}_j\right) \qquad [2.25]$$

or in dimensionless form:

$$\frac{dN_j}{d\tau} = 3\omega_j \left(\sum_l N_l \delta_l\right)^{2/3} \left(\theta_j^o - \mathbf{a}_j\right) \qquad [2.26]$$

where,

$$N_j = n_j \cdot \frac{3v_{\mathrm{Ref}}}{4\pi a_0^3}, \quad \tau = t \cdot \frac{k_{\mathrm{Ref}}^o v_{\mathrm{Ref}}}{a_0}, \quad \delta_j = \frac{v_j}{v_{\mathrm{Ref}}}; \quad \omega_j = \frac{k_i^o}{k_{\mathrm{Ref}}^o}; \quad \theta_j^o = \frac{c_{B,j}}{c_{sat,j}^o} \qquad [2.27]$$

The subindex Ref denotes the properties of one of the solutes chosen arbitrarily as a reference to define the dimensionless variables and parameters.

The prediction of the profile for the size and composition of a drop composed of m soluble oils requires the numerical resolution of a system of m coupled ordinary differential equations defined either by Eqs. [2.25] or [2.26]. The number of moles of each solute that is initially present in the drop must be provided. If, for example, the initial molar compositions $x_{j,0}$ are known, then the initial number of moles of solute j in the drop is given by:

$$n_{j,0} = \frac{4\pi a_0^3 x_{j,0}}{3\sum_l x_{l,0} v_l}; \quad N_{j,0} = \frac{x_{j,0}}{\sum_l x_{l,0} \delta_l} \qquad [2.28]$$

The solution of the system of equations is a collection of values of n_j (or N_j) at every instant t (or τ). Once these values are determined, the corresponding radius of the drop is readily obtained via Eq. [2.29]:

$$a = a_0 \left(\frac{\sum_l n_l v_l}{\sum_l n_{l,0} v_l} \right)^{1/3} = a_0 \left(\sum_l N_l \delta_l \right)^{1/3} \qquad [2.29]$$

2.2.2. Mixed kinetics with convection

The solubilization of single drops has been considered so far for limiting cases ($\Re_I >> \Re_D$ and $\Re_I << \Re_D$) in absence of hydrodynamic effects. In this section we analyze the more general case of mixed kinetics in the presence of convective currents, restricted to Reynolds numbers sufficiently low ($Re = u\rho/\eta < 0.1$ [41], with u being a characteristic velocity of the flow field in which the drop is embedded, and ρ and η being the density and viscosity of the matrix, respectively) to assure laminar flow around the droplet. We consider here the solubilization of pure oils in oil-free surfactant solutions for which the pressure jump across the interface can be neglected. It is also assumed that the solubilization of the drop does not alter significantly the average concentration of solute in the bulk phase, so $c_B \sim 0$ at all times. If these considerations hold, Eq. [2.2] becomes:

$$J = \frac{c^o_{sat}}{\Re^o_I + \Re^o_D} \quad \text{whence} \quad \frac{da}{dt} = -\frac{v c^o_{sat}}{\Re_I + \Re_D} \qquad [2.30]$$

The resistance to mass transport at the interface $\Re^o_I$ has been already defined as:

$$\Re^o_I = \frac{c^o_{sat}}{k^o} \qquad [2.31]$$

Whereas convection may not affect k^o as discussed earlier, it surely influences diffusional transport. The effect of convection on the transport of matter to/from spheres

in a laminar flow field has been considered by a number of authors [41-44]. In general, it has been found that the diffusional transport is enhanced by convection such that:

$$\frac{1}{\Re_D^o} = \frac{D}{a}\frac{Sh}{2} \quad ; \; Sh = f(Pe_u); \; Pe_u = \frac{ua}{D}. \qquad [2.32]$$

Sh and Pe_u are the Sherwood and Péclet numbers, respectively. Eq. [2.32] can be expressed in terms of a convective diffusion film of thickness ℓ around the sphere [32, 41]:

$$\frac{1}{\Re_D^o} = \frac{D}{\ell}\left(1+\frac{\ell}{a}\right) \quad ; \; \ell = \frac{a}{Sh/2-1} \qquad [2.33]$$

The value of Sh can be calculated with the expression:

$$Sh = 2 + \sqrt{\frac{8}{\pi}} Pe_u^{1/2}; \; Pe_u = \frac{ua}{D}, \qquad [2.34]$$

which is obtained from considerations presented by Bird *et al.* [41] for mass transfer of sparingly soluble materials to/from bubbles with mobile interfaces (i.e., interfaces where surface-active materials are either absent or adsorb/desorb continuously to sustain flow) exhibiting Rybczynski-Hadamard circulation, and for arbitrary Pe numbers. Retardation due to viscous resistance to circulation within the drop/bubble and interfacial tension gradients are embedded in the value of u when such velocity is measured experimentally [45]. For the sake of this analysis we will assume that:

$$u = u_0 r^n. \qquad [2.35]$$

where $r = a/a_0$ as before *and* u_0 and n are coefficients that will be determined experimentally. By substituting Eq. [2.35] in Eq. [2.34] we obtain:

$$\frac{Sh}{2} = 1 + \left(APe_0\right)^{1/2} r^{\frac{n+1}{2}}; \quad \mathrm{A} = \frac{2}{\pi}; \quad Pe_0 = \frac{u_0 a_0}{D} \qquad [2.36]$$

If Eqs. [2.30]-[2.32] hold, the rate of change of the size of a drop undergoing solubilization in a laminar flow field is given by:

$$\frac{da}{dt} = -\frac{1}{\frac{1}{k^o v} + \frac{2a}{Dvc^o_{sat} Sh}} \text{ whence } \frac{dr}{d\tau'} = -\frac{1}{\frac{1}{K} + \frac{r}{Sh(r)/2}} \qquad [2.37]$$

with

$$K = \frac{k^o a_0}{Dc^o_{sat}} \qquad [2.38]$$

and $\tau' = \left(Dvc^o_{sat} / a_0^2\right)t$ as before. K stands for the ratio of diffusional-to-interfacial resistance in absence of convection. Therefore, K >> 1 stands for diffusion-controlled kinetics, whereas K << 1 is indicative of interface-limited mass transfer. By substituting Eq. [2.36] in Eq. [2.37] we obtain:

$$\frac{dr}{d\tau'} = -\frac{1}{\frac{1}{K} + \frac{r}{1 + \left(A \cdot Pe_0\right)^{1/2} \cdot r^{\frac{n+1}{2}}}} \; . \qquad [2.39]$$

It will be shown later that the most relevant case for the systems considered in this study is consistent with n = 1. In such a case, Eq. [2.39] can be solved analytically to render:

$$\left[1 + \frac{K}{\left(A \cdot Pe_0\right)^{1/2}}\right](r-1) + \frac{K}{A \cdot Pe_0} \ln \frac{Sh(1)}{Sh(r)} = -K\tau' . \qquad [2.40]$$

Several particular cases can be considered from Eq. [2.40]. For example, in the limit $u \rightarrow 0$ ($Pe_0 \rightarrow 0$, stagnant drop), this equation becomes:

$$r - 1 + \frac{K}{2}\left[r^2 - 1\right] = -K\tau', \qquad [2.41]$$

whence

$$\left(r + \frac{1}{K}\right)^2 = \left(1 + \frac{1}{K}\right)^2 - 2\tau'. \qquad [2.42]$$

If in addition K >> 1 (diffusion-controlled solubilization), Eq. [2.42] becomes:

$$r^2 - 1 = -2\tau' \quad \text{whence} \quad a^2 = a_0^2 - 2Dvc_{sat}^{o}t \qquad [2.43]$$

On the other hand, for Pe_0 >> 1 (significant convection) and/or K << 1 (interface-controlled mass transfer), Eq. [2.40] becomes:

$$r - 1 = -K\tau' \quad \text{whence} \quad a = a_0 - k^{o}vt \qquad [2.44]$$

Eqs. [2.43] and [2.44] indicate that different profiles for the transient behavior of the drop size can be expected (either parabolic or linear), depending on the transport and hydrodynamic conditions under which solubilization takes place.

The analysis provided above accounts for the effect of forced convection on mass transfer. Natural convection can also be observed if the transferred solutes significantly affect the density of the surfactant solution. In this case, convection would be driven by changes in density in the surroundings of the drop due to the solubilization of the oil.

It seems that the effect of natural convection around bubbles of liquid droplets on mass transfer kinetics has not been accounted for as yet. Since it is customary to

establish analogies between theoretical results for heat and mass transfer processes in terms of equivalent dimensionless groups [41], some insight in the problem in hand can be obtained from the work of Jafarpur and Yovanovich [46], who indicated in their analysis of convective heat transfer from solid isothermal spheres that an expression of the form given by Eq. [2.34] can also be used to account for the enhancing effect of natural convection on conductive heat transport, provided that the velocity u is indeed characteristic of the natural convective flow field. The expression for u reported by these authors, expressed in terms of mass transport dimensionless numbers, is:

$$u^* = \frac{D}{a} Ra^{1/2} = u_0^* r^{1/2} \qquad [2.45]$$

where

$$Ra = \frac{a^3 g(\rho - \rho_I)}{D\eta}; \quad u_0^* = \frac{D}{a_o} Ra_o^{1/2}; \quad Ra_o = \frac{a_o^3 g(\rho - \rho_I)}{D\eta} \qquad [2.46]$$

The symbol * is used to indicate when a variable referred to natural convection. Here, Ra is the Rayleigh number, ρ_I is the density of the interfacial region and g has its usual meaning. Eq. [2.45] is valid for low Re and high Schmidt ($Sc = \eta/\rho D$) numbers. An estimate for $(\rho - \rho_I)$ can be obtained by assuming saturation in the interfacial region. If so, the expression for the Rayleigh number becomes:

$$Ra = \frac{a^3 g(\rho - \rho_I)}{D\eta} \cong \frac{a^3 g c_{sat}^o v(\rho - \rho_d)}{D\eta} \qquad [2.47]$$

where ρ_d is the density of the fluid in the drop. By substituting Eq. [2.45] in Eq. [2.34] the following result is obtained:

$$Sh^* = 2 + \sqrt{\frac{8}{\pi}} Ra^{1/4} \qquad [2.48]$$

with Sh^* being the Sherwood number for transport of matter enhanced by natural convection. In general,

$$Sh^* = 2 + H \cdot Ra^{1/4} \qquad [2.49]$$

The value of H in Eq. [2.48] [$(8/\pi)^{1/2} \sim 1.60$] might be considered as the low limit for H when mass transport due to natural convection and Rybczynski-Hadamard circulation occur concomitantly, since Eq. [2.34] is indeed valid for fluid-fluid systems, but Eq. [2.45] was derived for natural convection around solid spheres.

2.2.3. Mass transfer in emulsions

The models developed above for solubilization of individual droplets can be easily extended to a collection of drops dispersed in a surfactant solution. Let us consider the case in which only one solute is transferred. The concentration of solute in the micellar solution c_B can be obtained from an overall balance of dispersed phase in the emulsion. For the case depicted in Figure 2.1 (bottom) in which two different drop types are present but only one solute is soluble in the continuous phase, we obtain:

$$\Phi_{1,0} + \Phi_{2,0} + vc_{B,0} = \frac{4\pi}{3V}\left(\sum_{i=1}^{n_1} a_{i,1}^3 + \sum_{j=1}^{n_2} a_{j,2}^3\right) + vc_B \qquad [2.50]$$

The parameters $\Phi_{w,0}$ and n_w are the initial volume fraction and the initial number of type w drops in a volume V of emulsion.

The transient behavior of drop radii can be modeled using either Eq. [2.3] if diffusion is rate-limiting or Eq. [2.5] if mass transfer is assumed as dictated by interfacial

resistance. In what follows, the latter case is considered independently of convective effects.

The following expression can be obtained from Eq. [2.5] for pure drops by neglecting the effect of interfacial curvature on the surface concentration of solute, i.e., by assuming that $c_I / c^o_{sat} \sim 1$, then multiplying both sides by $4\pi a^2$, adding over the entire population of droplets and further rearranging:

$$\frac{d\omega_B}{dt} = k_i^* \left(\frac{A}{V}\right)\left(\omega_{sat} - \omega_B\right) \qquad [2.51]$$

Here, k_i^* is an overall mass-transfer coefficient with units of length·time^{-1}, A/V is the specific surface area of oil drops exposed to the aqueous phase per unit volume of emulsion, and ω_B and ω_{sat} are the mass fractions of oil solubilized in micelles in the bulk at time t and at saturation, respectively. The coefficients k^o and k_i^* are related by

$$k^o = c^o_{sat} \cdot k_i^* \qquad [2.52]$$

Equation [2.49] has been used to describe mass transfer in several emulsions where interfacial phenomena seem to determine transport rates, by yielding characteristic values of k_i^* in each case [1, 2, 9]. However, it does not allow keeping track of the size of individual droplets in time in a polydisperse emulsion, and therefore the transient behavior of the drop size distribution and related parameters such as the mean drop size cannot be followed using this approach.

Mass transfer in polydisperse emulsions can be evaluated using Equations [2.5], [2.6] and [2.50], but an analytical solution is not known and therefore the equations must

be solved numerically. The task is carried out in successive, constant time steps Δt, and the recursive formulae are developed below. Again, the theory is given for emulsions containing two drop types and one mobile solute. Emulsions with one drop type can be treated as particular cases of the derivation. In what follows, the index ° is suppressed and all concentrations and physical properties refer to the mobile solute, unless otherwise indicated.

The dimensionless concentration of solute in the bulk solution $\theta = c_B / c_{sat}$ can be readily obtained from Eq. [2.50]:

$$\theta = \theta_0 + \frac{1}{c_{sat} v}\left(\Phi_{1,0} + \Phi_{2,0}\right) - \frac{\kappa}{c_{sat} v}\left(\chi^3 \sum_{i=1}^{n_1} r_{i,1}^3 + \sum_{j=1}^{n_2} r_{j,2}^3 \right) \qquad [2.53]$$

where $\kappa = 4\pi a_{ref,2}^3 / 3V$, $r_{i,1} = a_{i,1} / a_{ref,1}$, $r_{i,2} = a_{i,2} / a_{ref,2}$ and $\chi = a_{ref,1} / a_{ref,2}$, with $a_{ref,1}$ and $a_{ref,2}$ as the reference radii for type 1 and type 2 drops, respectively. These reference radii are arbitrary, but it is advisable to choose plausible values such as a characteristic mean of the initial drop size distributions. When θ is calculated in successive iterations u and $u + 1$, from Eq. [2.53] we have:

$$\theta^{u+1} \leftarrow \theta^u - \frac{\kappa}{c_{sat} v}\left\{ \chi^3 \sum_{i=1}^{n_1} \left[\left(r_{i,1}^{u+1}\right)^3 - \left(r_{i,1}^u\right)^3 \right] + \sum_{j=1}^{n_2} \left[\left(r_{j,2}^{u+1}\right)^3 - \left(r_{j,2}^u\right)^3 \right] \right\} \qquad [2.54]$$

Equation [2.54] provides a way to calculate the bulk concentration at time step $u+1$. However, it is computationally inefficient if used as shown since either number of droplets n_1 or n_2 could be excessively large. A way to resolve this issue is to choose a number of droplets n^* large enough to be representative of the drop size distributions of

both drop types, but small enough to perform calculations within a reasonable computational time. If so, the following approximation can be made:

$$\theta^{u+1} \leftarrow \theta^{u} - \frac{\kappa}{n^{*} c_{sat} v} \sum_{i=1}^{n^{*}} \left\{ n_1 \chi^3 \left[\left(r_{i,1}^{u+1} \right)^3 - \left(r_{i,1}^{u} \right)^3 \right] + n_2 \left[\left(r_{i,2}^{u+1} \right)^3 - \left(r_{i,2}^{u} \right)^3 \right] \right\} \qquad [2.55]$$

Either Eq. [2.54] or Eq. [2.55] requires knowledge of the drop radii at time steps u and $u + 1$. Equation [2.5] can be written for the type 1 droplets as:

$$\frac{dr_{i,1}}{d\tau} = \frac{1}{\chi} \left[\theta - x_{i,1} \exp\left(\frac{\varsigma}{\chi r_{i,1}} \right) \right]; \quad 1 \le i \le n^{*} \qquad [2.56]$$

where $\tau = \left(k^{o} v / a_{ref,2} \right) \cdot t$ and $\varsigma = 2\sigma v / \mathbf{R} T a_{ref,2}$. For the type 2 drops we obtain:

$$\frac{dr_{i,2}}{d\tau} = \theta - x_{i,2} \exp\left(\frac{\varsigma}{r_{i,2}} \right); \quad 1 \le i \le n^{*} \qquad [2.57]$$

The finite difference formulation arises when the rate of change of the dimensionless radii is replaced by the forward difference approximation:

$$\frac{dr_{i,m}}{d\tau} \cong \frac{r_{i,m}^{u+1} - r_{i,m}^{u}}{\Delta\tau} \qquad [2.58]$$

with $\Delta\tau = \left(kv / a_{2,0} \right) \Delta t$. The combination of Eqs. [2.56]-[2.58] yields the following expressions for the radii of the two drop types at the iteration $u + 1$:

$$r_{i,1}^{u+1} \leftarrow r_{i,1}^{u} + \frac{\Delta\tau}{\chi} \left[\theta^{u} - x_{i,1}^{u} \exp\left(\frac{\varsigma}{\chi r_{i,1}^{u}} \right) \right]; \quad r_{i,2}^{u+1} \leftarrow r_{i,2}^{u} + \Delta\tau \left[\theta^{u} - x_{i,2}^{u} \exp\left(\frac{\varsigma}{r_{i,2}^{u}} \right) \right] \qquad [2.59]$$

A numerical solution for the transient behavior of each drop size within the sample of n^* type 1 and n^* type 2 drops, and for the transient behavior of the concentration of solute in the bulk, can be obtained by calculating $r_{i,1}^{u+1}$ and $r_{i,2}^{u+1}$ using Eq. [2.59], and then determining θ^{u+1} from Eq. [2.55]. These results are further assigned as initial values for the next time step. The drop population balance can be accounted for by assigning zero radius to drops for which $r_{i,m}^{u+1} < 0$, and subtracting the number of drops of either type for which this assignment is made from the corresponding sample population.

Finally, the molar fraction of mobile solute in each drop type $x_{i,m}$ that is needed in Eq. [2.59] is determined from a mass balance in the drop, from which the following expression is obtained:

$$x_{i,m} = \frac{r_{i,m}^3 - \phi_m \varpi_{i,m}}{r_{i,m}^3 - \phi_m \varpi_{i,m}(1-\delta)}; \; \varpi_{i,m} = \left(\frac{a_{i,m,t=0}}{a_{ref,m}} \right)^3; \delta = \frac{v}{v_I} \qquad [2.60]$$

or otherwise $x_{i,m}$ = 1 if pure drops of solute are considered. In Eq. [2.60], v and v_I are the molar volumes of the mobile and immobile species, and ϕ_m is the initial volume fraction of immobile compound present in the type m drops. Note that in the definition of $\varpi_{i,m}$, $a_{i,m,t=0}$ stands for the initial radius of drop i, whereas $a_{ref,m}$ is the reference size for the type m drops referred to earlier.

Equations [2.55] and [2.59] define an explicit numerical scheme, since the variables at the time step $u + 1$ can be calculated from their values at time step u. For this kind of system, Δt must be carefully selected since large values of this variable lead to numerical instabilities as discussed later.

2.2.4. LSW theory for interface-controlled Ostwald ripening in emulsions

The theoretical considerations of this chapter conclude by considering the Liftshitz-Slyozov-Wagner theory for Ostwald ripening referred to earlier for the case in which mass transport is limited by interfacial phenomena. Wagner [12] and Marqusee and Ross [47] have considered this case for the last stage of interface kinetic limited precipitation of solids, and we extend it here to the case of ripening emulsions. This theory will be used to assess the rate-controlling mechanism for a particular experiment, and also as a reference to test the numerical algorithm used in the simulations.

When applied to emulsions, the LSW theory is based on the following assumptions: (a) The rate controlling step for mass transfer is the molecular diffusion of the solute across the bulk phase. If so, Eq. [2.3] applies to describe the rate of change of the radius in a single droplet; (b) the drops are spherical and fixed in space; (c) the emulsion is dilute, that is, interactions among droplets are negligible; (d) the bulk concentration c_B is constant far from the drop surfaces; (e) the concentration of solute at the interface c_I is given by Eq. [2.6].

The most important results of this theory are: (a) there is a critical radius a_C given by:

$$a_C = \frac{\alpha}{\ln(c_B / c^o_{sat})}; \quad \alpha = \frac{2\sigma v}{RT} \qquad [2.61]$$

Droplets with $a > a_C$ will grow, whereas drops with $a < a_C$ will shrink. This result is easily obtained from Eq. [2.3] by setting $da/dt = 0$ at $a = a_C$. (b) The drop size distribution of the emulsion adopts an invariant shape when scaled to $u = a/a_C$. The expression for the number based distribution is:

$$p_{Dif}(u) = \begin{cases} \dfrac{81e}{\sqrt[3]{32}} u^2 (u+3)^{-7/3} \left(\frac{3}{2} - u\right)^{-11/3} e^{-\frac{1}{1-\frac{2}{3}u}} & ; \quad u < \frac{3}{2} \\ 0 & ; \quad u \geq \frac{3}{2} \end{cases} \qquad [2.62]$$

A plot of $p_{Dif}(u)$ is shown in Figure 2.3. It can be demonstrated that for this distribution the mean drop size $\bar{a}$ is given by:

$$\bar{u} = \int_0^\infty u \, p_{Dif}(u) \, du = 1 \;\Rightarrow\; \bar{a} = a_C \qquad [2.63]$$

(c) The third power of $\bar{a}$ increases linearly with time, at a rate ω_3 given by:

$$\omega_3 = \frac{d\bar{a}^3}{dt} = \frac{4}{9} \alpha D c^o_{sat} v \qquad [2.64]$$

Analogous results can be obtained for the case in which mass transfer kinetics is controlled by interfacial resistance, and not by molecular diffusion. In this case, the rate of change of the radius of a single drop is given by Eq. [2.5] instead of Eq. [2.3] and the theoretical analysis can be carried on as shown in the work of Lifshitz and Slyozov [11]. By doing so, the following results are obtained: (a) The critical radius a_C is given by Eq. [2.61] as before; (b) at long ripening times the emulsion adopts a drop size distribution, scaled to $u = a/a_C$, of the form:

$$p_{Int}(u) = \begin{cases} \dfrac{24u}{(2-u)^5} e^{-\frac{3u}{2-u}} & ; \quad u < 2 \\ 0 & ; \quad u \geq 2 \end{cases} \qquad [2.65]$$

The distribution function $p_{Int}(u)$ is plotted in Figure 2.3. It is readily seen that a broader drop size distribution is obtained if interfacial phenomena control mass transfer

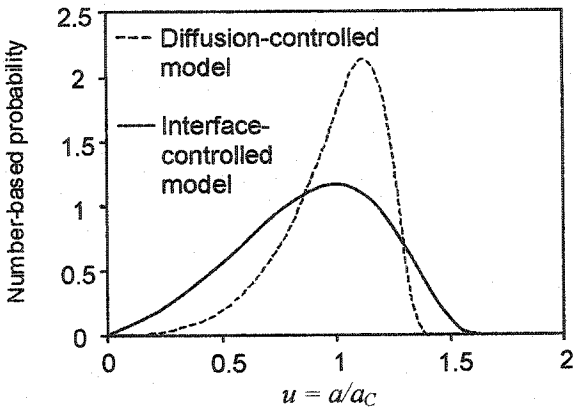


Figure 2.3. Plots of the asymptotic solutions for the number-based drop size distribution of emulsions undergoing Ostwald ripening.

kinetics when compared with the corresponding LSW distribution. It can be verified that both distributions are normalized, i.e., $\int_0^\infty p_{Dif}(u')du' = 1$ and $\int_0^\infty p_{Int}(u')du' = 1$. In addition, for this case $\bar{a}$ is related to a_C as follows:

$$\bar{u} = \int_0^\infty u\, p_{Int}(u)\, du = \frac{8}{9} \;\Rightarrow\; \bar{a} = \tfrac{8}{9} a_C \qquad [2.66]$$

Interestingly, an analytical expression can be obtained for the cumulative drop size distribution whenever interfacial phenomena are rate controlling:

$$P_{Int}(u) = \int_0^u p_{Int}(u')du' = \begin{cases} 1 - \dfrac{8}{(2-u)^3} e^{\frac{3u}{2-u}} & ;\quad u < 2 \\ 1 & ;\quad u \geq 2 \end{cases} \qquad [2.67]$$

(c) The second power of $\bar{a}$ increases linearly with time, at a rate ω_2 given by:

$$\omega_2 = \frac{d\bar{a}^2}{dt} = \tfrac{32}{81} \alpha k^\circ v \qquad [2.68]$$

The details of the derivation are omitted for the sake of brevity. However, it is worth mentioning that the expressions for $p_{Dif}(u)$ and $p_{Int}(u)$ and subsequent equations shown

above hold only for the case in which α/a << 1, since the approximation $exp(\alpha/a) \sim 1 + \alpha/a$ is made in their derivation.

2.3. COMPUTATIONAL PROCEDURES

Calculations on mass transport in single drop experiments for which analytical expressions are reported in section 2.2 were performed in Excel spreadsheets (Microsoft, v. 2000). The software Mathcad (Mathsoft, Inc. v. 2001 Professional) was used to solve the system of coupled ordinary differential equations that arises when calculating the transient solubilization of single drops of hydrocarbon mixtures. This software applies the fourth order Runge-Kutta method for this task.

The numerical algorithm described above to model mass transfer in emulsions was applied to experimental data found in the literature, for which the time-dependent behavior of the drop size distribution and/or associated parameters such as a given mean drop size or the concentration of oil as droplets in the emulsion were reported. In all cases, plots of the drop size distributions of the initial emulsions were available. Such plots were digitized and the corresponding cumulative distribution functions were calculated and satisfactorily fit in all cases to the cumulative form of the lognormal probability distribution function. It is shown in Appendix A that this distribution function and its cumulative form have two adjustable parameters, the geometric mean diameter d_g and the geometric standard deviation σ_g. Depending on whether the distribution is reported in terms of the number or volume of droplets, the fit renders the number-based (d_{gN}) or volume-weighted (d_{gV}) geometric mean diameter, respectively. It is also shown in Appendix A that the value of σ_g is independent of the base for which the data are reported, and that d_{gN} and d_{gV} are related by $d_{gV} = d_{gN} \cdot exp(3\sigma_g^2)$.

Once the parameters of the initial distribution are determined, a random number generator built in the software MATLAB (The Mathworks, Inc., Release 12) is used to generate n^* drop sizes representative of the initial drop size distribution of the emulsions to be modeled. This information is input to a FORTRAN 77 code along with the corresponding set of physical properties and parameters needed by the simulation. The sizes of the drops and the concentration of solute in the bulk are stored at predetermined times, and the data are further processed with a program developed in MATLAB to obtain the time-dependent drop size distributions and their characteristic parameters.

2.4. Materials and Methods

The nonionic surfactant $C_{12}E_8$ is a pure linear alcohol ethoxylate with molecular mass of 538 Da. It was supplied by Nikko Chemical and used without further treatment. The nonionic surfactant polyoxyethylene sorbitan monolaurate (Tween 20, Sigma) is a distribution of isomers with average molecular mass of 1228 Da. n-octane (114.2 Da), n-nonane (128.3 Da), n-decane (142.3 Da), n-undecane (156.3 Da) and squalane (422.8 Da) were obtained from Sigma with a purity of 99%, whereas n-hexadecane (226.4 Da) and n-tetradecane (198.4 Da) were supplied by Humphrey Chemical Co., 99% pure.

The solubilization rates of n-octane, n-nonane, n-decane, n-undecane and n-decane/squalane mixtures in 2.5 wt.% aqueous solutions of $C_{12}E_8$ were determined at room temperature (23 ±1 °C) using a technique described previously [34]. In each test, a tiny drop (a ~ 5-40 μm) of the oil of interest was injected with a micropipette into a 4 x 100 x 600 mm capillary glass cell filled with the aqueous surfactant solution. The time-dependent behavior of the system was followed through a video microscope equipped with a JV 6000 video micrometer to measure drop diameter. The same procedure was

applied to measure the solubilization rate of n-tetradecane in a 5 wt. % solution of Tween 20 at the same temperature.

The evaluation of the solubilization rates of the above-mentioned alkanes and several binary mixtures in aqueous solutions of $C_{12}E_8$ were also performed at 30.9 ± 0.1 °C. In these tests, small drops of oil (a ~ 5-40 μm) were injected in cylindrical capillaries (diameter = 1.7 mm, length = 90 mm) filled with the aqueous solutions and placed within a temperature-controlled cell (Mettler FP5) mounted on the microscope stage. The drop size was monitored as before. The usage of cylindrical capillaries instead of capillary glass cells significantly eased the observation and monitoring of droplets because capillaries restrict displacements of the drop to the axial direction, whereas with the glass cells droplets can be displaced in two dimensions. Todorov *et al.* [33] have adopted the usage of cylindrical capillaries for the observation of drops undergoing solubilization. These authors correctly indicate that the usage of small cylindrical capillaries as vessels for the surfactant solution suppresses uncontrollable thermal convection, which can sometimes lead to misinterpretation of kinetic data.

The equilibrium solubilization capacities of n-decane and n-undecane in 2.5 wt. % solutions of $C_{12}E_8$ at room temperature were determined by titration. In each case, successive additions of the oil were made to 55 cm^3 of the surfactant solution maintaining constant agitation with a magnetic stirrer, and the light transmittance in the solution was recorded with a Brinkmann PC800 colorimeter. The flask remained sealed throughout the tests to prevent evaporation. Results from turbidity measurements were easily confirmed by direct observation of samples under the microscope, since saturated solutions can be differentiated from unsaturated solutions by the presence of persistent droplets. This microscopic technique was also used to estimate the solubility of n-

octane, n-decane and n-undecane in solutions of $C_{12}E_8$ at 30.9 ± 0.1 °C. Samples of surfactant solutions with increasing concentration of the oil of interest were prepared and further agitated with vertical rotation at 8 rev/min during 10 days. The samples were placed in a controlled-temperature room at the above-mentioned temperature.

The interfacial tensions of n-decane, squalane and several binary mixtures of these oils with a 2.5 wt. % aqueous solution of $C_{12}E_8$ were measured at room temperature using a spinning drop tensiometer (Non Linear Systems, model 300). Similar experiments were carried out for n-tetradecane in a 5 wt. % aqueous solution of Tween 20, and n-hexadecane in a 2 wt. % solution of Tween 20. Measurements were made with fresh solutions without pre-equilibration, except for the n-tetradecane / Tween 20 (5 wt. %) in water system, which is further discussed as a case study for Ostwald ripening. For this system, the experiment was carried out by placing an oil drop taken from a n-tetradecane sample previously contacted with surfactant solution during 48 hours, into another sample of aqueous surfactant solution previously saturated with n-tetradecane. Interfacial tensions were also measured for n-octane, n-decane, n-undecane and squalane in contact with oil-free $C_{12}E_8$ solutions (2.5 wt.%) at 30 ± 1 °C.

2.5. Results and Discussion

2.5.1. Equilibrium solubilization capacity and interfacial tension measurements

Figure 2.4 shows the results for the measurement of light transmittance of n-decane and n-undecane dispersed in aqueous $C_{12}E_8$ at 2.5 wt. % (46.5 mol/m^3) at room temperature. The saturation of the surfactant solution was indicated by a persistent turbidity that reduced the transmitted light through the mixture. The equilibrium

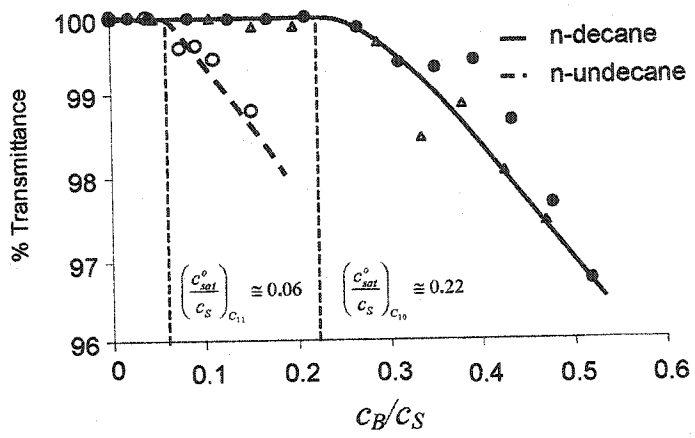


Figure 2.4. Light transmittance of aqueous $C_{12}E_8$ (2.5 wt.%) titrated with n-decane and n-undecane at room temperature. Triangles: Data obtained for n-decane allowing 4 hours between additions. Dots: Data obtained for n-decane allowing 10 hours between additions. Circles: Data for n-undecane allowing 10 hours between additions. The onset of a permanent turbidity indicates the solubility limit.

solubilization capacity c^o_{sat} was determined by interpolating for the highest concentration of n-decane at which such turbidity was not noted. Saturation for n-decane was apparently reached at $c^o_{sat} = 0.22 c_S = 10.2$ mol/m^3. Solubilization in the vicinity of the saturation concentration is very slow, so this figure may be regarded as a lower limit for the equilibrium solubilization capacity. This concentration is significantly larger than the molecular solubility of decane in water (4×10^{-4} mol/m^3 at 25 °C, Table 2.1). Thus, it is plausible to assume that most of the oil dissolved is located within micellar aggregates, and that the contribution of molecular solubility to the overall solute concentration in the aqueous phase is negligible. Also, the *cmc* of $C_{12}E_8$ in water is 7.1×10^{-2} mol/m^3 = 0.004 wt.% at 25 °C [48], and therefore c_S, the amount of surfactant forming micelles, can be taken as the overall concentration of surfactant without introducing significant error.

Similarly, the apparent equilibrium solubilization capacity for n-undecane was $c^o_{sat} = 0.06 c_S = 2.80$ mol/m^3. This figure is also significantly greater than the molecular solubility

Table 2.1. Molecular and micellar equilibrium solubilization capacities of alkanes in aqueous solutions of $C_{12}E_8$ (c_S = 2.5 wt.% = 46.5 mol/m^3)

Alkane	$c^o_{sat,w}$ [a] (mol/m^3)	T (°C)	c^o_{sat} (mol/m^3)	MSR [c]
n-octane	$6.2 \cdot 10^{-3}$	30.9 ± 0.1	44.5 [b]	
n-nonane	$1.4 \cdot 10^{-3}$	30.9 ± 0.1	35.2 [b]	
n-decane	$3.5 \cdot 10^{-4}$	23 ± 1	10.2	0.22
		30.9 ± 0.1	29.4	0.63
		30.9 ± 0.1	26.9 [b]	0.58
n-undecane	$8.7 \cdot 10^{-5}$	23 ± 1	2.8	0.06
		30.9 ± 0.1	15.4	0.33
		30.9 ± 0.1	15.4 [b]	0.33

[a] Molecular solubility in water. Estimated from data reported in Ref. [49]. T = 25°C

[b] Measurements performed via turbidimetry / microscopy

[c] Measurements performed by Lim [50] using gas chromatography

[d] MSR = molar solubilization ratio = c^o_{sat} / c_s

of n-undecane in water (9 x 10^{-5} mol/m^3 at 25 °C, Table 2.1), and therefore the alkane is solubilized primarily within the $C_{12}E_8$ micelles. Table 2.1 summarizes these results along with estimates for c^o_{sat} for n-decane and n-undecane at 30.9 °C using the microscopic technique described in section 2.4. Very accurate measurements for the solubility of n-octane, n-nonane, n-decane and n-undecane in $C_{12}E_8$ recently performed by Lim using gas chromatography are also included [50].

The data summarized in Table 2.1 indicate that the molar solubilization ratio $MSR = c^o_{sat} / c_s$ increases with temperature and decreases with the alkane carbon number (ACN) of the oil. The increase of solubility with temperature is a well-known effect for nonionic surfactants. It is related to the decrease hydration of the oxyethylene oxygens in the polyoxyethylene groups of the surfactant that leads to growth of the aggregation number in the micelles and to reduction of repulsion between micelles [51]. The formation of

larger micelles allows the incorporation of more oil within them. The increase in c^o_{sat} with concentration is related to the inventory of micelles available to solubilize oil. Finally, the solubilization capacity decreases with increase in the molar volume of the solute, which in turn increases with the ACN for the case of hydrocarbons.

It is not clear why the equilibrium solubilization capacity reported here for n-decane at room temperature does not agree with the value c^o_{sat}/c_S = 0.06 that has been reported for this system under similar conditions [14]. The permitted contact time between the oil and the surfactant solution in such experiments prior to detecting the onset of turbidity was not mentioned, so perhaps incomplete solubilization contributed to the discrepancy.

Interfacial tensions of the n-decane/squalane mixtures ranged from 1.1 mN/m for pure n-decane to 3.3 mN/m for pure squalane at room temperature, while the interfacial tensions for n-octane/n-undecane, n-decane/n-undecane and n-octane/squalane mixtures ranged from 0.7 mN/m for pure n-octane to 2.8 mN/m for pure squalane at 30.9 °C. These values are low enough to neglect the effect of interfacial curvature on the concentration of mobile oil at the interface c_I in the experiments discussed below, since all plausible sets of experimental conditions make the factor $\exp(2\sigma v / RTa)$ differ from unity by $3 \cdot 10^{-4}$ or less. The interfacial tension at room temperature of n-tetradecane in a 5 wt% aqueous solution of Tween 20 previously saturated with the alkane was 4.0 mN/m, and that of n-hexadecane in aqueous Tween 20 (2 wt.%) was 3.2 mN/m.

2.5.2. Solubilization tests for individual drops

Figure 2.5 shows results from solubilization tests with pure alkanes in oil-free 2.5 wt.% solutions of $C_{12}E_8$ in water (θ^o = 0) at the conditions described in the experimental

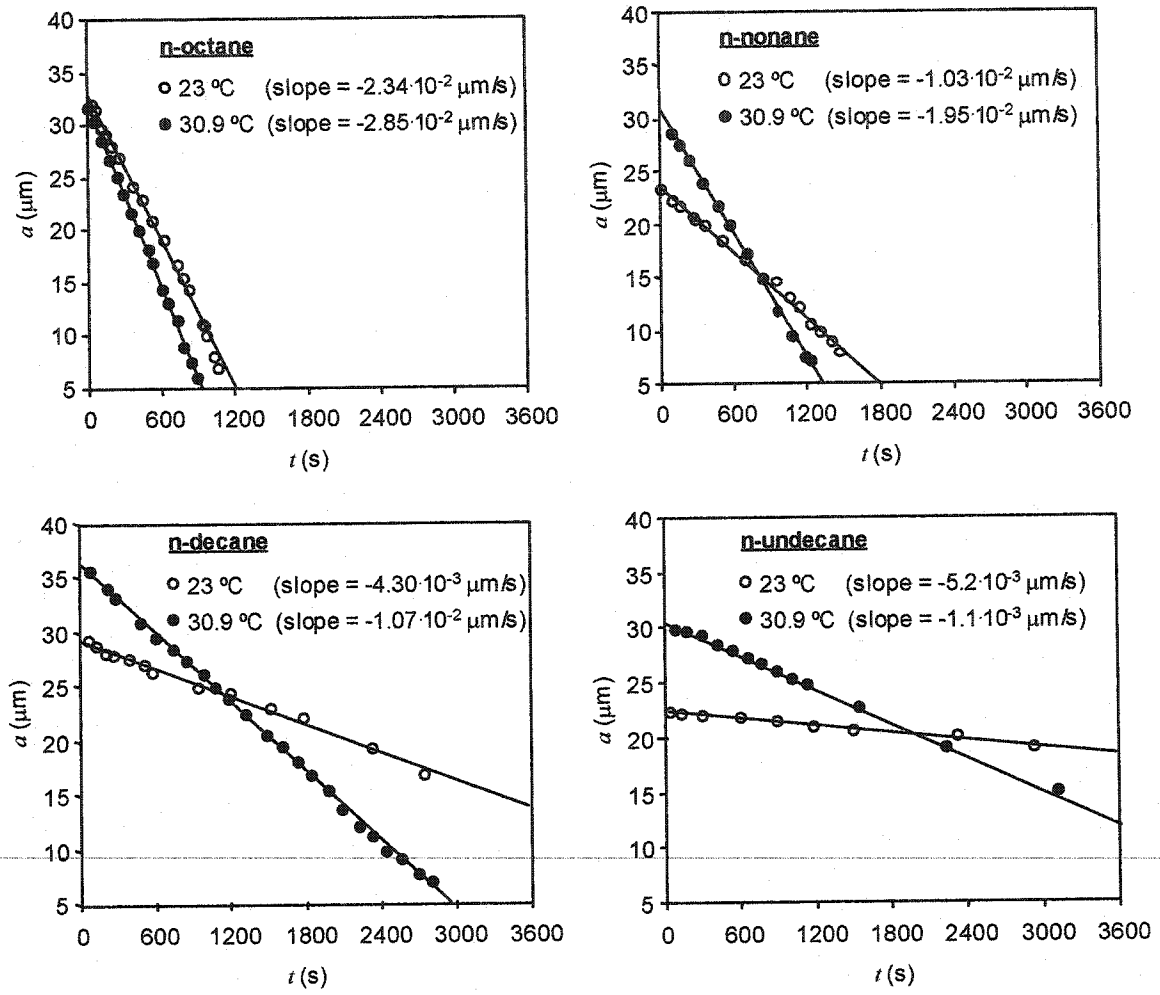


Figure 2.5. Solubilization of several drops of linear alkanes in oil-free solutions of $C_{12}E_8$ (2.5 wt.%) in water ($\theta^o = 0$) at two different temperatures.

section. It is seen that in all cases the drop radii decay linearly in time. Squalane drops did not exhibit measurable change in their sizes in similar tests.

A linear decay in drop size has been observed in a number of studies on the initial solubilization rate of individual drops of pure oils in aqueous solutions of nonionic surfactants [21, 22, 25]. If micellar solubilization at the interface limits mass transfer

Table 2.2. Mass transfer coefficients k^o (mol $m^{-2} s^{-1}$) for pure alkanes in $C_{12}E_8$ (2.5 wt.%)

T \ ACN	8	9	10	11
23 °C	$1.44 \cdot 10^{-4}$	$5.80 \cdot 10^{-5}$	$2.24 \cdot 10^{-5}$	$5.26 \cdot 10^{-6}$
30.9 °C	$1.74 \cdot 10^{-4}$	$1.09 \cdot 10^{-4}$	$5.53 \cdot 10^{-5}$	$2.50 \cdot 10^{-5}$

Table 2.3. Interfacial resistance $\Re_I^o = c_{sat}^o / k^o$ (s/m) for alkanes in $C_{12}E_8$ (2.5 wt.%)

T \ ACN	8	9	10	11
23 °C	---	---	$4.55 \cdot 10^5$	$5.32 \cdot 10^5$
30.9 °C	$2.55 \cdot 10^5$	$3.23 \cdot 10^5$	$4.86 \cdot 10^5$	$6.16 \cdot 10^5$

rates as suggested by these studies, then it is possible to obtain the specific solubilization rate constant k^o, since Eqs. [2.8] and [2.5] apply and they reduce to:

$$\tau = 1 - r \quad \text{whence} \quad \frac{dr}{d\tau} = -1 \quad \text{or} \quad \frac{da}{dt} = -k^o v \,. \qquad [2.69]$$

Table 2.2 summarizes the mass transfer coefficients that were determined for each of the oils. Data indicate that the solubilization rate increases with temperature and decreases when the alkane carbon number (ACN) of the oil is increased. The data reported in Tables 2.1 and 2.2 can be used to calculate effective interfacial resistances to mass transport $\Re_I^o = c_{sat}^o / k^o$ (Eq. [2.31]), which are reported in Table 2.3. It is seen in this table that $\Re_I^o$ increased with the ACN of the oil. From a kinetic standpoint, this result

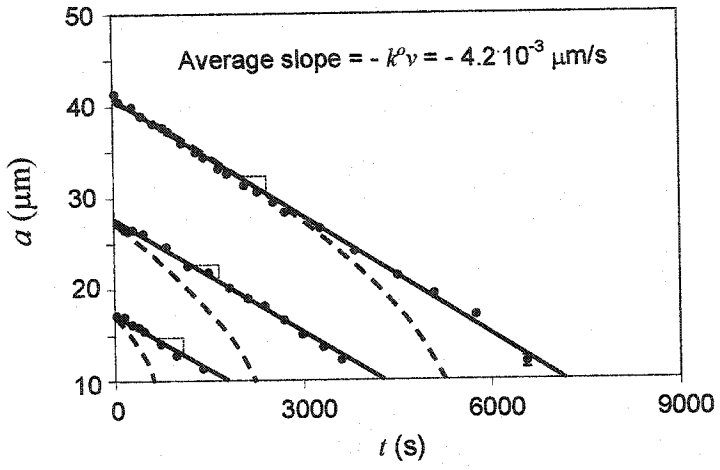


Figure 2.6. Solubilization of several drops of n-decane in an oil-free solution of $C_{12}E_8$ (2.5 wt. %) in water (θ^o = 0) at room temperature. Solid lines: linear fit of the data with Eq. [2.69]. Dashed line: predicted trend assuming mass transport controlled by micellar diffusion (Eq. [2.70]). Experimental error is shown in the last datum for the drop with largest initial radius.

suggests that the energy required to transfer an oil molecule from drop to micelle increases with the length of the hydrocarbon chain, and therefore with the molar volume of the alkane. This result has significant implications to the solubilization of hydrocarbon mixtures as discussed later in this section.

Figure 2.6 shows several experiments for the solubilization of drops of n-decane at room temperature. An average value for $k^o v$ (= - da/dt) of 4.2 · 10^{-3} μm/s was obtained from the results of five independent tests, including those shown in Figure 2.7, whence k^o = 2.24·10^{-5} mol/m^2·s. An important feature of Figure 2.7 is that the rates of change of drop radii are independent of the size of the drop, as suggested by Eq. [2.69]. This feature was confirmed for other alkanes both at 23 and 30.9 °C.

Figure 2.6 also shows in dashed lines the predicted time-dependent droplet sizes assuming mass transfer controlled by diffusion of micellar aggregates in the aqueous

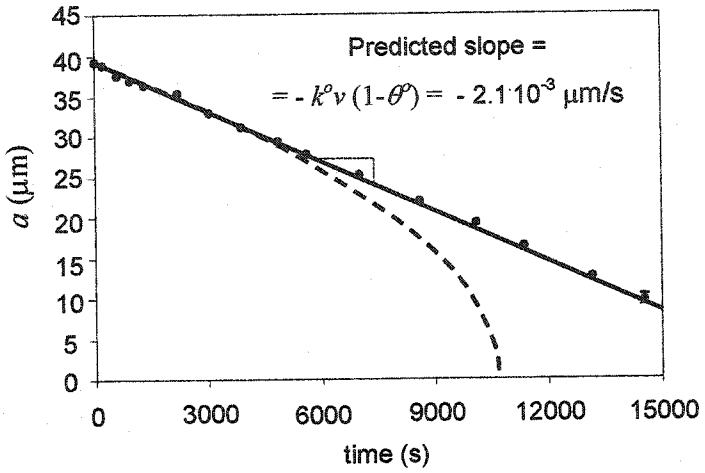


Figure 2.7. Solubilization of a drop of n-decane in aqueous $C_{12}E_8$ (2.5 wt. %) partially saturated with n-decane (θ^o = 0.50). Solid line: predicted trend assuming interfacial resistance as limiting (Eq. [2.69]). Dashed line: predicted trend when micellar diffusion is limiting (Eq. [2.70]).

bulk. These predictions were obtained using D = 7 x 10^{-11} m^2/s. This diffusion coefficient corresponds to T ~ 23 °C and it was calculated from data obtained by Brown *et al.* [48] for micelles of $C_{12}E_8$ in aqueous solution using pulse field gradient NMR and quasi-elastic light scattering. If diffusion is rate-limiting, Eqs. [2.11] and [2.3] apply and they simplify for the conditions of these tests to:

$$\tau' = \frac{1}{2}\left(1 - r^2\right) \quad \text{whence} \quad \frac{dr}{d\tau'} = -\frac{1}{r} \quad \text{or} \quad \frac{da}{dt} = -\frac{Dc^o_{sat} v}{a} \qquad [2.70]$$

where v is $1.95 \cdot 10^{-4}$ m^3/mol for n-decane and c^o_{sat} = 10.2 mol/m^3 as determined above. On this basis, Figure 2.6 shows that a classic diffusional approach is inadequate to describe the solubilization of pure n-decane in aqueous $C_{12}E_8$, since neither the fit of the experimental data nor the dependence of da/dt on the droplet size is satisfactory.

The time-dependent solubilization of n-decane in aqueous $C_{12}E_8$ (2.5 wt.%) partially saturated with this oil is reported in Figure 2.7 for an initial bulk concentration of n-decane (c_B) of 5.10 mol/m^3 ($\theta^o = c_B/c^o_{sat}$ = 0.50). Solid and dashed lines indicate the predictions of Eqs. [2.8] and [2.11], which simplify as follows,

$$\tau = \frac{1-r}{1-\theta^o} \quad \text{whence} \quad \frac{dr}{d\tau} = -\left(1-\theta^o\right) \quad \text{or} \quad \frac{da}{dt} = -k^o v\left(1-\theta^o\right) \qquad [2.71]$$

$$\tau' = \frac{1-r^2}{2\left(1-\theta^o\right)} \quad \text{whence} \quad \frac{dr}{d\tau'} = -\frac{\left(1-\theta^o\right)}{r} \quad \text{or} \quad \frac{da}{dt} = -\frac{Dc^o_{sat}v}{a}\left(1-\theta^o\right) \qquad [2.72]$$

The value of k^o determined above was used to generate the profile that corresponds to the interface-controlled mass transfer model in Figure 2.7, as well as in subsequent calculations using this model. In addition, θ^o was assumed constant in this and subsequent solubilization tests of individual droplets since the overall change in bulk concentration due to mass transfer is negligible in all cases. For example, it can be shown that the complete solubilization of the drop observed in this experiment would have raised c_B by only 0.005% of its initial value.

The trend shown for a in Figure 2.7 indicates that at a bulk concentration of n-decane of 5.10 mol/m^3 solubilization still took place and therefore the saturation limit had not been reached. In addition, it is seen that the drop radius diminished in a linear fashion as before, but at a rate reduced by a factor equal to the fractional saturation of the bulk phase. This is, when θ^o = 0.5, the rate of decay of the radius was 1-θ^o = 0.5 times that for θ^o = 0. These findings are reproduced satisfactorily by Eq. [2.71]. On the other hand, Eq. [2.72], which assumes diffusion control, correctly predicts the rate of reduction of the drop size at early times, but incorrectly forecasts an increasing rate as the radius diminishes. In additional experiments with initial bulk concentrations of n-decane of 2.55

mol/m^3 (θ^o = 0.25) and 7.65 mol/m^3 (θ^o = 0.75), linear decay of a was also observed and the slope $-da/dt$ was 71% and 31% of the reference value for θ^o = 0, whereas Eq. [2.71] predicts 75% and 25% respectively. Therefore, these results confirm interfacial resistance to mass transport as rate controlling and suggest that the proposed modeling is adequate to estimate the solubilization rate for various θ^o.

Two kinds of experiments were performed for the solubilization of mixtures of n-decane and squalane. Firstly, mixed drops with varying initial composition were placed in oil-free aqueous $C_{12}E_8$ (2.5 wt.%). Results of these tests are shown in Figure 2.8 for the case in which the initial mol fraction of n-decane in the mixture was x_0 = 0.89, 0.80 and 0.70, respectively. In general, it was found that drop radii diminished faster at early times with the rate of decrease slowing gradually, and droplets approached a limiting size in an asymptotic fashion. This limiting size coincided in all cases within experimental error with the calculated radius of a hypothetical drop that would contain only the squalane initially present in the original drop (dotted line). This result confirms that squalane was not solubilized in $C_{12}E_8$ micelles to a measurable extent even in the presence of a more soluble compound such as n-decane. Therefore, it is adequate to consider this oil as immobile in the sense described earlier when considering Figure 2.1 (bottom), so that the partitioning of squalane between the oil drops and the micelles was negligible and that the aggregates carried only n-decane.

Figure 2.8 also compares the experimental data with predictions of Eqs. [2.8] and [2.11] with θ^o = 0. The transient drop sizes are best modeled when interfacial resistance is assumed as rate controlling, whereas the diffusional approach predicts faster solubilization rates as it did for pure hydrocarbon drops. Both models yielded the same limiting size for the drop as might be expected.

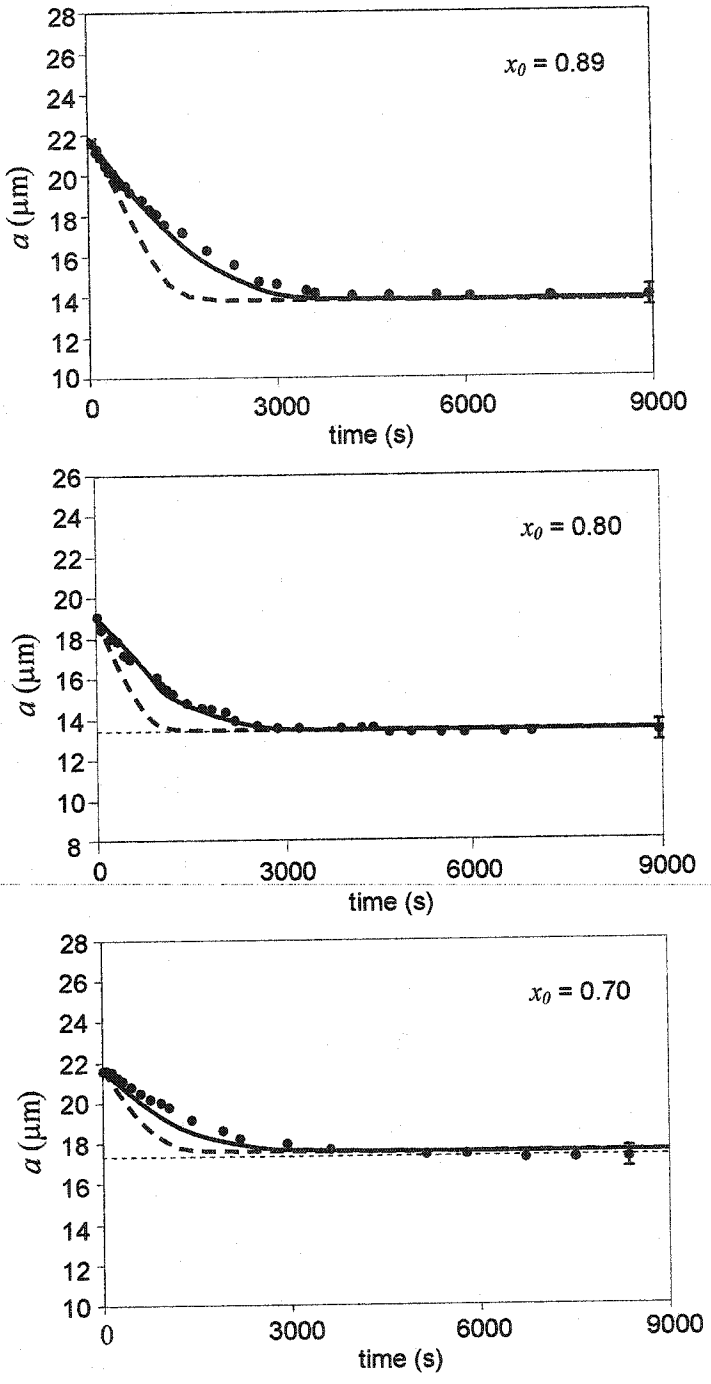


Figure 2.8. Solubilization of mixed drops of n-decane and squalane in an oil-free solution of $C_{12}E_8$ (2.5 wt. %) in water ($\theta^o = 0$) at 23 °C. Solid lines: predicted trends assuming mass transport controlled by interfacial resistance (Eq. [2.8]). Dashed lines: predicted trends assuming mass transport controlled by micellar diffusion (Eq. [2.11]). Dotted lines: predicted limiting sizes, determined from the condition $x = \theta^o$. x_0 is the molar fraction of n-decane in the drop at $t = 0$.

Secondly, drops of squalane were placed in partially saturated solutions of n-decane at room temperature. In this case, the droplet size is expected to increase in time because n-decane will be transferred from the aqueous bulk to the oil drop. This behavior does occur as shown in Figure 2.9, along with calculations made from Eqs. [2.8] and [2.11] for interface- and diffusion-limited mass transfer kinetics, respectively. According to these expressions, the size of the drops at equilibrium (dotted lines) is reached when the molar fraction of n-decane in the mixed oil equals the fractional saturation in the bulk, i.e., $x = \theta^o$. It is seen that the model that assumes interfacial phenomena as limiting provides the best fit of the transient data in all experiments. This is most noticeably for $\theta^o = 0.75$, in which case the difference between the predictions from the two models surpasses the experimental error.

Figure 2.10 reports results from solubilization experiments with drops of n-octane/squalane mixtures at 30.9°C for three different initial compositions of n-octane. As before, the drop size diminished to level in all cases to the drop size that can be calculated assuming that only squalane is left in the drop at the end of the experiment.

These results indicate that the solubility of squalane at 30.9 °C was still negligible within the timeframe of the experiments. The solid lines in these plots correspond to predictions for the transient drop sizes assuming interfacial resistance as rate-limiting (Eq. [2.8]). The model renders a satisfactory agreement with experimental data, exhibiting small deviations as the drop becomes rich in squalane. The same calculations were also performed with the model for solubilization of multicomponent mixtures proposed earlier (Eqs. [2.15]-[2.29]). When it was assumed that $\mathbf{a}_j = x_j$ (Eq. [2.18]), numerical results exactly matched the predictions from Eq. [2.8] as might be expected. The trends shown as dashed lines in Figure 2.10 correspond to results from the same

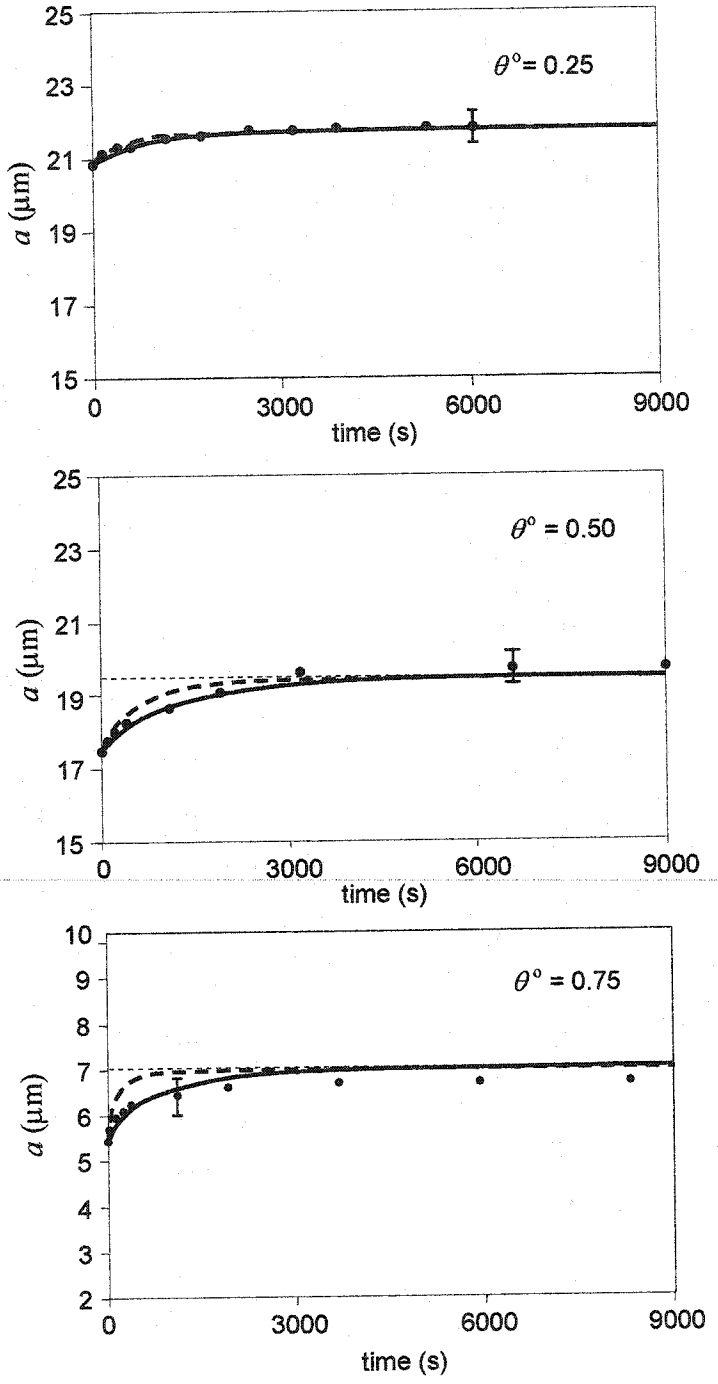


Figure 2.9. Swelling of drops of squalane in aqueous $C_{12}E_8$ (2.5 wt. %) partially saturated with n-decane at 23°C. Solid lines: predicted trends assuming interfacial phenomena as limiting (Eq. [2.8]). Dashed lines: predicted trends assuming micellar diffusion as limiting (Eq. [2.11]). Dotted lines: Predicted radii at equilibrium, determined from the condition $x = \theta^o$.

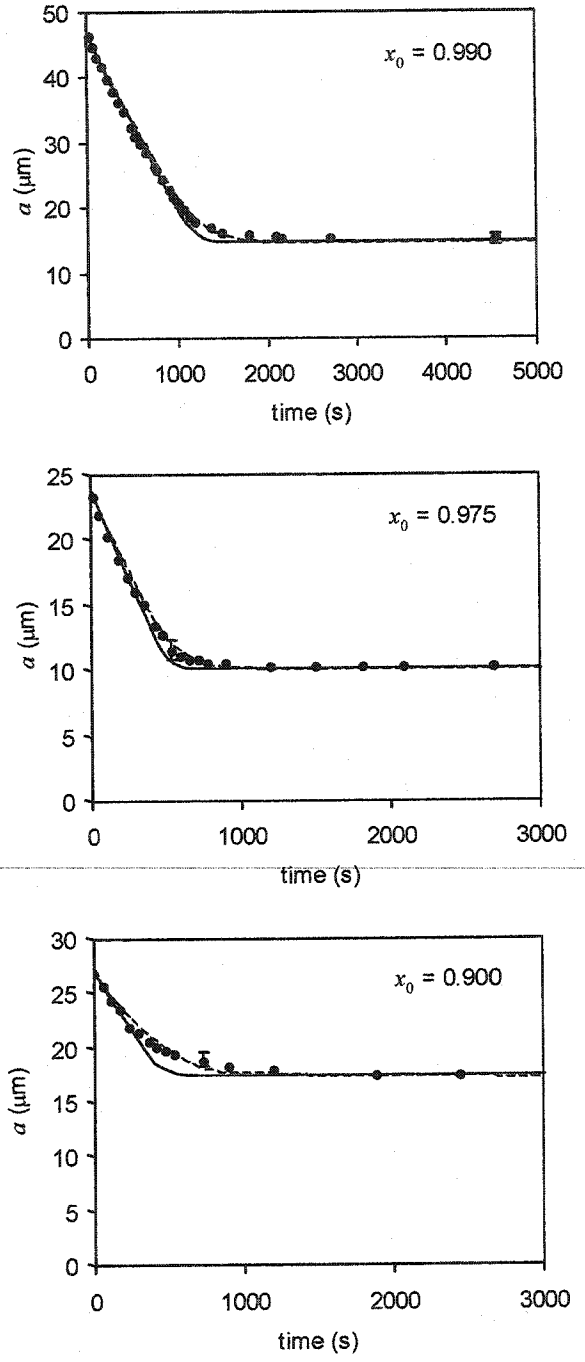


Figure 2.10. Solubilization of mixed drops of n-octane and squalane in an oil-free solution of $C_{12}E_8$ (2.5 wt. %) in water (θ^o = 0) at 30.9 °C. Solid lines: predicted trends assuming mass transport controlled by interfacial resistance and $\mathbf{a}_j = x_j$. Dashed lines: predicted trends assuming mass transport controlled by interfacial resistance and $\mathbf{a}_j = \phi_j$.

model assuming $\mathbf{a}_j = \phi_j$ (Eq. [2.19]). It is seen that this assumption removes the small deviations referred to above, and provides excellent agreement with the data. This was also verified for the small deviations that were observed for experiments with n-decane and squalane with x_0 = 0.89 and x_0 = 0.70 at 23 °C (Figure 2.9). For the mixture with x_0 = 0.80 the predictions with $\mathbf{a}_j = \phi_j$ rendered a slightly slower decay in the rate of reduction of the drop size than the one measured experimentally. In this case, the differences between measured and predicted drop sizes were of the order of the experimental error.

The ability of the multicomponent model to account for the solubilization of oil drops containing more than one solute with significant solubility in the surfactant solution was tested on mixtures of n-octane/n-undecane and n-decane/n-undecane in aqueous solutions of $C_{12}E_8$ (2.5 wt.%) at 30.9 °C. Lim [50] measured the activities ($\mathbf{a}_j = c_{sat,j}/c^o_{sat,j}$, see Eq. [2.16]) of n-octane, n-decane and n-undecane in n-octane/n-undecane and n-decane/n-undecane mixtures at the above-mentioned conditions using gas chromatography (GC), and following a procedure analogous to the one described by Prak *et al.* [52]. Figure 2.11 shows experimental measurements for $\mathbf{a}_j$ as a function of the molar composition of the oil phase in contact with the surfactant solution x_j. Symbols stand for the experimental data, and the solid lines are empirical fits using the following expressions:

$$\mathbf{a}_1 = x_1 \exp\left(A x_2^n\right); \quad \mathbf{a}_2 = x_2 \exp\left(A' x_1^{n'}\right) \qquad [2.73]$$

where A, A', n and n' are fitting parameters (n-octane/n-undecane mixture: A = -0.653; n = 0.730; A' = 0.236; n' = 0.427. n-decane/n-undecane mixture: A = -0.560; n = 0.815; A' = 0.507; n' = 1.321).

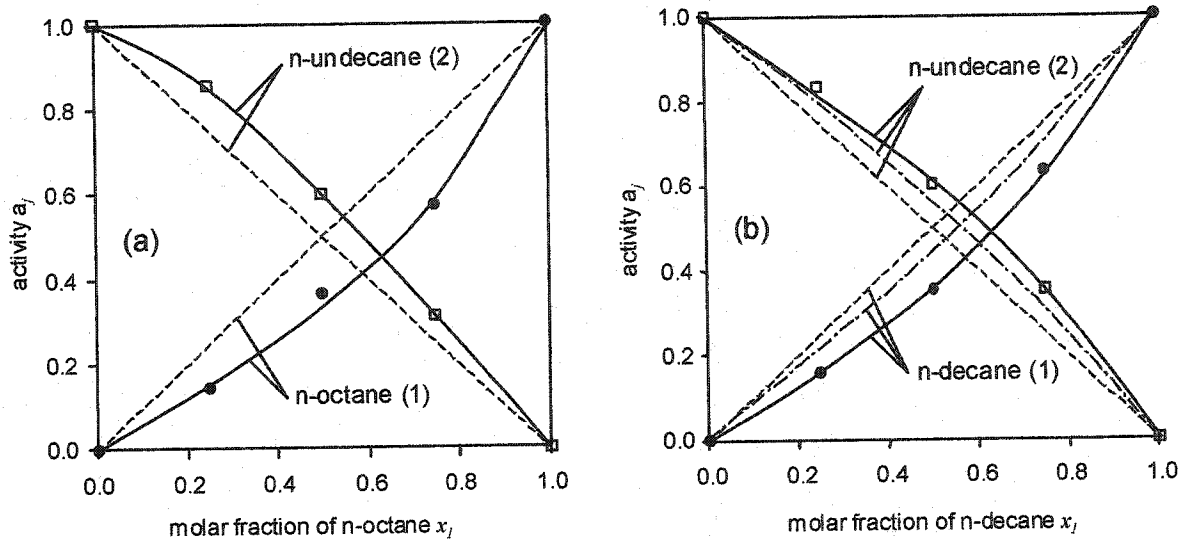


Figure 2.11. Measured activities ($\mathbf{a}_j = c_{sat,j} / c^{o}_{sat,j}$) of individual components in n-octane/n-undecane and n-decane/n-undecane mixtures in contact with a solution of $C_{12}E_8$ (2.5 wt.%) at 30.9°C [50].

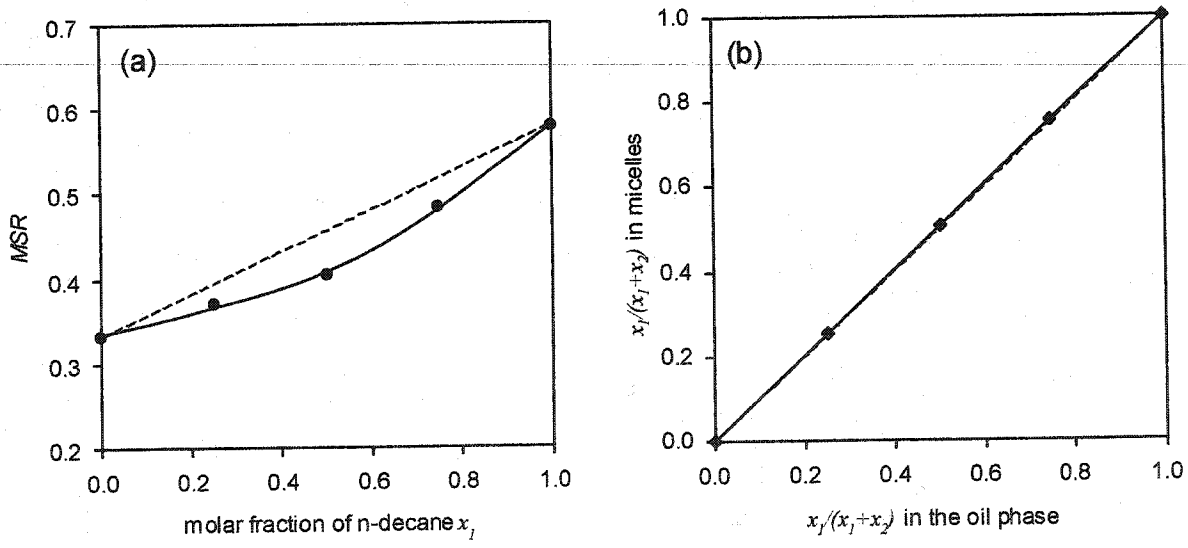


Figure 2.12. (a) Molar solubilization ratio, and (b) composition of oil and micellar phases in equilibrium for the n-decane/n-undecane system in solutions of $C_{12}E_8$ (2.5 wt.%) at 30.9°C [50].

The dashed lines in Figure 2.11 correspond to ideal solution behavior ($\mathbf{a}_j = x_j$). For the binary n-decane/n-undecane, plots for $\mathbf{a}_j = \phi_j$ are also included (dash-dot lines). It is seen that the systems exhibit moderate deviations from ideal solution behavior in both cases, probably due to the partitioning of $C_{12}E_8$ between the phases. Also, Figure 2.11(b) suggest that, in absence of experimental data, it is adequate to assume $\mathbf{a}_j = \phi_j$ instead of $\mathbf{a}_j = x_j$ if small deviations from ideal solution behavior are expected. The deviations from ideal behavior were mainly due to the non-linear variation of the molar solubilization ratio with composition, as shown in Figure 2.12(a) for the (1) n-decane/(2) n-undecane system. For such system, it seems that the ratio $x_1/(x_1+x_2)$ was nearly the same in the oil phase and in the micelles in equilibrium with it [Figure 2.12(b)].

Figure 2.13 shows data for the transient behavior of drops containing initially n-octane and n-undecane at three different initial compositions (top to bottom, x_0 = 0.25, 0.50 and 0.75 for n-octane, respectively). The solid and dashed lines correspond to predictions from the model with $\mathbf{a}_j = x_j$ and with the experimental values for $\mathbf{a}_j$ reported in Figure 2.12, respectively. It is seen that the assumption of ideal solution behavior provided a satisfactory agreement with the data. This agreement was slightly better when the experimental activity was considered instead, as might be expected. In any case, the difference between both trends is within experimental error, thus indicating that the effect of deviations from ideal behavior that are observed for these systems do not affect significantly the transient behavior of drop sizes. This observation is valid for the mixtures of linear alkanes reported in this study, but it may not hold for mixtures of components exhibiting very dissimilar chemical structures.

It is seen in Figure 2.13 that the radius of the drop with x_0 = 0.25 decayed with time in an apparently linear fashion. However, as the initial composition of n-octane was

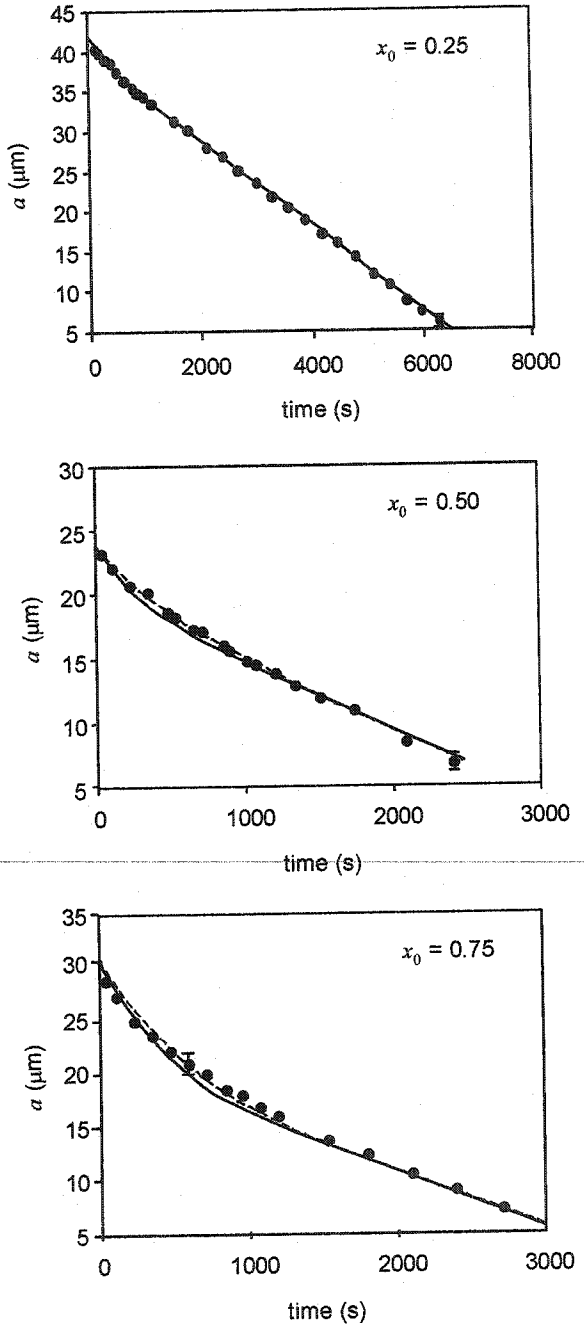


Figure 2.13. Solubilization of mixed drops of n-octane and n-undecane in an oil-free solution of $C_{12}E_8$ (2.5 wt. %) in water (θ^o = 0) at 30.9 °C. Solid lines: predicted trends assuming mass transport controlled by interfacial resistance and $\mathbf{a}_j = x_j$. Dashed lines: predicted trends assuming mass transport controlled by interfacial resistance with the experimental activities reported in Figure 2.12.

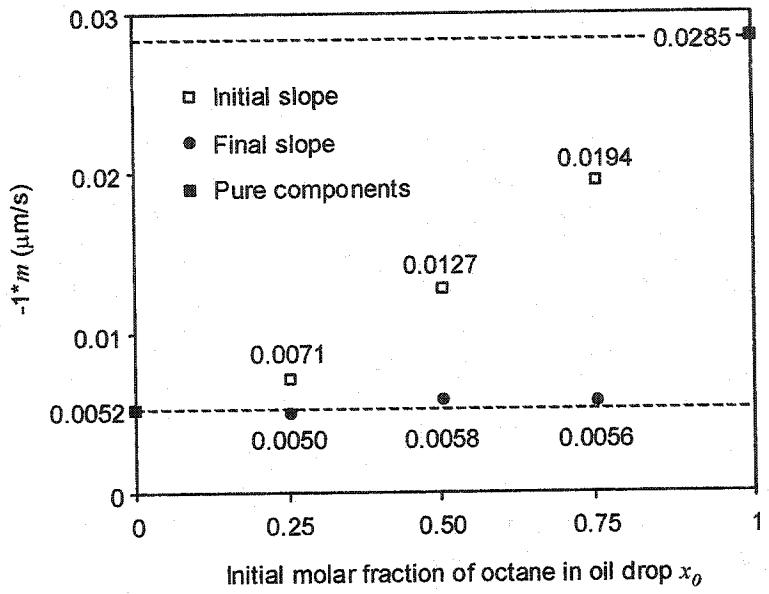


Figure 2.14. Experimental values for the initial and final rates of decay of drop radius of mixed drops of n-octane and n-undecane in an oil-free solution of $C_{12}E_8$ (2.5 wt. %) in water ($\theta^o = 0$) at 30.9 °C.

increased, the onset of a non-linear trend became evident in a fashion that suggests selective partitioning in the micellar solution in favor of n-octane. This effect was quantified by measuring the slopes $m = da/dt$ of lines tangent to the a vs. t data at the beginning and end of each experiment. Results from such measurements are summarized in Figure 2.14. This figure shows that the initial value for $-da/dt$ increased with the initial composition of n-octane. The most significant feature of Figure 2.14 is the fact that the final value of $-da/dt$ was practically equal to that of pure n-undecane for all the mixtures, thus suggesting that only n-undecane was left in the drops at the time the experiments were concluded. This result conclusively shows selective solubilization of the mixture in favor of the alkane with smallest molar volume, as was also observed for n-octane/squalane and n-decane/squalane mixtures.

Figure 2.15 shows predictions for the transient behavior of the composition of n-octane in the drop and bulk solutions for the three mixtures reported in Figure 2.13, using the model for multi-component mixtures and the experimental activities referred to above. The model clearly predicts selective solubilization in favor of n-octane as reported above. Furthermore, it is seen that at t ~ 2000 s practically all n-octane had been transferred to the surfactant solution. The final slopes reported in Figure 2.14 were indeed measured for t > 2000 s in all cases, thus reinforcing the idea that only n-undecane was left in the drops at the time the experiments concluded.

Figure 2.16 shows data for the transient behavior of drops containing initially n-decane and n-undecane at three different initial compositions (top to bottom, x_0 = 0.25, 0.50 and 0.75 for n-decane, respectively). In this case, the predictions of the multicomponent model using $\mathbf{a}_j = x_j$ and the experimental value of $\mathbf{a}_j$ overlap within the resolution of the plots and are presented as solid lines. Satisfactory agreement was obtained between the predictions from the model and the experimental data in all cases. The dash-dot lines are calculations for the transient drop size assuming that the initial rate of change of drop size $-da/dt$, which is given by:

$$-\left.\frac{da}{dt}\right|_{t=o} = k_1^o v_1 \mathbf{a}_{1,t=0} + k_2^o v_2 \mathbf{a}_{2,t=0} \qquad [2.74]$$

remains constant. The comparison between these lines, the experimental trends and the predictions from the model (solid) line, suggest that there was a slight reduction in $-da/dt$ with time, i.e., that selective solubilization may have also occurred for this system.

Figure 2.17 shows predictions for the composition of the oil drop and the surfactant solution as time proceeded for the three droplets using the experimental activities

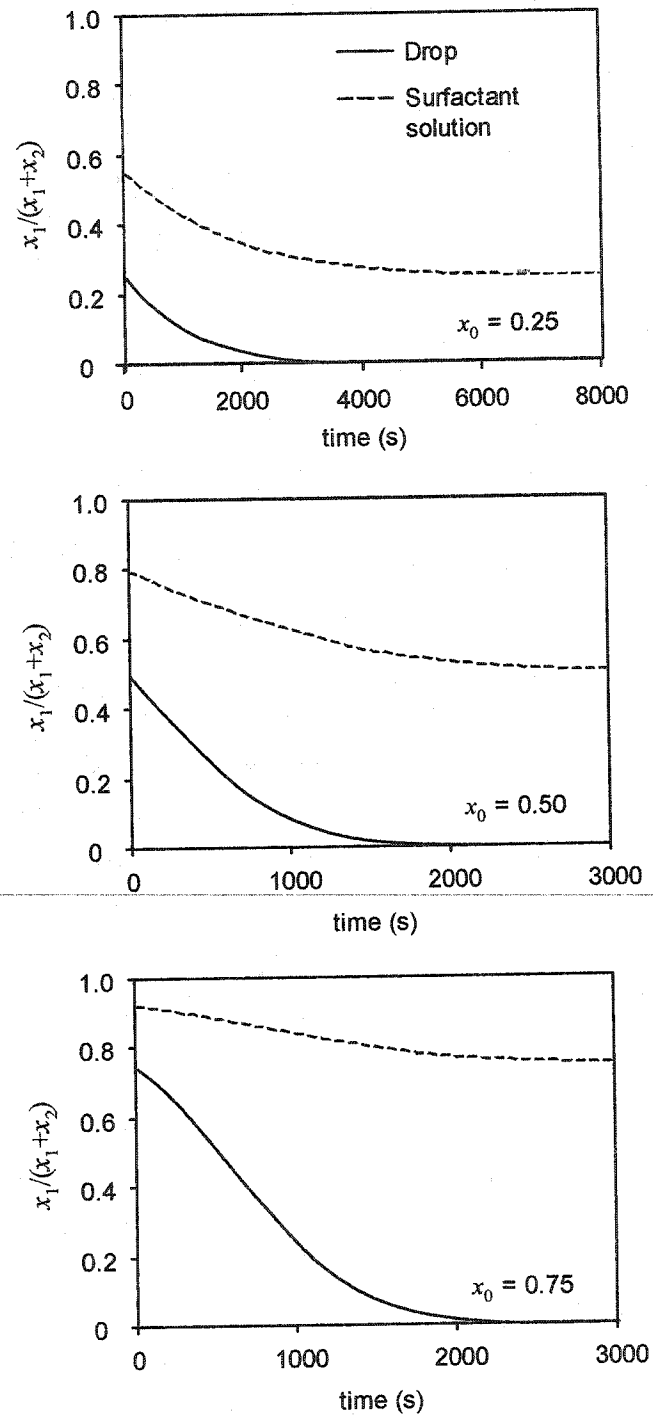


Figure 2.15. Predicted trends for the molar composition $x_1/(x_1+x_2)$ of the oil drops and surfactant solutions for the solubilization of mixtures of n-octane (1) / n-undecane (2) in $C_{12}E_8$ (2.5 wt.%) at 30.9 °C.

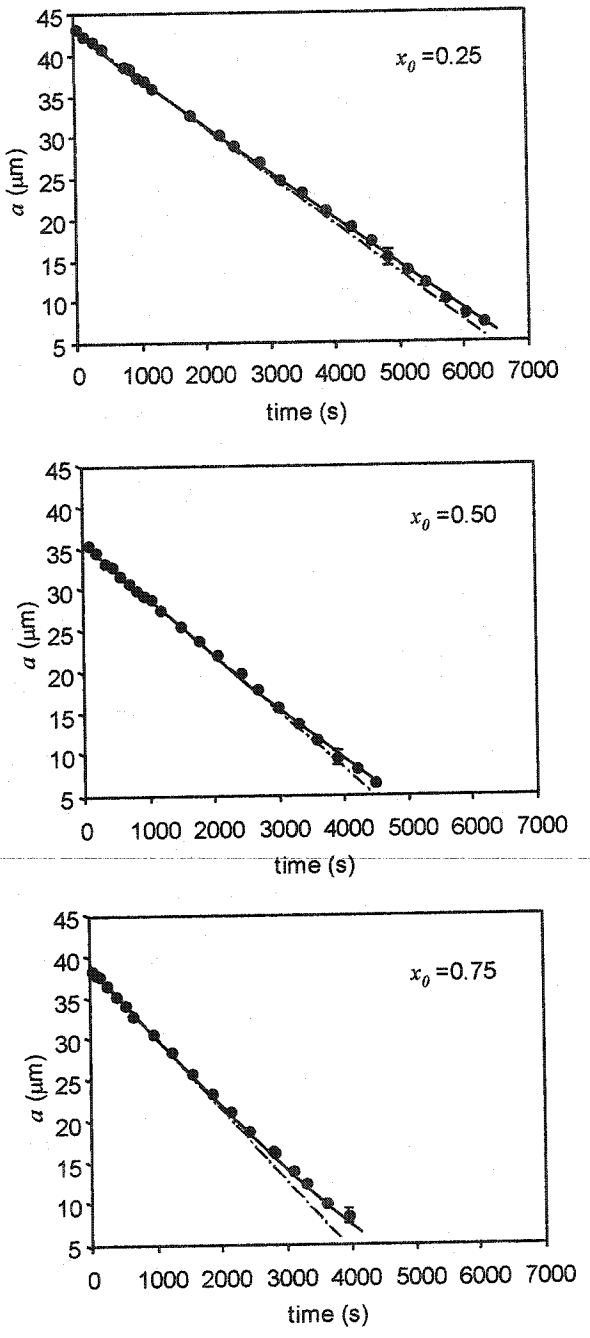


Figure 2.16. Solubilization of mixed drops of n-decane and n-undecane in oil-free solutions of $C_{12}E_8$ (2.5 wt. %) in water ($\theta = 0$) at 30.9 °C. Dots: Experimental data. Solid lines: Predictions from multicomponent mass transfer model assuming interface-controlled mass transfer. Dash-dot lines, Predictions assuming that the initial solubilization rate remains constant.

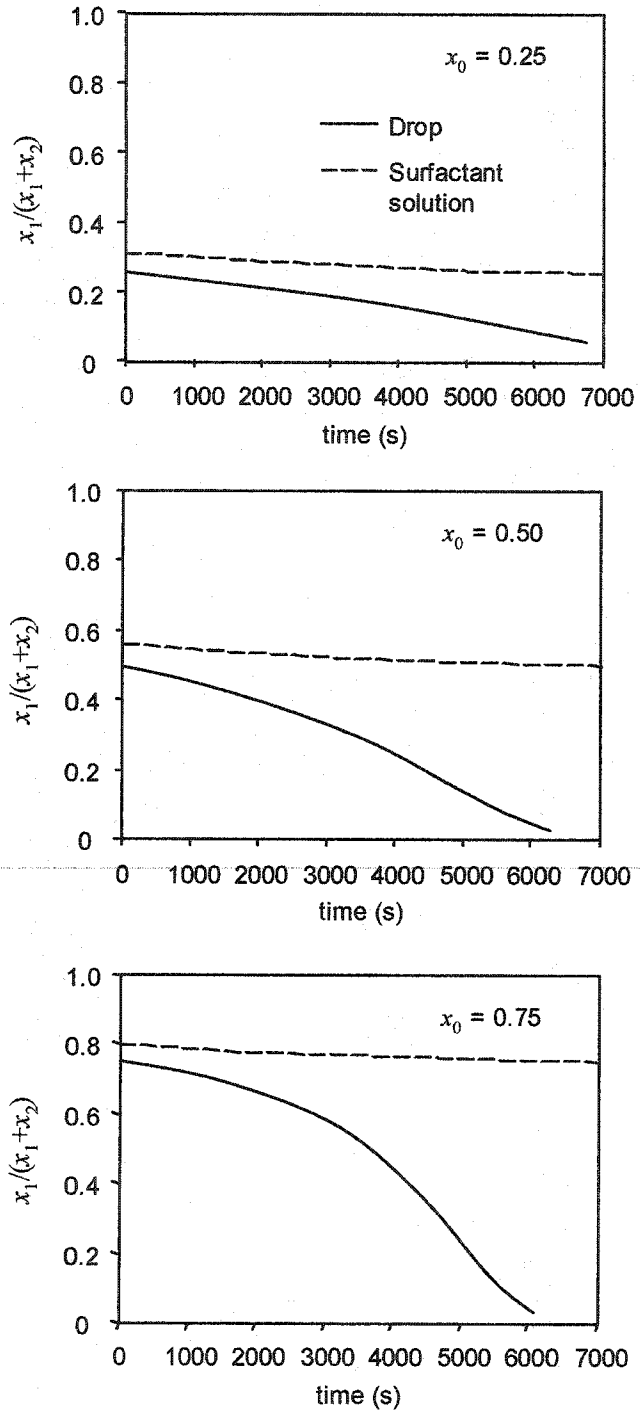


Figure 2.17. Predicted trends for the molar composition $x_1/(x_1+x_2)$ of the oil drops and surfactant solutions for the solubilization of mixtures of n-decane (1) / n-undecane (2) in $C_{12}E_8$ (2.5 wt.%) at 30.9 °C.

reported in Figure 2.11 for this system. These predictions also suggest selective solubilization for this system in favor of n-decane. However, the data shown in Figure 2.16 can also be correlated with linear trends and the differences between such trends and the corresponding experimental points are within experimental error. Calculations were performed for other compositions and initial drop sizes for which the initial droplet would remain nearly spherical when pressed against the capillary wall by buoyancy forces ($a_{0,\,MAX} \leq \sqrt{\sigma/g(\rho-\rho_d)}$ ~ 600 μm), and in all cases the resulting profile could be fitted linearly, and the differences between such fits and the calculated radii were within experimental error. Therefore, the interpretation of kinetics experiments for the n-decane/n-undecane system suggest slightly selective solubilization in favor of n-decane, but the small difference in solubilization rates between n-decane and n-undecane does not allow ruling out non-selective solubilization for this particular system. This is certainly not the case for the n-octane/n-undecane, n-octane/squalane and n-decane/squalane mixtures discussed above, for which selective solubilization was conclusively demonstrated.

An interesting corollary of the preceding analysis is that the size of drops of mixed oils undergoing selective solubilization can exhibit a transient decay that can be mistakenly interpreted as linear (i.e., non-selective), depending on the resolution of the experimental method or the prevailing experimental conditions. Carroll [24] suggested this idea as a possible explanation for the results previously reported by him and his co-workers [26] for the apparently non-selective solubilization of n-hexadecane/squalane mixtures in aqueous solutions of $C_{12}E_5$ (1 wt.%), which was later expected to be selective in light of the results reported in Ref. [24] for the selective solubilization of triolein/n-hexadecane mixtures in aqueous $C_{12}E_6$ (1 wt.%) at 45 °C in favor of n-hexadecane.

2.5.3. Mass transfer in emulsions

2.5.3.1. Case Study 1: Solubilization

Figure 2.18 (top) shows the transient behavior of the volume-weighted drop size distribution of an emulsion containing 0.04 wt. % n-hexadecane in an initially oil-free Tween 20 aqueous solution (2 wt. %), as reported by McClements and Dungan [1]. This concentration of oil corresponds exactly to the equilibrium solubilization capacity c_{sat}^{o}, and therefore $\theta^{o} < 1$ at all times during the experiment. If so, it seems plausible to expect a reduction in the sizes of all droplets (Figure 2.1, top) at a rate that would diminish as the saturation of the bulk phase is approached. However, the most relevant feature of Figure 2.18 (top) is the fact that the drop size distribution does not change significantly in time. No satisfactory explanation of this counterintuitive result was provided.

The solubilization process was simulated with the algorithm described above using the parameters listed in Table 2.4. The mass transfer coefficient k^{o} was calculated using Equation [2.52] and the value of k_i^{*} reported by McClements and Dungan for this system (1.62×10^{-9} m/s). The rest of the parameters were either measured as described above or taken from the original paper or from general sources of physical properties. No adjustable parameters were used in these calculations.

Figure 2.18 (center) shows the numerical results that are obtained for the volume-weighted drop size distribution using the model proposed above (Eqs. [2.50]-[2.60]). Results from simulations agree with the trend found experimentally, because they show that the shape and position of the distribution remain practically unchanged throughout the experiment. Indeed, a slight tendency of the volume-weighted drop size distribution to shift toward larger drop sizes is observed, and the calculated median of the

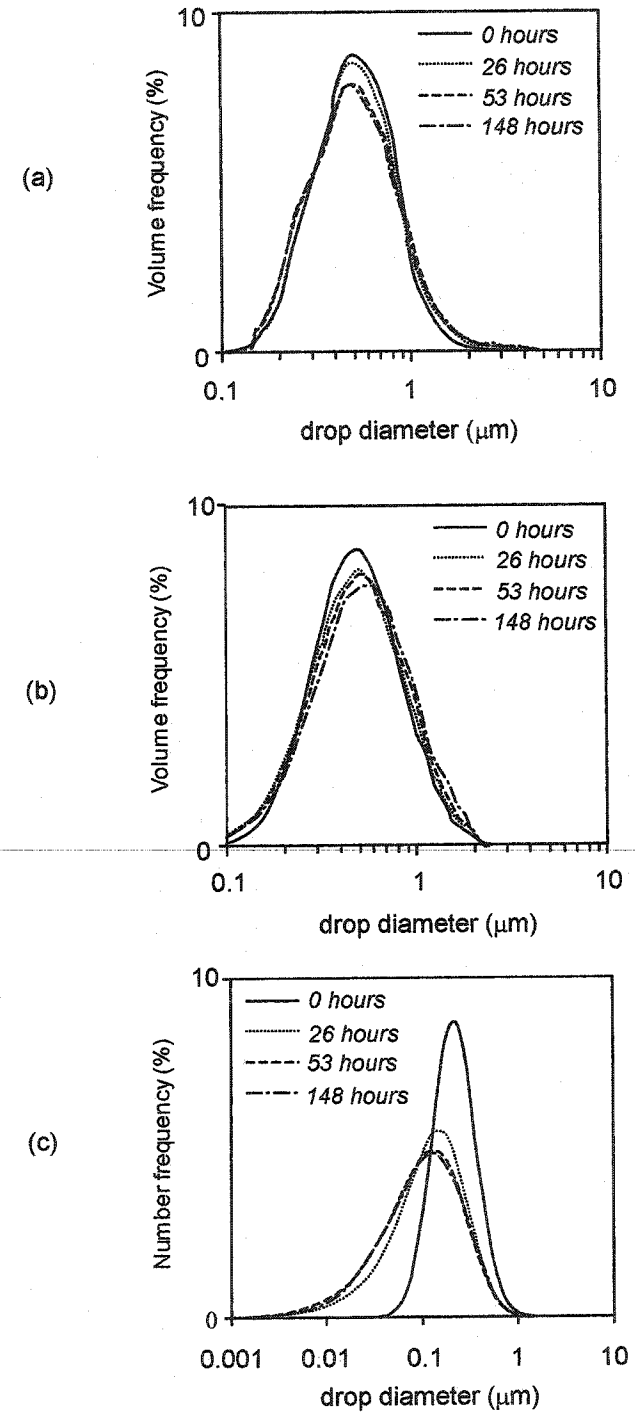


Figure 2.18. *Case study 1:* [(a)] Experimental data and [(b), (c)] simulation results for the transient volume (b) and number (c) drop size distribution of the emulsion.

Table 2.4. Parameters used in the simulations for case study 1

Parameter (units)	*Value*	*Parameter (units)*	*Value*
$d_{gV,0}$ (m) [a]	$4.83 \cdot 10^{-7}$	c^{o}_{sat} (mol/m^3)	1.766
σ_g [a]	0.521	c_S (mol/m^3)	16.29
n^*	$1.5 \cdot 10^{6}$	T (K)	303
Φ_0	$5.174 \cdot 10^{-4}$	σ (N/m)	$3.24 \cdot 10^{-3}$
x_0	1	v (m^3/mol)	$2.93 \cdot 10^{-4}$
θ_0	0	Δt (s)	30
k^o (mol/m^2 s)	$2.86 \cdot 10^{-9}$		

[a] $d_{gV,0}$ and σ_g are the geometric mean diameter and geometric standard deviation of the initial log-normal volume-weighted drop size distribution, respectively.

distribution increases as shown in Figure 2.19. The latter behavior was reported experimentally in Ref. [9] for hexadecane drops in aqueous solutions of Tween 20. In this study, the median of the volume-weighted drop size distribution was found to increase as solubilization took place, and the observed trend was explained as the outcome of simultaneous solubilization (which tends to decrease the mean droplet size) and Ostwald ripening (which tends to increase it).

However, Figure 2.18 (bottom) illustrates that if such distribution is reported in terms of the number of droplets rather than their volume, it becomes broader and extends towards smaller drop sizes with time as might be expected. In this case, the corresponding median *decreases* as shown in Figure 2.19.

Figure 2.19 also illustrates that the so-called Sauter or surface-volume mean drop diameter d_{AV}, which is calculated as

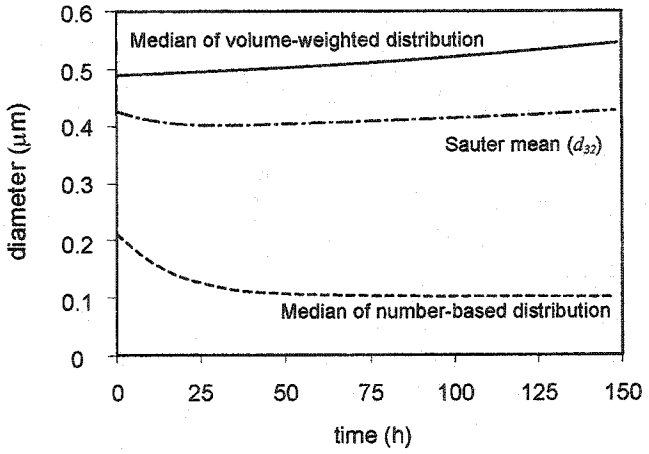


Figure 2.19. *Case study 1:* Numerical results for the transient behavior of the transient mean and Sauter drop sizes.

$$d_{AV} = \frac{\sum_l N_l d_l^3}{\sum_l N_l d_l^2} \,, \qquad [2.75]$$

was relatively *constant* and equal to 0.42 ± 0.02 μm. This figure is in excellent agreement with the findings of McClements and Dungan [1], who reported a value of 0.43 ± 0.02 μm for d_{AV}, and indicated that it remained practically invariant throughout the experiment. In Eq. [2.75], N_l and d_l are the droplet concentration and mean diameter, respectively, of the class l within the histogram of the drop size distribution.

Therefore, the assessment that the mean size and the drop size distribution remain unchanged or shift toward smaller or larger values depends on the basis used to calculate and report these characteristics of the emulsion. In a relatively broad volume-weighted drop size distribution, the volume fraction of the smaller drops is negligible when compared with that of the larger ones, and the relative change in sizes of the latter can be small enough as to have them within the same class of the histogram throughout the experiment. In consequence, the volume-weighted distribution appears not to

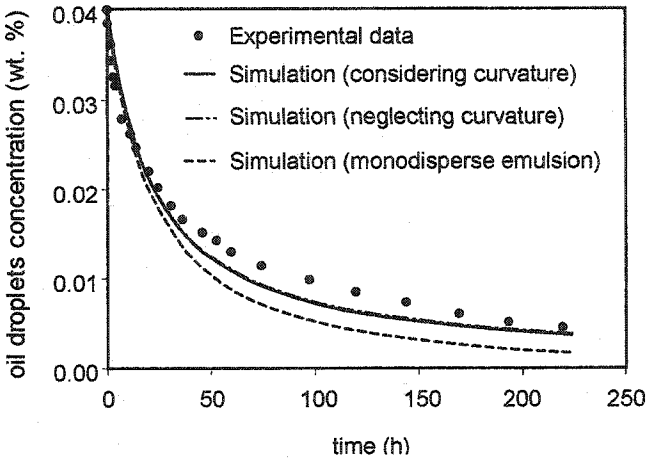


Figure 2.20. *Case study 1:* Experimental and numerical results for the concentration of oil present as droplets in the emulsion.

change significantly. In contrast, in the number-based drop size distribution small and large droplets contribute equally and therefore the effect of the solubilization is readily seen as a broadening of the distribution towards small sizes. Recently I became aware that Tai [53] performed numerical simulations for emulsions undergoing micellar solubilization using a population balance model and showed that the calculated volume-weighted drop size distribution does not change significantly in time, as found independently in this work.

Figure 2.20 shows in black dots turbidity measurements for the transient concentration of oil present as droplets for the same *n*-hexadecane-in-water emulsion. It indicates that as time proceeds, more *n*-hexadecane is solubilized in the surfactant solution. The process becomes considerably slower as saturation is approached.

The solid line in Figure 2.20 stands for the numerical simulation results. It can be shown that in this case, the concentration of oil present as droplets is simply given by (0.04 wt. %) x $\left(1-\theta^{o}\right)$. It is seen that the predicted behavior agrees well with the

experimental data, thus indicating that the proposed model properly accounts for the mass transport. This result also suggests that the mass transfer models represented by Equations [2.5] and [2.51] can be successfully related using Equation [2.52].

The dot-and-dash line in Figure 2.20 corresponds to the simulation when the contribution of the interfacial curvature to the chemical potential of the solute in the droplet is neglected, i.e., when $\exp(2\sigma v / RTa) \sim 1$. This trend does not depart significantly from the solid line, thus indicating that the solubilization process was driven by the difference in concentration between the interfacial region and the bulk solution, and that curvature effects are negligible. In general, this might be expected for most solubilization processes taking place well below the solubilization limit of the micellar solution.

The dashed line in Figure 2.20 is obtained by assuming that the emulsion is monodisperse with mean size equal to the computed Sauter diameter for the initial drop size distribution (0.42 μm). This assumption assures that the initial collection of droplets in the monodisperse emulsion has the same surface-to-volume ratio as drops in the initial polydisperse emulsion. It is seen that the calculated trend departs significantly from the experimental data and predicts a faster decay of the concentration of oil present as droplets in the emulsion. This significant result indicates that by neglecting the polydispersity of the initial emulsion, it is possible to obtain results inconsistent with experimental evidence, even though a model that is indeed representative of the underlying mass transfer mechanism is used to perform the calculations.

Finally, this case study is useful to illustrate the convergence characteristics of the algorithm used to model mass transfer in emulsions. Figure 2.21 shows the influence of

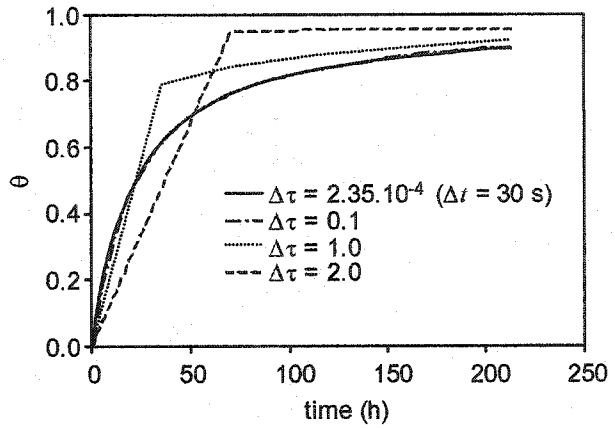


Figure 2.21. *Case study 1:* Effect of the selection of the time step $\Delta\tau$ on the numerical response of the proposed algorithm for case study 1.

$\Delta\tau$ on the calculated behavior of the dimensionless concentration of oil in the bulk phase θ for case study 1. It is seen that the value of $\Delta\tau$ that was chosen for these calculations ($\Delta\tau = 2.35 \cdot 10^{-4}$ or $\Delta t = 30$ s) was three orders of magnitude smaller than the one at which divergence of the numerical response starts to become noticeable. A similar criterion was applied to determine $\Delta\tau$ for the case studies 2 and 3 that are discussed below.

2.5.3.2. Case Study 2: Ostwald Ripening

Figure 2.22 shows in black dots the time-dependent behavior of the mean drop size for an emulsion of n-tetradecane (5 wt. %) dispersed in an aqueous solution of Tween 20 (5 wt. %) [6]. Data are represented either as $\bar{a}^2$ or $\bar{a}^3$ vs. time because a linear behavior should be observed in either case at long ripening times, depending on whether the mass transfer process is controlled by interfacial resistance or by diffusion, respectively. A common practice when processing Ostwald ripening data is to find the best linear fit by considering all experimental points. However, the LSW theory provides asymptotic solutions for the Ostwald ripening problem. Unless the initial drop size

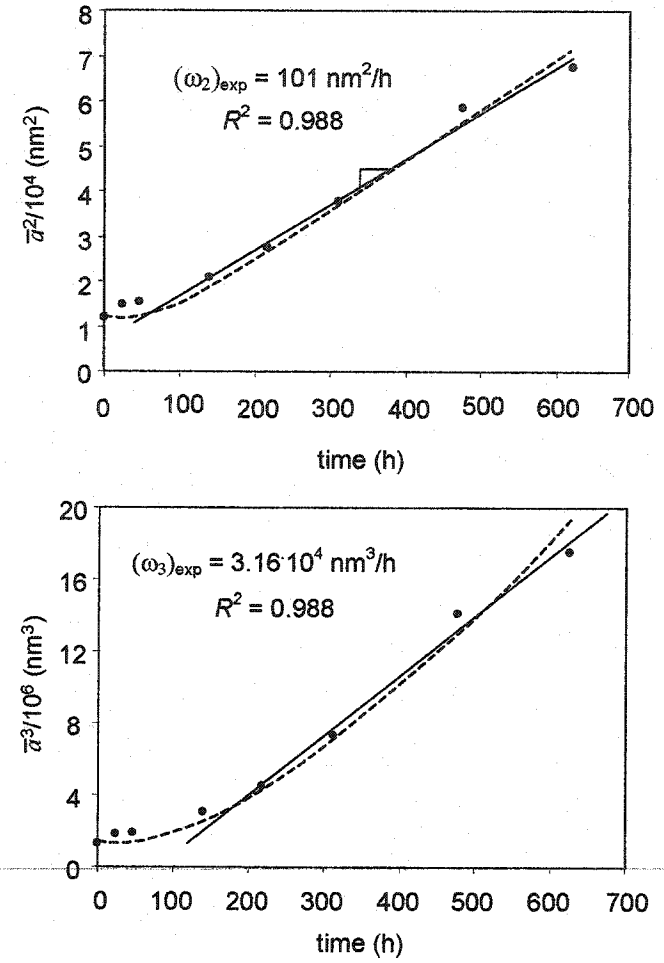


Figure 2.22. *Case study 2:* Experimental and numerical results for the transient behavior of the mean drop size. Top: plot of $\overline{a}^2$ vs. time. Bottom: plot of $\overline{a}^3$ vs. time. Black dots: experimental data. Solid lines: Linear fits at long ripening times. Dashed lines: Results from numerical simulations.

distribution is the same as the asymptotic distribution, there will be a transient as the system approaches the latter. This transient behavior is clearly seen in Figure 2.22 up to circa 200 hours. This is why linear fits (solid lines) are shown for experimental data for which t > 200 h. By doing so, correlation coefficients of 0.988 were obtained in both cases, and therefore it is not feasible to determine the limiting mass transfer mechanism based on the quality of the linear fit.

Table 2.5. Parameters used in the simulations for case study 2

Parameter (units)	*Value*	*Parameter (units)*	*Value*
$d_{gV,0}$ (m)	$2.34 \cdot 10^{-7}$	c^{o}_{sat} (mol/m^3)	5.80
σ_0	0.103	c_S (mol/m^3)	40.73
n^*	$4 \cdot 10^{5}$	T *(K)*	298
Φ_0	$6.45 \cdot 10^{-2}$	σ (N/m)	$3.96 \cdot 10^{-3}$
x_0	1	v (m^3/mol)	$2.60 \cdot 10^{-4}$
θ_0	0.08	Δt *(s)*	15
k^o (mol/m^{2}s)	$3.21 \cdot 10^{-7}$		

If diffusion dictates the Ostwald ripening rate, Equation [2.64] holds at long ripening times and the diffusion coefficient would be given by:

$$D = \frac{9}{4}\frac{\omega_3}{\alpha c^{o}_{sat} v} \qquad [2.76]$$

With the value of ω_3 obtained from Figure 2.22 (bottom) (ω_3 = $3.16 \cdot 10^{4}$ nm^3/h) and the physical properties listed in Table 2.5, a diffusion coefficient of $1.54 \cdot 10^{-14}$ m^2/s is calculated from Eq. [2.76]. Weiss *et al.* [6] report that the diffusion coefficient of Tween 20 micelles is approximately $4.2 \cdot 10^{-11}$ m^2/s. With this value, an Ostwald ripening rate a thousand-fold higher [$(\omega_3)_{\text{Micelles}}$ = $8.61 \cdot 10^{7}$ nm^3/h] is predicted. Therefore, the diffusion of micelles acting as carriers for the solute was not rate-limiting in this case.

In addition, the molecular diffusion coefficient of n-tetradecane in water is circa $5 \cdot 10^{-10}$ m^2/s. This value was obtained from the Wilke-Chang equation, which is recommended by Taylor [8] to estimate molecular diffusion coefficients for Ostwald ripening studies.

With this coefficient, the interfacial tension reported in Table 2.5 and the molecular solubility of n-tetradecane in water [54] ($1.1 \cdot 10^{-5}$ mol/m^3), an Ostwald ripening rate approximately eighteen times lower than the experimental one [$(\omega_3)_{Molecules}$ = $1.74 \cdot 10^3$ nm^3/h] is obtained. Hence, molecular diffusion cannot be primarily responsible for the observed ripening. Moreover, it seems unlikely that micelles would not play a major role in Ostwald ripening in view of their dominant role for solubilization and compositional ripening in similar systems, as demonstrated pervasively in this chapter.

On the other hand, if interfacial resistance limits mass transport kinetics, the mass transfer coefficient k^o can be calculated from Equation [2.68]:

$$k^o = \frac{81}{32}\frac{\omega_2}{\alpha v}. \qquad [2.77]$$

With the experimental Ostwald ripening rate of 101 nm^2/h reported in Figure 2.22 (top) and the parameters given in Table 2.5, an effective mass transfer rate k^o_{eff} = $3.21 \cdot 10^{-7}$ mol/m^2.s is obtained. An experimental value of k^o was calculated from solubilization tests of single drops of n-tetradecane in oil-free aqueous solution containing Tween 20 (5 wt. %). In these experiments, the drop size decayed linearly in time and the value of k^o was determined from the slope as discussed in the previous section for solubilization of individual droplets. An average value of k^o = $6.27 \cdot 10^{-8}$ mol/m^2.s was calculated from these experiments, whence an Ostwald ripening rate of 20 nm^2/h is obtained from Equation [2.68]. Also, Weiss *et al.* [6] report the mass transfer coefficient k_i^* for an emulsion of n-tetradecane suspended in a 2 wt% Tween 20 solution (k_i^* = 1.9 x 10^{-8} m.s^{-1}). Since solubilization rates of hydrocarbons in nonionic surfactant solutions are often proportional to the surfactant concentration [21, 22, 25, 26], it is plausible to scale k_i^* to

a concentration of Tween 20 of 5 wt.% and further use Eq. [2.48] to calculate k^o. By doing so, a value of k^o = 2.76 x 10^{-7} mol/m^2.s is obtained, from which an Ostwald ripening rate of 85 nm^2/h is predicted from Eq. [2.68].

Whereas coalescence is not expected to play a significant role in this ripening rate as noted by Weiss *et al.* [6], flocculation may well be responsible for the observed difference between experimental and theoretical rates for interface-controlled mass transfer. Flocculation by a depletion mechanism would be favored by the high concentration of nonionic surfactant that is present in the system (5 wt. %).

For droplets in contact it is plausible to consider other mechanisms in addition to micellar transport. Kumacheva *et al.* [55] used electron microphotography to show the formation of bridges between the adsorption layers at the interfaces of flocculated drops in a ripening oil-in-water emulsion stabilized with a nonionic surfactant (Proxanol-268), and claimed that such "bridging" intensified the process of Ostwald ripening and caused deviations of transient behavior of $\bar{a}^3$ from linearity. In this case it is plausible to think that mass transfer is aided by the transient opening of holes smaller than the critical size for coalescence across the films between flocculated droplets. Also, migration of oil associated with the tails of Tween 20 molecules adsorbing at the water-oil interfaces could take place. This mechanism would be aided by the fact that the aqueous thin films in contact with flocculated drops for which $a > a_C$ exhibit local supersaturation in n-tetradecane. The latter mechanism is analogous to that suggested by Wen and Papadopoulos [35] to explain transport rates of water in $W_1/O/W_2$ emulsions across a thin oil film via hydration of the head groups of an oil-soluble nonionic surfactant (SPAN 80). In this study, mass transfer rates between W_1/O and O/W_2 interfaces in contact were twenty times those found between separated interfaces.

The coefficient k_i^* noted above was obtained from tests with an emulsion in which flocculation might be expected. The fact that the corresponding rate k^o was larger but still comparable to that obtained from solubilization tests of individual droplets suggests that mass transfer was enhanced by concomitant mechanisms such as those suggested above.

The dashed lines in Figure 2.22 are numerical simulation results with the model presented in the theory section, using k_{eff}^o = 3.21·10^{-7} mol/m^2·s obtained from the slope shown in Figure 2.22 (top) and the constants specified in Table 2.5. As expected, the slopes at long ripening times in the plot of $\bar{a}^2$ vs. time for the solid and dashed lines are practically identical, and the difference between the two is explained by the approximation $exp(\alpha/a) \sim 1 + \alpha/a$ that holds for Equation [2.77], but not for the numerical simulations. The most relevant feature of the numerical results is that the model correctly accounts for the timeframe of the transition between the initial state and the asymptotic regime at long ripening times. Therefore, the mass transfer model proposed in this work based on interfacial control is adequate to simulate the ripening of the emulsion.

Finally, the Ostwald ripening theory for interface-controlled mass transfer kinetics was useful to validate the numerical algorithm used for emulsion, and vice versa. Figure 2.23 shows the time-dependent behavior of the cumulative drop size distribution and of the mean radius $\bar{a}$ with respect to the critical radius a_C using k_{eff}^o = 3.21·10^{-7} mol/m^2·s. The expression derived for the cumulative form of the limiting drop size distribution of the emulsion (Eq. [2.67]) is also plotted as a solid line for comparison. Numerical results show that the drop size distribution does adopt the theoretical limiting curve at ripening times beyond 218 hours. Also, the companion chart illustrates that the relationship

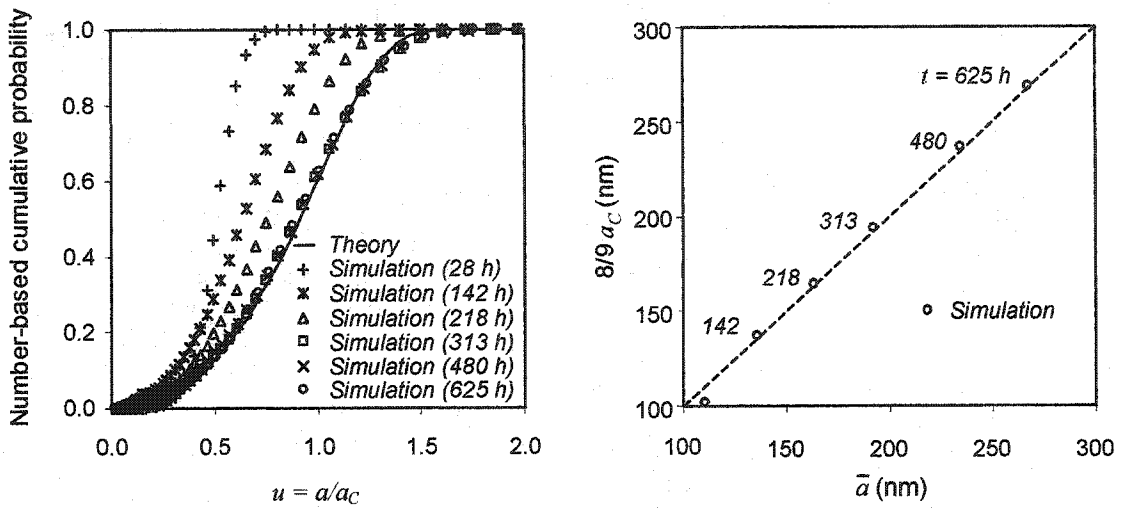


Figure 2.23. *Case study 2:* Validation of the extension of the LSW theory for interface-controlled Ostwald ripening via numerical simulations. Top: Transient behavior of the drop size distribution. Botton: correlation between the mean size $\bar{a}$ and the critical radius a_C.

$\bar{a} = \frac{8}{9} a_C$ is indeed correct. These findings are independent of the mass transfer coefficient that is used, as found in additional simulations with other values of k^o. Again, the match between the numerical results at long times and the theory is very close in all cases, but not exact, because of the approximation $exp(\alpha/a) \sim 1 + \alpha/a$ referred to earlier.

2.5.3.3. Case Study 3: Compositional Ripening

In this section, the experiment of Binks *et al.* [14] is considered in which two emulsions, one containing n-decane dispersed in a 2.5 wt. % solution of the nonionic surfactant $C_{12}E_8$, and another in which squalane is dispersed in a similar surfactant solution, are blended to make a mixed emulsion containing 7 vol. % of n-decane and 1 vol. % of squalane. Figure 2.24 shows the volume-weighted drop size distributions of the emulsions before mixing (solid bars), and the fit of such distributions with the lognormal distribution (dashed lines). The parameters of the initial distribution, along with the

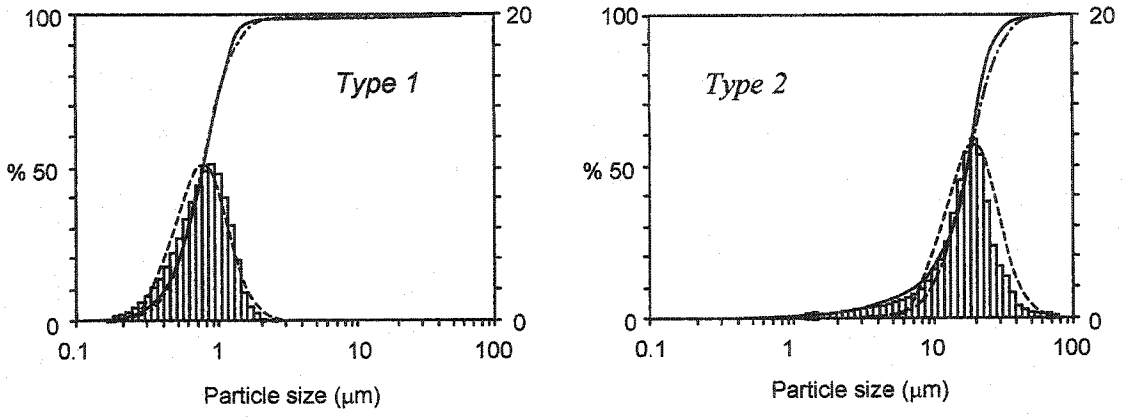


Figure 2.24. *Case study 3:* Drop size distributions of the initial emulsions before mixing them. Solid bars and lines: Experimental data. Dashed lines: Numerical fit using the log-normal p.d.f.

constants that were used in the simulations referred to later in this section, are reported in Table 2.6. In particular, the mass transfer coefficient for n-decane that was used in these calculations (k^o = $2.24 \cdot 10^{-5}$ mol/m^{2}s) was the one reported in Table 2.2 from solubilization tests of individual droplets at 23 $\pm$ 1 °C (see also Figure 2.7).

It was shown above that squalane is practically insoluble in the surfactant solution, whereas n-decane exhibits limited but measurable solubility. Therefore, it can be assumed that only n-decane is transferred through the continuous phase by the micellar aggregates. The sequence of events that takes place in this experiment is shown in Figure 2.1 (bottom). As time proceeds, the drops containing squalane (type 1) grow at the expense of the solubilization of the n-decane (type 2) droplets.

Figure 2.25 illustrates the time-dependent behavior of the volume-weighted drop size distributions for the mixed emulsion. The peak on the left hand side of each frame corresponds to the drops containing initially pure squalane (type 1), whereas the peak on the right hand side corresponds to n-decane (type 2) droplets. Clearly, the

Table 2.6. Parameters used in the simulations for case study 3

Parameter (units)	*Value*	*Parameter (units)*	*Value*
$(d_{gv})_{1,0}$ (m)	$7.80 \cdot 10^{-7}$	θ_0	0.15
$\sigma_{1,0}$	0.4417	k^o (mol/m^2·s)	$2.24 \cdot 10^{-5}$
$(d_{gv})_{2,0}$ (m)	$1.72 \cdot 10^{-5}$	c^o_{sat} (mol/m^3)	10.2
$\sigma_{2,0}$	0.4023	c_S (mol/m^3)	46.5
n^*	15000	T (K)	293
$\Phi_{1,0}$	0.01	σ (N/m)	$1.1 \cdot 10^{-3}$
$\Phi_{2,0}$	0.07	v (m^3/mol)	$1.95 \cdot 10^{-4}$
$x_{1,0}$	0	v_I (m^3/mol)	$5.22 \cdot 10^{-4}$
$x_{2,0}$	1	Δt (s)	1

experiment was devised to avoid significant overlapping of the two peaks to facilitate interpretation of the results and characterization of the transient distribution of each drop type.

The experimental data are given as solid bars for the drop size distribution, and as solid lines for the corresponding cumulative function. The continued solubilization of n-decane becomes evident, since the peak at the right hand side vanishes as time proceeds. The amount of decane initially present in the emulsion is significantly greater than the equilibrium solubilization capacity of decane in the surfactant solution (see Table 2.6), and therefore n-decane is transferred into the squalane drops until a single peak is obtained at the end of the experiment.

The numerical results are presented as dashed lines for the drop size distribution, and as dash-and-dot lines for the corresponding cumulative distribution function. It is

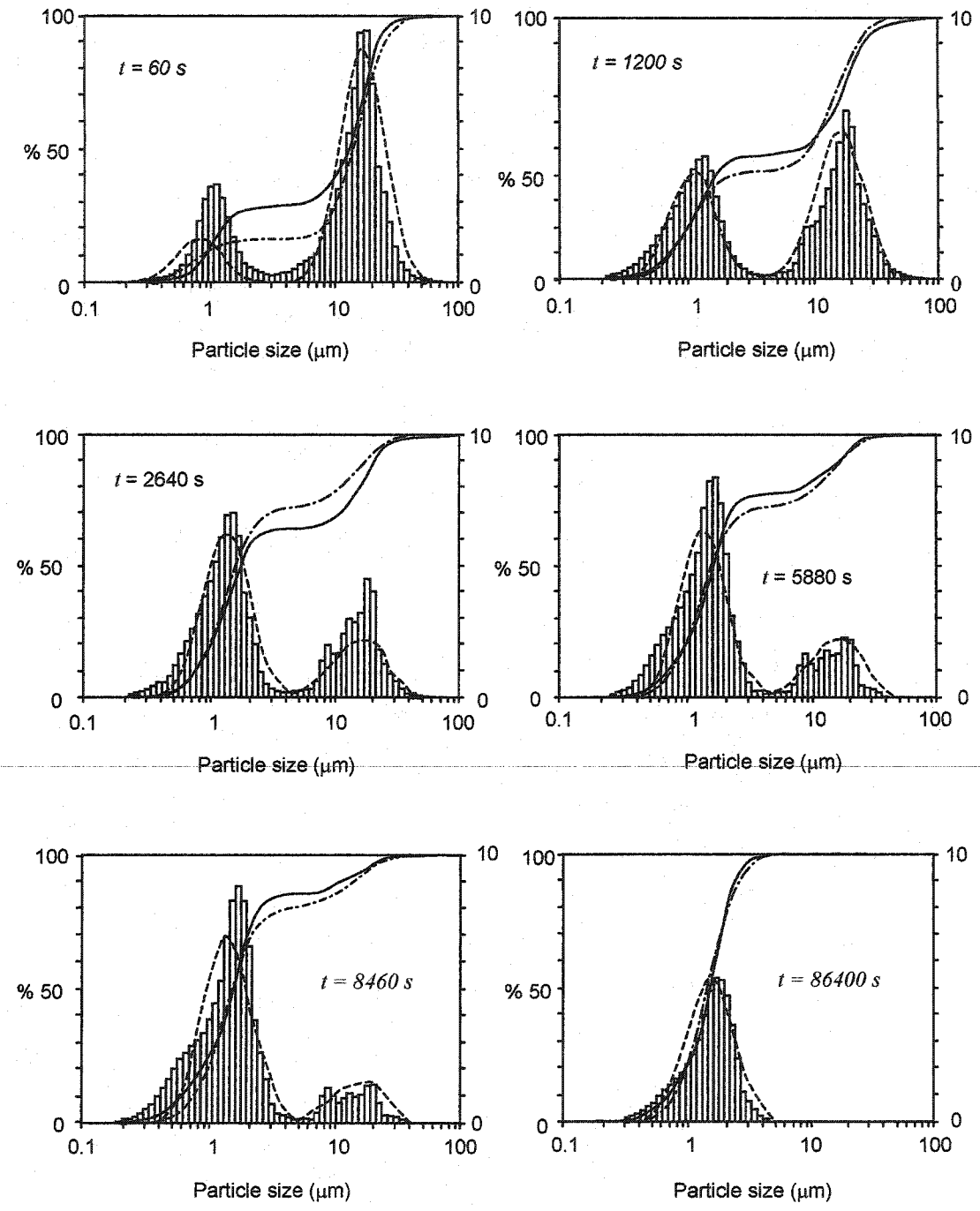


Figure 2.25. *Case study 3:* Transient behavior of the drop size distribution for the mixed emulsion. Solid bars and lines: Experimental data. Dashed lines: Results from numerical simulations.

seen that the agreement between experiments and numerical results is remarkable, even at t = 60 s when differences are more noticeable possibly due to the adjustment of the bulk concentration of n-decane at the beginning of the test. It is worth emphasizing that no adjustable parameters were used in the simulations. Importantly, since the algorithm keeps track of the transient behavior of every drop within the population n^*, it is feasible to assess the behavior of the distribution of sizes for each drop type individually. By doing so, some overlapping was observed at long times, but up to 8460 seconds it was always small and not likely to affect the characterization of each peak individually from the experimental data.

It is natural to wonder how is it that the two peaks do not overlap significantly, if the n-decane (type 2) drops, which are larger than the type 1 drops at the beginning of the experiment, are solubilized and their sizes reduced. This apparent paradox can be explained by considering two facts: (a) it can be calculated from the data provided in Table 2.6 that the population of type 1 drops is greater than that of type 2 droplets by a thousand-fold. Therefore, when drops of the two types are present in the same class of the histogram, the fraction of type 2 drops present is negligible; (b) the distributions reported in Figure 2.19 are volume-weighted, and not number-based. This is why regardless of the fact that the number of type 2 drops is much smaller, the corresponding peaks of the type 2 droplets contribute significantly to the overall distribution at large drop sizes, but not at the small drop sizes for which the contribution of type 1 drops is clearly more significant.

Figure 2.26 shows in black dots the transient behavior of the geometric mean size of the volume-weighted distribution for each drop type as reported by Binks *et al.* [14]. It is observed that whereas the average size of the drops containing squalane (Type 1)

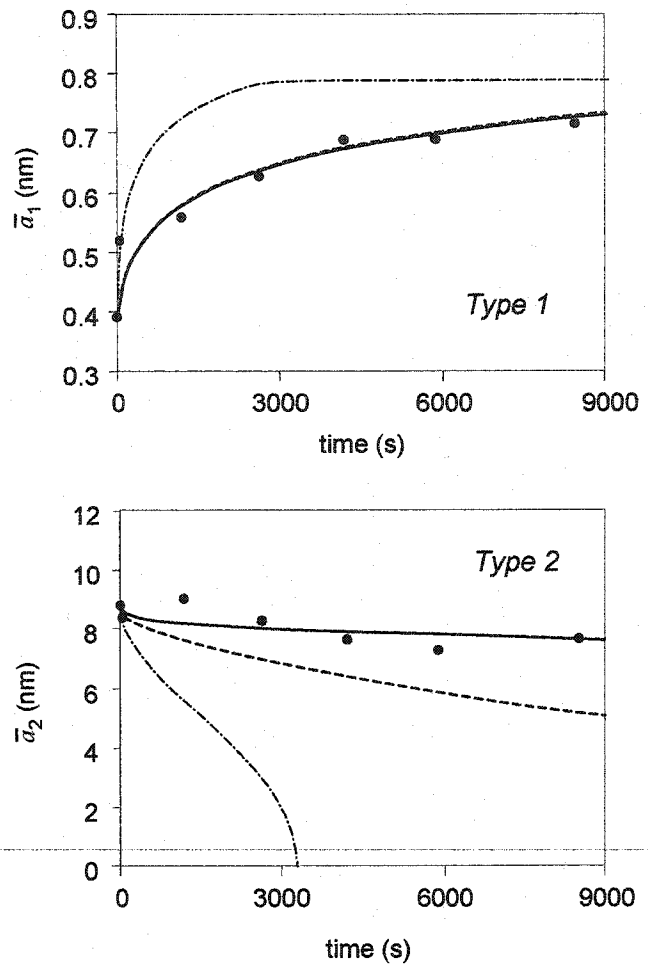


Figure 2.26. *Case study 3:* Transient behavior of the volume-weighted mean drop sizes of the two drop types present in the mixed emulsion. Dots: Experimental data. Solid lines: Numerical simulations with interface-controlled mass transfer model taking into account polydispersity in drop sizes. Dashed lines: Numerical simulations with interface-controlled mass transfer model neglecting polydispersity in drop sizes (Eq. [2.80]). Dash-and-dot lines: Numerical simulations with diffusion-controlled mass transfer model neglecting polydispersity in drop sizes (Eq. [2.82]).

increases steadily, the behavior of the type 2 drop mean size is rather erratic, but exhibits a slight decrease.

The dashed lines in Figure 2.26 are calculations from an interface-controlled mass transfer model analogous to the one presented above, but simplified for the case of a mixture of two monodisperse emulsions as follows: Consider a mixture of two collections

of monodisperse type 1 and type 2 droplets with concentration numbers N_1 and N_2. The simplified solution may be found by assuming a quasi-steady behavior for the concentration of mobile oil in aqueous environment [56]. In such a case, from Eq. [2.50] we obtain:

$$4\pi a_1^2 N_1 \frac{da_1}{dt} + 4\pi a_2^2 N_2 \frac{da_2}{dt} = 0 \qquad [2.78]$$

Under this assumption, the following dimensionless expression can be obtained for the concentration of oil in the bulk by using Eq. [2.5] in combination with Eq. [2.6] and Eq. [2.78]:

$$\theta = \frac{\beta r_1^2 x_1 \, exp(\varsigma/\gamma r_1) + \gamma r_2^2 x_2 \, exp(\varsigma/r_2)}{\beta r_1^2 + \gamma r_2^2} \qquad [2.79]$$

where $r_1 = a_1/a_{1,0}$, $r_2 = a_2/a_{2,0}$, $\gamma = a_{1,0}/a_{2,0}$, $\varsigma = 2\sigma v_m / RTa_{2,0}$ and $\beta = N_1 a_{1,0}^3 / N_2 a_{2,0}^3$ $= \Phi_{1,0}/\Phi_{2,0}$, $\Phi_{j,0}$ being the initial volume fraction of type j drops in the emulsion. Finally, Eq. [2.79] is substituted for c_B/c_{sat}^o in Eq. [2.5] to find an expression for the rate of change of the characteristic radius of type 1 drops:

$$\frac{dr_1}{d\tau} = \frac{r_2^2}{\beta r_1^2 + \gamma r_2^2}\left[x_2 \, exp\left(\frac{\varsigma}{r_2}\right) - x_1 \, exp\left(\frac{\varsigma}{\gamma r_1}\right)\right] \qquad [2.80]$$

with $\tau = \left(k^o v / a_{2,t=0}\right)t$ as defined earlier but with $a_{2,t=0}$ as the characteristic radius, and x_1, x_2 the molar fractions of the mobile oil in the type 1 and type 2 drops, respectively. Eq. [2.80] can be expressed as an ordinary differential equation in r_1 that can be solved numerically, and then the characteristic size of type 2 drops is readily calculated since the total volume of oil in the emulsion remains constant.

It is seen that the agreement between the calculated profile for the type 1 drops and the experimental data using this simplified model is excellent, whereas for the type 2 drops the model predicts a decay of the mean size somewhat more pronounced than the one observed experimentally.

Binks *et al.* [14] developed an analogous model for the case in which mass transfer is limited by the diffusion of oil through the aqueous phase, using Eq. [2.3] as the governing expression for da_1/dt and da_2/dt and following the quasi-steady approximation for the concentration of mobile oil in the bulk that led to Eq. [2.80]. Their results can be summarized as follows:

$$\theta = \frac{\beta r_1 x_1 \, exp(\varsigma/\gamma v_1) + \gamma^2 r_2 x_2 \, exp(\varsigma/r_2)}{\beta r_1 + \gamma^2 r_2} \qquad [2.81]$$

$$\frac{dr_1}{d\tau'} = \frac{r_2/r_1}{\beta r_1 + \gamma^2 r_2}\left[x_2 \, exp\left(\frac{\varsigma}{r_2}\right) - x_1 \, exp\left(\frac{\varsigma}{\gamma r_1}\right)\right] \qquad [2.82]$$

where the dimensionless time is again given as $\tau' = \left(Dc^{o}_{sat} v / a^2_{2,t=0}\right)t$ and the remaining variables and parameters are as defined before. The predictions of this model, shown in dash-and-dot lines in Figure 2.26, differ markedly from the experimental data since they indicate that n-decane drops are completely solubilized at about 3000 s and hence the growth of type 1 drops stops.

The results shown in Figure 2.26, in connection with those obtained in the various tests for solubilization of individual droplets of n-decane/squalane mixtures, indicate that the kinetics of compositional ripening in this experiment were limited by interfacial resistance to mass transfer and not by micellar diffusion as suggested by Binks *et al.* It is worth mentioning that the diffusion model provides an upper bound for the resistance to

mass transfer in the bulk since hydrodynamic effects are neglected. Convection surely occurred in the mixed emulsion -since it was gently agitated through the experiment to prevent creaming [14]-, and some convection was seen even in the solubilization tests reported above. In the absence of interfacial resistance, convection would cause droplet sizes in the mixed emulsion and in the solubilization tests to change even faster than predicted by the diffusion model, and thus to deviate even further from the experimental results. On the other hand, the agreement between experiments and predictions from the model that assumes interfacial resistance as controlling suggests that convective effects do not influence mass transfer in these systems.

The solid lines in Figure 2.26 are the predictions from the mass transfer model presented in this work, considering the polydispersity of the original emulsions before mixing them. It is seen that the model reproduces very well the experimental results both for the type 1 and type 2 droplets. Therefore, the lack of agreement between theory and experiments for the type 2 drops that had been reported by Binks *et al.* [14] when considering diffusion-controlled kinetics, and that is found here when assuming interface-controlled kinetics and a mixture of two monodisperse emulsions, can be attributed to the finite polydispersity of drop sizes in the emulsion.

The relative insensitivity of the prediction for type 1 drops to polydispersity suggests that the number-based drop size distribution changes in a different fashion depending on whether the drops are shrinking or growing. Figure 2.27 shows numerical results for the number-based drop size distributions for type 1 and type 2 drops separately. It illustrates that when the drops are shrinking the distribution becomes broader and tailed towards small drop sizes, the same as found in the solubilization example discussed earlier. If the distribution is volume-weighted, the relative contribution of the smaller drops

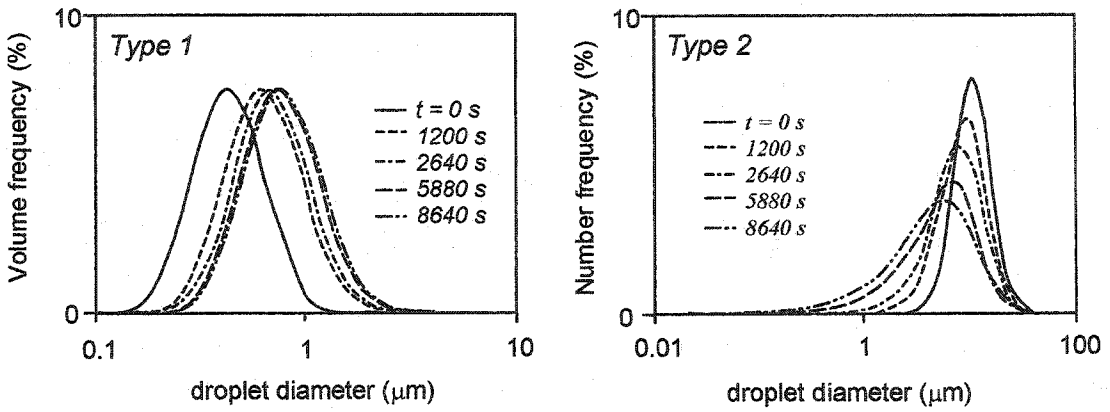


Figure 2.27. *Case study 3:* Numerical results for the time-dependent behavior of the number-based drop size distributions of the two drop types present in the mixed emulsion.

becomes negligible and the volume-weighted mean size exhibits a relatively small change. On the other hand, if the drops increase in size, the shape and width of the distribution remain practically unchanged and the geometric mean grows at the same rate at which the distribution is displaced toward larger drop sizes. This assessment is, in this case, practically independent of the base for which the distribution is reported since, as mentioned earlier, corresponding number-based and volume-weighted log-normal distributions have the same width σ_g and their geometric means differ by a constant factor if σ_g remains unaltered.

It is worth noting that the numerical results presented in this section for the model that considers the polydispersity of the emulsions were recalculated neglecting the contribution of interfacial curvature to the surface concentration of n-decane by setting $\mathbf{exp}(2\sigma v / \mathrm{R}Ta) \sim 1$. These calculations did not differ significantly from those reported above, thus confirming that mass transfer was driven by concentration gradients of decane between the drops and the bulk phase, and not by differences in drop sizes.

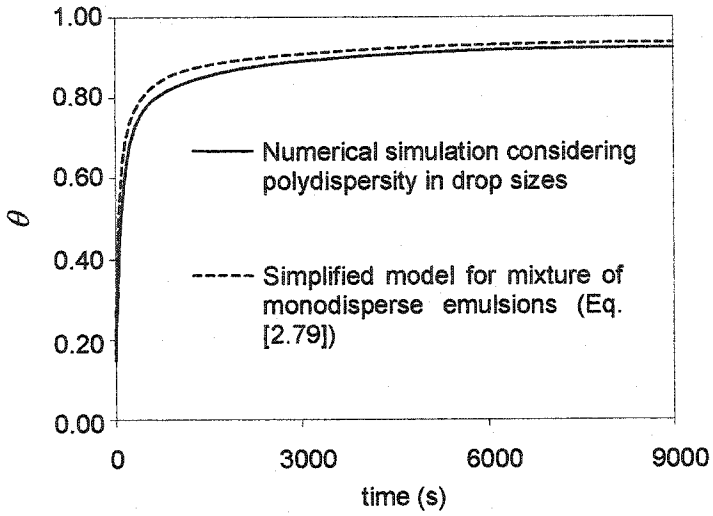


Figure 2.28. *Case study 3:* Transient behavior of the concentration of n-decane in the surfactant solution, expressed in dimensionless form $\theta^o = c_B / c^o_{sat}$

Therefore, this mixed emulsion was degraded mostly by compositional ripening as suggested above, and not by Ostwald ripening.

It is interesting to consider the transient behavior of the concentration of n-decane in the aqueous solution in this experiment. Figure 2.28 shows numerical results for the time-dependent behavior of θ_o when mass transfer kinetics are assumed as limited by interfacial resistance. The dashed line corresponds to the predictions from the model for a mixture of two monodisperse emulsions (Eq. [2.79]), and the solid line stands for the profile that is obtained when polydispersity is considered. The leveling of θ^o circa 0.9 after a short transient explains why the approximation of monodisperse emulsions works relatively well, and suggests that the ripening of this system took place at a bulk concentration of n-decane close to saturation for most of the experiment.

The controlling mechanism(s) for ripening of emulsions in the presence of ionic surfactants is influenced by the electrical repulsion between the micelles and the

adsorbed monolayer at the water/oil interfaces [5]. Since this effect is not a factor in emulsions stabilized with nonionic surfactants, the conclusions concerning compositional ripening reached in this work may not necessarily apply to solutions of ionic surfactants.

2.5.4. Effect of surfactant concentration on the solubilization kinetics of alkanes in nonionic surfactant solutions

Figure 2.29 shows the decay in drop size of droplets of n-octane in bi-distilled water and also in aqueous solutions of $C_{12}E_8$ at concentrations between 0.25 and 3.75 wt. %. All experiments were performed in cylindrical capillaries at 30.9 °C as indicated in section 2.4.

A wealth of information on the solubilization mechanism can be inferred from Figure 2.29. First, the comparison between the rate of decay of the drop size for octane in pure water and octane in aqueous solutions of $C_{12}E_8$ indicates that the presence of surfactant increased the solubilization rate up to three orders of magnitude. This provides compelling evidence to conclude that the solubilization process is micelle-mediated. Moreover, the rate of decay of the drop radius of n-octane in water shown in Figure 2.29 (m = -2.4·10^{-5} μm/s) agrees very well with the initial rate of solubilization that is predicted if molecular diffusion is assumed as rate-limiting. This rate is given, according to Eq. [2.72], by

$$\left.\frac{da}{dt}\right|_{t=0} = -\frac{D_w c^o_{sat,w} v}{a_o} = -2.5\cdot 10^{-5}\ \frac{\mu m}{s} \qquad [2.83]$$

where a_0 = 35.8 μm, v = 1.62·10^{-4} m^3/mol , D_w = 8.1 · 10^{-10} m^2/s is the molecular diffusivity of the oil in water and was estimated with the Wilke-Chang equation [57] for n-octane in

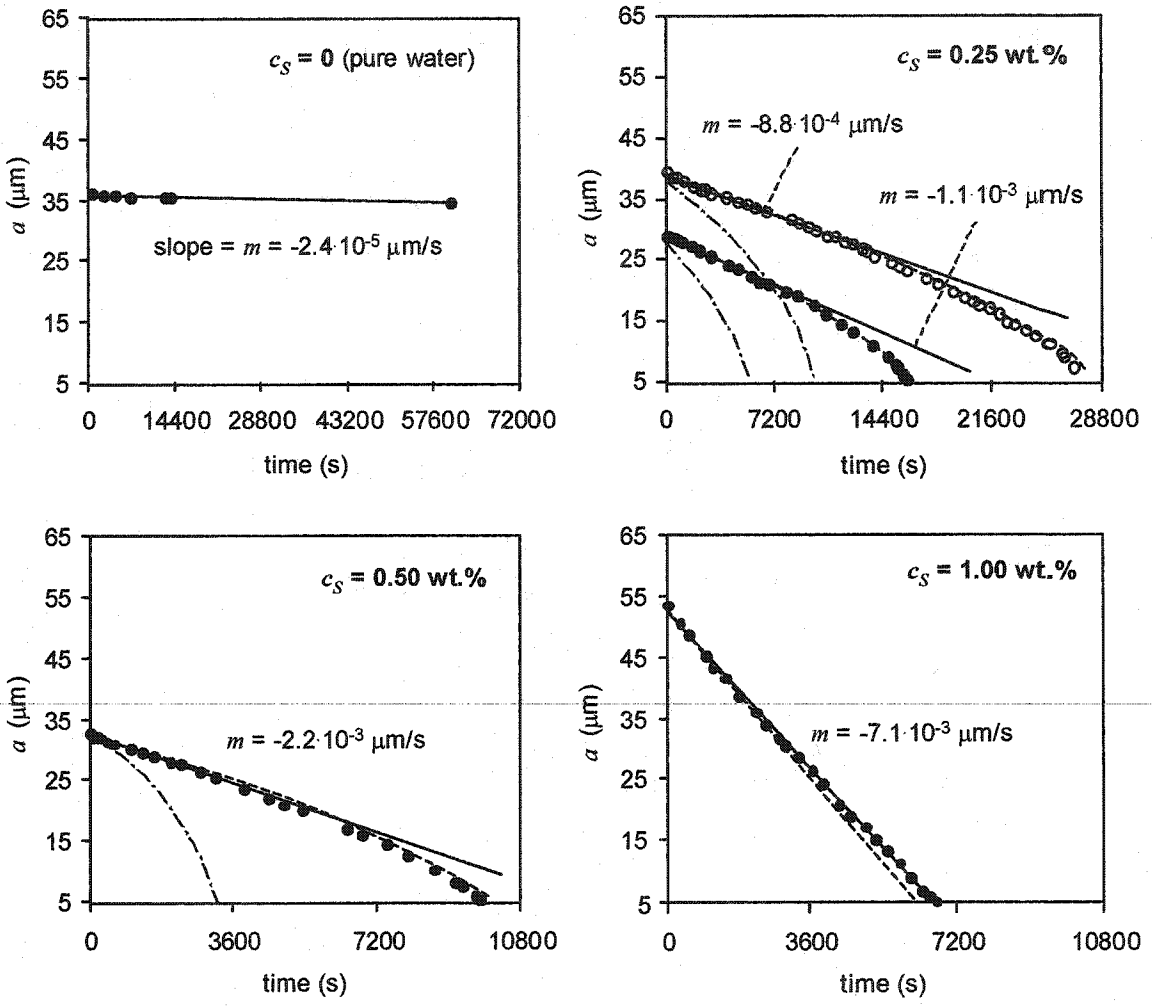


Figure 2.29. Solubilization of drops of n-octane in oil-free aqueous solutions of $C_{12}E_8$ at several surfactant concentrations. All experiments were performed at 30.9 ± 0.1 °C. Symbols, experimental data. Solid lines, linear fit of the data (only first six points for the data for experiments at 0.25 wt.% and 0.5 wt.% $C_{12}E_8$). The slopes that are reported correspond to the solid lines. Dash-dot lines, predicted trend assuming micellar diffusion as rate-controlling. Dashed lines, predicted trends assuming mixed kinetics and considering spontaneously-generated convection as the surfactant concentration is increased. $C_{12}E_8$ concentration: 1.00 wt.% = 18.60 mol/m^3. (Figure continues on next page).

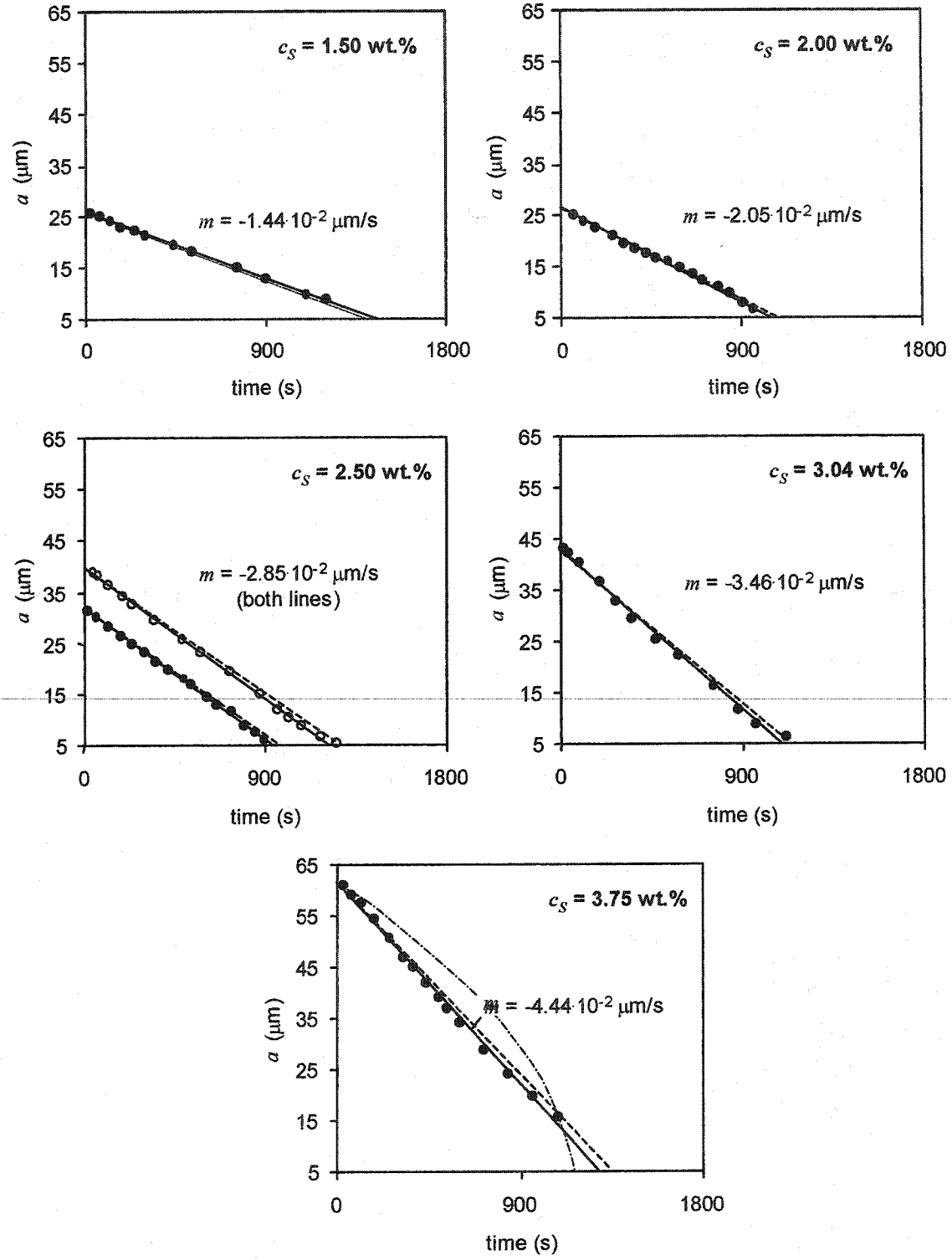


Figure 2.29 (continued)

water at 30.9 °C and $c^{o}_{sat,w}$ = 6.83·10^{-3} mol/m^3 was interpolated for T = 30.9 °C from data reported by Lide [49] for the solubility of n-octane in water at 25 °C (6.23·10^{-3} mol/m^3) and 50 °C (8.77·10^{-3} mol/m^3). Therefore, diffusion of molecular octane controls the solubilization rate in absence of surfactant.

Second, it is seen that at relatively low surfactant concentrations (0.25 and 0.50 wt.%) the rate of solubilization increases as the drop size diminishes and a slight dependence of the initial solubilization rate on the initial drop size is observed. These patterns are characteristic of diffusional solubilization kinetics, as was shown when discussing Figure 2.7. Eq. [2.83] indicates that molecular diffusion is too slow to account for the observed decay in drop sizes in these cases. If the diffusion of micelles is assumed as rate-limiting, Eqs. [2.43] applies and the transient drop radius would be given by:

$$a(t) = \sqrt{a_o^2 - 2Dvc^{o}_{sat}t} \qquad [2.84]$$

The data obtained by Brown *et al* [48] using quasi-elastic light scattering for the dependence for the diffusion coefficient of $C_{12}E_8$ micelles with surfactant concentration at 32.2 °C can be correlated as follows:

$$D = 5.80 \cdot 10^{-11} + 6.56 \cdot 10^{-14} c_S \qquad [2.85]$$

where D is given in m^2/s and c_S in mol/m^3. In addition, if micellar solubilization is much more significant than molecular solubilization it is plausible to assume that the equilibrium solubilization capacity is proportional to the surfactant concentration. Therefore, from Table 2.1 we obtain for octane solubilized in aqueous $C_{12}E_8$ at 30.9 °C:

$$c^{o}_{sat} = 0.98 \cdot c_S \qquad [2.86]$$

Eqs. [2.84]-[2.86] were used to calculate the dash-dot lines that are plotted in Figure 2.29 for c_S = 0.25 wt.% (4.65 mol/m^3), 0.50 wt% and 3.75 wt.%. The plots for c_S = 0.25 and 0.50 indicate that n-octane was solubilized at lower rates than the one that would be expected if micellar diffusion alone were rate-limiting. However, interfacial resistance alone cannot be rate-limiting because da/dt is not constant, but diminishes with the drop size. A plausible way to reconcile these results is to consider that *both* micellar diffusion and interfacial resistance to mass transfer significantly affected the solubilization of n-octane at low surfactant concentrations. In contrast, the plots for c_S = 3.75 wt.% indicate that at the beginning of the experiment solubilization took place at a faster pace than the one that would be expected if micellar diffusion would dictate solubilization. This suggests that micellar diffusion was not limiting in this case.

In an attempt to understand why micellar diffusion apparently affected solubilization kinetics at low surfactant concentrations but apparently not at high surfactant concentrations, additional solubilization experiments were performed placing drops of n-octane in $C_{12}E_8$ surfactant solutions containing monodisperse polystyrene (PS) particles (Polysciences, Inc. mean diameter = 2.134 μm; standard deviation = 0.039 μm). The particles were added with the objective of determining whether convective currents were present at the time solubilization took place. The solubilization process and the behavior of the particles were monitored under the microscope and recorded for further analysis.

Observation of surfactant solutions before placing the oil drops revealed that the PS particles exhibited Brownian motion and that no temperature-driven convective currents were present in the system. The same behavior for the particles was observed when air bubbles were placed in the capillary, regardless of the surfactant concentration. Particles still exhibited Brownian motion when n-octane drops were placed in dilute solutions of $C_{12}E_8$ (Figure 2.30). However, as the surfactant concentration was increased,

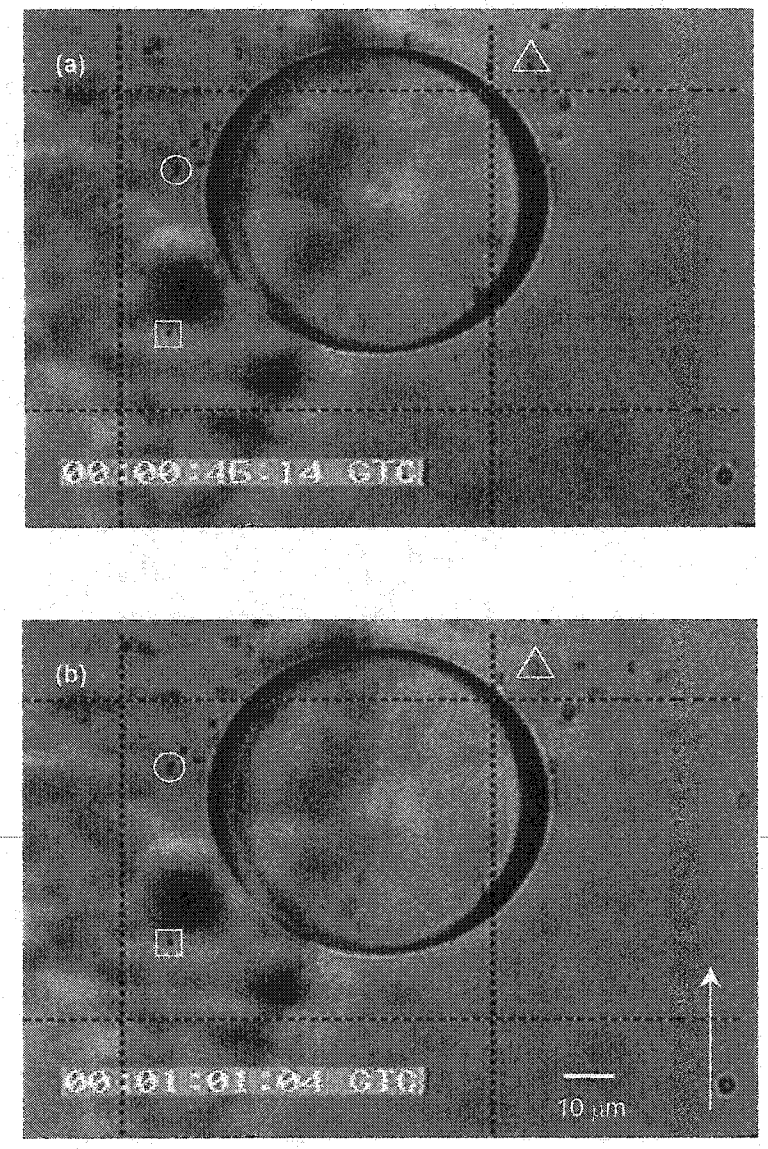


Figure 2.30. Solubilization of a drop of n-octane in a 0.25 wt.% aqueous solutions of $C_{12}E_8$ in the presence of polystyrene particles at 30.9 ± 0.1 °C. The comparison between frames (a) and (b) illustrates that particles practically did not change their position. The time difference between the frames is 14.3 s. The arrow indicates the axial direction of the cylindrical capillary in which the drop was injected. The apparent slight elongation of the drop in the direction normal to such axis is an optical effect due to the curvature of the capillary. Measurements are performed in the axial direction to avoid that such effect influences the reported drop sizes and particle velocities.

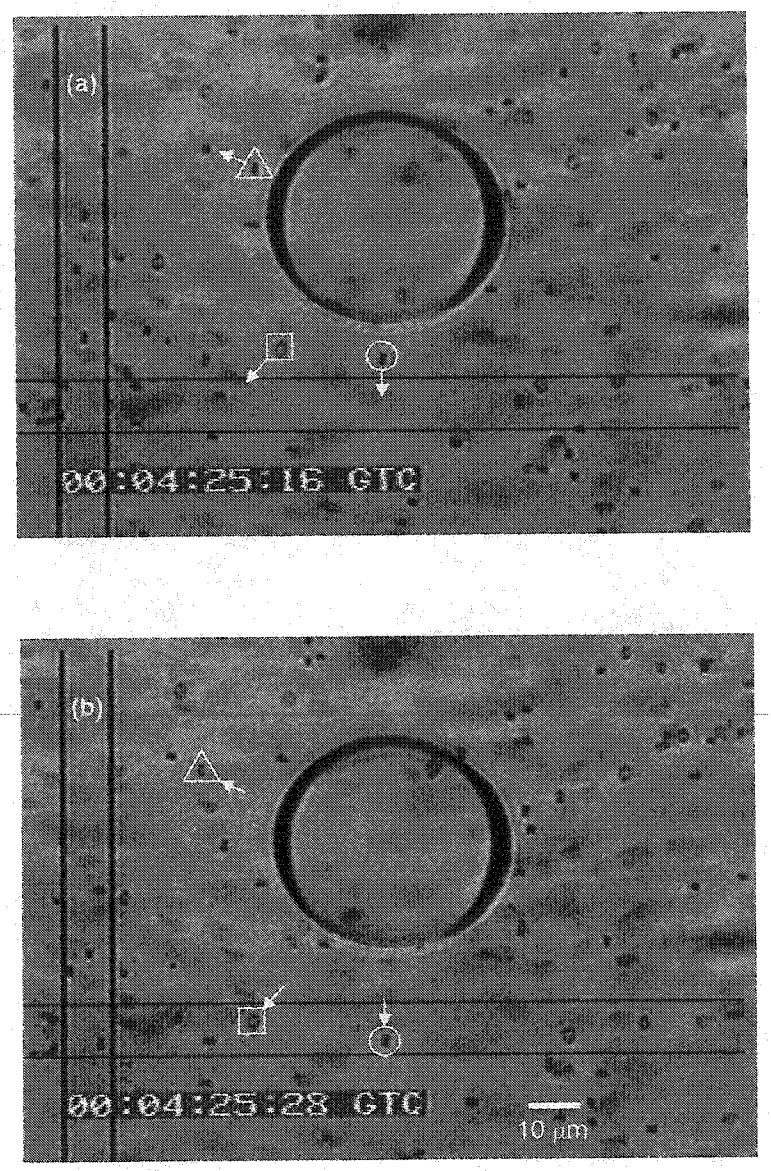


Figure 2.31. Solubilization of a drop of n-octane in a 2.50 wt.% aqueous solutions of $C_{12}E_8$ in the presence of polystyrene particles at 30.9 ± 0.1 °C. The comparison between frames (a) and (b) illustrates that particles are displaced away from the drop in the radial direction. The time difference between the frames is 0.4 s.

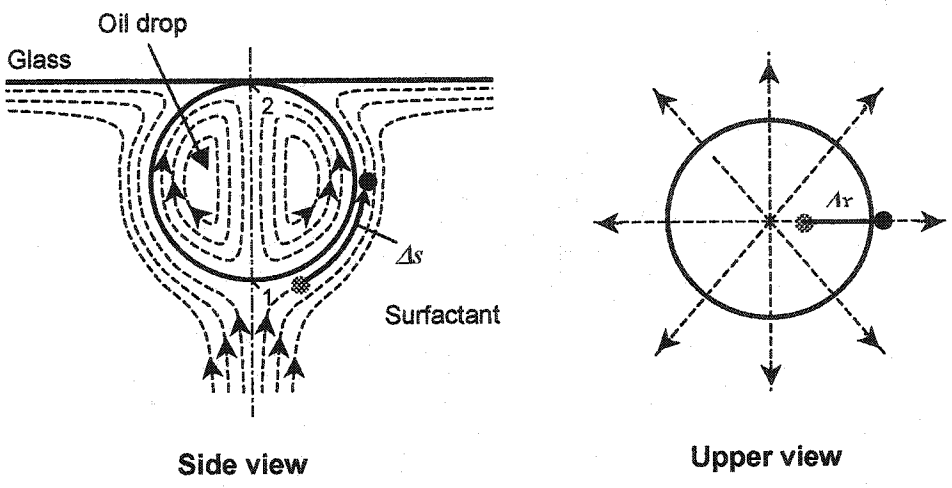


Figure 2.32. Schematic representation of the flow pattern that was observed at the onset of spontaneously-generated convection. Dashed lines, streamlines; arrowheads indicate direction of flow in the plane of observation.

spontaneously-generated convection was observed (Figure 2.31), and particles were displaced following the pattern that is illustrated schematically in Figure 2.32. A careful image analysis of solubilization experiments where convection was observed revealed that internal circulation in the droplets also took place as shown in Figure 2.32.

The onset of spontaneous convection was characterized by measuring the velocity of PS particles as a function of drop size and surfactant concentration. The average velocities u that are reported below were calculated by measuring the time Δt that would take for particles just below the glass surface to travel the distance Δs shown in Figure 2.32, i.e., $u = \Delta s/\Delta t$. In each case, the distance Δs was calculated from the drop radius a and the distance Δx shown in Figure 2.32 (right), which could be measured directly via videomicroscopy due to the fact that the oil drops were translucent. From basic geometry principles, it can be easily shown that $\Delta s = a \cos^{-1}(1-\Delta x/a)$.

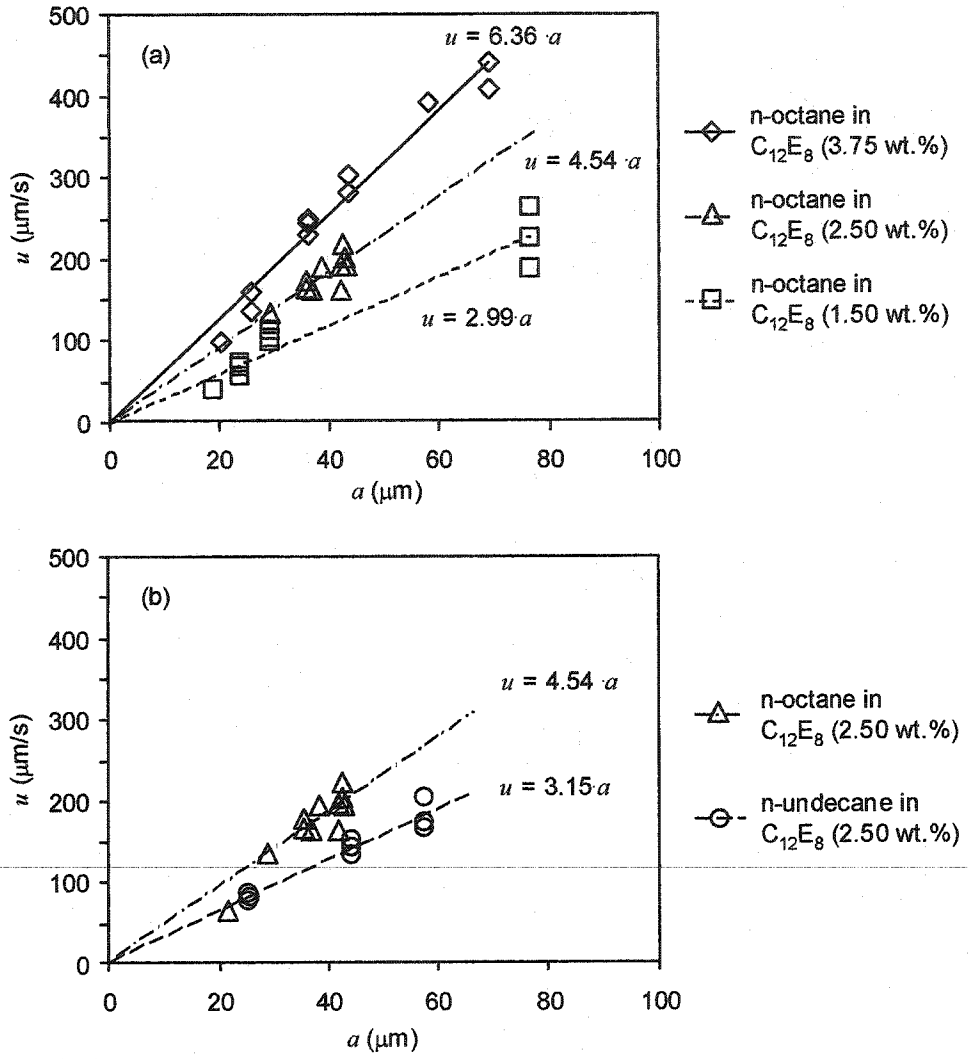


Figure 2.33. Effect of surfactant concentration, drop size and solubilized oil on the velocity of PS particles present in solubilization experiments.

Figure 2.33 (a) shows the effect of drop size and surfactant concentration on the average velocities of PS particles. It is seen that u increased with surfactant concentration and decreased in a fairly linear fashion with decreasing droplet size. The data shown in Figure 2.33 (a) can be correlated approximately as:

$$u = \chi \cdot a \qquad [2.87]$$

where χ is a constant that depends on surfactant concentration. The empirical correlation:

$$\chi = \begin{cases} 3.683\ln(c_S) - 9.266 & c_S \geq 12.64\ \text{mol/m}^3\ (0.68\ \text{wt.\%}) \\ 0 & c_S < 12.64\ \text{mol/m}^3 \end{cases} \qquad [2.88]$$

accounts for the data for χ shown in Figure 2.33(a), and also for the fact that no significant convection was observed at low surfactant concentrations. Spontaneously generated convection was also observed in solubilization experiments with n-undecane, as shown in Figure 2.33(b).

The mixed kinetic model developed in section 2.2.2 is useful to illustrate the extent to which the onset of convection affected the relative importance of diffusional and interfacial resistances to mass transport. To do so, let us postulate that the interface-limited mass transfer rate can be correlated to the surfactant concentration with an expression of the form:

$$k^o = P \cdot c_S^{\lambda} \qquad [2.89]$$

where P and λ are constants to be determined in the subsequent analysis. It will be shown later that λ carries information on the molecular mechanism that determines the interfacial resistance to mass transport.

The velocities reported in Figure 2.33 were correlated satisfactorily to the first power of the drop size (n = 1 for Eqs. [2.35]-[2.39]) and therefore Eq. [2.40] can be used to model the kinetic data reported in Figure 2.29:

$$\left[1+\frac{K}{(A\cdot Pe_0)^{1/2}}\right](r-1)+\frac{K}{A\cdot Pe_0}\ln\frac{Sh(1)}{Sh(r)}=-K\tau',$$

where

$$r=\frac{a}{a_o};\quad \tau'=\frac{Dvc^o_{sat}}{a_o^2}t;\quad \mathrm{Sh}(r)=2+2(A\cdot Pe_o)^{1/2}r;$$

$$A=\frac{2}{\pi};\quad Pe_0=\frac{u_0a_0}{D};\quad u_0=\chi a_0;\quad K=\frac{k^o a_o}{Dc^o_{sat}}$$

as stated in Eqs. [2.30]-[2.40], [2.87]. The dependence of all the physical parameters in these equations (c^o_{sat}, χ, k^o, D) on surfactant concentration was either measured (c^o_{sat}, χ) or reported in literature (D) and is given in empirical correlations (Eqs. [2.85], [2.86] and [2.88]), with P and λ in Eq. [2.89] remaining unknown.

The constants P and λ were used as adjustable parameters to fit the data reported in Figure 2.29 with Eq. [2.40]. The fits of the data are shown as dashed lines in Figure 2.29. The agreement between experiments and predicted trends is satisfactory in all cases, thus suggesting that the model is useful to account quantitatively for changes in the relative importance of diffusional and interfacial resistance as the surfactant concentration was increased.

The following values were obtained for P and λ: P = 4.21 and λ = 1.02. Therefore, $k^o \sim 4.21\cdot c_S^{1.02}$. Figure 2.34 compares the values for k^o that are calculated with this expression (solid line) with the effective mass transfer coefficients k_{eff} determined experimentally from the slopes reported in Figure 2.29 (k_{eff} = -m/v). It is seen that at low surfactant concentrations $k_{eff} < k^o$ because micellar diffusion plays a significant role in the

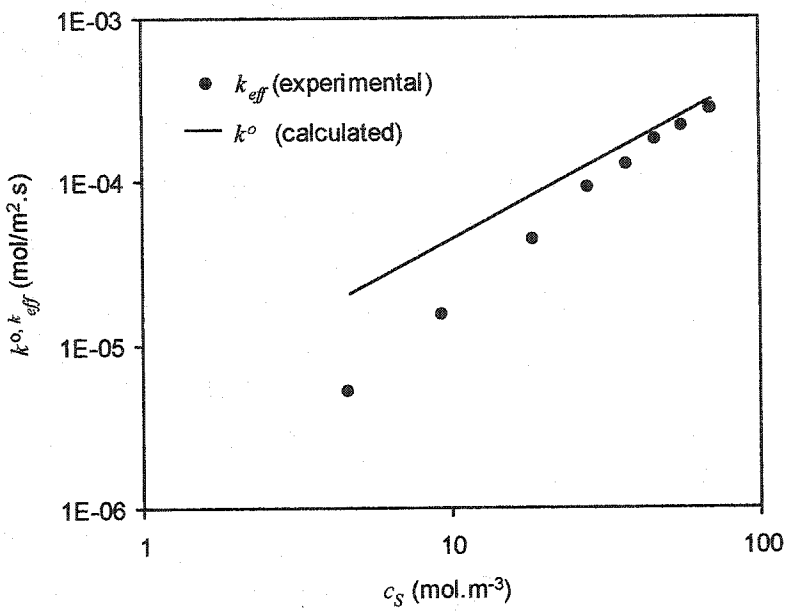


Figure 2.34. Effect of surfactant concentration, drop size and solubilized oil on the velocity of PS particles present in solubilization experiments.

observed rate. As the surfactant concentration is increased and the onset of convection takes place, a boundary layer forms and the diffusional resistance is reduced, thus leaving interfacial resistance as rate controlling ($k^o \sim k_{eff}$). This is clearly illustrated in Figure 2.35, where the values of K (Eq. [2.38]), The Péclet number Pe_u (Eq. [2.34]), the thickness of boundary layer ℓ (Eq. [2.33]), and the fractional contribution of interfacial resistance to the overall resistance to mass transport:

$$\frac{\Re_I}{\Re_I + \Re_B} = \frac{c^o_{sat}/k^o}{c^o_{sat}/k^o + 2a/DSh} = \frac{K^{-1}}{K^{-1} + (Sh/2)^{-1}}. \qquad [2.90]$$

are plotted for a reference drop size a = 20 μm. It is seen in Figure 2.34 that K, which stands for the ratio of diffusional-to-interfacial resistance to mass transport in absence of convection, exhibits a value near unity and is practically independent of surfactant

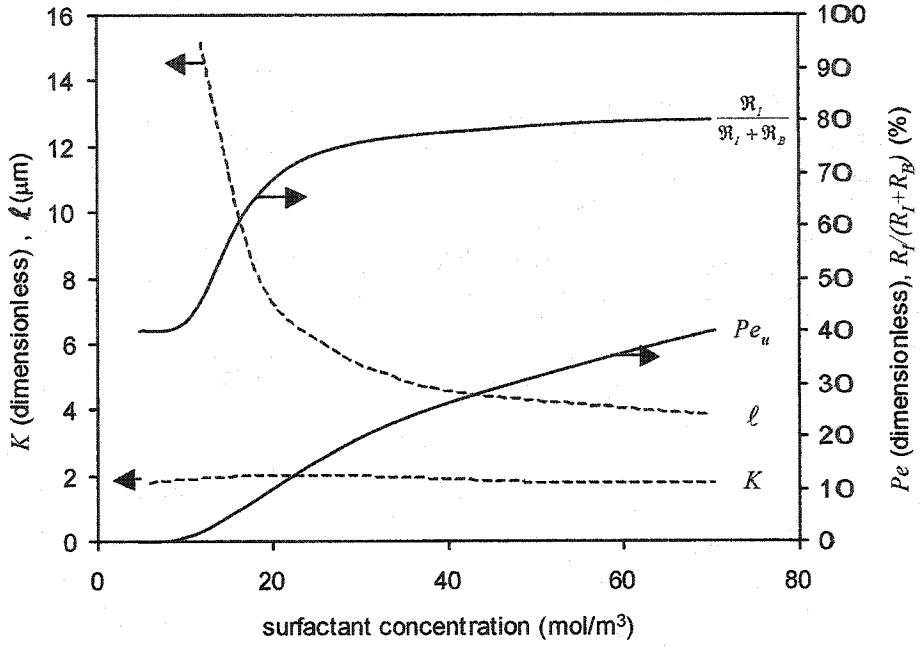


Figure 2.35. Effect of surfactant concentration on K, Pe_u, ℓ and $\Re_I/(\Re_I+\Re_B)$ for the solubilization of n-octane in $C_{12}E_8$ aqueous solutions at 30.9 °C.

concentration. However, as c_S is increased, convection occurs (shown by an increase in Pe_u). In consequence, the characteristic length of the diffusive boundary layer ℓ diminishes and the relative contribution of the diffusional resistance to mass transport [=1-$\Re_I/(\Re_I+\Re_B)$] diminishes from nearly 50% at low surfactant concentration to ~ 10% at high surfactant concentration. This reduction in the diffusional resistance to mass transport due to convection makes interfacial resistance rate-controlling.

It was demonstrated in this work that solubilization of n-octane in aqueous $C_{12}E_8$ is micelle-mediated. If so, two plausible molecular mechanisms can be proposed to explain solubilization kinetics at the interface (Figure 2.36):

(a) Solubilization occurs by the adsorption/fusion of micelles at the interface and the subsequent desorption/emission of a swollen micelle carrying the solute [Figure 2.36(a)].

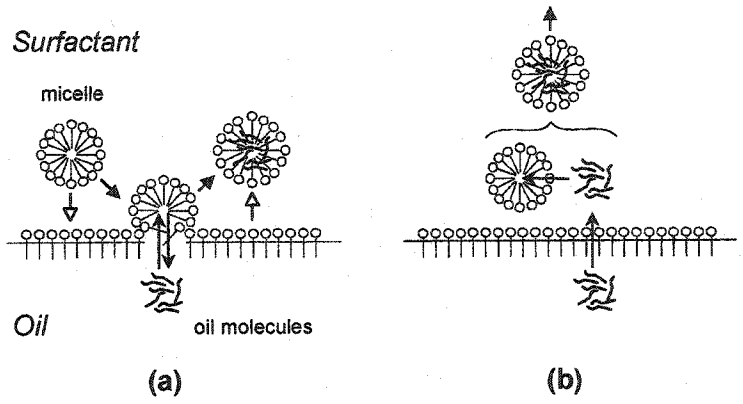


Figure 2.36. Schematic representation of plausible molecular mechanisms able to dictate interfacial resistance to mass transport. (a) Complete (white arrows) or partial (black arrows) adsorption of micelles, followed by emission/desorption; (b) molecular transport of solute, followed by irreversible incorporation in micelles.

In this case, the solubilization rate is expected to increase proportionally to the concentration of micelles in the bulk phase and therefore to the surfactant concentration [21, 22, 25]:

$$k^o \propto c_S \ (\lambda = 1). \qquad [2.91]$$

(b) Solubilization occurs by the dissolution of molecules of solute in the bulk solution near the interface, followed by molecular diffusion and subsequent irreversible incorporation of such molecules in nearby micelles [Figure 2.36(b)]. In this case, the interfacial micellar mass transfer coefficient k^o as defined in this chapter is related to the rate of incorporation of molecular oil in the micelle k_r^+ by [32, 58, 59]:

$$k^o = c^o_{sat,w}\sqrt{D_w k_r^+ \phi_{mic}}\ , \text{ whence } \ k^o \propto c_S^{1/2} \ (\lambda = ½). \qquad [2.92]$$

where ϕ_{mic} is the volume fraction of micelles in the aqueous solution. The relationship $k^o \propto c_S^{1/2}$ is obtained by considering that ϕ_{mic} is proportional to c_S.

A value for λ = 1.02 was determined in the calculations described above. Additional calculations were performed considering the experimental uncertainty of the parameters in the model, whence it was found that $0.9 < \lambda < 1.2$. This result indicates that mechanism (a) is more consistent with the experimental results reported in this section than mechanism (b). This result, which is not surprising for solubilization in micelles of small nonionic surfactant molecules such as $C_{12}E_8$, may not apply to micelles of ionic surfactants, which are prevented from approaching the interface due to Coulombic repulsion forces. It may not apply strictly either to micelles of nonionic surfactants with large polyethoxylated chains, which are sterically constrained to adsorb at the interfaces as suggested by Figure 2.36(a).

Finally, the data provided above demonstrate that the onset of spontaneously-generated convection is related to the occurrence of micellar solubilization, because no convective currents were observed in absence of oil or around air bubbles at any surfactant concentration, and the effect became significant in the presence of oil as the surfactant concentration was increased.

One hypothesis that can be advanced to explain this phenomenon is the onset of natural convection driven by buoyancy due to a reduction in the density of the surfactant solution near the drop as the oil is solubilized. This hypothesis can be tested by evaluating the Rayleigh number, which is given by Eq. [2.46]. Let us consider, for example, the solubilization experiment for n-octane in $C_{12}E_8$ (2.5 wt.%) that is depicted in Figure 2.29 in open circles. In this case, the initial Rayleigh number is:

$$Ra_o = \frac{a_o^3 g c_{sat}^o \nu(\rho - \rho_d)}{D\eta} = \frac{(40\cdot10^{-6}m)^3\left(9.81\frac{m}{s^2}\right)\left(44.5\frac{mol}{m^3}\right)\left(1.62\cdot10^{-4}\frac{m^3}{mol}\right)\left(297\frac{Kg}{m^3}\right)}{6.1\cdot10^{-11}\frac{m^2}{s}\cdot 0.8\cdot10^{-3}\frac{Kg}{m.s}} = 28 \quad [2.93]$$

and the characteristic velocity for natural convection when $a = a_0$ is given by Eq. [2.45]:

$$u_o^* = \frac{D}{a_o} Ra_o^{1/2} = \frac{\left(6.1\cdot10^{-11}\frac{m^2}{s}\right)(28)^{1/2}}{(40\cdot10^{-6}m)} = 8\cdot10^{-6}\frac{m}{s} = 8\frac{\mu m}{s} \quad [2.94]$$

The observed average velocity for the PS particles at this surfactant concentration and drop size is, according to Eqs. [2.87]-[2.88]:

$$u_o = \chi a_o = \left(4.54\,s^{-1}\right)(40\mu m) = 182\frac{\mu m}{s} \quad [2.95]$$

For the case of the solubilization of undecane drops in $C_{12}E_8$ (2.5 wt.%) with a_0 = 40 μm, Ra_0 = 9, u_o^* = 4.5 μm/s and u_0 = 126 μm/s. In average, estimates for u_0^* and u_0 differed by a factor 25 for the initial sizes of the drops that were tested. It is worth recalling that Eq. [2.94] provides a lower limit for Ra_0 because it strictly applies to natural convection around solid spheres. Higher values for u_o^* should be expected for a system exhibiting Rybczynski-Hadamard circulation, as was measured experimentally. In any case, the fact that the calculated and observed velocities differed significantly indicates that buoyancy may contribute to the onset of convection in this system, but other phenomena may act concomitantly.

Another possibility is the occurrence of Marangoni-type flow. This would require the interfacial tension at the top of the drop (σ_1, see Figure 2.32) to be higher than the interfacial tension at the bottom of the drop (σ_2), so internal circulation takes place in the

direction depicted in Figure 2.32. In this case, surface-active materials at the interface in the regions of low interfacial tension move toward the regions of high interfacial tension to reduce the interfacial tension gradient. Transfer of momentum to the bulk fluids that surround the interface generates the convective flow. In this case, the interface must be mobile, i.e., surfactant must be able to adsorb near the bottom of the drop and desorb in other regions to sustain flow. An estimate of the difference in interfacial tensions that is needed to promote convection to the extent observed in these experiments can be performed from the analysis of Ruckenstein [60] for the contribution of Marangoni flow to the velocity at the equator of a bubble (or drop) moving under the combined effect of buoyancy and interfacial tension gradients:

$$u_M = \frac{d\sigma/dz}{2\eta + 3\eta_d} a \qquad [2.96]$$

where $d\sigma/dz$ is the rate of change of the interfacial tension σ in the vertical direction z. If the approximation $d\sigma/dz \sim (\sigma_1-\sigma_2)/2a = \Delta\sigma/2a$ holds, Eq. [2.96] becomes:

$$u_M \sim \frac{\Delta\sigma}{4\eta + 6\eta_d} \quad whence \quad \Delta\sigma \sim (4\eta + 6\eta_d) u_M . \qquad [2.97]$$

Velocities between 0-450 μm/s were measured in the solubilization experiments with n-octane (Figure 2.33). The difference in interfacial tensions that is needed to render such velocities ranges between $0 < \Delta\sigma < 1.5 \cdot 10^{-6}$ N/m if Eq. [2.97] is assumed as valid. The interfacial tension of n-octane in $C_{12}E_8$ (2.5 wt.%) at 30.9 °C is 7.10^{-4} N/m. Therefore, a reduction in interfacial tension at the bottom of the drop of only 0.2% of its equilibrium value would suffice to initiate convective flow at the rates measured in these experiments. This minute difference could be caused, for example, by very small

temperature fluctuations. The temperature gradient that would render the $\Delta\sigma$ given above can be calculated as follows:

$$\frac{d\sigma}{dT} \sim \frac{\Delta\sigma}{\Delta T} \quad whence \quad \Delta T = \Delta\sigma \Big/ \left(\frac{d\sigma}{dT}\right). \qquad [2.98]$$

A value for $d\sigma/dT$ ~ - 5.10^{-5} N/m.K was estimated from measurements for the interfacial tension for n-octane in $C_{12}E_8$ (2.5 wt.%) at 23 °C (1.1 mN/m) and 30.9 °C (0.7 mN/m). If so, $0 > \Delta T = T_1 - T_2 > -0.03$ K. This is, Marangoni-type flow with characteristic velocities up to 450 μm/s could be observed if the imbalance in temperature between the bottom and top of the drop suffices to raise the temperature in the latter respect to the former by 0.03 K or less. It has been shown [61, 62] that temperature gradients that result from thermal effects due to heat of solubilization when two immiscible liquids are placed in contact can lead to spontaneous Marangoni-type interfacial convection. Therefore, an imbalance in the rates of adsorption/desorption of surfactant due to natural convection and/or small differences in local solubilization rates between the extremes of the drop perhaps sufficed to generate such small temperature fluctuations.

Although the calculations provided above to explain the causes of convection should be regarded as approximate, they strongly suggest that natural convection driven by buoyancy, and perhaps forced convection caused by minute interfacial tension gradients on the drop could act concomitantly and promote the onset of convective currents. These considerations may also apply to other solubilization studies of hydrocarbons in nonionic surfactant solutions for which the occurrence of spontaneously-generated convection has been reported [28]. Future investigations to ascertain the relative contribution of the mechanisms discussed in this section to the onset of convection, and the possibility of occurrence of other phenomena such as interfacial flow instabilities, are encouraged.

2.6. References

1. D.J. McClements and S.R. Dungan, Light scattering study of solubilization of emulsion droplets by non-ionic surfactant solutions, *Colloids Surf. A: Phys. Chem. Eng. Asp.*, **104** (1995) *127-135*

2. J. Weiss and D.J. McClements, Mass transport phenomena in oil-in-water emulsions containing surfactant micelles: solubilization, *Langmuir*, **16** (2000) *5879-5883*

3. A.S. Kabalnov, A.V. Pertzov, and E.D. Shchukin, Ostwald ripening in emulsions. 1. Direct observations of Ostwald ripening in emulsions., *J. Colloid Interface Sci.*, **118** (1987) *590-597*

4. A.S. Kabalnov and E.D. Shchukin, Ostwald ripening theory: applications to fluorocarbon emulsion stability, *Adv. Colloid Interface Sci.*, **38** (1992) *69-97*

5. A.S. Kabalnov, Can micelles mediate a mass transfer between oil droplets?, *Langmuir,* **10** (1994) *680-684*

6. J. Weiss, C. Canceliere, and D.J. McClements, Mass transport phenomena in oil-in-water emulsions containing surfactant micelles: Ostwald ripening, *Langmuir,* **16** (2000) *6833-6838*

7. J. Soma and K.D. Papadopoulos, Ostwald ripening in Sodium Dodecyl Sulfate-stabilized decane-in-water emulsions, *J. Colloid Interface Sci.,* **181** (1996) *225-231*

8. P. Taylor, Ostwald ripening in emulsions, *Adv. Colloid Interface Sci.,* **75** (1998) *107-163*

9. J. Weiss, J. Coupland, and D.J. McClements, Solubilization of hydrocarbon emulsion droplets suspended in nonionic surfactant micelle solutions, *J. Phys. Chem.*, **100** (1996) *1066-1071*

10. P.C. Hiemenz, "Principles of colloid and surface chemistry", Marcel Dekker, Inc., New York, 1986.

11. I.M. Lifshitz and V.V. Slyozov, The kinetics of precipitation from supersaturated solutions, *J. Phys. Chem. Solids*, **19** (1961) *35-50*

12. C. Wagner, Theorie der alterung von Niederschlägen durch umlösen, *Z. Elektrochemie*, **65** (1961) *581-591*

13. W.I. Higuchi and J. Misra, Physical degradation of emulsions via the molecular diffusion route and the possible prevention thereof, *J. Pharmacol. Sci.*, **51** (1962) *459-467*

14. B.P. Binks, J.H. Clint, P.D.I. Fletcher, S. Rippon, S.D. Lubetkin, and P.J. Mulqueen, Kinetics of swelling of oil-in-water emulsions, *Langmuir*, **14** (1998) *5402-5411*

15. B.P. Binks, J.H. Clint, P.D.I. Fletcher, S. Rippon, S.D. Lubetkin, and P.J. Mulqueen, Kinetics of swelling of oil-in-water emulsions by different surfactants, *Langmuir*, **15** (1999) *4495-4501*

16. A.S. Kabalnov, Ostwald ripening and related phenomena, *J. Dispersion Sci. Technol.*, **22** (2001) *1-12*

17. A.S. Kabalnov, K.N. Makarov, A.V. Pertzov, and E.D. Shchukin, Ostwald ripening in emulsions: 2. Ostwald ripening in hydrocarbon emulsions: experimental verification of equation for absolute rates, *J. Colloid Interface Sci.*, **138** (1990) *98-104*

18. A. Ghanem, W.I. Higuchi, and A.P. Simonelli, Interfacial barriers in interphase transport: retardation of the transport of diethylphtalate across the hexadecane-water interface by an adsorbed gelatin film, J. *Pharmaceutical Sci.*, **58** (1969) *165-174*

19. A. Ghanem, W.I. Higuchi, and A.P. Simonelli, Interfacial barriers in interphase transport II: influence of additives upon the transport of diethylphtalate across the hexadecane-gelatin-water interface, *J. Pharmaceutical Sci.*, **59** (1970) *232-237*

20. A. Ghanem, W.I. Higuchi, and A.P. Simonelli, Interfacial barrier in interphase transport III: transport of cholesterol and other organic solutes into hexadecane-gelatin-water matrices. *J. Pharmaceutical Sci.*, **59** (1970) *659-665*

21. B.J. Carroll, The kinetics of solubilization of non-polar oils by nonionic surfactant solutions, *J. Colloid Interface Sci.*, **79** (1981) *126-135*

22. B.J. Carroll, B.G.C. O'Rourke, and A.J.I. Ward, The kinetics of solubilization of single component non-polar oils by a non-ionic surfactant, *J. Pharm. Pharmacol.*, **34** (1982) *287-292*

23. B.J. Carroll, Solubilisation of two-component oil mixtures by micellar surfactant solutions, *J. Chem. Soc., Faraday Trans.* 1, **82** (1986) *3205-3214*

24. B.J. Carroll and P.J. Doyle, Solubilization kinetics of a tryglyceride/n-alkane mixture in a non-ionic surfactant solution, *J. Pharm. Pharmacol.*, **40** (1988) *229-232*

25. A.C. Donegan and A.J.I. Ward, Solubilization kinetics of n-alkanes by a non-ionic surfactant, *J. Pharm. Pharmacol.*, **39** (1987) *45-47*

26. B.G.C. O'Rourke, A.J.I. Ward, and B.J. Carroll, Investigation of the solubilization kinetics of binary mixtures of non-polar oils by non-ionic surfactants, *J. Pharm. Pharmacol.*, **39** (1987) *865-870*

27. B.H. Chen and C.A. Miller, Rates of solubilization of triolein into nonionic surfactant solutions, *Colloids Surf. A: Phys. Chem. Eng. Asp.*, **128** (1997) *129-143*

28. B.H. Chen, C.A. Miller, and P.R. Garrett, Rates of solubilization of triolein/fatty acid mixtures by nonionic surfactant solutions, *Langmuir*, **14** (1998) *31-41*

29. P.A. Kralchevsky, N.D. Denkov, P.D. Todorov, G.S. Marinov, G. Broze, and A. Mehreteab, Kinetics of triglyceride solubilization by micellar solutions of nonionic surfactant and triblock copolymer. 2. Theoretical model, *Langmuir*, **18** (2002) *7887-7895*

30. P.D. Todorov, G.S. Marinov, P.A. Kralchevsky, N.D. Denkov, P. Durbut, G. Broze, and A. Mehreteab, Kinetics of triglyceride solubilization by micellar solutions of nonionic surfactant and triblock copolymer. 3. Experiments with single drops., *Langmuir*, **18** (2002) *7896-7905*

31. N.C. Christov, N.D. Denkov, P.A. Kralchevsky, G. Broze, and A. Mehreteab, Kinetics of triglycerid solubilization by micellar solutions of nonionic surfactant and triblock copolymer. 1. Empty and swollen micelle, *Langmuir*, **18** (2002) *7880-7886*

32. S.R. Dungan, B.H. Tai, and N.I. Gerhardt, Transport mechanisms in the micellar solubilization of alkanes in oil-in-water emulsions, *Colloids Surf. A: Phys. Chem. Eng. Asp.*, **216** (2003) *149-166*

33. P.D. Todorov, P.A. Kralchevsky, N.D. Denkov, G. Broze, and A. Mehreteab, Kinetics of solubilization of n-decane and benzene by micellar solutions of sodium dodecyl sulfate, *J. Colloid Interface Sci.*, **245** (2002) *371-382*

34. J.C. Lim and C.A. Miller, Dynamic behavior and detergency in systems containing nonionic surfactants and mixtures of polar and nonpolar oils, *Langmuir*, **7** (1991) *2021-2027*

35. L. Wen and K.D. Papadopoulos, Visualization of water transport in W1/O/W2 emulsions, *Colloids Surf. A: Phys. Chem. Eng. Asp.*, **174** (2000) *159-167*

36. M.V. Smoluchowski, Versuch einer mathematischen theorie der koagulationskinetik kolloider lösungen, *Z. Phys. Chem.*, **92** (1918) *129-168*

37. A.H. Goldberg, W.I. Higuchi, N.F.H. Ho, and G. Zografi, Mechanisms of interphase transport 1: theoretical considerations of diffusion and interfacial barriers in transport of solubilized systems, *J. Pharm. Sci.*, **56** (1967) *1432-1440*

38. J. Weiss, J. Coupland, D. Brathwaite, and D.J. McClements, Influence of molecular structure of hydrocarbon emulsion droplets on their solubilization in nonionic surfactant micelles, *Colloids Surf. A: Phys. Chem. Eng Asp.*, **121** (1997) *53-60*

39. C.L. Williams, A.R. Bhakta, and P. Neogi, Mass transfer of a solubilizate in a micellar solution and across an interface, *J. Phys. Chem. B*, **103** (1999) *3242-3249*

40. R. Nagarajan and E. Ruckenstein, Theory of surfactant self-assembly: a predictive molecular thermodynamic approach, *Langmuir*, **7** (1991) *2934-2969*

41. R.B. Bird, W.E. Stewart, and E.N. Lightfoot, "Transport Phenomena", John Wiley & Sons, Inc., New York, 2002.

42. P.L.T. Brian and H.B. Hales, Effects of transpiration and changing diameter on heat and mass transfer to spheres, *AIChE J.*, **15** (1969) *419-425*

43. A.E. Nielsen, Diffusion controlled growth of a moving sphere. The kinetics of crystal growth in potasium perchlorate precipitation, *J. Phys. Chem.*, **65** (1961) *46-49*

44. R.C. Kerr, Convective crystal dissolution, *Contrib. Mineral. Petrol.*, **121** (1995) *237-246*

45. V.G. Levich, "Physicochemical Hydrodynamics", Prentice-Hall, Inc., Englewood Cliffs, N. J., 1962.

46. K. Jafarpur and M.M. Yovanovich, Laminar free convective heat transfer from isothermal spheres: a new analytical method, *Int. J. Heat Mass Transfer*, **35** (1992) *2195-2201*

47. J. A. Marqusee and J. Ross, Kinetics of phase transition: theory of Ostwald ripening, *J. Chem. Phys.*, **79** (1983) *373-378*

48. W. Brown, Z. Pu, and R. Rymdén, Size and shape of nonionic amphiphilic micelles: NMR self-diffusion and static and quasi-elastic light-scattering measurements on $C_{12}E_5$, $C_{12}E_7$ and $C_{12}E_8$ in aqueous solution, *J. Phys. Chem.*, **92** (1988) *6086-6094*

49. D.H. Lide, Ed., "CRC Handbook of Chemistry and Physics", 79th Edition ed., CRC Press, Boca Raton, USA, 1998.

50. M.J. Rosen, "Surfactants and Interfacial Phenomena", John Wiley & Sons, New York, 1989.

51. J.C. Lim, *Personal communication*. 2003.

52. D. Prak, L. Abriola, W. Weber, and K. Bocskay, Solubilization rates of n-alkanes in micellar solutions of nonionic surfactants, *Environ. Sci. Technol.*, **34** (2000) *476-482*

53. B.H. Tai, "The kinetics of solubilization and transport by micelles in oil-in-water emulsions". MS Thesis, 1999, University of California-Davis: Davis, USA.

54. D. Mackay and W.Y. Shiu, A critical review of Henry's laws constants for chemicals of environmental interest, *J. Phys. Chem. Ref. Data*, **10** (1981) *1175-1199*

55. E.E. Kumacheva, E.A. Amelina, and V.I. Popov, Effect of flocculation on enlargement of particles of aqueous emulsions of perfluorodecalin, *K. Zhurnal (English trans.)*, **51** (1989) *1212-1213*

56. J. Ugelstad, P.C. Mørk, A. Berge, T. Ellingsen, and A.A. Khan, Effects of additives on the formation of monomer emulsions and polymer dispersions, in "Emulsion polymerization", I. Piirma (Ed.). Academic Press, New York (1982)

57. R. Reid, J.M. Prausnitz, and B. Poling, "The properties of gases & liquids", 4th Edition, McGraw-Hill Company, New York, 1988.

58. E. L. Cussler. "Diffusion". Cambridge University Press, Cambridge, UK, 1997

59. A.S. Kabalnov and J. Weers, Kinetics of mass transfer in micellar systems: surfactant adsorption, solubilization kinetics, and ripening, *Langmuir*, **12** (1996) *3442-3448*

60. E. Ruckenstein, Analysis of transport phenomena using scaling and physical models, *Adv. Chem. Eng.*,**13** (1987) *11-112*

61. E.S. Pérez de Ortiz and H. Sawitowski, Interfacial stability of binary liquid-liquid systems - I. Stability analysis, *Chem. Eng. Sci.*, **28** (1973) *2051-2061*

62. E.S. Pérez de Ortiz and H. Sawitowski, Interfacial stability of binary liquid-liquid systems - II. Stability behavior of selected systems, *Chem. Eng. Sci.*, **28** (1973) *2063-2069*

Chapter 3

Enhanced characterization of oilfield emulsions via NMR diffusion and transverse relaxation experiments*

3.1 Introduction

The mean value and degree of polydispersity of drop sizes in emulsions have a significant effect on key properties such as stability [1, 2]; viscosity and rheological behavior [3-5]; color and appearance [6]; texture [7]; and retention of aroma [8] and flavor (food emulsions) [9]. For this reason, many experimental techniques have been applied to determine the mean droplet size and the drop size distribution in emulsions, including microphotography and video-enhanced microscopy, gravitational/centrifugal sedimentation, Coulter counting, turbidimetry, differential scanning calorimetry, dynamic and static light scattering, acoustic spectroscopy and nuclear magnetic resonance (NMR). Excellent reviews on the characterization of emulsions with these and other methods have been compiled by Orr [10] and by several authors in a recent book edited by Sjöblom [11].

NMR-based methods offer significant advantages that distinguish them from the other above-mentioned techniques [12]. The same sample can be tested as many times as desired. Dilution, cooling/heating, centrifugation, or confinement in a narrow gap are not necessary. Measurements are not influenced by the optical or dielectric properties of the system. Therefore, clear and opaque emulsions, and dispersions in which the continuous phase is non-conducting can be tested. A typical test is fast (approx. 5-10 min), and it requires a small sample ($\geq\sim$ 0.5 g). Furthermore, the composition of the emulsion can be resolved from the NMR data.

---

* Published in Peña, A. A. and Hirasaki, G. J. *Advances in Colloid and Interface Science.* **105** (2003) *103-150*

NMR microscopy on emulsions is based on the following few physical principles [13]: Some nuclei, such as protons (^{1}H), exhibit a permanent magnetic moment $\boldsymbol{p}$. When a steady uniform magnetic field $\boldsymbol{B_0}$ is applied on these nuclei, $\boldsymbol{p}$ precesses around the direction of $\boldsymbol{B_0}$ at the Larmor frequency $\omega_0 = \gamma B_0$, where γ is a constant. Nuclei with precessing $\boldsymbol{p}$ are termed *spins*. The ensemble of spins exhibit net magnetization $\boldsymbol{M}$ in the direction of $\boldsymbol{B_0}$. If a radio frequency (rf) pulse of a second magnetic field $\boldsymbol{B_1}$ orthogonal to $\boldsymbol{B_0}$ is applied, the net magnetization is rotated to an extent (typically 90° or 180°) that depends on the duration of the pulse. When the rf pulse ceases, $\boldsymbol{M}$ will *relax* toward and eventually reach the equilibrium state. Relaxation of $\boldsymbol{M}$ can be measured from the spins (protons) present in the emulsion, either in the direction of $\boldsymbol{B_0}$ (longitudinal magnetization), or transverse to it (transverse magnetization). In addition, the precession of spins at the same Larmor frequency is referred to as *coherent* or *in-phase*. If the steady magnetic field is not uniform as above, the Larmor frequency depends on the position of the nuclei [$\omega(r) = \gamma B(r)$]. Two spins at positions $\boldsymbol{r_1}$ and $\boldsymbol{r_2}$, such that $\boldsymbol{B}(\boldsymbol{r_1}) \neq \boldsymbol{B}(\boldsymbol{r_2})$, precess incoherently of out-of-phase. Magnetic field gradients are commonly applied to create a non-uniform magnetic field and adjust coherence.

Droplets in emulsions can be sized via NMR with at least two sequences of radio frequency and magnetic field gradient pulses: the echo train experiment introduced by Carr and Purcell [14] and refined by Meiboom and Gill (CPMG) [15], and the pulsed magnetic field gradient spin-echo experiment (PGSE) developed by Stejskal and Tanner [16]. This chapter describes classic views and novel contributions to the theory used to characterize emulsions from transverse magnetization data collected in these tests. The advantages and limitations of these methods are discussed. Furthermore, it is shown that a wealth of information on the emulsion besides the drop size distribution can be

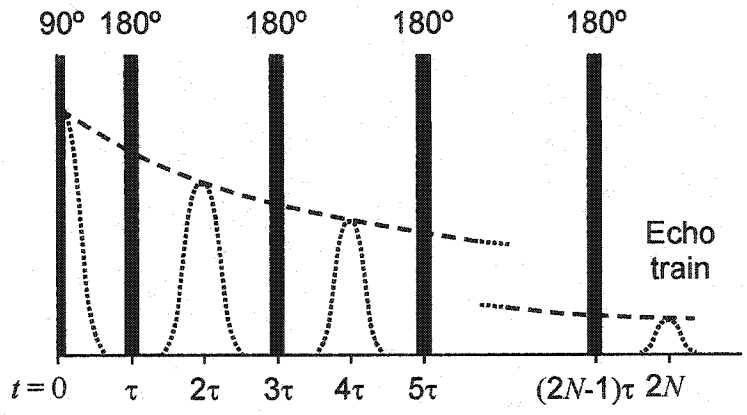


Figure 3.1. Sequence of events in a CPMG experiment.

obtained when results from both techniques are combined. The implementation of this combined CPMG-PGSE procedure is illustrated with the characterization of emulsions of water in several crude oils.

3.2. CPMG EXPERIMENT: BASIC THEORY AND INTERPRETATION

3.2.1. Description of the test

The CPMG sequence consists of a rf 90° pulse, followed by N rf 180° pulses that induce successive phase recoveries and generate a train of N spin-echoes (Figure 3.1). As time proceeds, relaxation of the magnetization takes place and the amplitude of the spin-echo that is generated after each 180° re-phasing decays. In this experiment, the transverse component of the magnetization vector $M_{xy}(2n\tau)$ is measured, and the resulting relaxation curve is fitted to a discrete multi-exponential function of the form:

$$\frac{M_{xy}(2n\tau)}{M_{xy}(0)} = \sum_{i=1}^{m} f_i \exp\left(-\frac{2n\tau}{T_{2,i}}\right) ; \quad 0 \le n \le N; \quad m < N; \quad \sum_{i=1}^{m} f_i = 1 \ . \qquad [3.1]$$

$M_{xy}(0)$ is the amplitude of signal that corresponds to the initial transverse magnetization and f_i is the fraction of ^{1}H nuclei with characteristic relaxation time $T_{2,i}$. The fitting procedure consists of calculating f_i values for a pre-established set of $T_{2,i}$, whence the so-called T_2 distribution is obtained. Fitting data to a multi-exponential sum is an ill-posed problem, i.e., multiple sets of f_i values can render a satisfactory fit [17]. For this reason, a so-called regularization method must be implemented to calculate the most representative T_2 distribution [18].

3.2.2. Determination of drop sizes in emulsions via CPMG

Eq. [3.1] arises naturally when the relaxation of magnetization is modeled for an isotropic fluid confined in a planar, cylindrical or spherical cavity in the presence of volume-like and surface-like magnetization sinks with average constant strength $1/T_{2,bulk}$ (*bulk relaxivity*) and ρ (*surface relaxivity*), respectively [19]. The contributions of bulk and surface relaxivity to the decay of transverse magnetization are accounted for in the $T_{2,i}$ values in the 'fast diffusion' mode as follows:

$$\frac{1}{T_{2,i}} = \frac{1}{T_{2,bulk}} + \rho\left(\frac{S}{V}\right)_i . \qquad [3.2]$$

provided that the measurement is performed in the fast diffusion mode, as discussed in section 3.2.3. $(S/V)_i$ is the surface-to-volume ratio of the cavity i. For a sphere of radius a_i, $(S/V)_i = 3/a_i$. Hence,

$$\frac{1}{T_{2,i}} = \frac{1}{T_{2,bulk}} + \rho\frac{3}{a_i} , \qquad [3.3]$$

and,

$$a_i = 3\rho\left(\frac{1}{T_{2,i}} - \frac{1}{T_{2,bulk}}\right)^{-1} . \qquad [3.4]$$

The number of protons present in a given volume of sample determines the signal amplitude. For this reason, the fraction f_i that is associated to each $T_{2,i}$ value renders a direct measurement of the fraction of fluid that is confined in cavities of corresponding surface-to-volume ratio $(S/V)_i$. Therefore, the T_2 distribution that is obtained from isotropic fluids contained in the interstices of a heterogeneous system contains valuable information on the distribution of sizes of such heterogeneities. This principle is commonly used, for example, in the interpretation of lab and well logging T_2 measurements to estimate the size distribution of pores in rocks which potentially may contain hydrocarbons [20, 21]. In a related application, the surface-to-volume ratio can be determined from independent measurements such as mercury porosimetry [22, 23], pore image analysis [24], or BET gas adsorption [25, 26] and the result is introduced in Eq. [3.2] to determine surface relaxivity at the rock-fluid interface.

Eq. [3.4] can be used to calculate the volume-weighted drop size distribution of emulsions containing spherical droplets, provided that:

(a) Measurements are performed in the "fast diffusion" mode.

(b) The surface relaxivity (ρ) and the bulk relaxivity ($1/ T_{2,bulk}$) of the drop phase (water in W/O emulsions or vice versa) are known. $T_{2,bulk}$ can be easily measured from a CPMG experiment on a bulk sample of the drop phase, either in absence of continuous phase or in contact with it, but not emulsified. An independent measurement of the surface-to-volume ratio is required to calculate ρ.

(c) $T_{2,bulk}$ for the dispersed phase is indeed single-valued and not a distribution of characteristic bulk relaxation times.

(d) Two independent sets of $T_{2,i}$ - f_i values can be resolved from the T_2 distribution of the emulsion for the oil and water phases, respectively. This task is straightforward if the water signal and oil signal appear as separate peaks in the T_2 distribution. Otherwise, the magnetic resonance fluid method recently introduced by Freedman et al. [27] can be used to discriminate water signal from oil signal for systems in which the T_2 distributions of these phases overlap.

3.2.3. Range of drop sizes that can be resolved via CPMG

Eq. [3.4] is valid in the so-called fast diffusion limit (FDL), in which the characteristic timescale for diffusion of the molecules confined in the drops (t_D) is much smaller than the characteristic timescale for surface relaxation (t_ρ):

$$\frac{t_D}{t_\rho} = \frac{a_i^2 / D}{a_i / \rho} << 1, \text{ whence } \frac{\rho a_i}{D} << 1. \qquad [3.5]$$

D is the self-diffusion coefficient of the drop phase. In practice, the relaxation of magnetization of fluids confined in spherical cavities occurs in the fast diffusion mode whenever:

$$\frac{\rho a_i}{D} \leq \frac{1}{4} \qquad [3.6]$$

as shown in Appendix C. Therefore, the maximum diameter ($d_{MAX,FDL}$) for which Eq. [3.6] holds is

$$d_{MAX,FDL} = \frac{D}{2\rho}. \qquad [3.7]$$

The signal-to-noise ratio (SNR) and the bulk relaxation time ($T_{2,bulk}$) can also determine d_{MAX}. The effect of surface relaxation on the decay of magnetization of fluid present in any droplet should be significantly greater than the intrinsic noise ν of the measurement. This condition can be expressed as follows:

$$\mathbf{max}\left|M_{xy}(t, a \to \infty) - M_{xy}(t, a)\right| \geq A\nu \,. \qquad [3.8]$$

where A > 1 is a constant. Eqs. [3.3], [3.8] and [C.5] in Appendix C can be combined to obtain,

$$\Delta M = A \cdot \nu; \;\; \Delta M = M_{xy}(0)\,\mathbf{exp}\left(-\frac{t'}{T_{2,bulk}}\right) - M_{xy}(0)\,\mathbf{exp}\left(-\frac{t'}{T_{2,bulk}} - \frac{6\rho t'}{d_{MAX,\nu}}\right), \qquad [3.9]$$

where t' is the time at which ΔM exhibits a maximum and $d_{MAX,\nu}$ is the maximum drop size that can be measured for given values of SNR and $T_{2,bulk}$.

Let the signal-to-noise ratio be defined as follows:

$$SNR = \frac{M_{xy}(0)}{\nu}. \qquad [3.10]$$

It can be shown from Eqs. [3.9]-[3.10] that t' = $T_{2,bulk}$ when SNR >> $A \cdot exp(1)$. If so, the following expression for $d_{MAX,\nu}$ is obtained:

$$d_{MAX,\nu} = \frac{6}{A \cdot \mathbf{exp}(1)} \rho \cdot SNR \cdot T_{2,bulk} \qquad [3.11]$$

In summary, the maximum drop size that can be determined via CPMG is:

$$d_{MAX} = \mathbf{min}\left\{d_{MAX,FDL}, d_{MAX,\nu}\right\} \qquad [3.12]$$

where $d_{MAX,FDL}$ and $d_{MAX,\nu}$ are given by Eqs. [3.7] and [3.11], respectively.

The self-diffusion coefficient of water at 25 °C is 2.30 x 10^{-9} m^2/s [28] and a plausible surface relaxivity for oilfield emulsions is ρ = 0.50 μm/s as shown later. For these conditions, water droplets up to $d_{MAX,FDL}$ = 2200 μm could be sized according to Eq. [3.7]. A typical signal-to-noise ratio for a CPMG experiment on emulsions is 250, and a plausible value for A is 3. In addition, $T_{2,bulk}$ for water at 25 °C is ca. 3 seconds. Therefore, from Eqs. [3.11]-[3.12] we obtain $d_{MAX} = d_{MAX,v} = 276\ \mu m$.

Eq. [3.12] restricts the T_2 values that can be considered to calculate the drop size distribution to an upper limit $T_{2,MAX}$:

$$\frac{1}{T_{2,MAX}} = \frac{1}{T_{2,bulk}} + \rho\frac{6}{d_{MAX}}. \qquad [3.13]$$

We suggest to interpret the signal of the drop phase that is measured for $T_{2,i} > T_{2,MAX}$ as if it were originated from bulk fluid, and not from fluid dispersed in drops.

The minimum drop diameter (d_{MIN}) that can be measured via CPMG and its corresponding relaxation time $T_{2,MIN}$ are determined by the echo spacing. Let us assume that a fraction ε of the transverse component of magnetization of the fluid present in the smallest drops has relaxed when the first echo is acquired at time 2τ. If so,

$$1-\varepsilon = \mathbf{exp}\left(-2\tau / T_{2,MIN}\right), \text{ whence } T_{2,MIN} \cong 2\tau/\varepsilon. \qquad [3.14]$$

By substituting Eq. [3.14] in Eq. [3.4] we obtain:

$$d_{MIN} = 6\rho\left(\frac{\varepsilon}{2\tau} - \frac{1}{T_{2,bulk}}\right)^{-1} \cong \frac{12\tau\rho}{\varepsilon}. \qquad [3.15]$$

The approximation that is made in Eq. [3.15] holds if $T_{2,MIN} << T_{2,bulk}$. A typical echo-spacing for a CPMG test is 2τ = 300 μs. If the surface relaxivity given above (0.5 μm/s) and ε = 0.1 are chosen, then $T_{2,MIN}$ = 3 ms and d_{MIN} = 9 nm.

3.2.4. Determination of the water/oil composition in emulsions

The amplitude of the signal that is obtained from each phase is proportional to the number of protons present in such phase. Therefore, the volume fraction ϕ_k of phase k is related to the T_2 distribution as follows:

$$\phi_k \propto \frac{\sum (f_i)_k}{HI_k}. \qquad [3.16]$$

HI is the so-called hydrogen index, which is defined as the number of protons in a sample divided by the number of protons present in the same volume of water [29]. Empirical correlations and diagrams to estimate HI are available for brines, and for light and heavy crude oils [30-32]. In general, HI ~ 1.0 for aqueous solutions and HI ~ 0.9-1.0 for most crude oils except for aromatic oils, which exhibit HI between 0.6-0.8 due to the low H/C ratio of aromatic compounds. If Eq. [3.16] holds, we have:

$$\phi_{DP} = \frac{\left[\sum (f_i)_{DP} / HI_{DP}\right]}{\left[\sum (f_i)_{CP} / HI_{CP}\right] + \left[\sum (f_i)_{DP} / HI_{DP}\right]}; \quad \phi_{CP} = 1 - \phi_{DP} \qquad [3.17]$$

where the subindexes DP and CP identify the drop and continuous phase, respectively.

Low-field NMR-CPMG has been regarded as superior to all other available techniques for the determination of water content in heavy oil, bitumen and oilfield emulsions [33, 34], and it is quickly becoming a standard procedure in the oil industry for

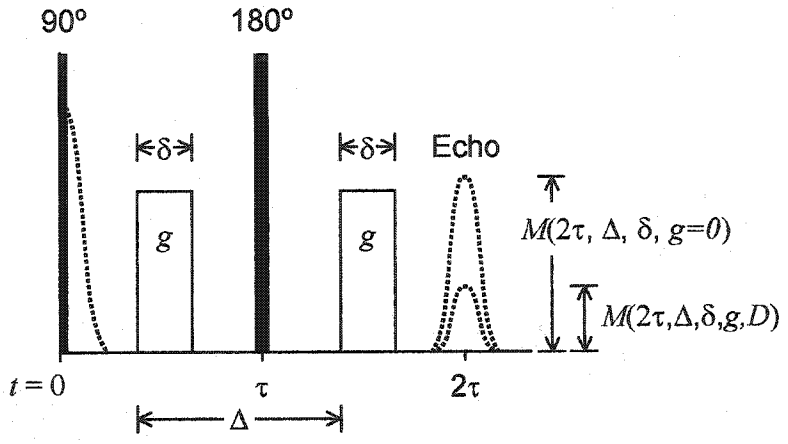


Figure 3.2. Sequence of events in a PGSE experiment.

such task. This application of the CPMG method has been discussed by LaTorraca et al. [29] and Hills [35]. Allsopp et al. [33] have developed and successfully tested *in situ* a low-field spectrometer suitable for usage in the field. The method was accurate to ± 5 % and measuring times were typically four minutes or less. This application is a natural extension of the usage of NMR relaxation measurements for the determination of porosity in minerals and rocks [20, 24, 26, 36].

3.3. PGSE EXPERIMENT: BASIC THEORY AND INTERPRETATION

3.3.1. Description of the test

The pulsed field gradient spin-echo experiments consists of a rf 90° pulse, followed by a rf 180° pulse at time τ. As a result of this sequence, a spin-echo is collected at time 2τ (Figure 3.2). The rf 180° pulse is sandwiched between two magnetic field gradient pulses of absolute strength g and duration δ that are separated by a time span Δ.

In a PGSE experiment, it is aimed to measure the amplitude of the spin-echoes in the presence and absence of gradient pulses ($g > 0$ and $g = 0$), respectively. In the latter case, the spin-echo is acquired in a homogeneous magnetic field and therefore $M_{xy}(2\tau, g = 0, \Delta, \delta)$ is independent of the spatial distribution of spins in the sample. On the other hand, when $g > 0$ the first gradient pulse imposes an inhomogeneous magnetic field, thus causing a loss of coherence in the phases of the spins to an extent that depends on the position of the nuclei at the time the gradient is applied. In absence of diffusion, the second gradient pulse would exactly revert the phase shifts. However, since molecules diffuse and change their position during the *diffusion time* Δ, the refocusing is incomplete and the amplitude of the echo that is recorded at time 2τ [$M_{xy}(2\tau, g > 0, \Delta, \delta, D)$] is smaller than $M_{xy}(2\tau, g = 0, \Delta, \delta)$. For this reason,

$$0 \leq M_{xy}(2\tau, g, \Delta, \delta, D) \leq M_{xy}(2\tau, g = 0, \Delta, \delta)$$

whence,

$$R = \frac{M_{xy}(2\tau, g, \Delta, \delta, D)}{M_{xy}(2\tau, g = 0, \Delta, \delta)};\ 0 \leq R \leq 1 \qquad [3.18]$$

R is termed the *spin-echo attenuation ratio*. In a typical PGSE experiment, attenuation ratios are measured changing systematically δ, Δ or g.

For isotropic bulk fluids in which molecules can diffuse freely (Fickian diffusion), the following expression holds [16]:

$$R_{bulk} = \mathbf{exp}\left[-\gamma^2 g^2 D \delta^2 \left(\Delta - \frac{\delta}{3}\right)\right] \qquad [3.19]$$

The constant γ was mentioned earlier. It is called the gyromagnetic ratio of the nuclei (γ= 2.67 x 10^8 rad.T^{-1}.s^{-1} for ^{1}H). When Eq. [3.19] holds, a plot of the logarithm of R vs. $g^2\delta^2(\Delta\text{-}\delta/3)$ renders a straight line, and D can be calculated from the slope. This method is one of the very few experimental techniques available to measure self-diffusion coefficients.

3.3.2. Determination of drop sizes in emulsions via PGSE

Eq. [3.19] does not apply to fluids confined in small geometries such as pores or droplets, because molecules cannot diffuse freely. In this case, the dimensions of the cavity influence the loss of coherence in the phase of the spins when the magnetic field gradient is applied, thus affecting the attenuation ratio R. Robertson [37] and Neuman [38] first proposed expressions for R for molecules confined between planes, within cylinders and spheres when a steady magnetic field gradient is applied. Murday and Cotts [39] extended Neuman's derivation for the PGSE sequence (Figure 3.2), for restricted diffusion within a sphere of radius a. In this case, the attenuation ratio R_{sp} was shown to be given by:

$$R_{sp} = \exp\left\{-2\gamma^2 g^2 \sum_{m=1}^{\infty} \frac{1}{\alpha_m^2\left(\alpha_m^2 a^2 - 2\right)}\left[\frac{2\delta}{\alpha_m^2 D} - \frac{\Psi}{\left(\alpha_m^2 D\right)^2}\right]\right\}, \qquad [3.20]$$

where,

$$\Psi = 2 + \exp\left[-\alpha_m^2 D(\Delta-\delta)\right] - 2\exp\left(-\alpha_m^2 D\Delta\right) - 2\exp\left(-\alpha_m^2 D\delta\right) + \exp\left[-\alpha_m^2 D(\Delta+\delta)\right], \qquad [3.21]$$

α_m is the m^{th} positive root of the equation:

$$\alpha a \cdot J_{5/2}(\alpha a) - J_{3/2}(\alpha a) = 0, \qquad [3.22]$$

and J_k is the Bessel function of the first kind, order k.

Two limiting cases of Eq. [3.20] are of interest. First, for very large spheres ($a \rightarrow \infty$), Eq. [3.20] reduces to Eq. [3.19] [$R_{sp}(a \rightarrow \infty) = R_{bulk}$] as might be expected, because the effect of restricted diffusion on R becomes negligible. Second, for very small spheres ($a \rightarrow 0$), Eq. [3.20] simplifies as follows:

$$R_{sp}(a \rightarrow 0) = 1 - \tfrac{16}{175}\gamma^2 g^2 D^{-1} \delta a^4 \rightarrow 1. \qquad [3.23]$$

The probability of the molecules to displace during the diffusion time Δ is reduced as $a \rightarrow 0$. For this reason, the loss of coherence in the phases of the spins caused by the magnetic field gradient diminishes and less attenuation of the spin-echo is observed, whence $R \rightarrow 1$ as predicted by Eq. [3.23].

In the derivation of Eq. [3.20] it is assumed that the phase shifts of spins diffusing in a bounded region exhibit a normal (Gaussian) distribution. However, this so-called Gaussian phase-distribution (GPD) approximation is exact only for spins undergoing free diffusion [38]. Balinov et al. [40] performed Brownian dynamics simulations for restricted diffusion in spheres of selected sizes at fixed g, Δ and for various δ, to calculate the exact attenuation ratio that would be observed in each case. Least-square fits of these results were performed using Eq. [3.20] and the sphere radius a as fitting parameter. The radii calculated with this expression differed by less than 5 % from the sizes set for the simulations. Whence, it was concluded that the GPD approximation and Eq. [3.20] are adequate to account for the decay of transverse magnetization of fluids confined in spheres.

For emulsion with a finite distribution of (spherical) droplet sizes, Packer and Rees [41] first proposed that the attenuation ratio of the drop phase (R_{DP}) can be calculated as the sum of the attenuation ratios $R_{sp}(a)$ that would be recorded for fluid confined in drops of radii a, weighted by the probability of finding drops with such sizes in the dispersion. This is:

$$R_{DP} = \int_0^\infty p_V(a) R_{sp}(a) da \Big/ \int_0^\infty p_V(a) da \qquad [3.24]$$

where $p_V(a)$ is the volume-weighted distribution of sizes. $R_{sp}(a)$ is determined from Eq. [3.20]. The task of determining $p_V(a)$ from the PGSE data is feasible, but requires a large number of measurements of R for which the duration of the test may become impractical as discussed later. Instead, a few data are usually taken and an empirical form of $p_V(a)$ is assumed. The lognormal probability distribution function (p.d.f.),

$$p_V(a) = \frac{1}{2a\sigma(2\pi)^{1/2}} \exp\left\{-\left[\frac{\ln(2a) - \ln(d_{gV})}{2\sigma^2}\right]\right\} \qquad [3.25]$$

is the classic assumption for the drop size distribution in absence of additional information, because it is well known that sequential break-up processes, such as grinding of solids or disruption of droplets under mechanical agitation, lead to a lognormal distribution of particle and drop sizes, respectively [42, 43]. In Eq. [3.25], d_{gV} and σ are the geometric volume-based mean diameter and the width or geometric standard deviation of the distribution, respectively. The determination of the drop size distribution consists of performing a least-square fit of the experimental data for R with Eqs. [3.24]-[3.25], using d_{gV} and σ as fitting parameters.

In the original work of Packer and Rees and most of the subsequent publications about this method [12, 44-52], Eqs. [3.24]-[3.25] are expressed in terms of the number-based drop size distribution $p_N(a)$. It is shown in Appendix A that if $p_V(a)$ is lognormal with characteristic parameters d_{gV} and σ, the corresponding number-based distribution $p_N(a)$ is also lognormal with the same geometric standard deviation σ and number-based mean size $d_{gN} = d_{gV} \cdot \exp(-3\sigma^2)$ [53]. Although both approaches are numerically equivalent, it is more proper to express these equations in terms of the volume-weighted distribution because the amplitude of transverse magnetization that is measured in a PGSE test is proportional to the volume of liquid present in the system as drops, and not to the number of droplets.

Packer and Rees [41] correctly pointed out that their procedure is useful to determine the drop size distribution when the following assumptions are valid:

(a) The spin-echo is originated solely from only one component of the emulsion, i.e., the drop phase. Therefore,

$$R_{EMUL} = R_{DP} \qquad [3.26]$$

This assumption limits the applicability of the method to emulsions for which the signal from the continuous phase is suppressed (i.e., emulsions of oil in D_2O). Eq. [3.26] also applies if the transverse magnetization of the continuous phase has relaxed completely and the natural (bulk) relaxation of the drop phase is small at the time the spin-echo is acquired. Namely,

$$\left(T_{2,bulk}\right)_{CP} << 2\tau << \left(T_{2,bulk}\right)_{DP} \qquad [3.27]$$

where $(T_{2,\ bulk})_{CP}$ and $(T_{2,\ bulk})_{DP}$ are the characteristic bulk relaxation times of the continuous and drop phases, respectively. Emulsions of water in viscous oils often satisfy Eq. [3.27]. This explains why the PGSE method is commonly applied in the determination of drop sizes in margarine, butter and low-calorie spreads [44, 46, 47, 49, 54] and water-in-crude-oil emulsions [45].

(b) The distribution of drop sizes is indeed lognormal. This is a significant shortcoming of the method, because the shape of the distribution is not resolved independently, but assumed *a priori*. Drop sizes are often, but not always, distributed in a lognormal fashion [53], and therefore Eq. [3.25] does not provide a satisfactory fit of the PGSE data in all cases [50, 54, 55].

(c) The effect of surface relaxation on the amplitude of the spin-echo is negligible. In the derivation of Eq. [3.20], Murday and Cotts assumed $\rho = 0$. For this reason, surface relaxation is not accounted for in the Packer-Rees method. It can be anticipate that this effect is indeed negligible in a PGSE experiment performed in the fast diffusion regime, because in such regime the relaxation due to diffusion of the spins is much more significant than surface relaxation ($1/t_D >> 1/t_\rho$ whence $\rho a/D << 1$, see Eq. [3.5]).

Dunn and Sun [34] considered the effect of surface relaxation on the attenuation ratio R_{sp} by changing the boundary condition in Neuman's and Murday and Cotts' derivation for the solution of the diffusion propagator of the spins P (see Eq. (11) in Neuman's paper) from:

$$D\nabla P\big|_{r=a} = 0 \qquad [3.28]$$

to:

$$D\nabla P + \rho P\big|_{r=a} = 0 \qquad [3.29]$$

to obtain:

$$R_{sp,\rho} = \exp\left\{-2\gamma^2 g^2 \sum_{m=1}^{\infty} \frac{1}{\alpha_m^2\left(\alpha_m^2 a^2 - 2 + \rho^2 a^2 / D^2 - \rho a / D\right)}\left[\frac{2\delta}{\alpha_m^2 D} - \frac{\Psi}{\left(\alpha_m^2 D\right)^2}\right]\right\}, \qquad [3.30]$$

where Ψ is given by Eq. [3.21] as before and α_m is the m^{th} positive root of the equation:

$$\alpha a \cdot J_{5/2}(\alpha a) - \left(1 + \frac{\rho a}{D}\right) J_{3/2}(\alpha a) = 0 \quad . \qquad [3.31]$$

Eq. [3.30] applies only for small ρ and large D so the probability of finding a spin anywhere in the drop is nearly uniform and the GPD approximation is satisfied (see discussion after Eq. [3.23]). Otherwise, significant surface relaxation would take place and a non-Gaussian distribution of the phase shifts of the spins near the water/oil interfaces would be observed. Eq. [3.30] reduces to Eq. [3.20] in the limit $\rho a/D \rightarrow 0$, as might be expected.

The PGSE experiment has been used not only to size drops in emulsions as discussed above, but also pores in mineral samples [56-58], biological cells [16, 56, 59] and heterogeneities in organic tissue [60, 61]. The three-dimensional packing of non-spherical drops in highly concentrated emulsions (ϕ_{DP} ~1) has also been studied with this method [62, 63]. Other applications in connection with emulsions include the characterization of micelles, bicontinuous structures in microemulsions, vesicles and liquid crystals in surfactant/oil/water systems [47, 64-67].

Several modifications of the basic PGSE sequence shown in Figure 3.2 have been proposed and used in emulsion studies. The stimulated spin-echo (SSE) [68] and the longitudinal-eddy-current-delay (LED) [69] modification allow better resolution for systems exhibiting significantly different longitudinal and transverse relaxation times. The flow-compensating PGSE [51] is used to characterize emulsions in laminar flow. The interpretation of the spin-echo attenuation of the drop phase via Eqs. [3.20]-[3.25] also holds for these sequences.

3.3.3. A novel theory to resolve PGSE data in the time domain

The first limitation listed above for the PGSE test, namely the impossibility to resolve for the drop size distribution when the contribution of the magnetization of the continuous phase to the spin-echo is significant, was overcome with the introduction of the Fourier-transform PGSE method (FT-PGSE). Excellent reviews on this method and its applications in the characterization of water/oil/surfactant systems have been published by Stilbs [70] and Söderman and Stilbs [71]. In the FT-PGSE procedure, the second half of the spin-echo that is generated in the PGSE sequence is Fourier-transformed, and the individual contributions of the components to the spin-echo appear as separate peaks in the frequency domain due to differences in chemical shift. Lönnqvist et al. [52] applied this technique to resolve for the individual signal of water and oil in simple (W/O) and multiple (W/O/W) emulsions. Ambrosone et al. [54] used the method to isolate the water signal from margarine and emulsions of water in olive oil.

Better resolution of the Fourier spectrum is attained as the strength of the permanent magnetic field is increased. For this reason, high-field magnets with Larmor frequencies typically above 80 MHz are used in FT-PGSE studies. Unfortunately, individual peaks

cannot be resolved satisfactorily at the frequencies at which low-field NMR spectrometers operate (~ 2 MHz). Therefore, the determination of the individual contributions of water and oil to the spin-echo that is obtained from an emulsion in the time domain is relevant. The following theoretical framework aims to address this matter. Details on the derivation of the equations are provided in Appendix C.

We propose that the attenuation ratio of emulsions should be computed as follows:

$$R_{EMUL} = (1-\kappa)R_{DP} + \kappa R_{CP} \;; \quad 0 \le \kappa \le 1, \qquad [3.32]$$

where R_{DP} and R_{CP} are the time-resolved attenuation ratios of the drop and continuous phases, respectively. κ is a parameter associated to the bulk relaxation of the transverse component of the magnetization of both phases. It is shown in Appendix C that for the basic PGSE sequence (Figure 3.2), κ is given by:

$$\kappa = \left[1 + \frac{\sum (f_i)_{DP} \exp\left[-2\tau/(T_{2,i})_{DP}\right]}{\sum (f_i)_{CP} \exp\left[-2\tau/(T_{2,i})_{CP}\right]}\right]^{-1} \cong$$

$$\cong \left[1 + \frac{\phi_{DP}}{\phi_{CP}} \frac{HI_{DP}}{HI_{CP}} \frac{\exp\left[-2\tau/(T_{2,bulk})^*_{DP}\right]}{\sum (x_i)^*_{CP} \exp\left[-2\tau/(T_{2,i})^*_{CP}\right]}\right]^{-1} \;;\; (x_i)^*_{CP} = \frac{(f_i)^*_{CP}}{\sum_j (f_j)^*_{CP}}, \qquad [3.33]$$

where the $T_{2,i}$–f_i values for each phase in the exact expression are determined from the T_2 distribution of the emulsion via CPMG as explained above. The approximation shown in Eq. [3.33] allows the evaluation of κ from the T_2 distribution of the phases tested independently or in contact as bulk fluids [parameters noted with (*)]. It is also implied in the approximation that the drop phase exhibits a single characteristic relaxation time, whereas the continuous phase is allowed to exhibit a distribution of relaxation times.

The emulsions that can be characterized with the Packer-Rees approach fall within the particular cases of this derivation. When the signal of the continuous phase is suppressed, or it has relaxed completely at the time the spin-echo is acquired, $\kappa \rightarrow 0$ according to Eq. [3.33]. Therefore, Eq. [3.32] reduces to Eq. [3.26]. On the other hand, $\kappa \rightarrow 1$ corresponds to the case in which the attenuation ratio is determined solely by the continuous phase. These limiting cases are discussed in Appendix C.

R_{DP} in Eq. [3.32] is given by Eq. [3.24] as before. $R_{sp}(a)$ is calculated using Eq. [3.20]. Eq. [3.30] can be used instead of Eq. [3.20] if it is desired to consider the effect of ρ on $R_{sp}(a)$. Predictions from Eqs. [3.20] and [3.30] are compared in Section 3.7.6.

For the general case in which the continuous phase exhibits a distribution of diffusion coefficients p_D that is either known or determined independently, R_{CP} can be calculated according to:

$$R_{CP} = \int_0^\infty p_D(D_{CP}) R_{bulk,CP}(D_{CP}) dD_{CP} \Big/ \int_0^\infty p_D(D_{CP}) dD_{CP} \,. \qquad [3.34]$$

For diluted emulsions ($\phi_{DP} << 1$), it can be assumed that the spins diffuse freely, whence $R_{bulk,CP}$ is given by Eq. [3.19]. As the volume fraction of the drop phase increases, droplets restrict the diffusion paths of the spins in the continuous phase [72]. This effect is commonly accounted for by defining an obstruction factor ζ as the ratio between the measured (effective) self-diffusion coefficient $D_{CP,eff}$ and its actual value D_{CP}. For diffusion restricted by spheres of uniform size, Jönsson et al. [73] showed that:

$$\zeta = \frac{D_{CP,eff}}{D_{CP}} = \frac{1}{1 + \frac{1}{2}\phi_{DP}} \,. \qquad [3.35]$$

This expression holds independently of the spatial arrangement of the spheres up to $\phi_{DP} \sim 0.30$ [74, 75]. ζ has been computed in simulations of self-diffusion in a fcc lattice of spheres [75]. We have correlated such results with the following empirical equation:

$$\zeta = \frac{1}{1+\frac{1}{2}\phi_{DP}+\frac{1}{4}\left(\phi_{DP}/\phi_{MAX,fcc}\right)^{9}};\ \phi_{DP} < \phi_{MAX,fcc} \qquad [3.36]$$

where $\phi_{MAX,\,fcc} = \sqrt{2}\pi/6 \cong 0.7405$ is the volume fraction at which droplets reach close-packing. Analogous expressions to Eq. [3.36] can be derived for sc and bcc lattices from the data reported in Refs. [74, 75].

The effect of restricted diffusion on R_{CP} is taken into account by replacing $p_D(D)$ with $p_{\zeta D}(D)$ in Eq. [3.34], and computing ζ from Eq. [3.36]. This approach is exact for regularly arranged, monodisperse drops, but approximate for irregularly arranged, polydisperse ones. In any case, Jönsson et al. [73] showed that the minimum value of ζ is obtained for diffusion amidst regularly arranged spheres, and that it increases only moderately for random arrangements. According to their model, polydispersity would not affect ζ in systems with moderate concentration of droplets ($\phi_{DP} \sim< 0.20$).

3.3.4. Range of drop sizes that can be resolved via PGSE

The maximum drop size that can be determined via PGSE is related to the one-dimension root-mean-square displacement of spins undergoing free (Fickian) self-diffusion in isotropic, isothermal media during the diffusion time Δ:

$$d_{MAX} \approx \sqrt{2}\left\langle x^2\right\rangle^{1/2} = \sqrt{2}\left\{\int_{-\infty}^{\infty}(x-x_0)^2\,\frac{\exp\left[-(x-x_0)^2/4D_{DP}t\right]}{\sqrt{4\pi D_{DP}t}}dx\right|_{t=\Delta}\Bigg\}^{1/2} = 2\sqrt{D_{DP}\Delta}\,. \qquad [3.37]$$

Most of the molecules confined in a droplet with diameter much larger than d_{MAX} would not "feel" any restriction in their diffusion path due to the presence of the water/oil interface. For this reason, such drop would not be sized accurately. This expression for d_{MAX} is also obtained by requiring the characteristic diffusion time in the drops with size d_{MAX} to be comparable to Δ ($t_{D,MAX} = a_{MAX}^2 / D_{DP} \approx \Delta$). The factor $\sqrt{2}$ has been included in Eq. [3.37] to assure consistency between these two approaches.

Eq. [3.37] suggests that d_{MAX} can be increased at will with Δ. However, the diffusion time must be adjusted keeping in mind that $\Delta < (T_{2,bulk})_{DP}$. Otherwise, the data will be affected by natural (bulk) and surface relaxation of the magnetization, and therefore by a reduction in the signal-to-noise ratio.

Low self-diffusivities render small values for d_{MAX}. In addition, low-mobility molecules usually exhibit short relaxation times [27] and therefore short values of Δ must be chosen in such cases. In general, it is not possible to determine droplet sizes via PGSE for drop phases exhibiting self-diffusion coefficients below 10^{-12} m^2/s [12].

An expression for the minimum drop size d_{MIN} that are measurable from PGSE data can be obtained from Eq. [3.23]:

$$d_{MIN} = \left(175\lambda \frac{D_{DP}}{\gamma^2 g^2 \delta_{MAX}} \right)^{1/4},$$

where $\lambda = 1 - R_{sp}(a = d_{MIN}/2, \delta = \delta_{MAX})$ and δ_{MAX} is the maximum duration that is chosen for the magnetic field gradient pulse. In all cases δ must be smaller that Δ. Otherwise, the first pulsed gradient would overlap with the 180° rf pulse (see Figure 3.2). In order to avoid such problem we suggest choosing $\delta_{MAX} = \Delta/3$ and $\tau = \Delta$ for

experiments performed varying δ at constant Δ and g. With this definition of δ_{MAX}, the expression given above becomes:

$$d_{MIN} = \left(525\lambda \frac{D_{DP}}{\gamma^2 g^2 \Delta} \right)^{1/4} . \qquad [3.38]$$

It was shown via Eq. [3.23] that $R_{sp}(a \rightarrow 0) \rightarrow 1$. Therefore, the reduction in the attenuation ratio λ when $a = d_{MIN}/2$ is small ($0 < \lambda << 1$), yet it must be measurable in order to resolve for d_{MIN}. Plausible values for λ are $0.05 \geq \lambda \geq 0.01$.

The usefulness of Eqs. [3.37]-[3.38] can be illustrated with typical conditions for a PGSE test on W/O emulsions, for which $D_{DP} = 2.30 \times 10^{-9}$ m^2/s (T = 25 °C); Δ = 200 ms; g = 0.25 T/m. For this example, the attenuation ratio is sensitive to drop sizes between d_{MIN} = 1 μm (λ = 0.01) and d_{MAX} = 42 μm, according to Eqs. [3.38] and [3.37], respectively. These calculations agree with the assessment of Balinov et al. [12], who pointed out that the PGSE method allows resolution of droplet sizes between 1 and 50 μm when $g \sim 1$ T/m. It is worth emphasizing that Eqs. [3.37]-[3.38] can be used to calculate d_{MIN} and d_{MAX} for arbitrary sets of PGSE parameters.

3.4. COMBINED CPMG-PGSE METHOD

3.4.1. Advantages and limitations of the CPMG experiment

The main advantage of the CPMG method is that thousands of spin-echoes are acquired in one test. From the large dataset that is obtained in this experiment, drop size distributions with arbitrary shape can be determined. The calculations reported above suggest that the method can resolve drop sizes ranging from ~ 0.01 to ~ 300 microns. In

addition, the water/oil composition of the emulsion can be calculated. A CPMG test typically takes about five minutes to be completed, as reported later. The short duration of the test makes it suitable to keep track of the stability of the emulsion and of rapid changes in the drop size distribution. Finally, the CPMG test is independent of the self-diffusivity of the phases because it is performed in absence of magnetic field gradients. Therefore, the T_2 distribution of the emulsion can be fully interpreted in terms of bulk and surface relaxation. On the other hand, the surface relaxivity cannot be determined from CPMG. An independent measurement of the surface-to-volume ratio is required to evaluate ρ.

3.4.2. Advantages and limitations of the PGSE experiment

In the PGSE method, the contributions of the water and oil phases can be resolved independently in the frequency domain with a high-field spectrometer if the FT-PGSE technique is applied, or in the time domain with the theoretical framework introduced in this paper. Also, in the fast diffusion regime the attenuation ratio is not affected by surface relaxation and therefore the PGSE data can be interpreted solely in terms of self-diffusivity and bulk relaxation. As a result, an independent measurement of the drop size distribution, and therefore of the surface-to-volume ratio of the drop phase in the emulsion, can be performed with this procedure.

Nevertheless, the PGSE method is very slow: acquiring a dataset comparable to that of a single CPMG test would take several days. For this reason, in a typical PGSE experiment only a few (~10 - 20) attenuation ratios are measured in 5 – 20 min. Due to lack of data, the drop size distribution is resolved assuming in advance a p.d.f. to

describe it. Finally, the range of drop sizes that can be determine precisely with this method is narrow (~1 - 50 μm).

3.4.3. Combining experimental data from both methods

The shortcomings of the two methods can be overcome, and their advantages integrated, by combining data from both experiments. In the proposed approach, a CPMG test followed by a typical PGSE experiment as described above are performed on the same emulsion sample and the data are processed as follows:

(a) The T_2 distribution of the emulsion is determined from the transverse relaxation (CPMG) dataset using Eq. [3.1] and a suitable regularization method [17]. The water/oil composition is calculated from Eq. [3.17]. The parameter κ is determined using Eq. [3.33].

(b) An initial value is assumed for the surface relaxivity.

(c) The volume-weighted drop size distribution is determined from the T_2 distribution of the drop phase via Eq. [3.4]. The corresponding cumulative distribution $P_{V,EXP}(a_i)$ is calculated as:

$$P_{V,EXP}(a_i) = \sum_{j=1}^{i} (f_j)_{DP} \Big/ \sum_{j=1}^{m} (f_j)_{DP} \quad / \quad 1 \le i \le m \,. \qquad [3.39]$$

(d) The cumulative distribution of sizes is fitted (least-square analysis) with a modified form of the bimodal Weibull cumulative probability distribution function [76],

$$P_V(a) = \begin{cases} 0 & a < a_0 \\ \omega\left\{1 - \exp\left[-\left(\dfrac{u}{\sigma_1}\right)^{m_1}\right]\right\} + (1-\omega)\left\{1 - \exp\left[-\left(\dfrac{u}{\sigma_2}\right)^{m_2}\right]\right\}; \quad u = \ln\dfrac{a}{a_0}; & a > a_0 \end{cases} \qquad [3.40]$$

where $0 \leq \omega \leq 1$; m_1, $m_2 > 0$; σ_1, $\sigma_2 > 0$ are adjustable parameters and a_0 is the smallest drop size a_i calculated from the T_2 distribution of the drop phase such that $f_i = 0$ and $f_{i+1} > 0$. The set of parameters that are determined with this procedure defines the volume-based drop size distribution $p_V(a)$, which is given by:

$$p_V(a) = \frac{dP_V(a)}{da} = \begin{cases} 0 & a < a_0 \\ \frac{1}{a}\left\{\frac{\omega m_1}{\sigma_1^{m_1}} u^{m_1-1} \exp\left[-\left(u/\sigma_1\right)^{m_1}\right] + \frac{(1-\omega)m_2}{\sigma_2^{m_2}} u^{m_2-1} \exp\left[-\left(u/\sigma_2\right)^{m_2}\right]\right\} & a > a_0 \end{cases} \quad [3.41]$$

This p.d.f. has been chosen because it can fit unimodal and bimodal, symmetric, left-skewed and right-skewed distributions. However, if the experimental drop size distribution is unimodal and log-symmetric, the fit can be performed with the cumulative form of the lognormal distribution:

$$P_V(a) = \frac{1}{2}\left[1 + erf\left(\frac{\ln(2a) - \ln(d_{gV})}{\sqrt{2}\sigma}\right)\right] \quad [3.42]$$

where $erf(z) = \frac{2}{\sqrt{\pi}} \int_0^z e^{-t^2} dt$ is the error function.

(e) To calculate the attenuation ratios of the drop phase R_{DP}, the distribution $p_V(a)$ is substituted into Eq. [3.24] along with a suitable expression for $R_{sp}(a)$ (Eq. [3.20]). The same set of parameter δ, Δ and g chosen for the PGSE experiment must be used in the calculations. R_{CP} is calculated using Eq. [3.34]. R_{EMUL} is calculated from Eq. [3.32].

(f) The value of ρ is adjusted in successive iterations, and the procedure repeated until:

$$\min\left\{\chi^2(\rho)\right\} = \min\left\{\sum_{j=1}^{I}\left[\left(R_{EMUL,EXP}\right)_j - \left(R_{EMUL}\right)_j\right]^2\right\} \qquad [3.43]$$

is attained. $R_{EMUL,EXP}$ stands for the set of I experimental R acquired in the PGSE test.

3.4.4. Limitations of the combined CPMG-PGSE method

The CPMG-PGSE method has the limitations that are inherent to the PGSE and CPMG experiments. The most important of those is the fact that the characterization of oil-in-water emulsions is feasible in a limited number of cases. In practice, oils with self-diffusion coefficients above 10^{-12} m^2/s are required for sizing O/W emulsions via PGSE [12]. Also, the characteristic bulk relaxation time of the oil phase has to be unique and long enough so the contribution of surface relaxation to the overall decay in magnetization becomes significant.

Finally, a single T_2 value should be obtained for pure fluids like water when performing a CPMG test. In practice, the regularization method that is used to carry on the multi-exponential fit results in a finite distribution of T_2 values around $T_{2,bulk}$. This is a shortcoming of the technique, particularly for the characterization of emulsion with very narrow distribution of drop sizes. In such cases, the apparent width of the distribution could be an artifact of the T_2 measurement. This issue is detected easily by the impossibility to reach a satisfactory fit of the PGSE data with the shape of the distribution that is obtained from the CPMG experiment. In such cases, a measurement of the surface relaxivity is still feasible. The recommended procedure is to characterize the drop size distribution via the classic PGSE method (Section 3.3) or with an alternative procedure. Thereafter, the Sauter mean diameter d_{AV} is calculated as indicated in Table 1.1. An estimation of the surface relaxivity is then feasible from Eq. [3.4] as follows:

$$\rho = \frac{d_{AV}}{6}\left(\frac{1}{T_{2,LM}} - \frac{1}{T_{2,Bulk}}\right) \qquad [3.44]$$

Here, $T_{2,LM}$, the logarithmic mean relaxation time for the water peak in the T_2 distribution, is calculated as follows:

$$T_{2,LM} = \exp\left[\sum\left(f_i \ln T_{2,i}\right)_{DP} / \sum\left(f_i\right)_{DPr}\right] \qquad [3.45]$$

3.5. COMPUTATIONAL PROCEDURES

The T_2 distributions were calculated from CPMG relaxation data with codes developed by Huang [77] in Matlab (The MathWorks, Inc.) and FORTRAN. The calculation of κ, and the least-square analysis referred to above were performed with a Matlab program (Appendix D). Excel spreadsheets (Microsoft) were also developed to verify numerical results.

The multidimensional downhill simplex method was chosen to perform least-square minimization in steps (d) and (f) of Section 3.4.3. Code published in the text of Press et al. [78] was adapted for this task. The following arbitrary definitions were made for the determination of the parameters of the Weibull distribution:

$$m_1 = \Lambda_1^2;\ \ m_2 = \Lambda_2^2;\ \ \sigma_1 = \Lambda_3^2;\ \ \sigma_2 = \Lambda_4^2; \omega = \left[1 + \exp\left(-\Lambda_5\right)\right]^{-1} \qquad [3.46]$$

and the minimization of the error was performed adjusting the values of Λ_1 through Λ_5. The definitions given in Eq. [3.46] make the fitting parameters unbounded ($-\infty < \{\Lambda_1, \Lambda_2, \Lambda_3, \Lambda_4, \Lambda_5\} < \infty$) and avoid constrains for the reflections of the simplex.

The integrals depicted in Eq. [3.24] were solved numerically using 24-point Gauss integration [79]. This method requires modifying the integration range from (0, ∞) to (-1,1). For the Weibull distribution, this is achieved with negligible error via the following change of variables:

$$u_{WD} = 2\frac{\ln a - \ln a_0}{\ln a_N - \ln a_0} - 1 \qquad [3.47]$$

where a_N is the largest drop size of the experimental drop size distribution for which f_N = 0 and $f_{N-1} > 0$. If the lognormal distribution (Eq. [3.25]) is used instead to describe $p_V(a)$, integration is performed in terms of u_{LND},

$$u_{LND} = \frac{a^{1/\sigma} - \left(d_{gV}/2\right)^{1/\sigma}}{a^{1/\sigma} + \left(d_{gV}/2\right)^{1/\sigma}}. \qquad [3.48]$$

We have found that using Eq. [3.48] instead of the definition for u_{LND} suggested by Söderman et al. [47] [$u_{LND} = (a-d_{gV}/2)/(a+d_{gV}/2)$], reduces the error made with numerical integrations in the calculation of R_{DP}, particularly for narrow drop size distributions.

Forty sets of synthetic transverse relaxation and restricted diffusion data were generated at varying signal-to-noise ratio. These data were further used to evaluate the convergence characteristics of the code. Convergence to the expected solution was achieved in all cases. The difference between calculated and actual values of the parameters was in proportion to the noise level imposed to the signal. The time needed for convergence of the two annealed simplex minimizations was typically 15 seconds in a computer equipped with a 750 MHz processor.

3.6. EXPERIMENTAL

Synthetic water-in-crude-oil emulsions were made with distilled water dispersed in three crude oils, further referred to as MP6, SHU and PBB. The properties and composition of the oils are described in Appendix B. Indigenous materials present in the oils, such as asphaltenes and resins, sufficed to stabilize the emulsions.

The NMR measurements were performed using a MARAN II Spectrometer (2.2 MHz, Resonance Inc.). A thermocouple placed in the center of the samples after each test consistently reported 25.5 $\pm$ 0.5 °C. In the CPMG experiments, the echo spacing was 315 μs, the number of echoes was 12288. PGSE parameters are indicated for each test in Section 3.7. CPMG and PGSE experiments were performed on 10-ml samples of water and crude oils, placed in plastic cylindrical containers (1" ID) to determine hydrogen indexes and distribution of diffusion coefficients in the oils as discussed later.

Water/oil mixtures and emulsion samples of 20 ml were prepared as follows: the water and oil phases were poured carefully in the containers to prevent emulsification, and left in contact during 24 hours. When the formation of emulsions was sought, the phases were dispersed with a rectangular paddle (0.8" x 0.4") placed at the tip of a rod connected to a rotating device. Each sample was stirred at 750 rpm for 10 minutes. Some samples were ultrasonicated (Branson sonifier 450) to further reduce the drop sizes.

Drop size distributions of selected emulsions were also determined via microphotography. The procedure required pre-treating 0.4 x 4 x 40 mm glass cells via chemical reaction with octadecyltrichlorosilane (Sigma) to make their surfaces hydrophobic and thus avoid spreading of water droplets [80]. Since the emulsions were

not transparent, they were diluted with toluene to allow observation under the microscope. Digital pictures were taken with 20x and 40x objectives at different levels throughout the 0.4 mm gap with a Nikon Eclipse TE300 microscope connected to a Kodak Ekta Pro motion analyzer, model 1000 HRC, and images were further processed with a kit of macros for Adobe Photoshop. In all cases, 1063 droplets were randomly chosen and their sizes measured. This number assures statistical significance of 5% error with 99% confidence for the resulting drop size distribution [81].

3.7. Results and Discussion

3.7.1. Properties of the pure fluids

Figure 3.3 summarizes CPMG results for the T_2 distributions of the oils used in these experiments, along with their corresponding logarithmic mean. In all cases, broad distributions of relaxation times were obtained.

Low relaxation times are typically observed at high viscosity/temperature ratios and vice versa [82]. This explains why PBB, which had the highest shear viscosity (Appendix B) relaxed, in average, faster than MP6 and SHU. MP6 and SHU oils had nearly the same viscosity, yet the ratio of the T_{2LM} values (MP6:SHU) was 1.6:1. It is shown in Appendix B that SHU contained more aromatics and resins than MP6, and also a higher concentration of paramagnetic materials such as Fe and V. Aromatic compounds exhibit shorter T_2 values than alkanes with similar carbon number. Macromolecules with aromatic rings such as asphaltenes and resins also exhibit short relaxation times, in the order of 0.1 – 5 ms. Also, paramagnetic materials generate inhomogeneities in the

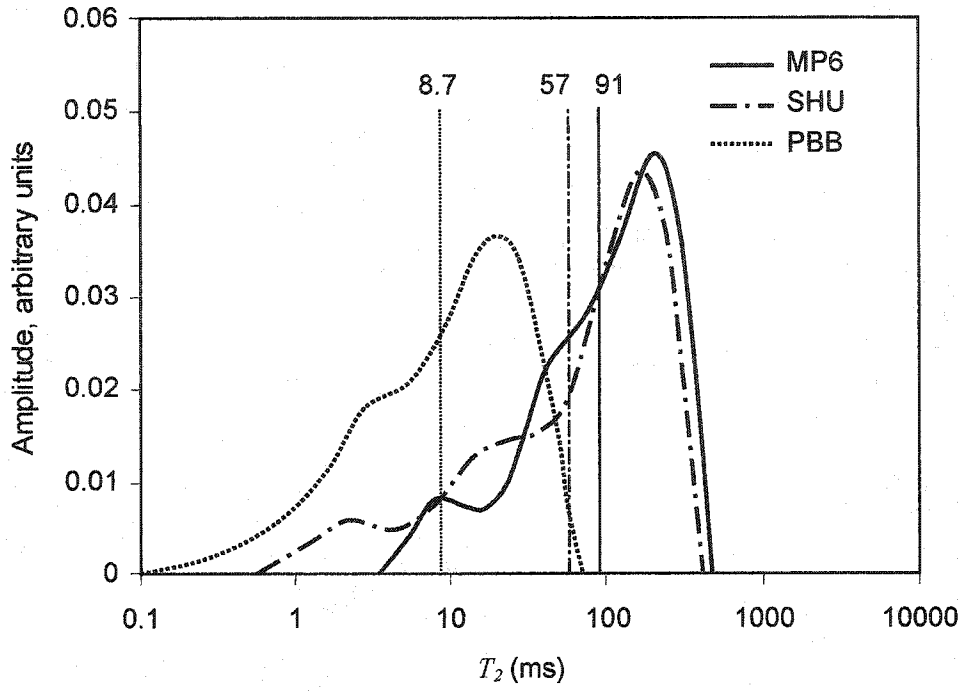


Figure 3.3. T_2 distributions of the oils used in this study.

steady magnetic field that lead to faster relaxation of the magnetization. These facts may explain the referred difference in T_2. Finally, a CPMG test was also performed on a sample of pure water. In this case, the decay of magnetization could be described with a single relaxation time of 2.8 s.

The apparent hydrogen indexes (*HI*) that are reported in Appendix B were determined from the same CPMG transverse magnetization data for the three oils reported above, and also from relaxation data for an equal-volume sample of water. In each case, the amplitude of the first ten spin-echoes was extrapolated to evaluate the initial magnetization *M(0)*, and *HI* was calculated for the oil k as follows:

$$HI_k = M(0)_k / M(0)_{water} \qquad [3.49]$$

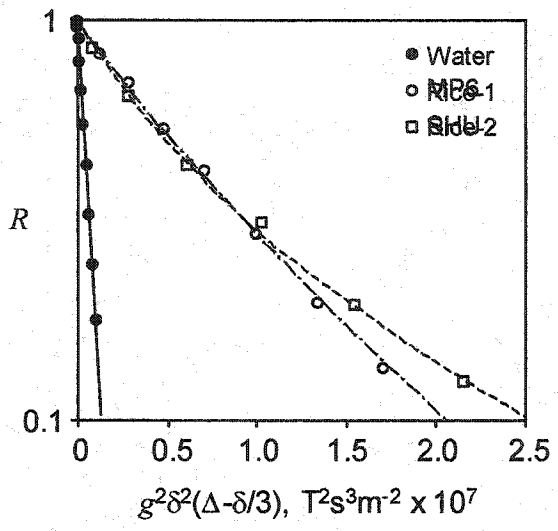


Figure 3.4. PGSE data for water and crude oils MP6 and SHU.

Linear and branched alkanes have higher H/C ratio than aromatic compounds, resins and asphaltenes [31]. For this reason, the HI for MP6 and SHU correlated well with their saturates:aromatics ratios (Appendix B). The relatively low HI of PBB is influenced by the high content of polynuclear aromatics (resins and asphaltenes) and also by the fast relaxation of these heavy components. In this case, a fraction of the proton magnetization is lost before the first echo is acquired. For these reasons, the apparent HI of heavy oils decreases with the API gravity [30].

Figure 3.4 shows results from PGSE measurements for MP6, SHU and water (g = 0.131, 0.161 and 0.025 T/m, respectively; Δ = 50 ms and δ = 0 - 20 ms in all cases), plotted as logarithm of the attenuation ratio R vs. $g^2\delta^2(\Delta-\delta/3)$. If Eq. [3.19] holds, such a plot should render a straight line. This is clearly the case for water, and nearly so for MP6. From the slope of the plot for water, a self-diffusion coefficient of 2.28 x 10^{-9} m^2/s

was determined. This value agrees well with D = 2.3 x 10^{-9} m^2/s reported earlier for water at 25 °C.

The non-linear trend of the data for SHU indicates that the oil exhibits a distribution of diffusion coefficients p_D. The lognormal p.d.f. has been used to correlate diffusion coefficients in crude oils [27], and we have adopted it to correlate the PGSE data shown in Figure 3.4:

$$p_D(D) = \frac{1}{D\sigma_D(2\pi)^{1/2}} \exp\left\{-\left[\frac{\ln(D)-\ln(D_{LM})}{2\sigma_D^2}\right]\right\} \qquad [3.50]$$

where D_{LM} and σ_D are the logarithmic-mean diffusion coefficient and the geometric standard deviation of the distribution, respectively. Appendix B summarizes the values of D_{LM} and σ_D that rendered the best fit of the data for MP6 and SHU (dashed lines in Figure 3.4). D_{LM} is very close for both oils (1.78 x 10^{-10} and 1.75 x 10^{-10} m^2/s, respectively), and an order of magnitude smaller than that of water. However, the width of the distribution is significantly larger for SHU.

The short relaxation times of PBB did not allow the characterization of this oil via PGSE. Instead, D_{LM} was estimated for this oil with the so-called constituent viscosity model [27], which correlates diffusivity, temperature and shear viscosity η as follows:

$$D_{LM} = \frac{bT}{\eta} \qquad [3.51]$$

In absence of experimental data, b = 5.05 x 10^{-15} $Pa.m^2.K^{-1}$ was suggested for crude oils. This expression is an empirical modification of the well-known Stokes-Einstein

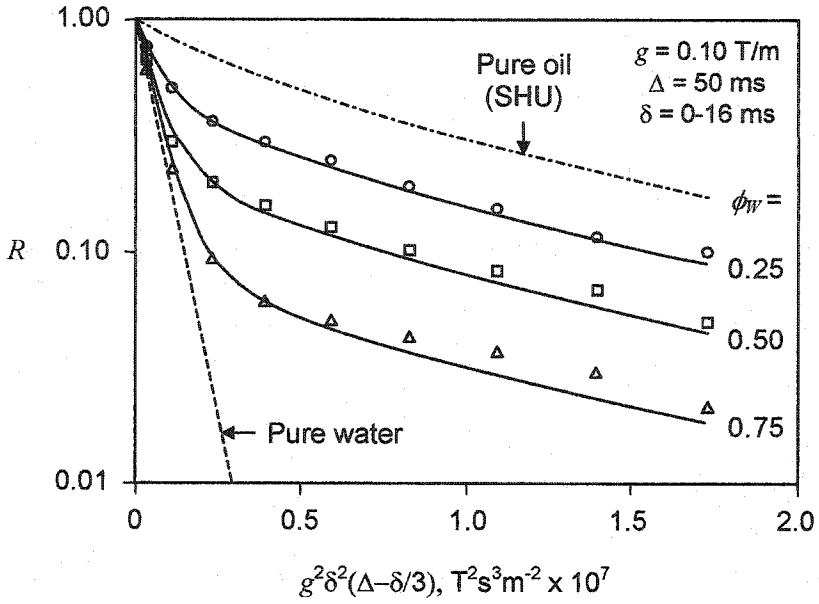


Figure 3.5. PGSE results for mixtures of water and SHU at several water-oil compositions. No parameters have been adjusted in the calculations and the comparison with the experimental data is absolute.

equation. From Eq. [3.51] and the data reported in Appendix B, $D_{LM} = 7.3 \times 10^{-12}$ m^2/s is estimated for PBB.

3.7.2. Validation of Eq. [3.32]

Figure 3.5 shows (symbols) PGSE measurements for samples of water and SHU contacted as bulk fluids, not emulsified. The parameters used in the PGSE tests are also reported in Figure 3.5. These parameters were chosen to assure only partial attenuation of the oil phase at the time the spin-echo was acquired. Three different compositions (ϕ_W = 0.25, 0.50 and 0.75) were tested. The dashed and dash-dot lines stand for calculations of the decay of the attenuation ratio that would be expected for the pure water and the crude oil using Eqs. [3.19] and [3.34], respectively, and the diffusion coefficients reported above. No correction for restricted diffusion in the oil phase was made for these calculations. Data indicate that as the water content was increased, the attenuation ratio

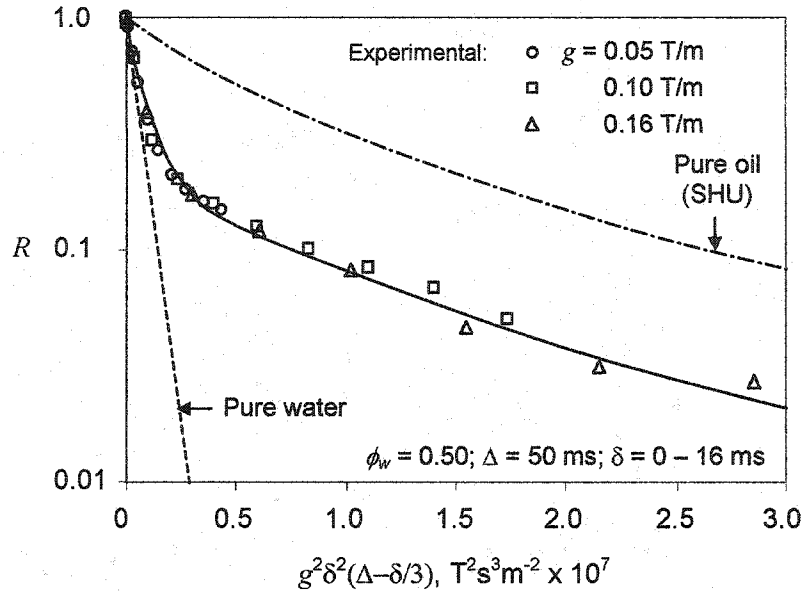


Figure 3.6. PGSE results for a mixture of water (50 vol.%) and SHU contacted as bulk fluid, not emulsified. Measurements were performed at different values of g.

departed from that of the oil phase (R_O) and approached that of water phase (R_W), as might be expected.

The solid lines in Figure 3.5 are predicted attenuation ratios for the mixture not emulsified, R_{MIX}, according to Eq. [3.32]:

$$R_{MIX} = (1-\kappa)R_W + \kappa R_O \,. \qquad [3.52]$$

Eq. [3.52] is obtained from Eq. [3.32] by choosing arbitrarily the oil phase as the continuous phase. It can be shown that the calculation of R_{MIX} for bulk fluids in contact in is independent of such choice. Clearly, this remark does not apply to emulsions.

The following values of 1-κ were calculated with Eq. [3.33] and the data for the pure fluids reported above: 0.522, 0.766 and 0.908 for ϕ_W = 0.25, 0.50 and 0.75, respectively. This is, 52.2%, 76.6% and 90.8% of R_{MIX} was given by the attenuation of the signal from

the aqueous phase in each case, respectively. Good agreement was found between experiments and theory in all cases.

Figure 3.6 shows results from three PGSE experiments on a mixture of SHU and water (ϕ_W = 0.50, bulk fluids in contact). In this case, the strength of the magnetic field gradient g was modified. It was found that the trends overlap when log(R) is plotted vs. $g^2\delta^2(\Delta-\delta/3)$. This fact is not surprising since magnetization decays at the bulk relaxation rate in both phases in proportion to g^2, according to Eqs. [3.19] and [3.34], and the factor g^2 has been included in the abscissas. Furthermore, the overlapping in the data indicates that the magnetic field gradient was calibrated correctly.

The dashed and dash-dot lines in Figure 3.6 are calculations for the attenuation ratio of pure water and pure oil using Eqs. [3.19] and [3.34], respectively. The solid lines are the predicted profiles for the water/oil mixture, which were calculated as above (Eq. [3.52]). The parameter κ is independent of g (κ = 1-0.766 = 0.234 in all cases) and so is the prediction of Eq. [3.52] when the data are plotted as log(R) vs. $g^2\delta^2(\Delta-\delta/3)$. It is seen in Figure 3.6 that the model correlated well the experimental data in all cases. Moreover, this figure also illustrates that a significant error would be made if the contribution of the magnetization of the oil phase to the attenuation ratio of the mixture is neglected, i.e., if R_{MIX} is said to depend only on R_W.

Figure 3.7 shows (symbols) results from PGSE experiments on mixtures of water with each of the oils used in this study at fixed composition (ϕ_W = 0.50). The calculated attenuation profile for pure water is also plotted (dashed line). This figure suggests that the attenuation ratio was dominated by the signal from the water phase as the characteristic relaxation time of the oil decreased. Less signal was collected from the oil phase in the spin-echo when the oil exhibited faster relaxation (i.e., shorter $T_{2,LM}$).

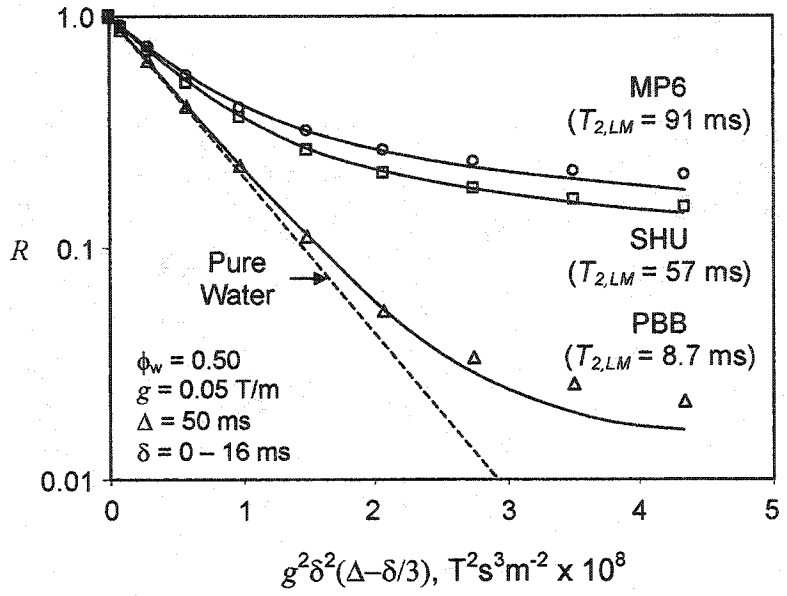


Figure 3.7. PGSE results for mixtures of water (50 vol.%) and MP6 (○), SHU (□) and PBB (Δ) contacted as bulk fluids, not emulsified.

The solid lines in Figure 3.7 stand for the predicted profiles for each of the systems using Eq. [3.52]. The calculated values of κ were 0.283, 0.234 and 0.014 for the MP6/water, SHU/water and PBB/water systems, respectively. The agreement between experiments and theory was satisfactory.

The experiments depicted in Figures 3.5 through 3.7 demonstrate that the weighted average for R_{MIX} that is obtained from Eq. [3.52] correctly predicts the trend for the attenuation ratio of water/oil mixtures, independently of the composition of the mixture, of the type of oil that is used and of the PGSE parameters chosen for the test. The model is based on fundamental concepts of NMR spectroscopy and does not require adjustable parameters.

Figure 3.8 shows (circles) experimental data for sample containing water (5 vol. % and 10 vol.%) and MP6 (95 vol.% and 90 vol.%, respectively) in contact as bulk fluids,

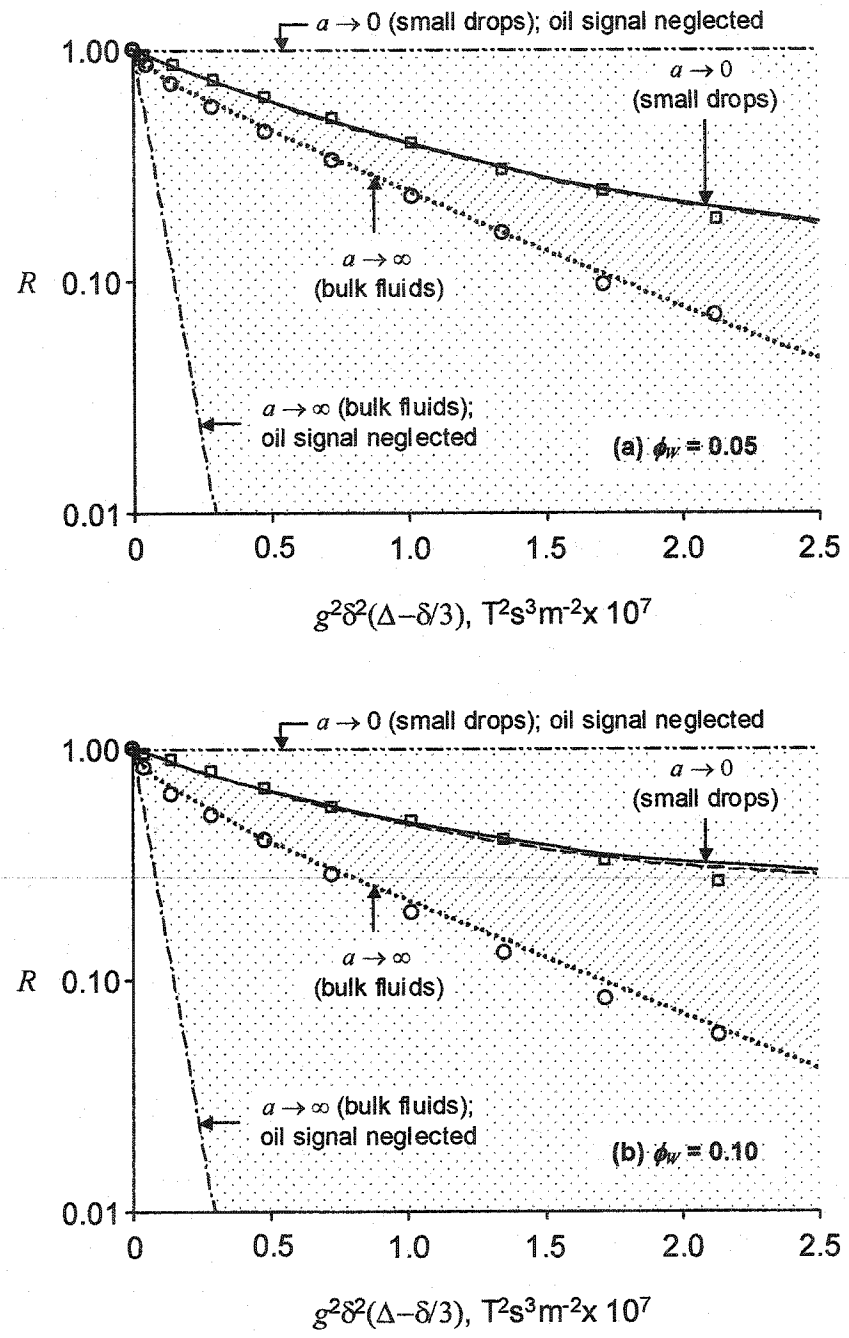


Figure 3.8. Effect of the transverse magnetization of the continuous phase on the PGSE response of mixtures of water and MP6, contacted as bulk fluids and emulsified. The features of the plot are explained in the text. (a) Mixtures with ϕ_W = 0.05; (b) mixtures with ϕ_W = 0.10.

and for W/O emulsions (squares) made from the same water/MP6 mixtures. Test conditions were g = 0.131 T/m, Δ = 50 ms and δ = 0-16 ms. The emulsions were sonicated until the drop sizes were below the resolution limit of the PGSE experiment, which is d_{MIN} ~ 3 μm, according to Eq. [3.38]. The mean drop size was followed via microphotography, and the final emulsions exhibited a narrow distribution of droplets with sizes close to the resolution limit of the 40x objective used in this study, i.e., 0.5 μm. The increase in R that is observed for the emulsions with respect to the corresponding mixture of bulk fluids is caused by restricted diffusion of water molecules, which is imposed by the size of the drops.

The dotted curves in Figure 3.8 stand for the predicted behavior for the samples before emulsification using Eq. [3.52]. The attenuation ratio for either phase was calculated as indicated in the former experiments. In these cases, κ = 0.862 and 0.755 were calculated from Eq. [3.33] for the systems with 5 vol.% and 10 vol.% water, respectively, which indicates that 86.2% and 75.5% of the attenuation ratio of the mixtures were given by the oil phase for each of these systems.

The predicted behavior for the attenuation ratios of the emulsions via Eq. [3.32] is also shown (continuous line). Since water is the drop phase, $R_{EMUL} = (1-\kappa)R_W + \kappa R_O$. The attenuation ratio R_W was not calculated from Eq. [3.19] (free diffusion), but from Eq. [3.23] because water molecules are confined in droplets with sizes below the resolution limit of the test. Therefore, if d = 0.5 μm as reported above, $R_W = 1 - 2 \times 10^{-4}\delta(s) \sim 1$. The attenuation ratios of the oil phase were calculated with Eqs. [3.34] and [3.50], using the parameters D_{LM} and σ_D given in Appendix B for MP6. Restricted diffusion in the oil phase was considered by correcting the logarithmic-mean diameter D_{LM} in Eq. [3.50]

with the obstruction factor ζ = 0.976 and 0.952 (Eq. [3.36]) for the systems with 5 vol.% and 10 vol.% water, respectively. Good agreement was found between experiments and calculations for these systems. These results show that Eq. [3.32] is valid for mixtures of bulk fluids and also for emulsions.

The attenuation profiles that would be obtained for the emulsions without considering the obstruction factor are also shown (dashed lines). The effect of this correction is very small due to the relatively low drop phase content. In any case, these calculations correctly indicate that restricted diffusion in the continuous phase would increase the attenuation ratio of the emulsion.

The dash-dot and dash-dot-dot lines in Figure 3.8 stand for the attenuation profiles that would be obtained for the same system before and after emulsification, respectively, if the contribution of the oil signal to the spin-echo amplitude is neglected. The areas of the plots between these two lines have been shaded in light tone to indicate the range of conditions in which the attenuation ratios for emulsions with any given drop size distribution could be found if the oil signal were indeed negligible, i.e., if Eq. [3.26] were correct. If Eq. [3.32] holds instead as experiments suggest, such conditions are restricted to the areas shaded in dark tone. Clearly, neglecting the signal from the oil phase would lead to significant error in the prediction of the attenuation profile for this system.

It is worth noting that the parameters of a PGSE experiment should be chosen in order to *minimize* the effect of the continuous phase on the spin-echo and therefore on the attenuation ratio of the emulsion, while maintaining a satisfactory signal-to-noise ratio. The idea is to broaden the range of conditions at which attenuation ratios can be

obtained (this is, to expand the extension of the dark-shaded area in Figure 3.8), so the uncertainty in the drop size distribution that is determined from the PGSE diminishes. Therefore, Eq. [3.32] can be used as a tool to predict limiting attenuation profiles and optimize the selection of parameters for PGSE tests.

3.7.3. The combined CPMG-PGSE method in practice

Figure 3.9 (a) shows the T_2 distribution of a sample of SHU (dotted line) and also of a mixture of water (30 vol.%) and SHU in contact, not emulsified (solid line). It is seen that the position of the oil peak is not affected by the presence of water. The water signal is shown as a narrow peak with logarithmic mean of 3.0 s.

Figure 3.9 (b) shows the same T_2 distribution of the water/oil mixture (dashed line) mentioned above, and also of the same sample right after dispersing the system to form a W/O emulsion (solid line). The most relevant feature of Figure 3.9(b) is that emulsification leads to a significant displacement of the water signal toward shorter relaxation times. This difference in relaxation times can be explained by an enhanced decay of transverse magnetization at the water-oil interfaces (surface relaxation), in connection with the increase of interfacial area that results from the formation of droplets.

Figure 3.9 (c) shows the T_2 distribution of the same emulsion 48 hours after emulsification (solid line). The T_2 distribution for the fresh emulsion (dash-dot line) is also included for comparison. In this case, the relaxation times of the water phase increase because, as drop sizes grow and phase separation takes place, the interfacial area diminishes and the contribution of surface relaxation to the decay of magnetization is reduced.

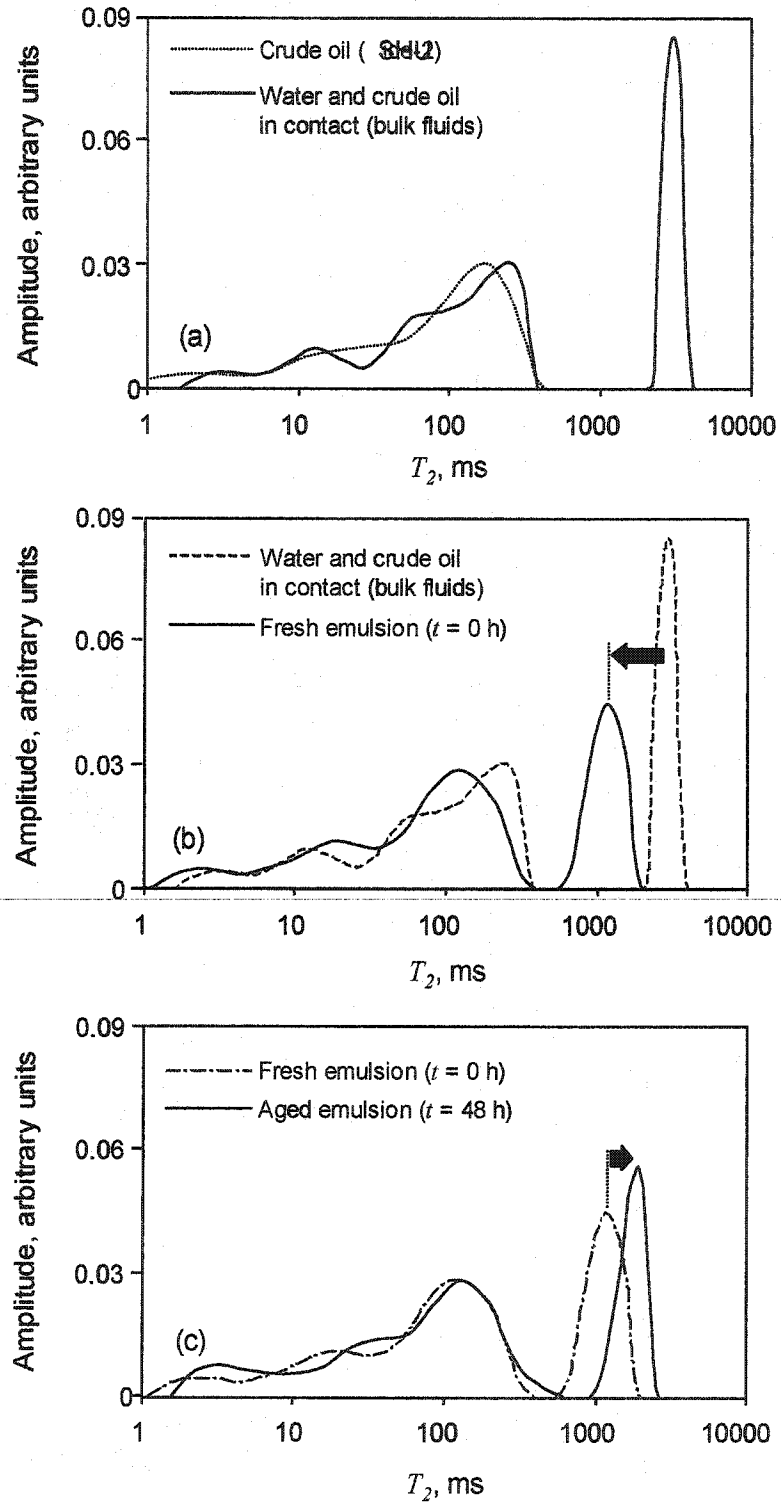


Figure 3.9. T_2 distribution of mixtures of water (30 vol.%) and SHU, contacted as bulk fluids and emulsified.

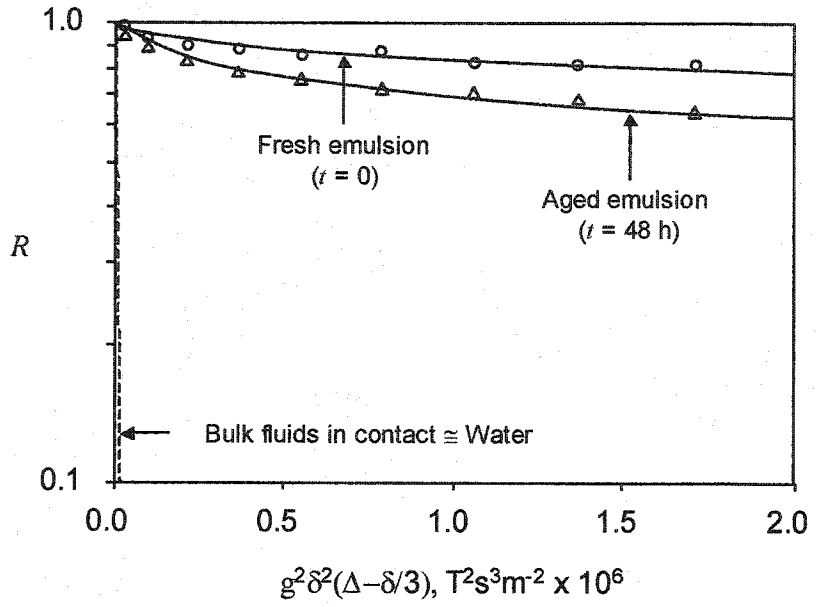


Figure 3.10. PGSE data for fresh (t = 0) and aged (t = 48 h) emulsions of water (30 vol.%) in crude oil SHU.

In the CPMG experiments that originated the results depicted in Figure 3.9, 16 stacks were accumulated and an average noise level of 0.45% was obtained. It took 3.7 minutes to complete each test.

Figure 3.10 shows results from PGSE experiments on the emulsions discussed above at t = 0 (circles) and t = 48 h (triangles). The parameters used for these tests were g = 0.10 T/m, Δ = 0.2 s, δ = 0 – 0.04 s. The profile that would be obtained for the mixture before emulsification (R_{MIX}) was calculated using Eq. [3.52] and is also plotted in Figure 3.10 (dashed line). In this case κ = 0.0025, i.e., the oil phase had relaxed almost completely at $t = 2\tau$, and the attenuation ratio of the mixture was nearly that of the water phase ($R_{MIX} \sim R_W$). Emulsification led to a significant increase in the attenuation ratio of the emulsion, when compared to R_{MIX}, due to restricted diffusion of water molecules within the drops. The reduction in the attenuation ratio from fresh to aged emulsion

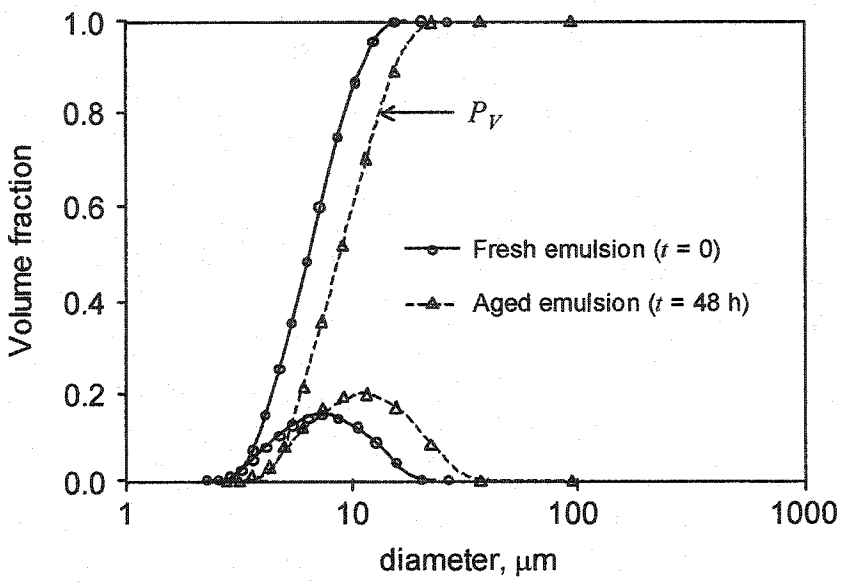


Figure 3.11. NMR results for the drop size distribution of fresh (t = 0) and aged (t = 48 h) emulsions of water (30 vol.%) in SHU.

indicates an enlargement of the average displacement in the spins, and suggests an increase in droplet sizes.

The drop size distributions shown in Figure 3.11 were calculated from the CPMG and PGSE data given in Figures 3.9 and 3.10, respectively, and following the combined procedure explained above. The solid lines in Figure 3.10 stand for the calculated profile for the attenuation ratios that are obtained with Eq. [3.32] and these distributions of sizes. It is seen in Figure 3.11 that the volume-weighted mean size of the emulsion increased from 6.9 μm to 8.8 μm. Also, the width of the distribution remained practically unchanged. This example illustrates that both CPMG and PGSE are suitable to study the stability of emulsions.

Once the drop size distribution is determined, it is important to verify that the fast diffusion approximation is valid. The following surface relaxivities (ρ) were determined

from the combined CPMG-PGSE procedure for these emulsions: 0.66 μm/s (t = 0) and 0.48 μm/s (t = 48 h). In addition, the largest drop diameters that were measured were 22 μm (t = 0) and 45 μm (t = 48 h), as shown in Figure 3.11. Therefore,

$$\left.\frac{\rho a_i}{D}\right|_{t=0} \leq 0.007; \qquad \left.\frac{\rho a_i}{D}\right|_{t=48h} \leq 0.010$$

These figures are well below the practical limit for fast diffusion established in Eq. [3.6]. For this reason, it can be said that the effect of surface relaxation on the attenuation profiles shown in Figure 3.10 was negligible.

Figure 3.12(a) compares the results from the NMR technique (circles) with measurements on the drops size distribution via microphotography (bars) for the fresh emulsion. Results are reported based on the volume of droplets. The volume-weighted mean size of the distribution determined via microphotography was 7.7 μm. This result is in good agreement with the NMR results (6.9 μm, see above). The agreement is also satisfactory for the width of the distribution. The solid and dashed lines in Figure 3.12(a) stand for the best fit of the CPMG data using the bimodal Weibull (Eqs. [3.40]-[3.41]) and lognormal (Eqs. [3.25], [3.42]) distributions, respectively. With the parameters that are determined from the fitting procedure (lognormal: d_{gV} = 6.9 μm; σ = 0.424; Weibull: ω = 0.8228; m_1 = 2.9381; m_2 = 6.2584; σ_1 = 1.0775; σ_2 = 1.5504; a_0 = 1.21 μm), the number-based drop size distribution $p_N(a)$ can be calculated according to:

$$p_N(a) = a^{-3} p_V(a) \Big/ \int_0^\infty a^{-3} p_V(a) da \,. \qquad [3.51]$$

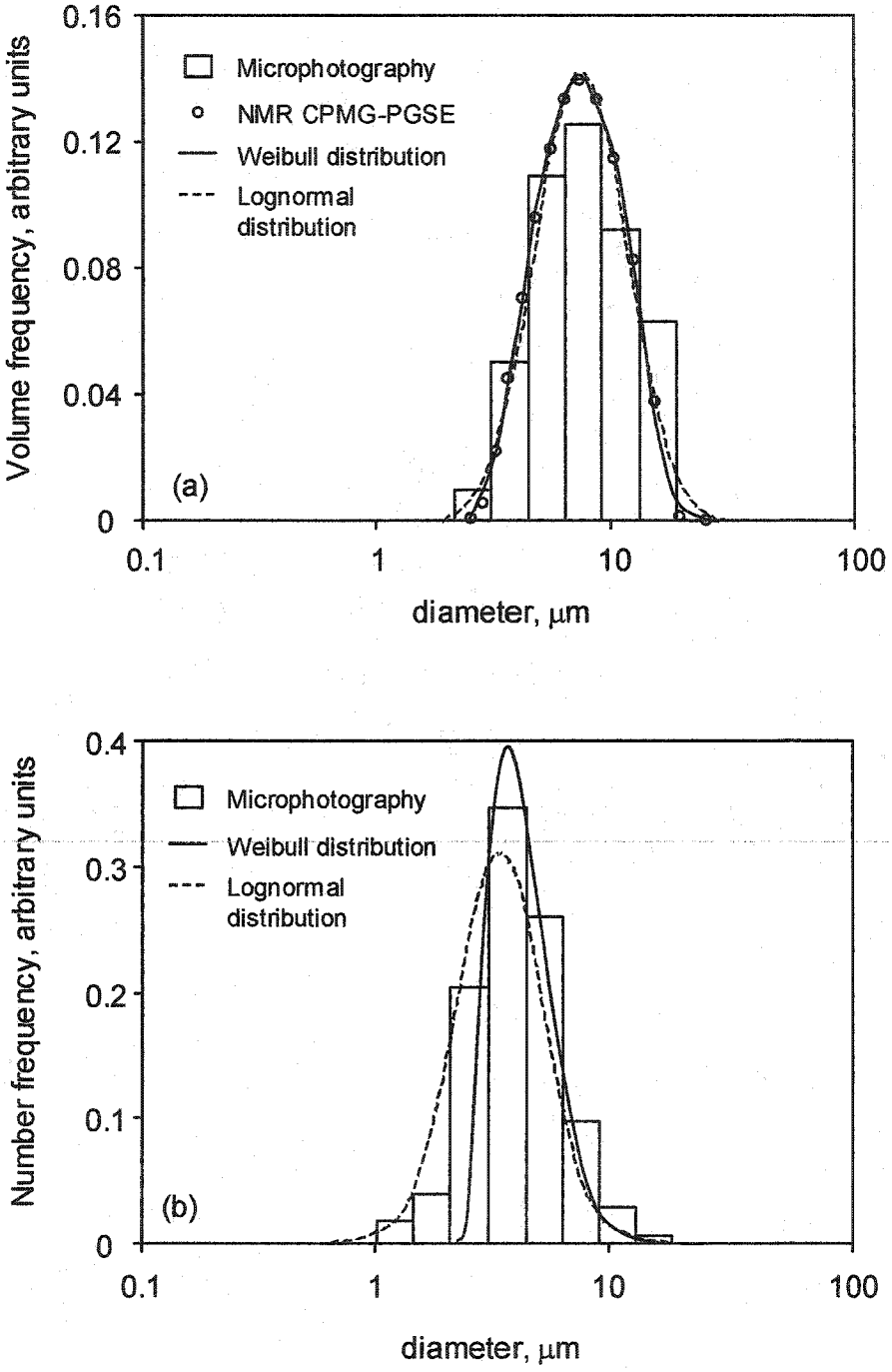


Figure 3.12. Drop size distribution of the fresh emulsion: Comparison of NMR and microphotography results. (a) Volume-weighted distribution; (b) number-based distribution.

Figure 3.12 (b) compares the number-based drop size distribution via microphotography (bars) with those calculated from the bimodal Weibull (solid line) and lognormal (dashed line) fits of the CPMG data. The medians of these distributions are 4.2, 4.5 and 4.0 μm, respectively. Good agreement is observed in both cases, although it is noted that the lognormal function exhibited slightly better correlation of the small drop sizes in this experiment.

The ability of the PGSE-CPMG method to account for drop size distributions not exhibiting a lognormal shape was tested by mixing equal volumes of two emulsions of water in SHU, both containing 30 vol. % water. Each emulsion was made following a different emulsification procedure. The first emulsion was stirred and the second was stirred and further ultrasonicated according to the protocol described above.

Figure 3.13 shows the T_2 distribution of the mixed emulsion (solid line). Two independent peaks were obtained, one corresponding to the oil signal between 0.4 ms and 316 ms, and another to the water phase between 383 ms and 2610 ms. The T_2 distributions of a sample of SHU (dotted line), and of a mixture of water (30 vol.%) and SHU contacted as bulk fluids (dashed line) are also included. Again, the shift in the water peak toward low relaxation times is caused by surface relaxation. In these experiments, 16 stacks were accumulated and an average noise level of 0.30% was obtained. It took 4.7 minutes to complete each test.

Figure 3.14 exhibits (triangles) the experimental decay of the attenuation ratio R that was obtained from the PGSE experiment on the mixed emulsion. The same parameters of the previous test were chosen. Also, $\kappa = 0.0025$ as before. The solid line corresponds to the best fit of the PGSE data that was obtained using Eq. [3.32] and the Weibull fit of

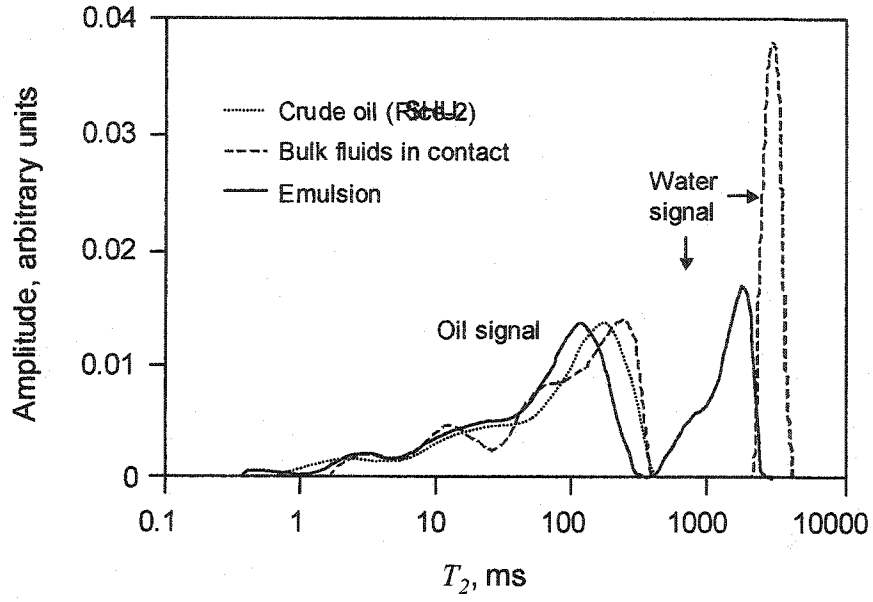


Figure 3.13. T_2 distribution of a blend of two emulsions of water (30 vol.%) in SHU.

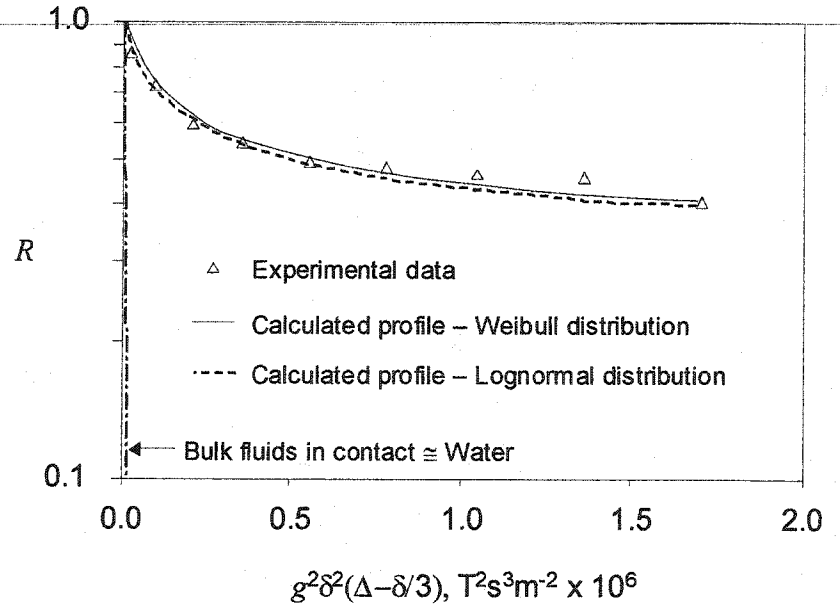


Figure 3.14. PGSE data for the blend of two emulsions of water (30 vol.%) in SHU.

the drop size distribution that was calculated from the T_2 distribution. The dashed line corresponds to the same fit, but using the lognormal p.d.f. for the correlation of the drop size distribution instead.

Figure 3.15(a) reports results for the volume-weighted drop size distribution, measured via microphotography (bars) and NMR-CPMG (circles) with ρ = 0.88 μm/s. The solid line stands for the best fit to the CPMG drop size distribution data using the bimodal Weibull p.d.f., and the dashed line is the best fit to the same data with the lognormal p.d.f. The following parameters were obtained in each case: lognormal, d_{gV} = 13.0 μm; σ = 0.756; Weibull, ω = 0.3838; m_1 = 2.0288; m_2 = 4.9783; σ_1 = 1.2047; σ_2 = 2.2063; a_0 = 1.15 μm. With these parameters, the number-based drop size distribution was calculated and plotted together with the microphotography data in Figure 3.15(b). From this figure it becomes clear that the usage of the lognormal p.d.f. can lead to significant error in the characterization of the drop size distribution for systems in which lognormality is not observed. The proposed form of the Weibull distribution gave a satisfactory estimation of $p_N(a)$.

It is worth noting that the shapes of the Weibull and lognormal plots in Figure 3.15 were significantly different, yet the predicted attenuation decays that are calculated from such plots and reported in Figure 3.14 were very similar. This feature indicates that it is not always adequate to resolve for the shape of the drop size distribution from a reduced PGSE dataset. In general, The T_2 distribution that is obtained from a CPMG test is more sensitive than the attenuation profile measured from a corresponding PGSE experiment to the shape of the drop size distribution. For this reason, we recommend estimating the shape of the drop size distribution from CPMG data, and not from PGSE measurements as suggested by Ambrosone et al. [54, 55].

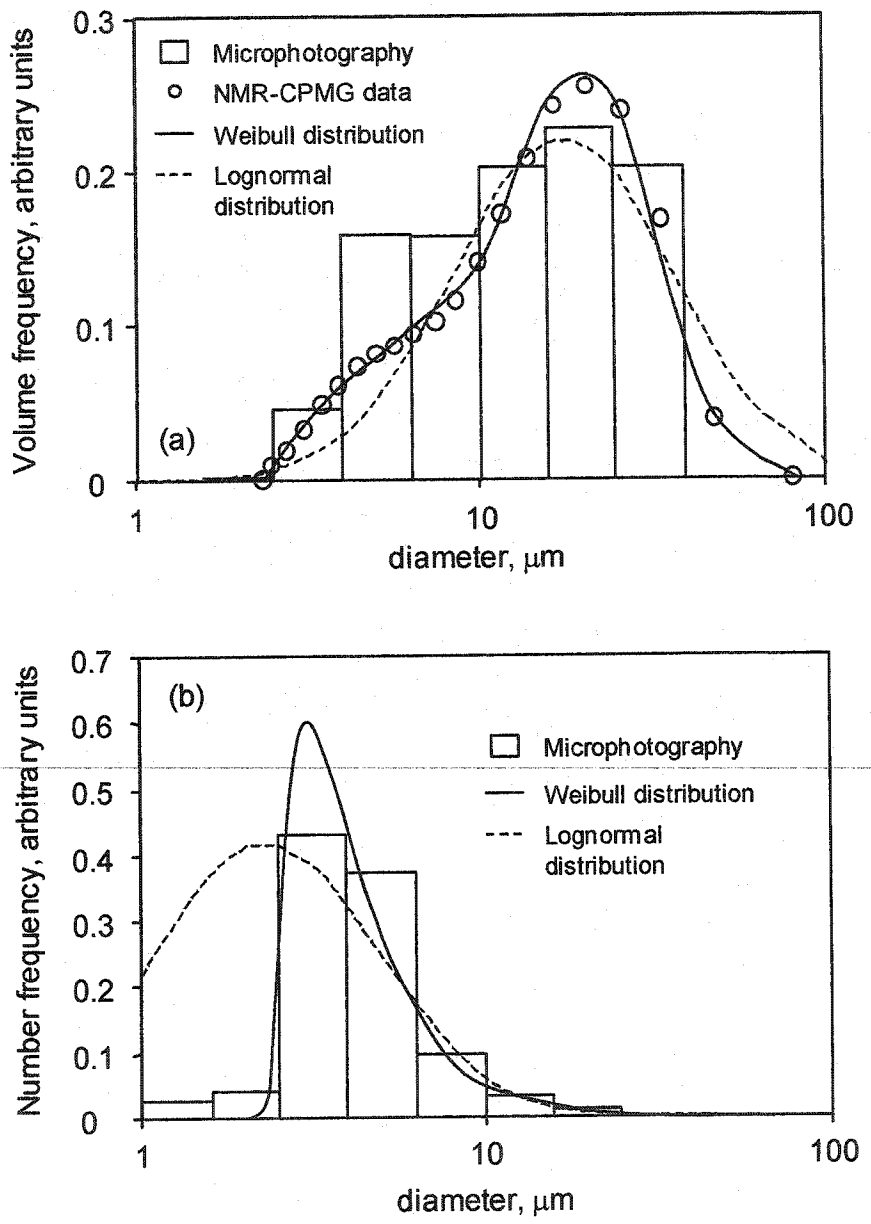


Figure 3.15. Drop size distribution of the blend of two emulsions of water (30 vol.%) in SHU: Comparison between NMR and microphotography results. (a) Volume-weighted distribution; (b) number-based distribution.

Figures 3.16-3.18 summarize an example of the application of the combined method to a bimodal emulsion of water (30 vol.%) in PBB. In this case, the emulsion was made with mechanical stirring, and ultrasonication was applied at a particular location of the emulsion to cause a local reduction in drop sizes. The procedure was repeated until a second peak in the water signal of the T_2 distribution appeared (Figure 3.16). In these experiments, 16 stacks were accumulated and an average noise level of 0.42% was obtained. It took 4.7 minutes to complete each test. A bimodal distribution of drop sizes was obtained (Figure 3.18), in correspondence with the bimodal T_2 distribution of the drop phase. The parameters of the PGSE test were g = 0.327 T/m, Δ = 0.02 s, δ = 0 – 0.008 s. In addition, κ = 0.0259 according to Eq. [3.33]. The fit of the CPMG drop size distribution with the Weibull p.d.f. rendered the following parameters: ω = 0.7612; m_1 = 9.9399; m_2 = 2.6876; σ_1 = 1.9042; σ_2 = 0.6057; a_0 = 0.832 μm. A lognormal fit of the CPMG data is inadequate in this case, since it would render a unimodal distribution. The surface relaxivity measured in this experiment was 2.18 μm/s.

3.7.4. Morphology of the emulsion

NMR allows screening if an emulsion is W/O or O/W in a straightforward manner. The experimental data shown in Figure 3.17 (triangles) were fitted (solid line) assuming that the emulsion is water-in-oil. If the opposite (O/W) configuration were considered instead, the profile shown as a dotted line would be obtained. In the latter case, the response of the O/W emulsion would be very close to that of bulk water, because water is now the continuous phase and the contribution of the oil phase to the attenuation ratio is very small as discussed above. Therefore, the notorious difference between attenuation profiles can be used to infer the morphology of the emulsion.

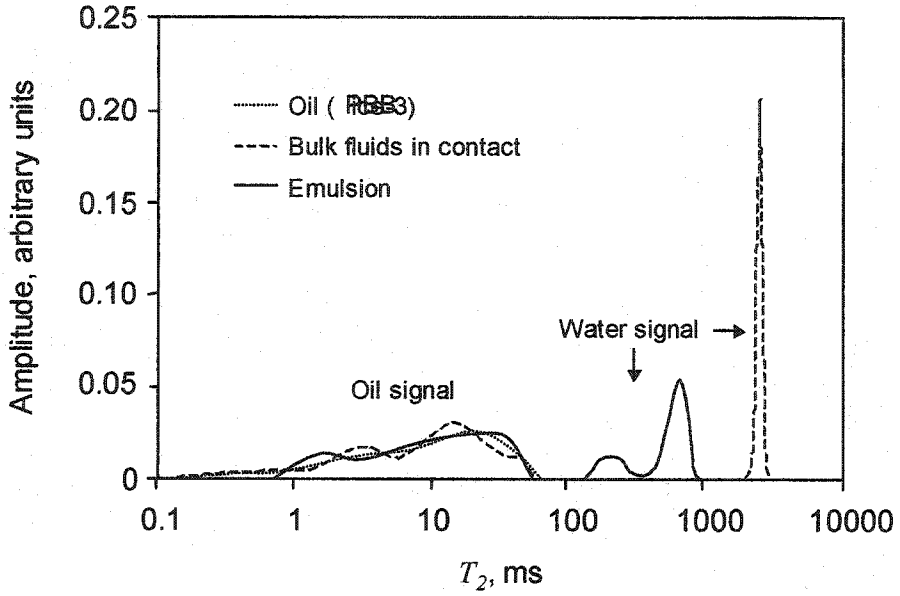


Figure 3.16. T_2 distribution of a bimodal emulsion of water (30 vol.%) in PBB.

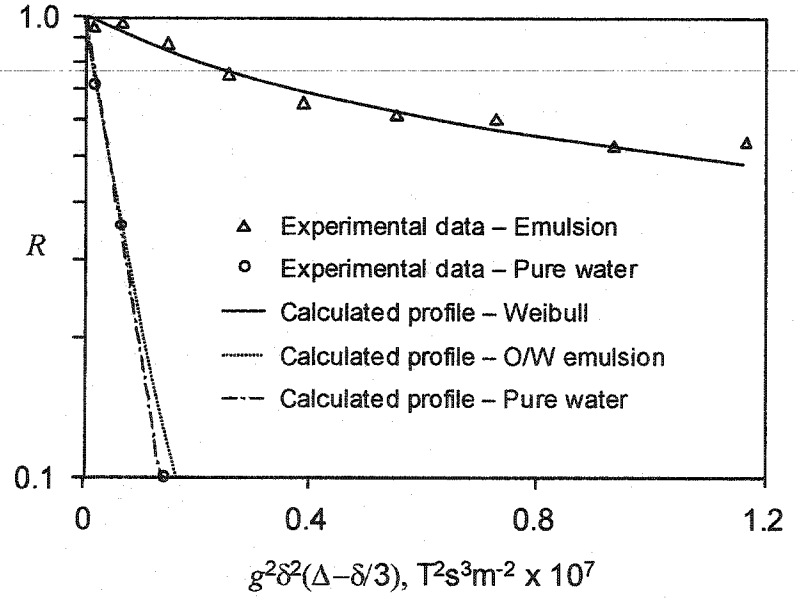


Figure 3.17. PGSE data of a bimodal emulsion of water (30 vol.%) in PBB.

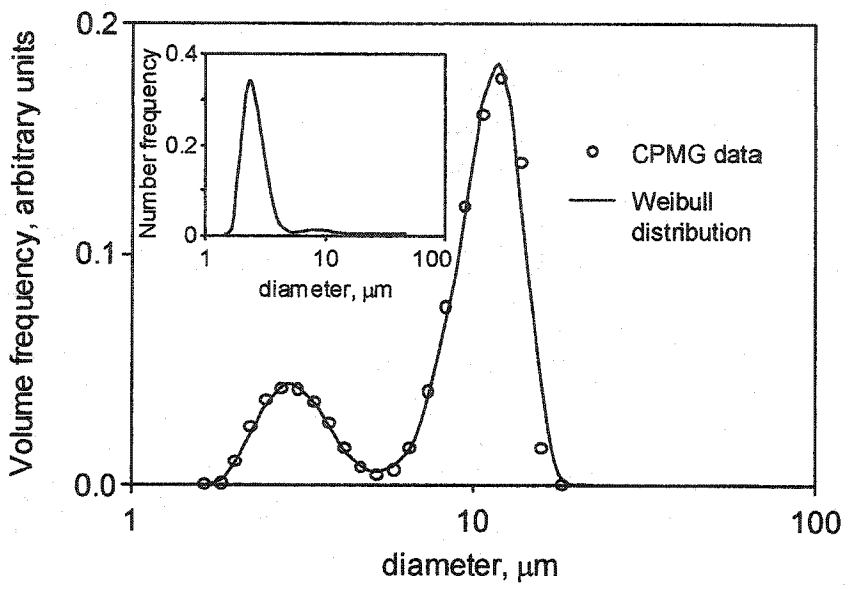


Figure 3.18. Volume-weighted and number-based drop size distribution of a bimodal

The basis for the discrimination of the emulsion type via attenuation ratio profiles is the contrast in self-diffusivities between the oil and water phases. For systems in which D_W and D_O are similar, the resolution of the morphology of the emulsion with this method is not clear-cut.

3.7.5. Oil/water composition

Thirty W/O emulsions were prepared using each of the crude oils at increasing water/oil ratios, and a CPMG experiment was performed on each sample. Figure 3.19 shows results for water/SHU emulsions. Figure 3.19(a) illustrates the T_2 distribution of six of these samples. The actual water content was in each case (a) 1.0 vol.%; (b) 4.8 vol.%; (c) 9.1 vol.%; (d) 18.4 vol.%; (e) 26.0 vol.%; (f) 32.2 vol.%. Data are shown normalized with respect to the oil signal. In these experiments, the water/oil mixtures were gently shaken by hand to minimize formation of very small drops and prevent

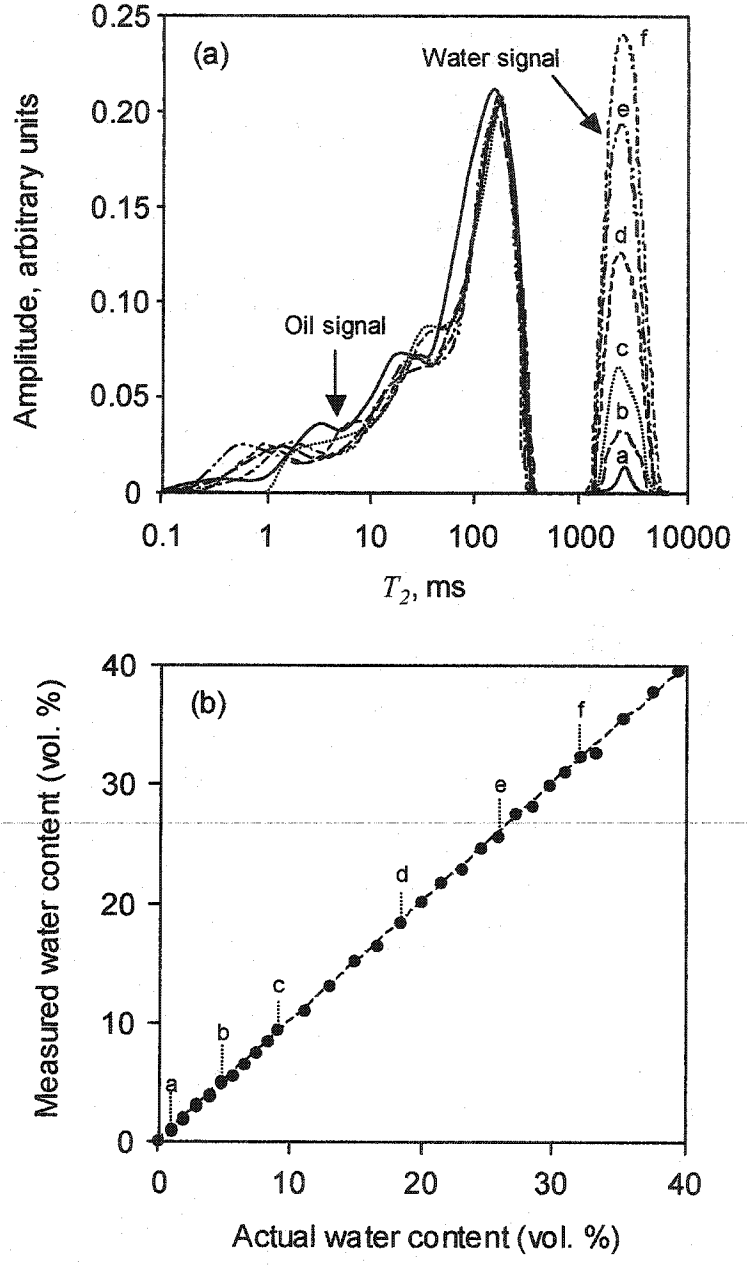


Figure 3.19. Determination of water composition via CPMG. (a) T_2 distribution of selected emulsions of water in SHU. Data were normalized with respect to the oil signal; (b) comparison between actual and NMR-measured water contents.

significant displacement of the T_2 signal of the water phase. This figure clearly illustrates how the signal from the water phase increases with the water content, as might be expected. Figure 3.19(b) compares the actual water content of these and other mixtures with the water content that is calculated with Eq. [3.17]. The calculated ϕ_W for the systems considered in Figure 3.19(a) were: (a) 0.9 vol.%; (b) 4.8 vol.%; (c) 9.3 vol. %; (d) 18.4 vol.%; (e) 25.7 vol.%; (f) 32.4 vol.%. Excellent agreement was found between actual and measured water contents, with errors averaging $\pm$ 0.2 vol.%.

Finally, calculations were performed with synthetic data to assess the accuracy of this method. Noise levels of 0 %, 0.1%, 1.0 %, 3.0 % and 5.0 % were tested, and ten simulated experiments were run on a hypothetical emulsion of water (35 vol.%) in PBB for each noise level. The maximum error in the water content calculated from the synthetic relaxation data was 0%, 0.2%, 1.0%, 1.5% and 4.0%, respectively. These simulations suggest that the uncertainty of the water content corresponds roughly to the noise level.

3.7.6. Surface relaxivities

Table 3.1 summarizes surface relaxivity measurements on emulsions of water in MP6, SHU and PBB, along with selected composition data from Appendix B. Data suggests that asphaltenes, resins and paramagnetic materials may play a role in the prevailing relaxation mechanism, since ρ increased monotonically with the content of asphaltenes and resins (A + R), and also Fe in the crude oil. Asphaltene-resin structures exhibit surface activity and might be expected to adsorb at the water-oil interfaces. Protons of these structures appear to exhibit short relaxation time constants [29] and

Table 3.1. Summary of surface relaxivities measured in this study.

Oil phase	ρ (μm/s)	d_{gV} (μm)	σ	A + R (wt.%)	Fe (ppm)
MP6	0.39	20.0	0.60		
	0.39	22.1	0.61		
	0.54	13.4	0.05		
	$\bar{\rho}$ = 0.46± 0.08			**10.50**	**2.4**
SHU	0.48	8.8	0.42		
	0.66	6.9	0.40		
	0.88	13.0	0.76		
	$\bar{\rho}$ = 0.68 ± 0.20			**16.62**	**7.9**
PBB	2.17	8.6	0.47		
	2.01	8.1	0.55		
	2.06	9.1	0.33		
	$\bar{\rho}$ = 2.09 ± 0.08			**48.7**	**51**

A + R = Content of asphaltenes and resins in topped oil (wt. %), as reported in Appendix B.

d_{gV}, σ = Volume-weighted mean size and geometric standard deviation of the drop size distribution from which ρ is calculated (best fit with lognormal distribution).

they may well contribute to increase surface relaxivity in the water-in-crude oil emulsion. Paramagnetic ions adsorbed at the interfaces in the water-in-crude oil emulsion would also increase ρ. On the other hand, no conclusive relationships between mean drop size, polydispersity and surface relaxivity was observed for the few systems reported in Table 3.1.

The surface relaxivities of these emulsions are low with respect to those found for sandstones (~ 5-20 μm/s) [31], but are still comparable to those of SiO_2 and SiC grain

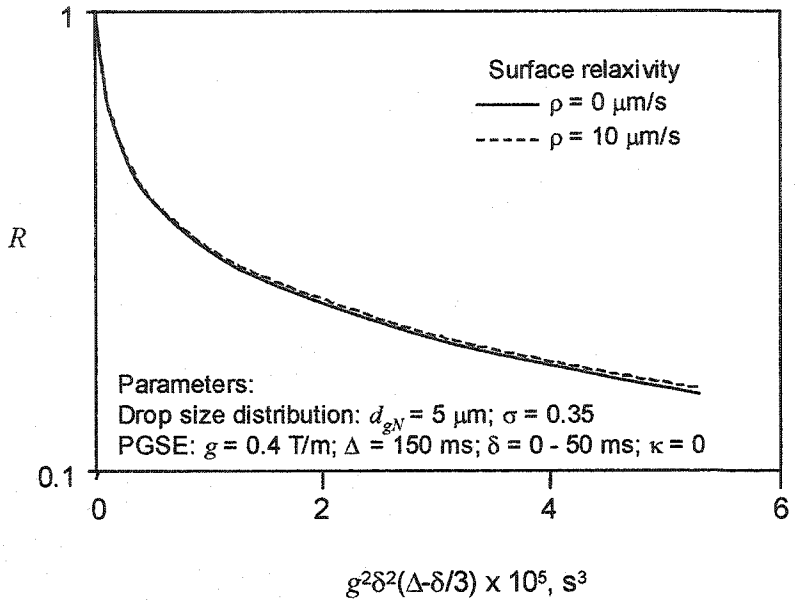


Figure 3.20. Simulated attenuation profiles at two different surface relaxations for a hypothetical W/O model emulsion at 25 °C.

packs and other natural rocks [83]. This result may have implications to NMR characterization of multiphase flow in porous media because the assumption that is often made of negligible surface relaxivity at the liquid-liquid interfaces with respect to that at the rock-fluid interfaces may not be adequate in all practical cases.

It is worth noting that the calculations of the attenuation ratios for the drop phase in the PGSE experiments were made using Eq. [3.20], i.e., neglecting the effect of surface relaxation on R. The calculations were also performed taking into account this effect with Eq. [3.30]. In all cases, the difference between R_{sp} and $R_{sp,\rho}$ was equal to or less than 0.002. Also, Figure 3.20 summarizes simulated attenuation profiles for a hypothetical W/O emulsion exhibiting lognormal distribution of drops sizes (d_{gN} = 5 μm, σ = 0.35) for surface relaxivities of 0 μm/s (solid line, Eq. [3.20]) and 10 μm/s (dashed line, Eq. [3.30]). These trends suggest that the effect of ρ on R for emulsions exhibiting surface

relaxations up to 2.1 μm/s (see Table 3.1) can be neglected. We conclude that it is appropriate to neglect the effect of ρ on the attenuation ratio when PGSE measurements are performed in the fast diffusion mode.

Callaghan [84] has developed a matrix formalism to interpret restricted diffusion data from pulsed sequences with gradient pulses of arbitrary shape, of which the finite-width gradient pulse PGSE is a particular case. Codd and Callaghan [85] have extended such formalism to account for surface relaxation at the walls of spheres. These authors noted that when ρ = 1-10 μm/s and the magnetization data is collected from water confined in pores of the order of 10 μm, the effect of surface relaxation on the attenuation ratio can be neglected. The small difference between calculations from Eqs. [3.20] and [3.30] that was reported above concurs with this assessment.

Finally, it is worth mentioning that the combined method is useful whenever the contribution of surface relaxation to the decay of transverse magnetization in CPMG tests is significant, as was shown for oilfield emulsions. We have performed preliminary tests on emulsions of water in lubricant oil free of paramagnetic impurities, and stabilized with nonionic surfactants (SPAN 80, 5 wt.%). For such systems, surface relaxivities in the order of 0.2 μm/s were measured. Not surprisingly, this figure is smaller than the surface relaxivities reported in Table 3.1. In any case, the applicability of the method for emulsions that may potentially exhibit low surface relaxivities, such as food emulsions, has not been fully ascertained.

3.8. REFERENCES

1. P. Walstra, "Emulsion stability", in Encyclopedia of emulsion technology, P. Becher, Editor, Volume 4. Marcel Dekker, New York, 1996, Chapter 1.
2. A. A. Peña and C.A. Miller, "Transient behavior of polydisperse emulsions undergoing mass transfer", *Ind. Eng. Chem. Res.*, **41** (2002) *6284-6296*
3. Y. Otsubo and R.K. Prud'homme, Effect of drop size distribution on the flow behavior of oil-in-water emulsions, *Rheol. Acta*, **33** (1994) *303-306*
4. M. Ramírez, J. Bullón, J. Andérez, I. Mira, and J.L. Salager, Drop size distribution and its effect on O/W emulsion viscosity, *J. Disp. Sci. Technol.*, **23** (2002) *309-321*
5. R. Pal, Effect of droplet size on the rheology of emulsions, *AIChE J.*, **42** (1996) *3181-3190*
6. D.J. McClements, Theoretical prediction of emulsion color, *Adv. Colloid Interface Sci.*, **97** (2002) *63-89*
7. D. Kilcast and S. Clegg, Sensory perception of creaminess and its relationship with food structure, *Food Qual. Pref.*, **13** (2002) *609-623*
8. S.M. van Ruth, G. de Vries, M. Geary, and P. Giannouli, Influence of composition and structure of oil-in-water emulsions on retention of aroma compounds, *J. Sci. Food Agricul.*, **82** (2002) *1028-1035*
9. M. Charles, V. Rosselin, L. Beck, F. Sauvageot, and D. Guichard, Flavor release from salad dressings: sensory and physicochemical approaches in relation with the structure, *J. Agricul. Food Chem.*, **48** (2000) *1810-1816*
10. C. Orr, Determination of particle size, in "Encyclopedia of Emulsion Technology", P. Becher, Editor, Vol. 3. Marcel Dekker, New York, 1988, Chapter 3.
11. J. Sjöblom, Editor, "Encyclopedic handbook of emulsion technology", Marcel Dekker, New York, 2001.
12. B. Balinov and O. Söderman, Emulsions - the NMR perspective, in "Encyclopedic Handbook of Emulsion Technology", J. Sjöblom, Editor, Marcel Dekker, New York, 2001, Chapter 12.
13. P. Callaghan, "Principles of nuclear magnetic resonance microscopy", Oxford University Press, New York, 1991.
14. H.Y. Carr and E.M. Purcell, Effects of diffusion on free precession in nuclear magnetic resonance experiments, *Phys. Rev.*, **94** (1954) *630-638*
15. S. Meiboom and D. Gill, Modified spin-echo method for measuring nuclear relaxation times, *Rev. Sci. Instrum.*, **29** (1959) *688-691*
16. E.O. Stejskal and J.E. Tanner, Spin diffusion measurements: spin echoes in the presence of a time-dependent field gradient, *J. Chem. Phys.*, **42** (1965) *288-292*
17. A.N. Tikhonov and V.Y. Arsenin, "Solution of ill-posed problems", Winston & Sons, Washignton D.C., 1977.
18. K.J. Dunn, G.A. LaTorraca, J.L. Warner, and D.J. Bergman, "On the calculation and interpretation of NMR relaxation times distribution", 69th Annual SPE Technical Conference and Exhibition, New Orleans, USA, 25-28 Sept., 1994, Paper SPE 28367
19. K.R. Brownstein and C.E. Tarr, Importance of classical diffusion in NMR studies of water in biological cells, *Phys. Rev. A*, **19** (1979) *2446-2453*

20. B. Clark and R.L. Kleinberg, Physics in oil exploration, *Physics Today*, April (2002) *48-53*

21. S. Davies, K.J. Packer, D.R. Roberts, and F.O. Zelaya, Pore-size distributions from NMR spin-lattice relaxation data, *Magn. Reson. Imaging*, **9** (1991) *681-685*

22. C.E. Morriss, J. MacInns, R. Freedman, J. Smaardyk, C. Straley, W.E. Kenyon, H.J. Vinegar, and P.N. Tutunjian, "Field test of an experimental pulsed nuclear magnetism tool", Transactions of the SPWLA 34th Annual Logging Symposium, 1993, Paper GGG

23. R.L. Kleinberg, Utility of NMR T_2 distributions, connection with capillary pressure, clay effect, and determination of the surface relaxivity parameter ρ_2, *Magn. Reson. Imag.*, **14** (1996) *761-767*

24. W.E. Kenyon, Nuclear magnetic resonance as a petrophysical measurement, *Nuc. Geophys.*, **6** (1992) *153-171*

25. I. Foley, S.A. Farooqui, and R.L. Kleinberg, Effect of paramagnetic ions on NMR relaxation of fluids at solid surfaces, *J. Magn. Reson.*, Ser. A, **123** (1996) *95-104*

26. A. Matteson, J.P. Tomanic, M.M. Herron, D.F. Allen, and W.E. Kenyon, NMR relaxation of clay/brine mixtures, *SPE Res. Eval. Eng.*, **3** (2000) *408-413*

27. R. Freedman, S.W. Lo, M. Flaum, G.J. Hirasaki, A. Matteson, and A. Sezginer, A new NMR method of fluid characterization in reservoir rocks: experimental confirmation and simulation results, *SPE J.*, December (2001) *452-464*

28. R. Mills, Self-Diffusion in Normal and Heavy Water in the Range 1-45°, *J. Phys. Chem.*, **77** (1973) *685-688*

29. G.A. LaTorraca, K.J. Dunn, P.R. Webber, and R.M. Carlson, Low-field NMR determinations of the properties of heavy oils and water-in-oil emulsions, *Magn. Reson. Imaging*, **16** (1998) *659-662*

30. D.E. Cannon, C. Cao Minh, and R.L. Kleinberg, "Quantitative NMR interpretation", SPE Annual Technical Conference and Exhibition, New Orleans, USA, 27-30 September, 1998, SPE Paper 49010

31. Q. Zhang, S.W. Lo, C.C. Huang, and G.J. Hirasaki, "Some exceptions to the default NMR rock and fluid properties", SPWLA 39th Annual Logging Symposium, Keystone, Colorado, May 26-29, 1998, Paper FF

32. R.L. Kleinberg and H.J. Vinegar, NMR properties of reservoir fluids, *Log Analyst*, **37** (1996) *20-32*

33. K. Allsopp, I. Wright, D. Lastockin, K. Mirotchnik, and A. Kantzas, Determination of oil and water compositions of oil/water emulsions using low field NMR relaxometry, *J. Can. Pet. Technol.*, **40** (2001) *58-61*

34. K.J. Dunn and B. Sun, *Personal communication*, 2002.

35. B.P. Hills, H.R. Tang, P. Manoj, and C. Destruel, NMR diffusometry of oil-in-water emulsions, *Magn. Reson. Imaging*, **19** (2001) *449-451*

36. W.D. Logan, J.P. Horkowitz, R. Laronga, and D.W. Cromwell, Practical application of NMR logging in carbonate reservoirs, SPE Res. Eval. Eng., **1** (1998) *438-448*

37. B. Robertson, Spin-echo decay of spins diffusing in a bounded region, *Phys. Rev.*, **151** (1966) *273-277*

38. C.H. Neuman, Spin echo of spins diffusing in a bounded medium, *J. Chem. Phys.*, **60** (1974) *4508-4511*

39. J.S. Murday and R.M. Cotts, Self-diffusion coefficient of liquid lithium, *J. Chem. Phys.*, **48** (1968) *4938-4945*

40. B. Balinov, B. Jönsson, P. Linse, and O. Söderman, The NMR self-diffusion method applied to restricted diffusion - simulation of echo attenuation from molecules in spheres and between planes, *J. Magn. Reson. Ser. A*, **104** (1993) *17-25*

41. K.J. Packer and C. Rees, Pulsed NMR studies of restricted diffusion. I. droplet size distribution in emulsions, *J. Colloid Interface Sci.*, **40** (1972) *206-218*

42. B. Epstein, Logaritmico-normal distribution in breakage of solids, *Ind. Eng. Chem.*, **40** (1948) *2289-2290*

43. J.L. Salager, M. Pérez-Sénchez, M. Ramírez-Gouveia, J.M. Andérez, and M.I. Briceño-Rivas, Stirring-formulation coupling in emulsions, Récent Progrès en Génie des Procédés, **11** (1997) *123-130*

44. B. Balinov, O. Söderman, and T. Warnheim, Determination of water droplet size in margarines and low-calorie spreads by nuclear-magnetic-resonance self-diffusion, *J. Am. Oil Chem. Soc.*, **71** (1994) *513-518*

45. B. Balinov, O. Urdahl, O. Söderman, and J. Sjöblom, Characterization of water-in-crude-oil emulsions by the NMR self-diffusion technique, *Colloid Surfaces A-Physicochem. Eng. Asp.*, **82** (1994) *173-181*

46. J.C. Van Den Enden, D. Waddington, H. Vanaalst, C.G. Vankralingen, and K.J. Packer, Rapid determination of water droplet size distributions by PFG- NMR, *J. Colloid Interface Sci.*, **140** (1990) *105-113*

47. O. Söderman, I. Lönnqvist, and B. Balinov, NMR self-diffusion studies of emulsion systems. Droplet sizes and microstructure of the continuous phase, in "Emulsions - A Fundamental and Practical Approach", J. Sjöblom, Editor, Kluwer Academic Publishers, The Netherlands, 1992, pp. 239-258.

48. I. Fourel, J.P. Guillement, and D. Le Botlan, Determination of water droplet size distributions by low-resolution PFG-NMR 1. "Liquid" emulsions, *J. Colloid Interface Sci.*, **164** (1994) *48-53*

49. I. Fourel, J.P. Guillement, and D. Le Botlan, Determination of water droplet size distributions by low-resolution PFG-NMR. 2. Solid emulsions, *J. Colloid Interface Sci.*, **169** (1995) *119-124*

50. H.Y. Lee, M.J. McCarthy, and S.R. Dungan, Experimental characterization of emulsion formation and coalescence by nuclear magnetic resonance restricted diffusion techniques, *J. Am. Oil Chem. Soc.*, **75** (1998) *463-475*

51. M.L. Johns and L.F. Gladden, Sizing of emulsion droplets under flow using flow-compensating NMR-PFG techniques, *J. Magn. Reson.*, **154** (2002) *142-145*

52. I. Lönnqvist, B. Håkansson, B. Balinov, and O. Söderman, NMR self-diffusion studies of the water and the oil components in a W/O/W emulsion, *J. Colloid Interface Sci.*, **192** (1997) *66-73*

53. C. Orr, Emulsion Droplet Size Data, in "Encyclopedia of Emulsion Technology", P. Becher, Editor, Volume 1. Marcel Dekker, New York, 1983, pp. 369-404.

54. L. Ambrosone, A. Ceglie, G. Colafemmina, and G. Palazzo, NMR studies of food emulsions: the dispersed phase self-diffusion coefficient calculated by the least variance method, *Prog. Colloid Polym. Sci.*, **115** (2000) *161-165*

55. L. Ambrosone, G. Colafemmina, M. Giustini, G. Palazzo, and A. Ceglie, Size distribution in emulsions, *Prog. Colloid Polym. Sci.*, **112** (1999) *86-88*

56. J.E. Tanner and E.O. Stejskal, Restricted self-diffusion of protons in colloidal systems by the pulsed-gradient, spin-echo method, *J. Chem. Phys.*, **49** (1968) *1768-1777*

57. D.J. Bergman and K.J. Dunn, Theory of diffusion in a porous-medium with applications to pulsed-field-gradient NMR, *Phys. Rev. B,* **50** (1994) *9153-9156*

58. M.D. Hürlimann, K.G. Helmer, L.L. Latour, and C.H. Sotak, Restricted diffusion in sedimentary-rocks - Determination of surface-area-to-volume ratio and surface relaxivity, *J. Magn. Reson. Ser. A*, **111** (1994) *169-178*

59. L.L. Latour, K. Svoboda, P.P. Mitra, and C.H. Sotak, Time-dependent diffusion of water in a biological model system, *Proc. Natl. Acad. Sci. USA,* **91** (1994) *1229-1233*

60. D. Topgaard and O. Söderman, Diffusion of water absorbed in cellulose fibers studied with ^{1}H-NMR, *Langmuir*, **17** (2001) *2694-2702*

61. W. Ngwa, O. Geier, L. Naji, J. Schiller, and K. Arnold, Cation diffusion in cartilage measured by pulsed field gradient NMR, *Eur. Biophys. J.*, **31** (2002) *73-80*

62. B. Håkansson, R. Pons, and O. Söderman, Structure determination of a highly concentrated W/O emulsion using pulsed-field-gradient spin-echo nuclear magnetic resonance "diffusion diffractograms", *Langmuir*, **15** (1999) *988-991*

63. B. Balinov, O. Söderman, and J.C. Ravey, Diffraction-like effects observed in the PGSE experiment when applied to a highly concentrated water/oil emulsion, *J. Phys. Chem.*, **98** (1994) *393-395*

64. O. Söderman and U. Olsson, Dynamics of amphiphilic systems studied using NMR relaxation and pulsed field gradient experiments, *Curr. Opin. Colloid Interface Sci.*, **2** (1997) *131-136*

65. M. Giustini, G. Palazzo, A. Ceglie, J. Eastoe, A. Bumujdad, and R.K. Heenan, Studies of cationic an noionic surfactant mixed microemulsions by small-angle neutron scattering and pulsed field gradient NMR, *Prog. Colloid Polym. Sci.*, **115** (2000) *25-30*

66. O. Söderman and M. Nydén, NMR in microemulsions. NMR translational diffusion studies of a model microemulsion, *Colloid Surf. A-Physicochem. Eng. Asp.*, **158** (1999) *273-280*

67. H. Wennerström, O. Söderman, U. Olsson, and B. Lindman, Macroemulsions versus microemulsions, *Colloid Surf. A-Physicochem. Eng. Asp.*, **123** (1997) *13-26*

68. J.E. Tanner, Use of the stimulated echo in NMR diffusion studies, *J. Chem. Phys.*, **52** (1970) *2523-2526*

69. S.J. Gibbs and C.S. Johnson, Jr., A PFG NMR experiment for accurate diffusion and flow studies in the presence of eddy currents, *J. Magn. Reson.*, **93** (1991) *395-402*

70. P. Stilbs, Fourier transform pulsed-gradient spin-echo studies of molecular diffusion, *Prog. NMR Spectrosc.*, **19** (1987) *1-45*

71. O. Söderman and P. Stilbs, NMR studies of complex surfactant systems, *Prog. NMR Spectrosc.*, **26** (1994) *445-482*

72. I. Lönnqvist, A. Khan, and O. Söderman, Characterization of emulsions by NMR methods, *J. Colloid Interface Sci.*, **144** (1991) *401-411*

73. B. Jönsson, H. Wennerström, P.G. Nilsson, and P. Linse, Self-diffusion of small molecules in colloidal systems, *Colloid Polym. Sci.*, **264** (1986) *77-88*

74. M.H. Blees and J.C. Leyte, The effective translational self-diffusion coefficient of small molecules in colloidal crystals of spherical particles, *J. Colloid Interface Sci.*, **116** (1994) *118-127*

75. H. Jóhannesson and B. Halle, Solvent diffusion in ordered macrofluids: a stochastic simulation study of the obstruction effect, *J. Chem. Phys.*, **104** (1996) *6807-6817*

76. H. Peterlik and D. Loidl, Bimodal strength distributions and flaw populations of ceramics and fibres, *Eng. Fract. Mec.*, **68** (2001) *253-261*

77. C.C. Huang, "Estimation of rock properties by NMR relaxation methods", MSc Thesis, Rice University, Houston, USA, 1997.

78. W.H. Press, S.A. Teukolsky, W.T. Vetterling, and B.P. Flannery, "Numerical recipes in FORTRAN: The art of scientific computing", Cambridge University Press, Cambridge, UK, 1992.

79. M. Abramowitz and J. Stegun, Eds., "Handbook of mathematical functions, with formulas, graphs and mathematical tables", Dover Publications, New York, 1965.

80. L. Wen and K.D. Papadopoulos, Visualization of water transport in $W_1/O/W_2$ emulsions, *Colloids Surfaces A - Phys. Chem. Eng. Aspects*, **174** (2000) *159-167*

81. W. Dixon and F. Massey, "Introduction to statistical analysis", McGraw-Hill, New York, 1957.

82. Y. Zhang, G.J. Hirasaki, W. House, and R. Kobayashi, "Oil and gas NMR properties: the light and heavy ends", SPWLA 43rd Annual Logging Symposium, Oiso, Japan, 2002, Paper HHH

83. S. Godefroy, J.P. Korb, M. Fleury, and R.G. Bryant, Surface nuclear magnetic relaxation and dynamics of water and oil in macroporous media, *Phys. Rev. E*, **64** (2001) Art. # 021605

84. P. Callaghan, A simple matrix formalism for spin echo analysis of restricted diffusion under generalized gradient waveforms, *J. Magn. Reson.*, **129** (1997) *74-84*

85. S.L. Codd and P.T. Callaghan, Spin echo analysis of restricted diffusion under generalized gradient waveforms: Planar, cylindrical and spherical pores with wall relaxivity, *J. Magn. Reson.*, **137** (1999) *358-372*

Chapter 4

Destabilization of emulsions via aggregation, sedimentation and coalescence

Dehydration of water-in-crude oil emulsions by means of chemical treatment

4.1. INTRODUCTION

Aggregation, sedimentation and coalescence are pervasively recognized as the chief mechanisms affecting emulsion stability in many applications of practical relevance [1-3]. The destabilization of emulsions formed in crude oil extraction operations is an example where these mechanisms play a significant role, as demonstrated in this chapter. In such operations, water is often present together with oil in the reservoir or is injected as steam or as primary solvent of complex fluids. Water and oil can mix intimately while rising through the well and also when passing through valves and pumps to form relatively stable dispersions of water droplets in crude oil in most cases. The presence of water is undesirable because it alters negatively the transport properties of the crude and undermines its commercial value and the operation of refining equipment. For these reasons, the prevention and remediation of oilfield emulsions is a problem of technological importance for the petroleum industry.

This chapter focuses on the destabilization of oilfield emulsions by chemical means. Experimental data on the effect of chemicals of known structure and composition (alkylphenol polyalkoxylated resins and cross-linked polyurethanes) on the stability and properties of brine-in-crude-oil emulsions are reported. Traditional techniques, such as the well-known bottle test and interfacial tension measurements, were applied in combination with less conventional methods in this field, such as rheometry and nuclear magnetic resonance relaxometry, to measure and explain relative rates of water

separation and changes of the drop size distributions in time. It was found that the phenolic resins promoted coalescence of droplets. Optimum performance was obtained with resins exhibiting intermediate hydrophilicity and balanced affinity for the oil and water phases, in a fashion consistent with the optimum formulation for formation of microemulsions in conventional oil-water-surfactant systems. In contrast, cross-linked polyurethanes promoted aggregation and some coalescence. The performance of these latter chemicals improved as their molecular weights increased. Polyurethanes aided phase separation by "bridging" nearby droplets when added at a concentration at which the number of molecules and the number of droplets present in the system were comparable. However, when added at an excessive concentration they retarded coalescence via steric stabilization. These two types of chemicals acted synergistically when added in combination, rendering water separation rates significantly higher than those observed when they are used individually. These findings could be interpreted qualitatively with a mechanism that suggests the formation and growth of "holes" between droplets as the limiting stage for coalescence, with group sedimentation dictating the macroscopic rate of phase separation. The discussion of results is preceded by a literature review on the subject.

4.2. OILFIELD EMULSIONS AND CHEMICAL DEMULSIFICATION: A LITERATURE REVIEW

4.2.1. Surface-active materials in crude oils: asphaltenes, resins and naphthenates

Crude oils are complex mixtures of a number of species that differ significantly in molecular weight, structure and elementary composition.

The simplest and most often used way to classify such species is in solubility classes. In this regard, asphaltenes are defined as the components of crude oil or residues that are insoluble in light hydrocarbons such as n-pentane or n-heptane, but that are soluble in aromatic solvents like toluene. The elemental analysis of asphaltenes

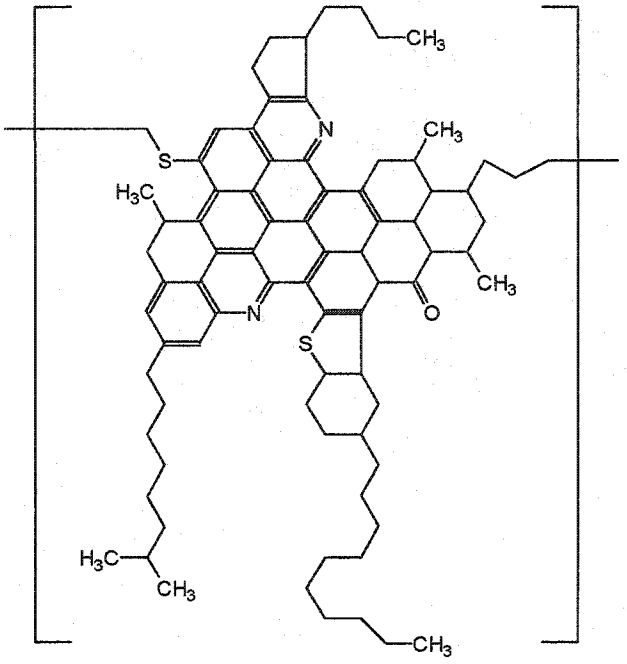


Figure 4.1. Hypothetical structure of an asphaltene molecule [5].

shows that carbon (~ 80 wt.%) and hydrogen (~ 8 wt.%) are the main components of their structure, and that heteroatoms (S, O, N, Ni, V) are commonly present in amounts that vary considerably for asphaltenes from different sources. Oxygen is usually present in carboxylic, phenolic, ketonic and ester functions. Most of the nitrogen is located in pyridine, carbazole, pyrrole and other heterocyclic species, whereas sulfur is found in benzothiophenes and similar structures. Nickel and vanadium are usually present in much smaller amounts (few hundreds of ppm), and are found mainly in porphyrins [4].

Several tentative chemical structures have been proposed for asphaltenes. Figure 4.1 shows an hypothetical representation of an asphaltene molecule [5]. This display is representative of the classic view of these macromolecules as constituted by a large structure of condensed polynuclear aromatic rings connected to alkyl side-chains. Figure

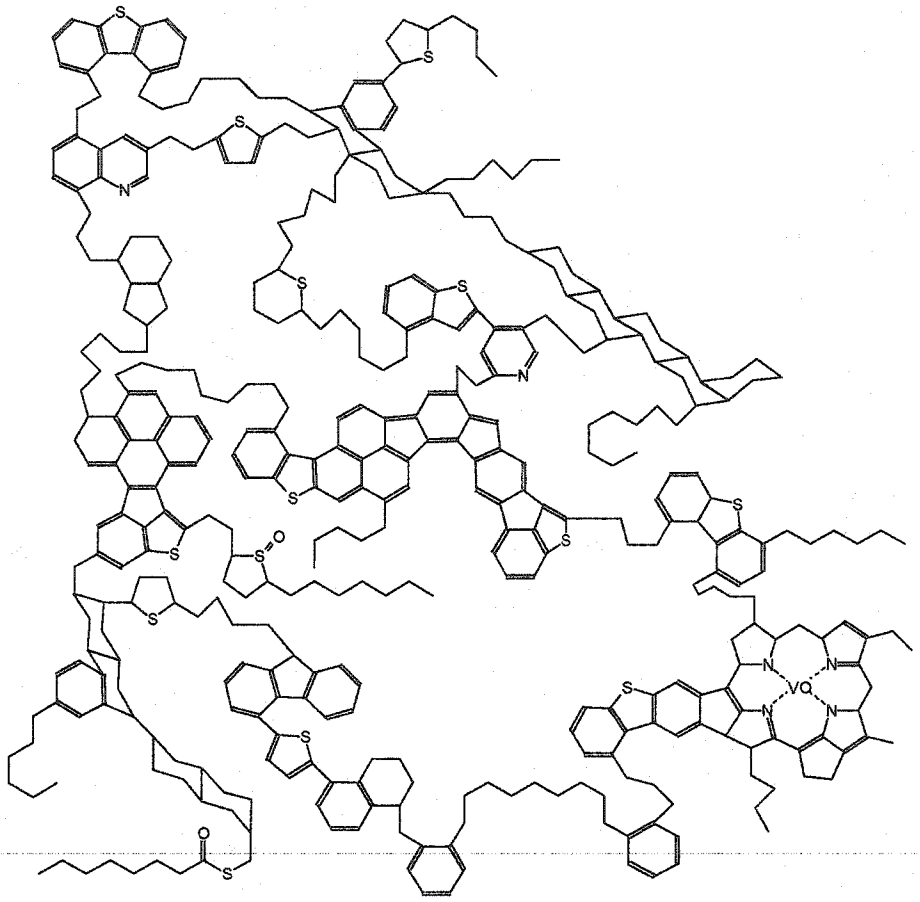


Figure 4.2. Proposed structure for asphaltenes in Athabasca bitumen [6].

4.2 illustrates the proposed structure of asphaltenes present in Athabasca bitumen [6]. It contains small groups of aromatic rings interconnected by alkyl chains and naphthenic and aliphatic rings, in a fashion that has been termed the *archipelago* model [7].

Elementary asphaltene molecules exhibit sizes between 2 and 10 nanometers, and they usually associate to form micelles, flocs, vesicles and gel-like structures that can reach sizes of up to 100 microns. The critical micelle concentration is circa 0.1 wt.%, which indicates that asphaltenes are present as aggregates even at small concentrations. Aggregation is thought to take place by stacking of the planar

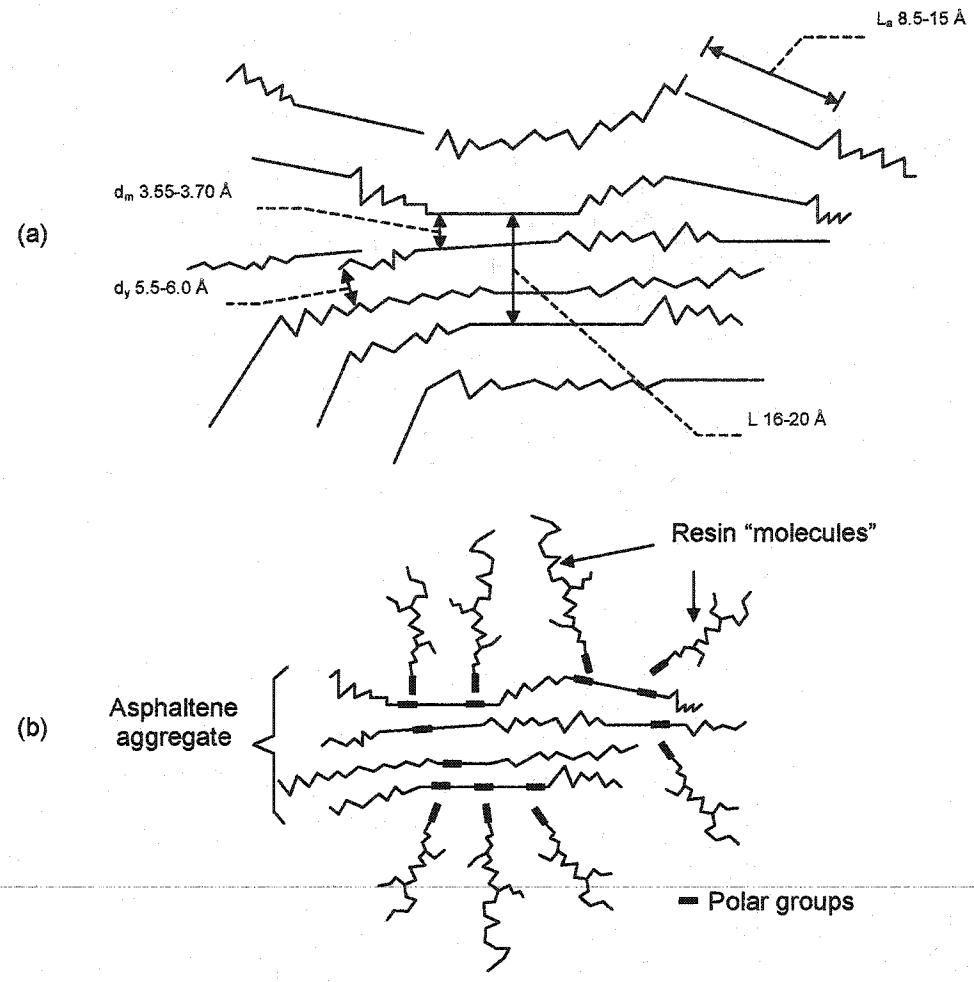


Figure 4.3. (a) Asphaltene aggregate [10, 11]. L_a = diameter of aromatic sheet; d_m = spacing between aromatic sheets; d_γ = spacing between aliphatic side-chains; L = Characteristic length of aromatic cluster. (b) resin-solubilized asphaltene colloid [9].

polynuclear aromatic parts of the molecules, probably due to π-π interactions or hydrogen bonding of the polar groups. Figure 4.3(a) shows a basic asphaltene aggregate that is consistent with the structure depicted in Figure 4.1. Aggregation and polydispersity in sizes make the determination of the molecular weight of asphaltenes a difficult and ambiguous task. Reported average molecular weights range between 600 Da and 300,000 Da, although most experimental data point to values between 600 - 4000 Da.

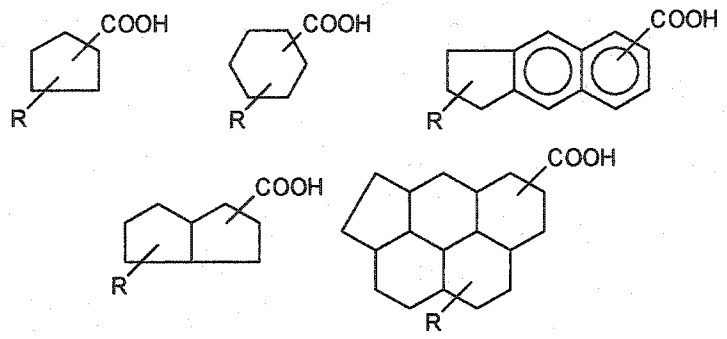


Figure 4.4. Chemical structure of some naphthenic acids present in crude oils from Angola and the North Sea [13].

The fraction of a crude oil that is soluble in light hydrocarbons such as n-pentane or n-heptane is referred to as the *maltenes*, and it contains three different classes of compounds, to know the *saturates*, the *aromatics* and the *resins* (SAR). Resins can be separated from saturates and aromatics through several chromatographic methods [8].

Resins and asphaltenes are two contiguous classes of components separated by a continuum of molecules, and therefore both exhibit similarities in chemical structure. In general, resins are smaller than asphaltenes, exhibit higher ratios of naphthenic-to-aromatic rings and much longer aliphatic side chains. Due to their similarity in structure but difference in solubility, resins play a key role in the solubilization of asphaltene aggregates in crude oil. In particular, they are thought to solvate the edges of the aromatic clusters of asphaltene colloids [9] [Figure 4.3(b)].

Finally, naphthenic acids are carboxylic acids exhibiting aliphatic rings of 5-6 carbon atoms, and aromatic rings in some cases (Figure 4.4). They have molecular weights between 100-500 Da and become surface-active when the corresponding salt (naphthenate) is formed after the ionization of the carboxylic group. It has been suggested that naphthenates may play a role in the stabilization of asphaltene

aggregates [12], although supporting evidence is yet to be presented. Naphthenates could be considered as a sub-class of resins since the latter may exhibit other polar groups such as phenolic, ketonic and ester functions, and heteroatoms such as nitrogen and sulfur.

4.2.2. Stabilizing mechanism for water-in-crude oil emulsions

In the stabilization of water-in-oil emulsions, other forces different from the electrostatic interactions described in Section 1.2.4.2 prevent aggregation and further coalescence. Because the dielectric constant of most oils is very low as well as the solubility of ionic species, electrical double-layer interactions are weak.

For the case of emulsions of water dispersed in crude oil, at least three mechanisms have been referenced in literature as responsible for their stability [13, 14]: (a) steric repulsion / mechanical stabilization due to the adsorption of asphaltenes and resins, followed by the organization and formation of elastic films at the water/oil interfaces; (b) formation of long-range particle structure inside the film between two approaching drops; (c) steric repulsion due to the adsorption of naphthenates at high pH.

Regarding mechanism (a), the ability of asphaltenes to form elastic films at water/oil interfaces is well documented [15-17]. The thickness of such films can be several hundreds nanometers and their elasticity is conferred by π-π interactions and hydrogen bonds between asphaltene molecules/aggregates [18].

The solubility state of asphaltenes has been consistently found to influence the formation of elastic films and therefore emulsion stability. In particular, it seems that emulsions are more stable at the onset of asphaltene precipitation [19, 20]. McLean and Kilpatrick [21] worked with model emulsions of water in mixtures of heptane and toluene stabilized by asphaltenes and resins from Saudi Arabia, Alaska and Venezuela and

suggested that at the point of incipient precipitation and at an optimum resin/asphaltene ratio (1:3 in weight), there exists an "ideal" solvency state of asphaltene/resin colloidal aggregates for emulsion stability. By increasing the aromaticity of the oil phase (i.e., the toluene/heptane ratio) and the resin/asphaltene ratio, the average number of asphaltene molecules present in the colloid diminishes and therefore their solubilization in the oil phase is favored. Conversely, decreasing the aromaticity of the oil and/or the resin/asphaltene ratio leads to an increase in the asphaltene aggregation number and therefore to precipitation. In either case, the resulting colloidal structure is less likely than the "ideal" configuration to adsorb at the water/oil interfaces and form an interfacial film to stabilize the emulsion.

The chemical structure of the asphaltene affects its tendency to adsorb at the water/oil interfaces and therefore to stabilize emulsions. A recent study by Masliyah *et al.* [17] on emulsions of water in Athabasca bitumen shows that asphaltenes with lower H/C ratio (1.1) (i.e., higher aromaticity) and higher O/C (0.03) (i.e., more polar characteristics) adsorb preferentially at the water/oil interfaces, whereas those with higher H/C ratio (1.2-1.3) and lower O/C ratio (0.01-0.02) are solubilized in the oil phase. It was observed that emulsion stability was conferred mainly by the fraction of asphaltenes that is less soluble in the crude oil, i.e., by those asphalthenes exhibiting low H/C and high O/C ratios. Stable emulsions can be formed using only this less-soluble fraction of asphaltenes when it is dispersed in a good (aromatic) solvent or when present with resins at a moderate to high resin/asphaltene ratio [18].

When the formation of long-range particle structure inside the film between two approaching drops is observed, the drainage of the thin film takes place stepwise (see section 1.2.2.3). This is shown in Figure 4.5 for a horizontal film of n-heptane/toluene

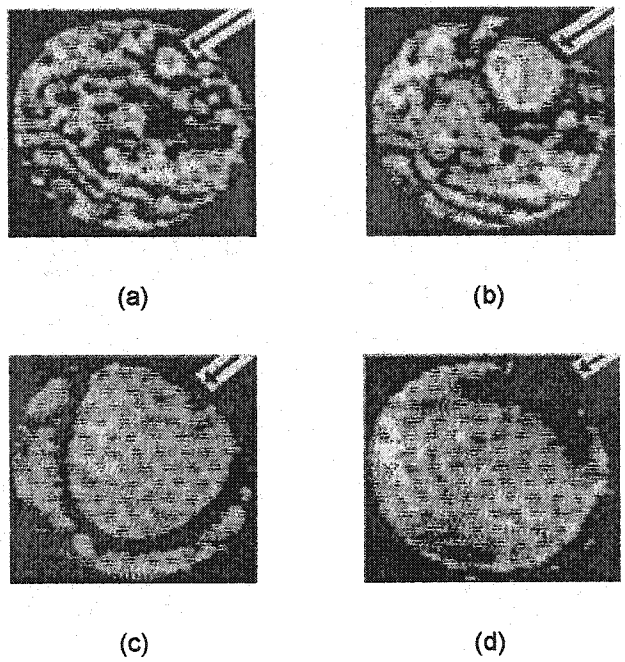


Figure 4.5. Stepwise drainage of an oil film stabilized by asphaltenes (7 vol.%) [22].

(1:1) stabilized with asphaltene particles (7 vol.%) [22]. These particles form random structures as shown in Figure 4.5(a). The initial thickness of the film is about 300 nm. As time proceeds, a clear spot (gray film) with thickness of about 100 nm appears and expands throughout the film (Figures 4.5 b, c and d).

Khristov *et al.* [23] have reported a similar thinning mechanism for films of bitumen diluted with n-heptane (n-heptane : bitumen weight ratio > 1.7). Due to their limited solubility in this alkane, the asphaltenes that are present in the oil precipitate, thus forming a network of repeatable geometric patterns. It was observed that the lifetime of the film diminished as the n-heptane:bitumen ratio was increased. On the other hand, when the bitumen was diluted with toluene, asphaltenes were completely solubilized and asymmetric drainage took place as shown in Figure 1.7 and ended in all cases with the formation of gray films. Stepwise drainage was not observed in the latter experiments

and therefore the first mechanism referred to above, i.e., steric repulsion due to soluble macromolecules adsorbed at the water/oil interfaces, most probably dictated the lifetime of the film.

Finally, Goldszal *et al.* [13] concluded that naphthenates can play a key role in stabilizing water-in-oil emulsions. These authors showed how emulsions of water dispersed in acidic crude oils from Angola and the North Sea exhibited a significant increase in stability, while the interfacial tension between the oil and the decanted water phase decreased, as the pH was raised. A plausible mechanism that was suggested to explain these findings is the ionization of naphthenic acid molecules initially present in the crude into naphthenates that migrate toward the water/oil interfaces and stabilize the dispersion via steric repulsion of the hydrophobic tails. The fact that the oil-water interfacial tension diminished when the pH was raised is indicative of an increasing concentration of surface-active species in the system. Kilpatrick [18] has suggested that naphthenates stabilize emulsions via formation of mesomorphic/liquid crystalline elastic films that can be several tens of nanometers in thickness.

4.2.3. Chemical demulsification

Methods to separate water-in-crude oil emulsions can be classified in three main categories: mechanical, electrical and chemical [24]. Mechanical methods rely on the action of a physical barrier and/or on the difference in density between the aqueous and oil phases to achieve separation. Electrical demulsification consists of the application of an electric field to deform the droplets into ellipsoid-like shapes and generate a force of attraction between drops, thus favoring coalescence. Chemical demulsification refers to the usage of additives able to promote flocculation and/or modify the properties of the interfacial films that are responsible for emulsion stability. Chemical demulsification is

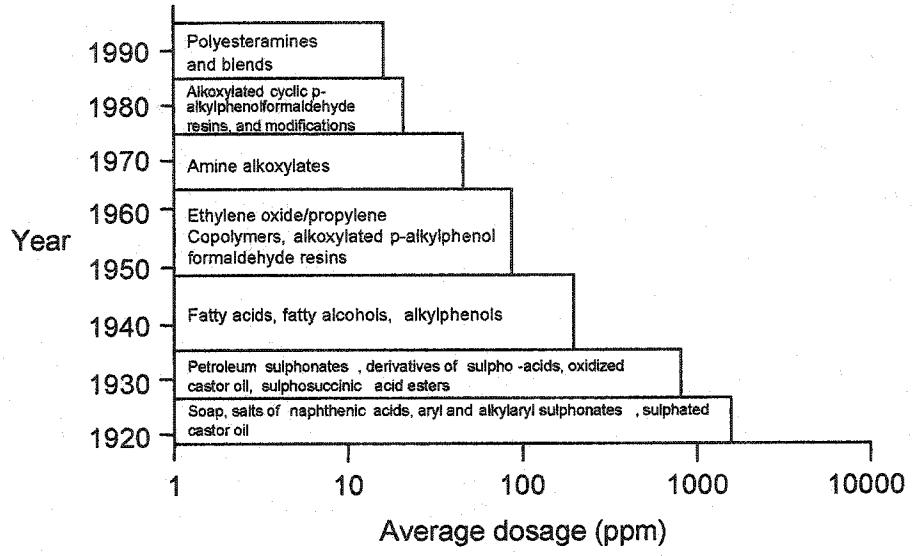


Figure 4.6. Evolution in the chemistry and average dosage of demulsifiers [16].

the most economical and commonly used method of dehydration of crude oils [25] and a combination of chemical and mechanical or chemical and electrical is often the best choice for most practical applications.

Figure 4.6 summarizes the evolution of the chemistry of demulsifiers since formulations were first commercialized in the 1920's [16, 26]. A more exhaustive list of chemicals can be found in a recent review by Angle [25]. In the beginning of demulsification operations, soaps and salts were used in relatively large dosages aiming to favor emulsion inversion (i.e., reversing the average affinity of the surface-active species at the interfaces to form oil-in-water instead of water-in-oil emulsions). Nowadays, demulsifying formulations are preferentially oil-soluble mixtures of high molecular weight compounds (large polymeric surfactants), low molecular weight polymeric and non-polymeric surface-active agents and solvents/cosolvents. These

formulations are intended to displace indigenous materials that are present at the water/oil interfaces, and to modify the mechanical and rheological properties of the films that prevent droplet coalescence as discussed further below. As a result of the increase in complexity and specificity in the chemistry and formulation of demulsifiers, a significant reduction in the average dosage that is needed to resolve oilfield emulsions has been observed throughout the years (Figure 4.6).

Each component plays a specific role in the performance of a modern demulsifying formulation. Amphiphilic molecules with moderate-to-high molecular weight (typically 3,000-10,000 Da), such as polyalkoxylated alkylphenolformaldehyde resins and complex block copolymers, are usually responsible for the separation of a large fraction of the dispersed aqueous phase. For that reason, they are often termed *water droppers*. These molecules penetrate the stabilizing film at the water/oil interfaces and modify its compressibility and rheological properties by disrupting the tight conformation of adsorbed asphaltenes, which in turn favors coalescence.

Molecules with very high molecular weight (usually above 10,000 Da) such as ethoxylated/propoxylated amine polyols act as flocculants by adsorbing at the water/oil interfaces and interacting with like molecules also adsorbed at the interfaces of nearby drops. These molecules act more slowly due to their lower diffusivities, and are effective in removing remaining small water drops and tight, fine emulsions once most of the dispersed phase has been removed by the water droppers [27].

Low molecular weight compounds (typically below 3,000 Da), such as common surfactants, aid phase separation through several mechanisms [28]. Firstly, they exhibit high interfacial activity and diffuse faster than other components with higher molecular weight. Therefore, they can suppress more effectively the interfacial tension gradients

that occur in deforming interfaces of approaching drops, which otherwise would retard drainage of the corresponding thin films that precedes film rupture and coalescence. Secondly, they alter the wettability (from hydrophobic to hydrophilic) of solid particles and colloidal waxes that are often adsorbed at the interface and that also contribute to the stability of the film.

Solvents are used as carriers of the active components, and they can play a critical role on the performance of a demulsifying formula. Good solvents are those in which the demulsifiers do not aggregate to a significant extent and remain surface active. Poor solvents do not allow efficient dispersion and therefore reduce the effective concentration of the demulsifier once dosed to the emulsion. Aromatic hydrocarbons such as toluene and xylene and water-miscible hydroxycompounds such as n-butanol, isopropanol and monoethylene glycols are often used as solvents in the formulation of commercial demulsifiers [25].

4.2.4. Effect of demulsifiers on interfacial properties of water/crude oil systems

4.2.4.1. Transient interfacial tension, diffusivity and film dilatational modulus

Kim *et al.* [14] reported results from field tests on the performance of chemical blends in the demulsification of water-in-oil emulsions from Gulf Coast, LA (API density of crude oil, 28°; water content, 54 vol.%; volume-weighted geometric mean diameter of drops, 0.8 μm), and subsequent lab tests with a film rheometer to determine the film dilatational modulus (E) and the apparent diffusivity of the demulsifier in the film (D). E was determined from data obtained in dynamic film tension experiments, in which the area of the film was expanded at a constant rate (2.7×10^{-2} mm^2/s). In such tests, the film tension 2σ, with σ being the interfacial tension, was determined from the Laplace equation and E was further calculated according to:

$$E = \frac{2d\sigma}{d\ln(A/A_0)} \qquad [4.1]$$

where A and A_0 are the instantaneous and initial areas of the film.

The kinetics of mass transport of demulsifier toward the water/oil interfaces was studied via experiments in which the film was suddenly expanded and the area kept constant thereafter. The change in film tension was related to D through a diffusion-controlled kinetic model:

$$\frac{1}{\Delta\sigma} = \frac{1}{RT}\left[\frac{1}{2c\sqrt{\frac{Dt}{\pi}}} - a_0\right] \qquad [4.2]$$

where $\Delta\sigma = \sigma - \sigma_0$, with σ_0 being the initial film tension after the expansion, c the bulk concentration of surface active materials and a_0 the area occupied by a surface active molecule. D is thus obtained from the slope of a $1/\Delta\sigma$ vs. $t^{-1/2}$ plot.

The film dilatational modulus is a measure of the film elasticity. Films with low E should exhibit low film tension gradients, which in turn would represent enhanced drainage rates and lower film (and emulsion) stability. For a chemical demulsifier, high diffusivity and high interfacial activity are desired to assure fast adsorption and suppression of film tension gradients, and therefore low film elasticity and minimum stability.

These facts were verified experimentally in the study referred to above, in which the performance of several chemical blends of oxyalkylated phenol/formaldehyde resins and EPON crosslinked derivatives in field bottle tests and in-lab film rheology experiments was determined and compared. In effect, the blend that exhibited the highest apparent

diffusion coefficient (D = 20.1 x 10^{-4} cm^2/s) also rendered the lowest film dilatational modulus (E = 7.9 mN/m), and also exhibited the highest water separation rate in experiments with emulsions (bottle tests). However, it is not clear from this study why D is significantly higher than that of common surfactant molecules in liquids (10^{-5} – 10^{-6} cm^2/s) since the blend contained active species with molecular weights of order 135,000 Da.

Another relevant conclusion of this study is that synergistic effects are important in the formulation of chemical demulsifiers. It was found that a given chemical blend exhibited better performance than its individual components at equal dosage in the reduction of film tension, thus indicating that the performance of a mixture of chemicals cannot always be inferred from that of its individual components.

Breen [29] performed stress relaxation experiments and also observed that a minimum in E corresponds to a maximum water separation rate. He noted that E is directly related to the rate of decay of the transient interfacial tension $d\sigma/dt$ when the rate of change of the interfacial area dA/dt is controlled or known, since Eq. [4.1] can be rewritten as:

$$E \propto \frac{d\sigma}{d\ln A} \propto \left(\frac{d\sigma}{dt}\right)\left(\frac{dt}{d\ln A}\right) \qquad [4.3]$$

It was also noted that the adsorption kinetics of demulsifiers (polypropylene glycols, and oxyalkylated phenolic resins) on water/heptane and water/toluene interfaces was not diffusion-controlled, because the characteristic relaxation times for the interfacial tension that can be estimated using a plausible diffusion coefficient for the demulsifiers (D = 1x10^{-6} cm^2/s) were at least two orders of magnitude smaller than those observed

experimentally. No alternative adsorption mechanism was proposed as rate-limiting to explain the observed experimental trends in dynamic interfacial tension.

Mukherjee and Kushnick [30] performed electron spin resonance experiments on nonylphenol resins with covalently attached spin labels, and concluded that demulsifiers reach the interface in clusters, probably forming reverse micelles. By comparing results from measurements performed in different solvents (toluene and isopropanol), they concluded that clustering is weaker as the polarity of the oil phase is increased. They suggested that relaxation of interfacial tension is not limited by the diffusion of the demulsifier molecules toward the water/oil interfaces, but by the unclustering of the ethylene oxide groups and subsequent rearrangement of such molecules at the interface.

4.2.4.2. Compressibility of the interfacial film

Ese *et al.* [31] reported plots of surface/interface pressure vs. mean molecular area (Π-A isotherms) of air/water and oil/water interfaces in the presence of asphaltenes, resins and demulsifiers. The surface pressure $\Pi_{A/W}$ and interface pressure $\Pi_{O/W}$ are defined as:

$$\Pi = \sigma_0 - \sigma \qquad [4.4]$$

where σ_0 and σ are the interfacial tensions at the air/water or oil/water interfaces before and after addition of surface-active species, respectively. In a Langmuir experiment, an interfacial film is formed in a rectangular container (trough) and further compressed by displacing a physical barrier along the interface. The surface/interfacial tension is measured as the compression of the film takes place, and the available surface per molecule (mean molecular area) is readily calculated from the geometry of the trough.

Nearly incompressible (rigid) films exhibit a sharp increase in surface/interface pressure as the area is reduced, whereas for compressible films such increase is gradual. The study of the rigidity of the film is relevant to emulsion stability because highly compressible films, which can be disrupted more easily than incompressible films, would favor coalescence.

Figure 4.7(a) shows Π-A isotherms for asphaltene/resin mixtures spread from pure toluene on pure water at several asphaltene/resin ratios. It is observed that the structure of the film changes from rigid to compressible when the amount of resins is increased. A similar effect is observed in monolayers of asphaltenes at the water/air interface when a high molecular weight demulsifier (reported as complex block copolymer in the original reference) is added (Figure 4.7(b)). The similar role of demulsifier and resins in disrupting the rigid network of colloidal asphaltenes that is observed in these isotherms agrees with observations made via atomic force microscopy on Langmuir-Blodgett films (Figure 4.8).

The Π-A isotherms reported in Figures 4.7(a) and (b) were obtained from films at the water/air interface. Figures 4.7(c) and (d) show analogous results when the measurements are carried on at the water/oil interface, which represent a more realistic condition for emulsion stability. The oil used in these experiments is a mixture of decane and toluene (49:1 volume ratio) containing asphaltenes (0.01 wt.%) and resins (0-0.05 wt%) that were previously extracted from a French crude oil. It is observed that the asphaltene films that form at the water/oil interfaces are less rigid than those observed at the air/water interfaces, probably because in the latter case the conformation of the film is not affected by oil/asphaltene interactions. In any case, it is seen in Figures 4.7(c) and (d) that the addition of resins or demulsifier reduces the adsorption of asphaltenes at the

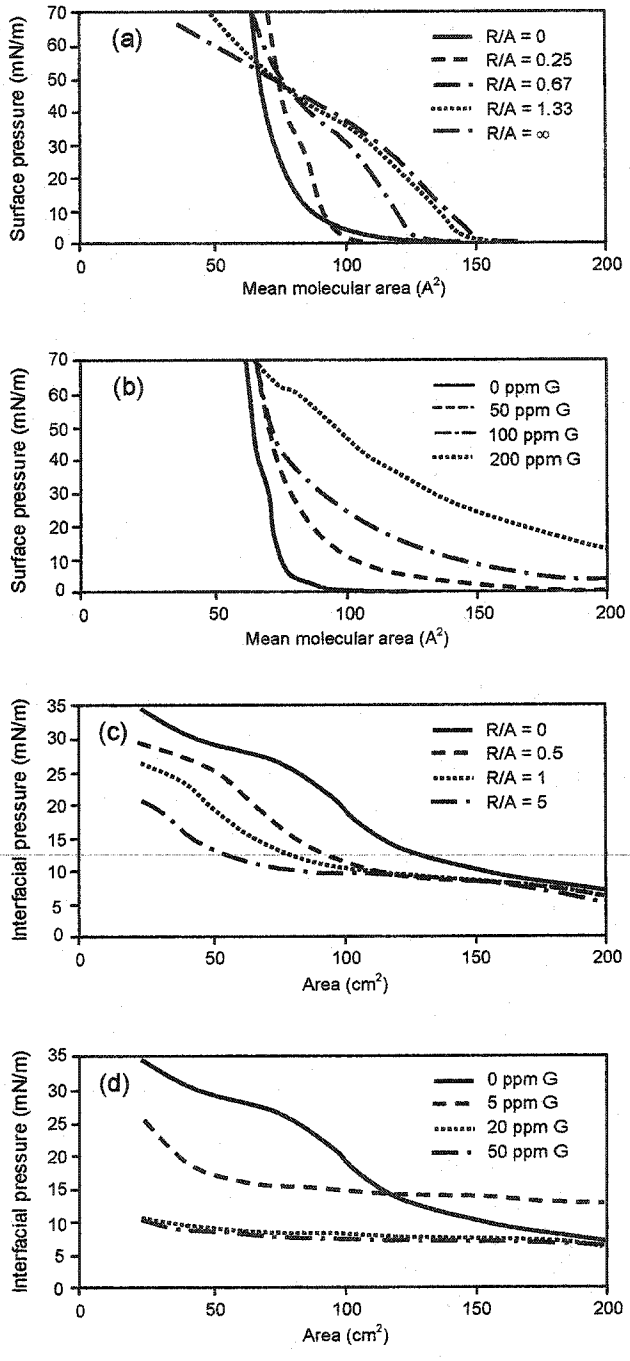


Figure 4.7. Π-A isotherms for (a) asphaltene/resins mixtures at the air/water interface; (b) asphaltene/demulsifier (G) mixtures at the air/water interface; (c) asphaltene/resins mixtures at the oil/water interface; (d) asphaltene/demulsifier mixtures at the oil/water interface.

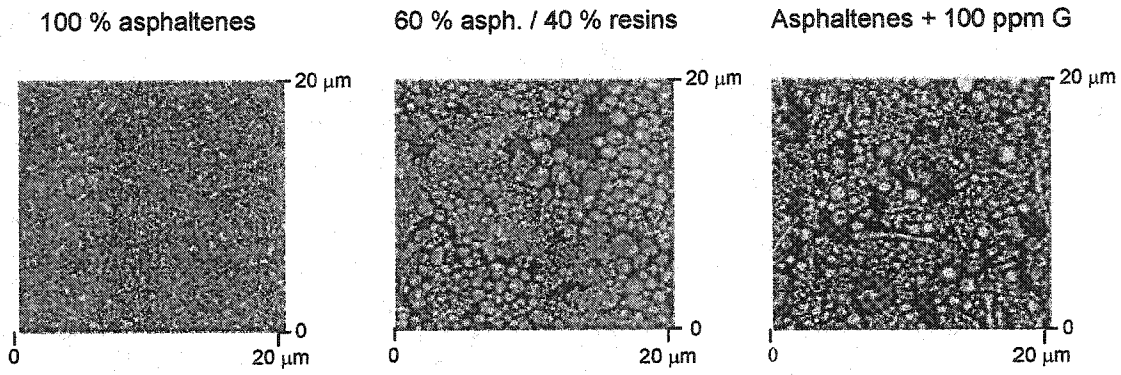


Figure 4.8. Langmuir-Blodgett films of asphaltenes, asphaltenes + resins and asphaltenes + high molecular weight demulsifier (G) at the water/air interface, studied by means of atomic force microscopy (AFM). Resins and demulsifier modify the structure of the asphaltene film in a similar fashion [28].

water/oil interfaces, which is noted as a reduction in the interfacial pressure at constant interfacial area, and therefore increases the compressibility of the film.

4.2.4.3. Interfacial shear viscosity and interfacial primary yield value

Interfacial rheology refers to the study of the deformation and flow of materials at the interfaces due to an applied stress, and it has been useful to demonstrate that changes in the structure of the films that prevent coalescence in emulsions due to the presence of resins and/or addition of demulsifiers affect the mechanical and hydrodynamic properties of such films [32] as discussed below.

High interfacial shear viscosities (η_S) reduce the rate of drainage of the thin films between approaching drops, thus favoring their stability (See Eq. [1.24]). This assessment agrees with data reported by Malhotra and Wasan [33], in which good correlation between high interfacial shear viscosity and high emulsion stability was observed. Mukherjee and Kushnick [30] indicated that while high surface viscosities indeed slow down thin film drainage and retard film rupture and coalescence, the

opposite is not necessarily true. Their results suggest that low interfacial viscosity is necessary but not sufficient to warrant effective demulsification. In addition, the demulsifier must effectively suppress interfacial tension gradients that may develop in the film thinning process, which otherwise would lead to retardation of the film drainage [34].

High surface pressures account for the high surface viscosity of stabilizing films [35] and vice versa. Therefore, from the data reported in section 4.2.4.2 it can be inferred that rigid films should exhibit high η_s, and vice versa for compressible films. Different studies [32, 36] confirm that in most cases the interfacial shear viscosity (a) increases with asphaltene content; (b) diminishes as the resin/asphaltene ratio is increased; (c) diminishes with the addition of demulsifiers; (d) increases with the aging of the film.

The interfacial primary yield value (IFPYV) is defined as the shear stress at quasi-zero shear rate [37]. It has been considered as a measure of the mechanical strength of the film [32, 36]. Not surprisingly, it has been found that changes in the structure of the stabilizing film at the water/oil interfaces affect η_s and IFPYV in a similar fashion. Namely, the IFPYV (a) increases with asphaltene content; (b) increases with the aging of the film when the emulsion is stabilized by asphaltenes; (c) is practically zero and independent of the age of the film when only resins are added. Also, it has been found that both η_s and IFPYV decrease with an increase in the temperature of the system.

4.2.5. On the relationship between chemical structure of demulsifiers and efficiency of emulsion breakup

A few studies are found in the literature reporting the effect of systematic changes in the chemistry of demulsifiers on their performance as emulsion breakers, probably

because such information is sensitive in many cases to commercial applications and therefore results from research on this subject are left unpublished or patent-protected.

Abdel-Azim *et al.* [38] reported the effect of changes in the degree of ethoxylation, number of amino groups and the degree of substitutions in aromatic rings of polyalkoxylated amines used in the break-up of synthetic water-in-benzene emulsions stabilized by asphaltenes. These authors found that (a) removal of water was favored by an increase in the degree of ethoxylation (i.e., by an increase in the hydrophilic-liphophilic balance (HLB) of the demulsifier from 6 to 14); (b) polyalkoxylated p-diaminobenzenes were more efficient as emulsion breakers than polyalkoxylated monoaminobenzenes with the same HLB; (c) binuclear aromatic amines (polyalkoxylated 1-naphthyl-amine) were more efficient than mononuclear aromatic amines (polyalkoxylated aniline) with the same HLB. Therefore, demulsification was favored by an increase in the number of polar groups and in aromaticity. The authors claimed that such changes in the structure of the demulsifiers favor their adsorption at the water-oil interfaces and therefore the displacement/solubilization of asphaltenes clustered in this region.

Importantly, it was shown in the same study that in all cases there is an optimum dosage for demulsification. Optimum dosages ranged between 50 ppm for the binuclear aromatic amines and 300 ppm for the polyalkoxylated ethylene diamines. Addition of demulsifiers beyond their optimum resulted in an increase of the stability of the emulsion, probably due to the formation of a new stabilizing film in which the excess of demulsifier would play a significant role.

Amaravathi and Pandey [39] presented a survey of patent literature for the synthesis and chemistry of ethylene oxide (EO) - propylene oxide (PO) polymeric demulsifiers and

their performance on resolving water-in-crude oil emulsions. The description includes EO-PO copolymers of alkoxylated alkylphenolformaldehyde resins, bisphenol A bis (glycidylether) EO-PO copolymers, EO-PO copolymers of amino compounds, esters of polypropylene glycols and polyethylene glycols and EO-PO copolymers of sulfur compounds. In contrast to the former study, these authors noted that in some cases an increase in EO content could reduce the effectiveness of the demulsifier.

Finally, a recent study by Breen [27] shows that the efficiency of a given chemistry depends heavily on the H/C ratio of the oil phase. In general, demulsifiers are more effective when the oil phase exhibits high aromaticity, i.e., low H/C ratio. The stability of untreated emulsions also diminished with an increase in the aromaticity of the oil, probably due to enhanced solubilization of the asphaltenes in the bulk oil. Some observations on the chemistry of the demulsifier are made in this study. It is reported, for example, that propoxylated resins performed significantly worse than ethoxylated resins in emulsions made with an oil phase exhibiting low aromaticity.

Other studies regarding the relationship between chemical structure and demulsifier performance are mentioned in section 4.4 as they become relevant to the discussion of experimental results obtained in this investigation.

4.3. Materials and Methods

Water-in-crude oil emulsions were prepared by dispersing brine (5 wt.% NaCl) in crude oil SHU. Relevant properties and results from chemical analyses of this crude oil are listed in Appendix B. No additives were used to stabilize the emulsions.

Two homologous series of chemicals were provided by OndeoNalco Energy Services, L.P. to perform demulsification tests, namely: (a) six polyoxyethylene (EO)/

Table 4.1. EO/PO content of the phenolic resins PR_X used in this investigation

Phenolic resin	PR_1	PR_2	PR_3	PR_4	PR_5	PR_6
EO + PO in molecule (wt.%)	25 %	33 %	41 %	46 %	54 %	66 %

Table 4.2. Weight-average molecular weight of the polyurethanes PU_Y used in this investigation

Polyurethane	PU_1	PU_2	PU_3	PU_4	PU_5
Molecular weight (Da)	12125	14200	16243	18878	20455

polyoxypropylene (PO) alkylphenolformaldehyde resins (further referred to as PR_X), with molecular weights around 3,500 Da and varying amounts of EO/PO groups in their structure (Table 4.1) at constant EO/PO ratio (3:1); (b) five crosslinked polyurethanes (PU_Y) obtained from the polymerization of polypropylene glycol with toluene di-isocyanate. The polyurethanes were synthesized to differ in molecular weight (Table 4.2) by controlling the extent of cross-linking. Figure 4.9 shows plausible chemical structures for these compounds. A blend of xylenes (Fisher Scientific) was used to disperse the chemical (chemical : xylene ratio = 1.5:1 (wt.) in all cases) before using them in tests.

The ability of these chemicals to destabilize W/O emulsions was tested via the so-called "bottle tests", which simply consist of determining by inspection the amount of water that separates from a quiescent emulsion sample with time. For each bottle test, a 200-mL batch of emulsion was prepared by mixing brine (30 vol.%) and crude oil (70 vol.%) in a standard 250-mL glass beaker (ID = 75 mm) with a six-blade turbine (Figure 4.10 (a)). Figure 4.10 (b) shows a sketch of the configuration that was adopted to make

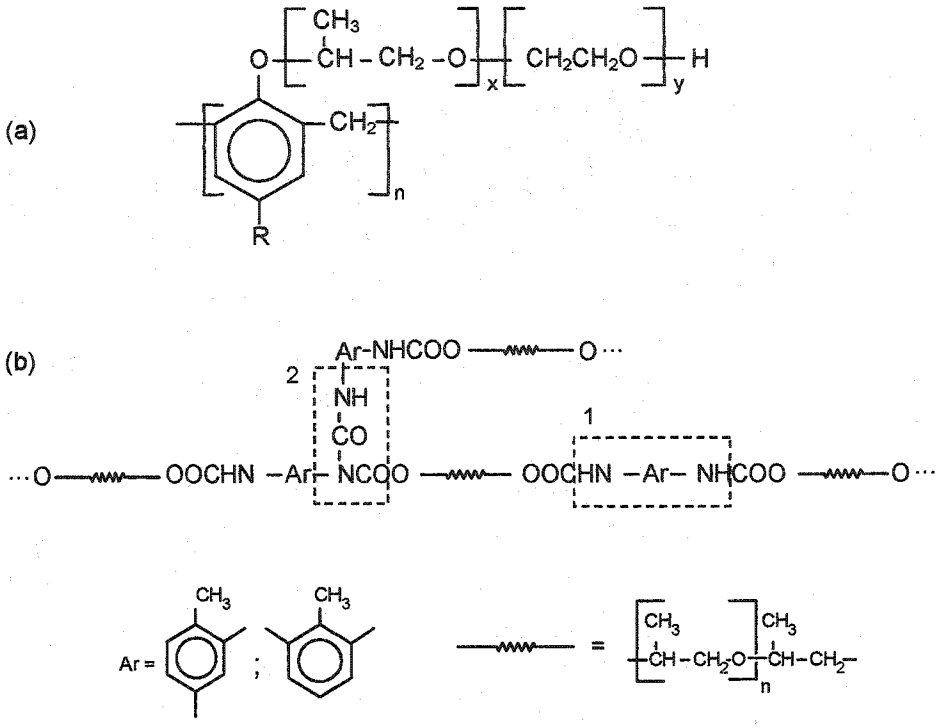


Figure 4.9. Plausible structures of the chemicals used in demulsification experiments. (a) EO/PO alkylphenolformaldehyde resins (PR_X); (b) cross-linked polyurethanes PU_Y, showing the basic groups for linear (1) and crossed (2) linking (after Refs. [40, 41]).

emulsions for bottle tests. Stirring was performed at 3000 rev/min during 30 min. Prior to emulsification, the aqueous and oil phases were left in contact during 24 hours, with the container placed in a thermostatic bath (Haake K35, precision = ± 0.1 °C) at the temperature at which the bottle test would be performed later. Once an emulsion batch was prepared, up to six 30-mL emulsion samples were poured in 35-mL calibrated glass vials (ID = 30 mm) provided with cap. The chemicals were further dosed to each sample with a 100-μl digital microdispenser (Drummond). Afterwards, all the samples were shaken by hand at the same time during 1 minute and further placed in the thermostatic bath. The samples were examined periodically to record the amount of decanted water.

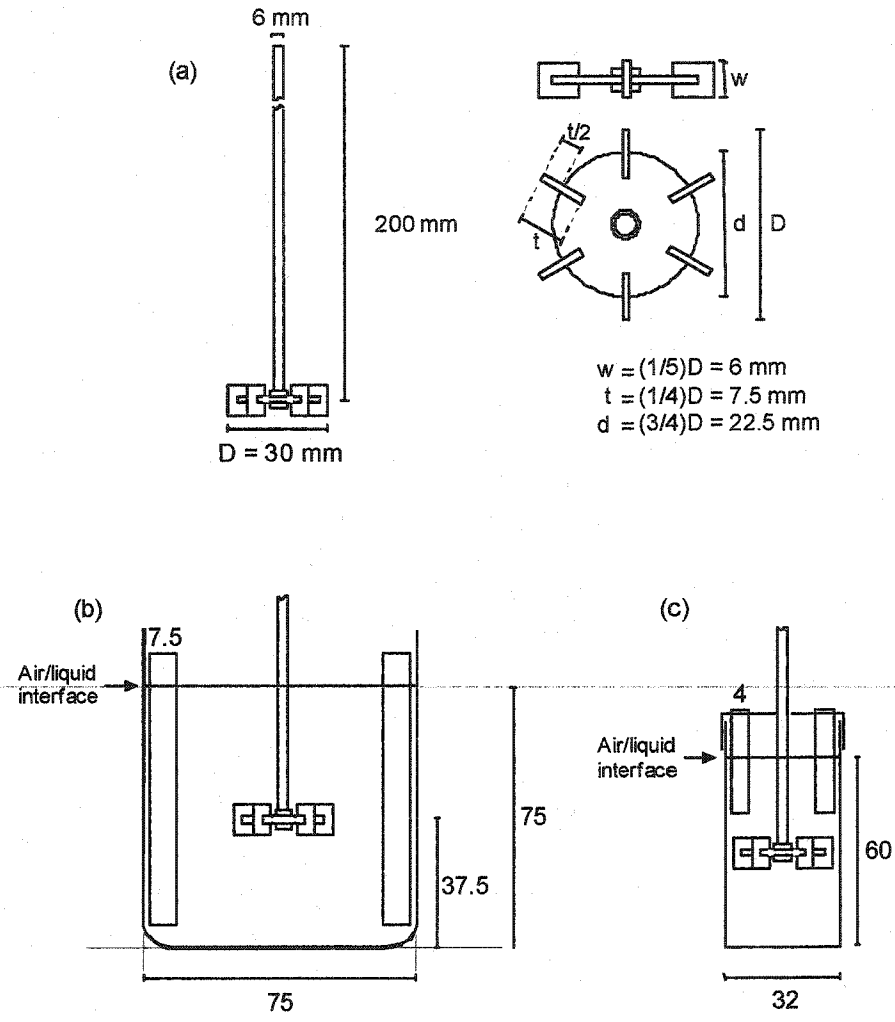


Figure 4.10. (a) Dimension of the mixer used in the preparation of water-in-oil emulsions; (b) experimental setting for the formation of emulsions for bottle tests; (c) experimental setting for the formation of emulsions for viscosity tests.

The transient shear viscosities of emulsions undergoing phase separation were measured with a Brookfield DV-III + rheometer. A spindle (#18, viscosity range = 1.3 – 30,000 mPa.s) is immersed in a cylindrical cell containing approximately 7 mL of sample, and it is further set to rotate at a given angular velocity. The unit is provided with a transducer that measures the torque needed to maintain such velocity, whence the viscosity is calculated. Since only one sample can be characterized per test, emulsion samples for viscosity measurements were prepared in small cylindrical plastic containers (ID = 32 mm) to reduce crude oil waste. Each 30-mL sample (30 vol.% water / 70 vol. % oil) was pre-equilibrated for 24 hours as before. Stirring was performed with the same turbine described above. The stirrer was initially placed in the center of the sample and operated at 1300 rev/min during 3 minutes, and further moved to the bottom of the container and operated at 2500 rev/min during 7 minutes. The containers were sealed with a plastic cap, which had four small baffles attached, as shown in Figure 4.10 (c). This stirring protocol yielded emulsions with initial viscosities similar to the ones obtained with the protocol adopted for the bottle tests ($\eta_{t=0}$ ~ 50 - 60 mPa.s). Once the emulsion was made, the chemical to be tested was dosed as explained for the bottle tests, the sample was shaken by hand for 1 minute and an aliquot was placed in the cylindrical container of the rheometer. The container was placed within a jacket through which fluid from the thermostatic bath was circulated. The spindle was set to rotate at 50 rev/min and the rheometer stored automatically in memory viscosity measurements at times previously specified by the user. Viscosity measurements were performed at T = 30.0 $\pm$ 0.1 °C.

It is worth mentioning that the emulsification protocols described above were designed to minimize vortex formation and intake of air bubbles. Air bubbles are

undesirable because they create air/liquid interfacial area within the dispersion and increase the viscosity of the emulsion.

Drop size distributions were measured using the nuclear magnetic resonance (NMR) techniques that were described in Chapter 3. For these experiments, emulsion samples were prepared as indicated for the viscosity tests, and then they were stirred with a high-speed device (non-aerating stirrer, Glas-col apparatus company) at 10,000 rev/min during 10 minutes to further reduce the initial drop sizes to values for which the NMR-PGSE experiment is more sensitive (d_0 ~ 10 μm).

Finally, the equilibrium interfacial tensions of brine and crude oil after phase separation were measured at 30 ± 1 °C using a spinning drop tensiometer (Non Linear Systems, model 300). Aliquots of oil and water were withdrawn with a 5-mL syringe equipped with a 2"-needle. The tip of the needle was placed approx. 3 mm above or 3 mm below the water-oil interface before sampling, respectively. The placement of the needle was found critical for reproducibility, particularly in systems for which the formation of a third phase (microemulsion) was expected.

4.4. Results and Discussion

4.4.1. Performance of polyalkoxylated alkylphenolformaldehide resins

Figure 4.11 shows (filled circles) results from a bottle test in a W/O emulsion treated with 240 ppm (vol.) of the phenolic resin PR_3 (the actual dosage was 400 ppm, which includes 160 ppm of xylene). Pictures of the sample at the beginning and end of the test are inserted in the plot. It is seen that the phenolic resin promoted water separation, since a clear layer of decanted water was collected at the bottom of the container. Interestingly, it is also seen in Figure 4.11 that most of the water (approx. 80%) was

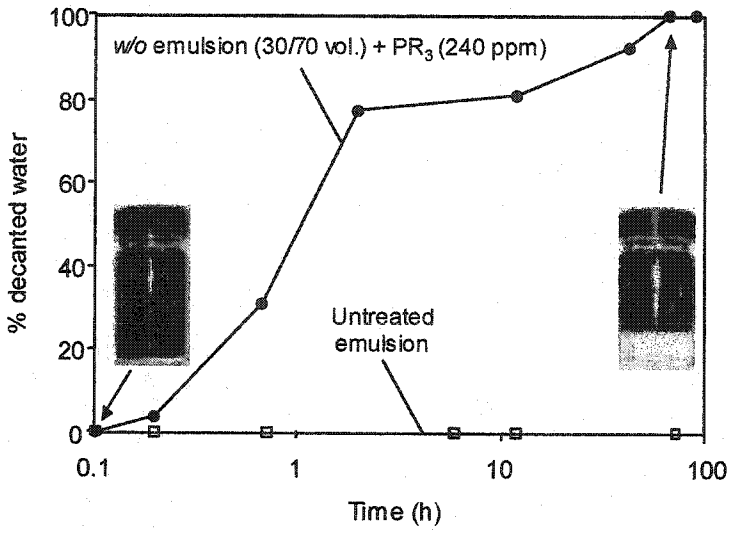


Figure 4.11. Bottle test results for an untreated emulsions (squares) and for and emulsion treated with the phenolic resin PR_3 (filled circles). The inserted pictures show the appearance of the bottles at the beginning and end of the test when the resin PR_3 was used.

separated within the first two hours of the test, but it took nearly 4 days to separate the remaining 20 %. This trend indicates that the phenolic resin caused separation of most of the water in a relatively short time, but did not render complete separation of the water phase in a practical timescale. Figure 4.11 also indicates that no water separation is observed in absence of demulsifier (squares).

Bottle tests were performed on emulsions treated with all the phenolic resins listed in Table 4.1. Figure 4.12 shows (filled circles) the percentage of water separated after 12 hours at 30 °C, as a function of the relative content of EO/PO groups in the phenolic resin. An increase in the length of the EO/PO head group confers hydrophilicity to the phenolic resins. For that reason, the affinity of the resin shifts from lipophilic to hydrophilic as the EO + PO content is increased. The results shown in Figure 4.12 for T = 30 °C clearly indicate that the performance of the phenolic resin is optimum for the resin PR_3, which exhibits an intermediate EO/PO content.

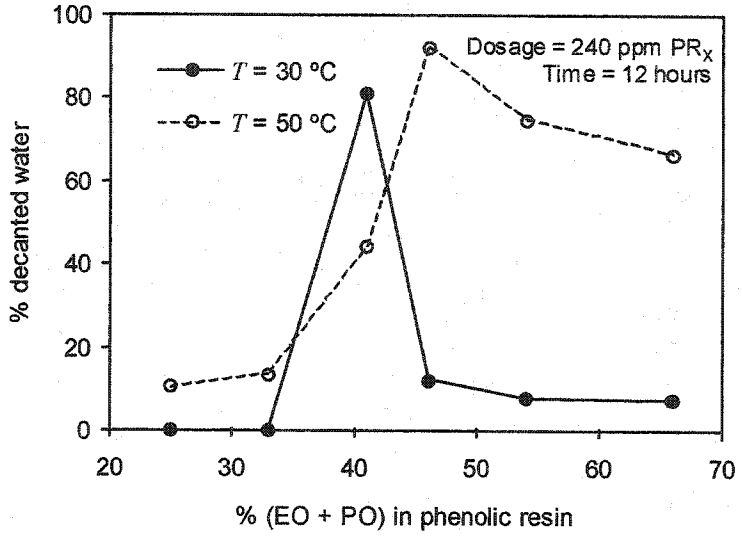


Figure 4.12. Effect of EO/PO content and temperature on the performance of the phenolic resins in bottle tests.

In agreement with this result, Taylor [16] showed that the minimum stability of emulsions of water in a Kuwaiti crude oil treated with commercial ethoxylated nonylphenol formaldehyde resins (Novolak and Resol series) is achieved with an intermediate number (five) of ethylene oxide (EO) units per phenol group. Molecules with lower or higher number of EO groups would be solubilized preferentially in the oil or water phase, respectively, and would exhibit lower efficiency in water removal. Molecules with the optimum degree of ethoxylation for demulsification would exhibit intermediate crude oil/water solubility. Optimum demulsification performance of chemicals exhibiting intermediate hydrophilicity or balanced partitioning of the demulsifier between the liquid phases has been observed in other investigations [34, 42, 43]. Perhaps the results reported by Abdel-Azim *et al.* [38] and Amaravathi and Pandey [39], which indicate that an increase in the degree of ethoxylation leads to a monotonic *increase* or to a monotonic *decrease* of the demulsification efficiency, respectively, (see

section 4.2.5) were performed with chemicals exhibiting an EO content *below* or *above* the one required for balanced affinity towards the oil and water phases, respectively.

Optimum demulsification performance of polyalkoxylated resins with intermediate hydrophilicity was also observed by Goldzsal and Bourrel [42]. To explain this behavior, these authors invoked the Winsor's R parameter [44], which is often used to describe the phase behavior of water-oil-surfactant systems [45]:

$$R = \frac{A_{CO}}{A_{CW}} \qquad [4.5]$$

where A_{CO} and A_{CW} stand for the net surfactant-oil and surfactant-water interaction energies per unit interfacial area, respectively. If the surfactant is lipophilic, $A_{CO} > A_{CW}$, whence $R > 1$. Contrarily, $R < 1$ is representative of hydrophilic surfactants. Importantly, a relationship between R and the emulsion type that most likely would form upon dispersing the water/oil/surfactant system has been established [44]. Lipophilic surfactants ($R > 1$) at concentrations above the cmc favor the formation of W/O emulsions, whereas hydrophilic surfactants ($R < 1$) promote the formation of O/W emulsions. When the interactions of the surfactant with both phases are balanced ($R = 1$), a number of distinctive features arise, namely [44-46]: (a) surfactant, oil and water tend to form a *microemulsion*, i.e., a thermodynamically stable phase which incorporates most of the surfactant, along with oil and water solubilized in apparently continuous nano-sized domains; (b) interfacial tension between this microemulsion phase and either oil and water is very low (typically 3-5 orders of magnitude smaller than the water/oil interfacial tension in absence of surfactant); (c) emulsion stability is also very low, as discussed later in this section. Goldszal and Bourrel [42] suggested that a maximum in demulsification performance corresponds to a physicochemical condition for which $R = 1$.

Figure 4.12 also shows the amount of water separated after 12 hours in bottle tests performed at 50 °C (open circles). The most significant feature of this figure is the fact that the maximum water separation was observed when using the resin PR_4, and not the resin PR_3 as before. Therefore, an increase in temperature requires an increase in the fraction of EO/PO groups present in the phenolic resin to observe maximum water separation. This trend is consistent with the above-mentioned ideas: an increase in temperature leads to a decrease in the interactions between the surfactant and the water phase (i.e., to a reduction in A_{CW}), due to temperature-driven dehydration of the polyalkoxylated surfactant headgroups (see the discussion that follows Table 2.1, section 2.1.5). For that reason, a transition $R = 1 \rightarrow R > 1$ occurs for the resin PR_3, whence emulsion stability *increases*. For the same reason, a transition $R < 1 \rightarrow R = 1$ takes place for the resin PR_4, whence emulsion stability *diminishes*. Water separation improved with respect to the tests performed at 30 °C when using phenolic resins with low (PR_1 and PR_2) and high (PR_5 and PR_6) EO/PO content, because an increase in temperature causes a reduction in the viscosity of the oil phase, and therefore leads to an increase in the sedimentation velocity of droplets (see section 1.2.4.1). The enhancement in water separation is much less pronounced for phenolic resins PR_1 and PR_2, because they are lipophilic ($R > 1$) and thus favor the persistence of the initial emulsion type (W/O) as mentioned above.

Figure 4.13 shows a picture of the samples from the bottle test at 30 °C reported in Fig. 4.12, five months after performing the experiment. Very distinct features could be observed, depending on the phenolic resin that was used in the experiment. First, complete water separation was not observed for the most lipophilic resin PR_1. Instead, large water domains surrounded by oil-continuous films were present. These oil-

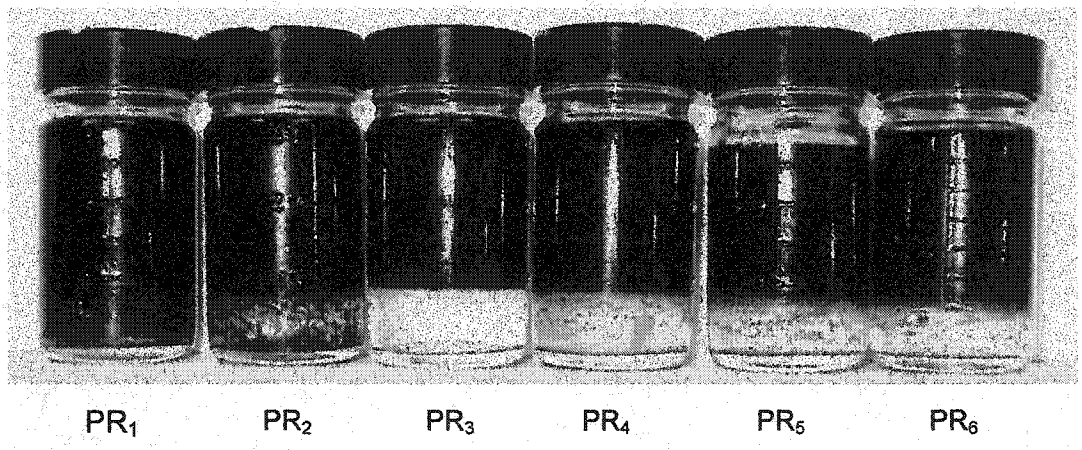


Figure 4.13. Appearance of the bottles used in the experiment reported in Figure 4.12 at 30 °C, five months after the beginning of the test. The acronym PR_X indicates the phenolic resin that was dosed in each case (240 ppm).

continuous domains were clearly observed at the bottom of the sample treated with resin PR_2. In contrast, the resin that rendered the best performance (PR_3) leads to the formation of a very clean water layer. Oil-continuous domains were present neither in this case, nor when more hydrophilic resins were used (PR_4 through PR_6). However, when a hydrophilic resin was used, some turbidity was observed in the decanted water layer. This fact is indicative of selective partitioning of the resins toward the aqueous phase. It was confirmed via microscopy that the observed turbidity is due to the presence of micron-sized particles, apparently oil droplets, which are unable to cream due to Brownian forces. Hydrophilic resins would favor the formation of O/W emulsions as mentioned above, and they probably stabilize the observed oil droplets against coalescence.

Figure 4.14 shows (filled circles) results from equilibrium interfacial tension measurements on the samples depicted in Figure 4.13 at 30 $\pm$ 1 °C, five months after performing the test. Such a long separation time was permitted, aiming to collect enough decanted water from the samples that separated more slowly so the interfacial tension

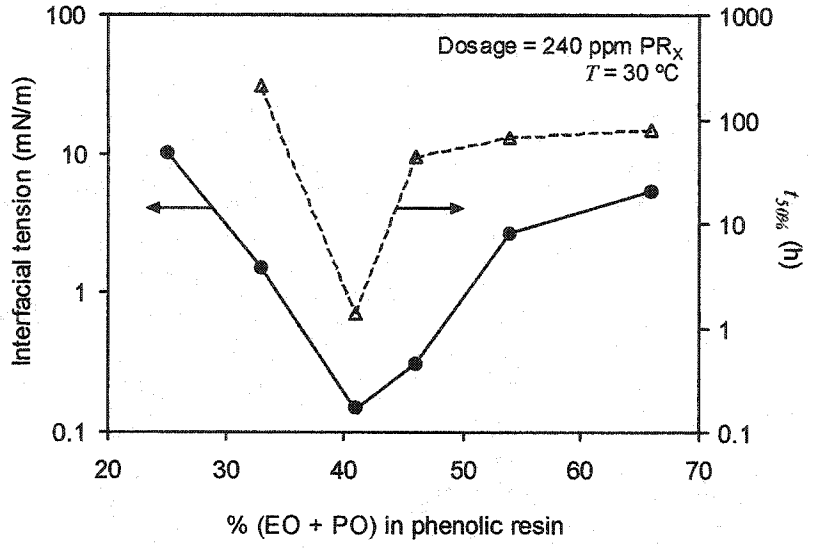


Figure 4.14. Effect of EO/PO content on the equilibrium interfacial tensions of emulsions treated with phenolic resins (filled circles). The times required in bottle tests to decant 50 % of the brine initially present in the emulsion are also plotted (triangles).

measurement could be performed, without applying centrifugation to the sample. It is observed that a minimum in interfacial tension was measured for the sample treated with the phenolic resin PR_3. The interfacial tension recorded for this sample (0.15 mN/m) was approx. two orders of magnitude smaller that those measured from samples treated with the minimum and maximum EO/PO content (10.22 mN/m for PR_1 and 5.40 mN/m for PR_6, respectively). The interfacial tension of water and crude oil in absence of demulsifier was 23 mN/m. Results from bottle tests are also included in this figure (triangles), expressed here as the time required to separate 50 % of the water phase ($t_{50\%}$). The agreement between these trends is qualitative, i.e., fastest separation was observed for the system that exhibited minimal equilibrium interfacial tension. This finding is consistent with the interpretation of the optimum demulsification efficiency as the results of balanced physicochemical affinity of the demulsifier (either by itself or associated with indigenous materials of the oil –asphaltenes, resins and naphthenates-)

for both phases. Finally, the interfacial tension that was measured at the optimum EO + PO content (0.15 mN/m) is higher than the values typically found for microemulsion/water interfaces (0.01 – 0.0001 mN/m) [45]. A middle (microemulsion) layer was not observed in this test, probably because of the low concentration of demulsifier used in these experiments (240 ppm), which is comparable to the dosage used in oilfield applications (see Figure 4.6).

The performance of phenolic resins was also studied via transient viscosity measurements. Figure 4.15 (a) is a sketch of the sequence of events that take place in a typical experiment. At the beginning of the test, the spindle is immersed in the emulsion sample, which exhibits a uniform water/oil composition. As time proceeds, sedimentation of water droplets and phase separation occurs. In consequence, the water content of the liquid that is confined in the gap between the container and the spindle diminishes over time. The viscosity of an emulsion (η) increases when the volume fraction of the dispersed phase ϕ is also increased, and it matches the viscosity of the continuous phase η_C in the limit $\phi \rightarrow 0$ (see Section 1.2.3). For that reason, the apparent viscosity of an emulsion diminishes as phase separation takes place. Figure 4.15 (b) shows transient shear viscosity measurements for an untreated emulsion with ϕ = 0.30 (open circles), and also for an emulsion treated with 240 ppm of phenolic resin PR_3 (filled circles). The dashed line indicates the shear viscosity of the crude oil η_C = 23 mPa.s. This plot indicates that some sedimentation of water droplets occurred for the untreated emulsion. Clearly, the addition of the phenolic resin significantly enhanced the water separation rate. The fact that η did not reach η_C indicates that some water still remained dispersed in the oil phase at the end of the experiment. Very importantly, while the bottle tests measure the amount of water that can be detected visually at the bottom of the

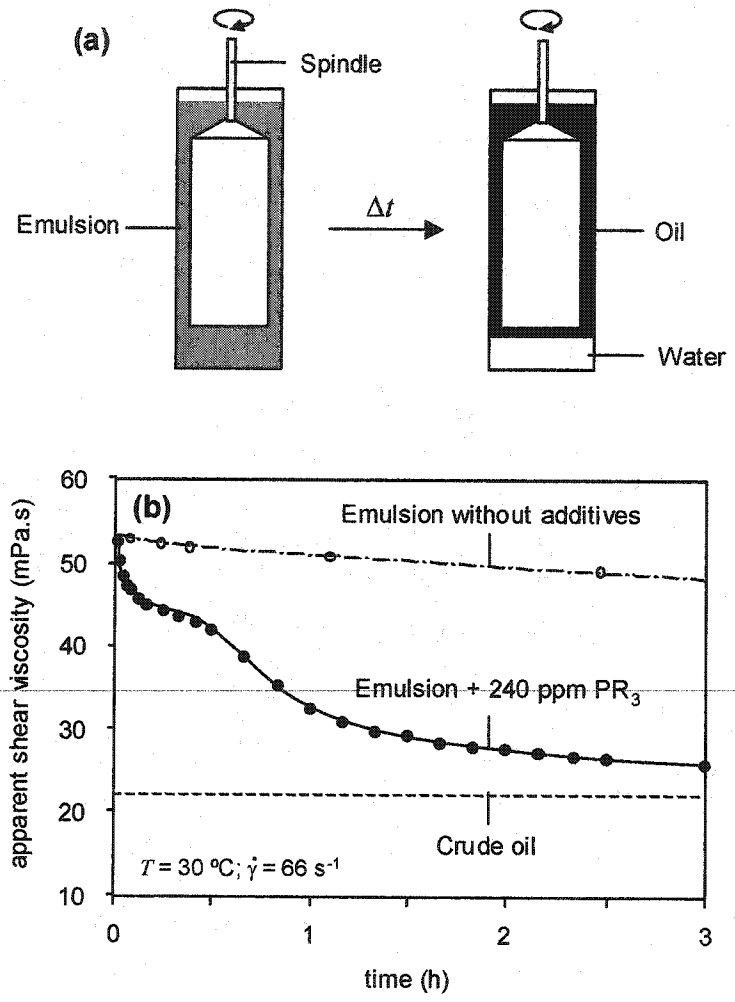


Figure 4.15. (a) Schematic representation of the events that take place in a viscosity test; (b) transient viscosity of an untreated emulsion (open circles) and of an emulsion treated with the phenolic resin PR_3. The viscosity of the crude oil SHU that is reported in Appendix B is also shown for comparison.

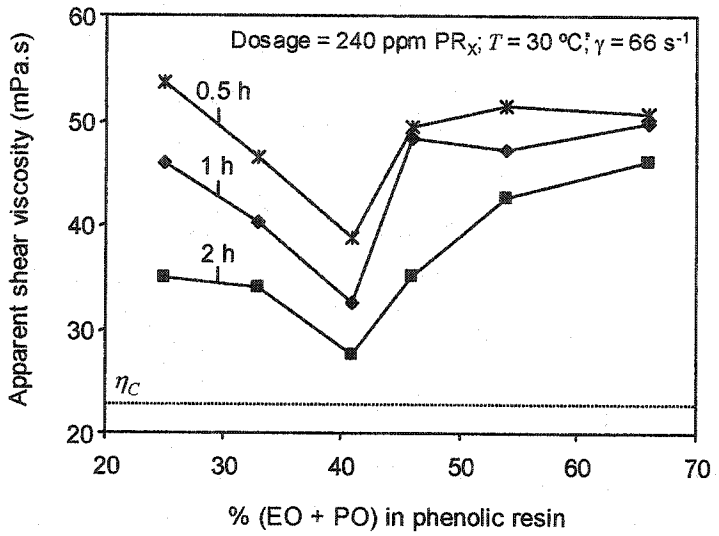


Figure 4.16. Effect of the EO/PO content of the phenolic resins on the transient behavior of the shear viscosity.

container, the viscosity test provides an indication of the amount of water that remains dispersed in the oil phase. Therefore, viscosity measurements can render information on changes in composition of the emulsion when visual observation is not possible, as shown later. Also, reporting the performance of a demulsifier in terms of its ability to reduce η can be appealing in practice, particularly when the demulsifier is advertised as a *viscosity reducer*, i.e. when it is expected to avoid or suppress the onset of high viscosities that are often associated with emulsion formation in oil extraction and transport operations.

Figure 4.16 shows viscosity measurements for emulsions treated with the phenolic resins PR_1 through PR_6 as a function of their EO/PO content at three different times and at T = 30 °C. It is seen that the decay in shear viscosity was more pronounced for the emulsion treated with the resin PR_3. This result is consistent with the bottle tests, and

also with the fact that emulsion stability is minimal at the optimum formulation for demulsification.

4.4.2. Performance of cross-linked polyurethanes

Bottle tests were performed at T = 30 °C by adding 240 ppm of cross-linked polyurethanes PU_Y to a set of emulsion samples. Figure 4.17 shows a picture of the samples five months after performing the experiment. In this case, a clear layer of decanted water did not form. Instead, the bottom of the samples exhibited a brownish coloration, which is indicative of a higher concentration of water droplets in that region (this coloration results from the refraction of light that is caused by water droplets near the glass [47]). The onset of this colored layer was already evident a few hours after the beginning of the test. These results show that cross-linked polyurethanes are not as effective as alkylphenol formaldehyde resins in promoting coalescence of droplets.

Figure 4.18 reports viscosity measurements for emulsion samples treated with the cross-linked polyurethanes at T = 30 °C. Data are reported at three different times as a function of the molecular weight of the cross-linked polymer. It is seen that these chemicals promote flocculation and settling, since the emulsion viscosity diminished with time in all cases. Furthermore, the decay in viscosity was significantly faster for the polymer exhibiting the highest molecular weight (PU_5). These results, along with the observations reported above from bottle tests, suggest that these molecules act mainly as flocculants and promote phase separation via group sedimentation (Figure 4.19, see also Section 1.2.4.1).

This hypothesis was tested in bottle tests in which 200 ppm of polymer PU_Y were added together with 40 ppm of the phenolic resin PR_3 at T = 30 °C. Results from such

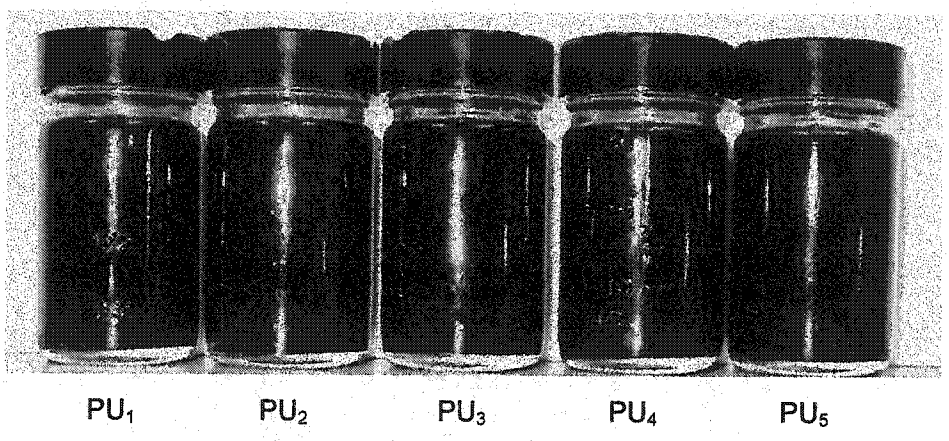


Figure 4.17. Appearance of the samples used in the bottle tests with the cross-linked polyurethanes PU_Y (240 ppm), five months after the beginning of the test.

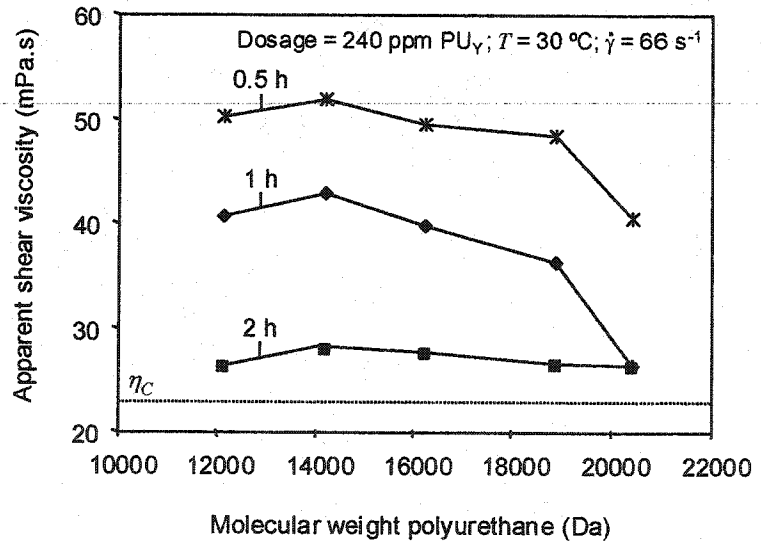


Figure 4.18. Effect of the molecular weight of the polyurethanes on the transient behavior of the shear viscosity.

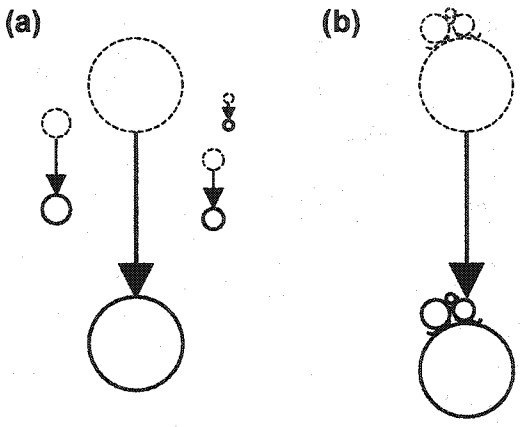
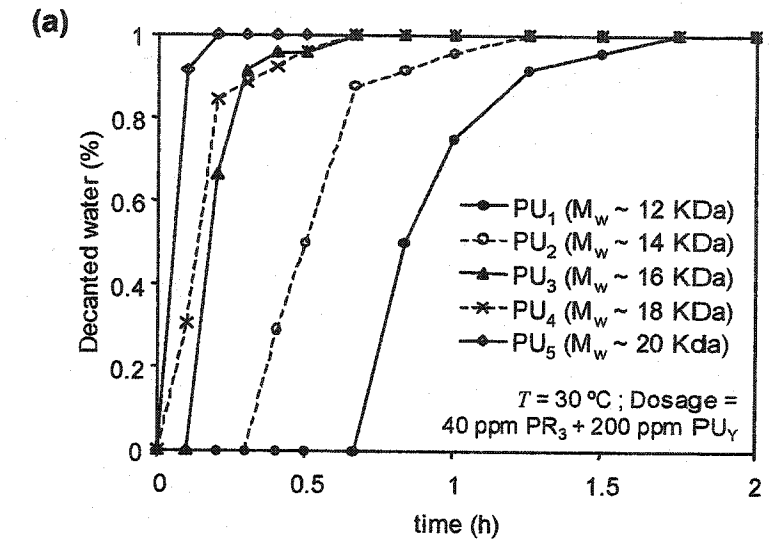


Figure 4.19. (a) schematic representation of droplets sedimenting individually (the lengths of the arrows are proportional to d^2); (b) the same droplets sedimenting in a single aggregate. Group sedimentation enhances the overall sedimentation rate.

tests are summarized in Figure 4.20. In all cases, complete water separation was achieved in 2 hours or less, and after only 12 minutes when the polyurethane with highest molecular weight (PU_5) was used. The time needed to separate 50 % of the water phase decreased monotonically from 26 min to 9 min as the molecular weight of the polyurethane was increased (Figure 4.21, triangles). These results (a) confirm that the effectiveness of the cross-linked polymer increases with its molecular weight. This finding is consistent with a mechanism postulating that these molecules act as flocculants, because as the molecular weight is increased, so does the number of polar groups present in the polymer molecule through which it can "anchor" at the water/oil interfaces; (b) suggest that the two chemistries (phenolic resins in combination with crosslinked polyurethane) act synergistically, because the time required for complete separation was significantly shorter than those that would be observed for the individual components (see Figs. 4.11 and 4.17). This synergistic action is evaluated and discussed more formally in the next section.

Equilibrium interfacial tension measurements were performed on the samples pictured in Figure 4.20 (b) one week after the beginning of the bottle test. Results from



(b)

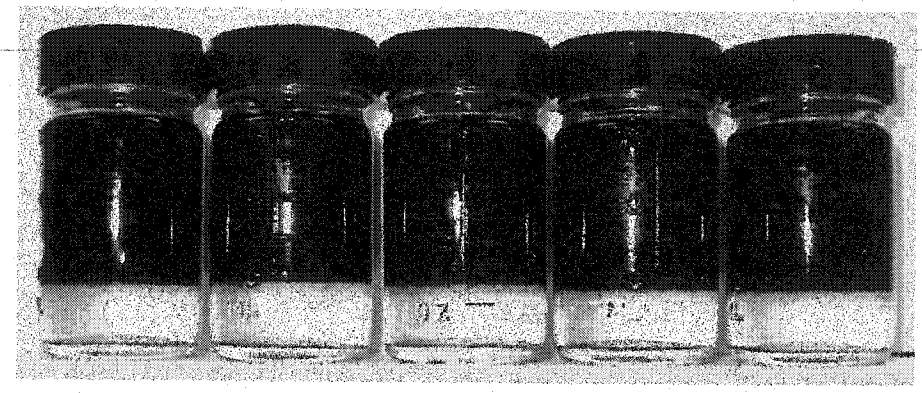


Figure 4.20. Effect of the molecular weight of the cross-linked polyurethane (200 ppm) on the transient amount of water separated in bottle tests, when dosed along with the phenolic resin PR_3 (40 ppm); (b) appearance of the samples one week after the beginning of the test.

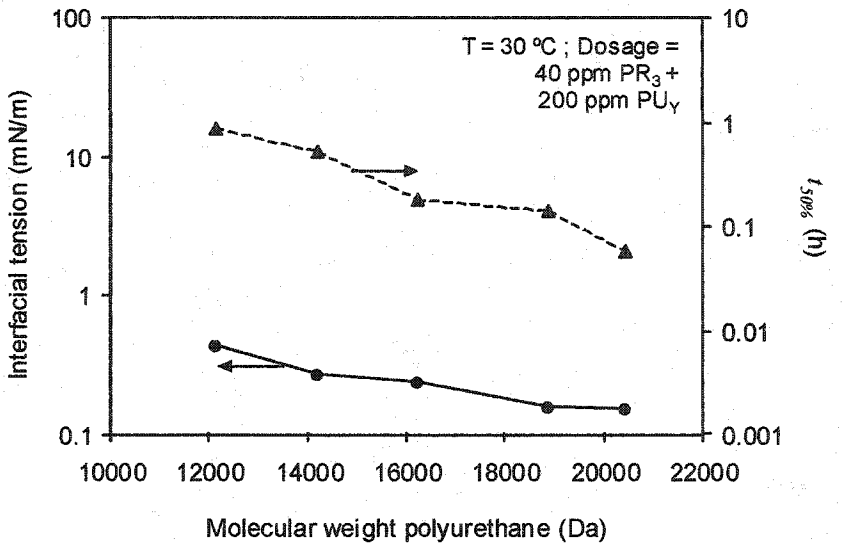
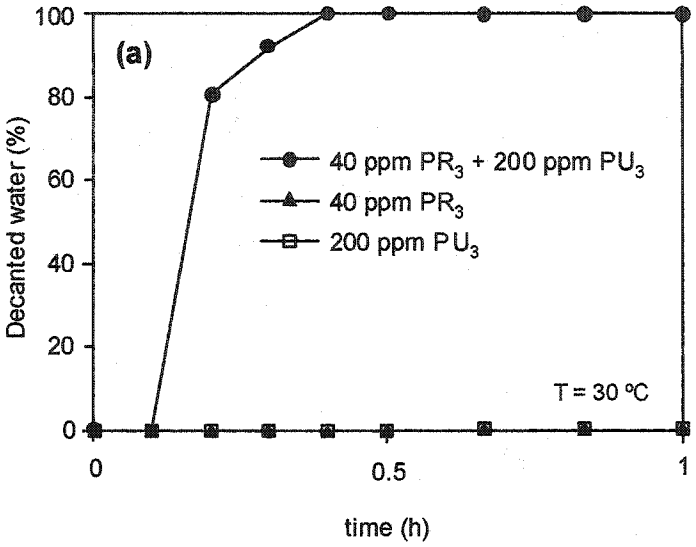


Figure 4.21. Effect of the molecular weight of the cross-linked polyurethane on the equilibrium interfacial tensions of emulsions treated with PU_Y (200 ppm) and 40 ppm of phenolic resin PR_3 (filled circles). The times required in bottle tests to decant 50 % of the brine initially present in the emulsion are also plotted (triangles).

such measurements are summarized in Figure 4.21. Interfacial tensions ranged between 0.43 mN/m and 0.15 mN/m, i.e., they were comparable to the minimum in interfacial tension that was obtained when testing the resin PR_3 in absence of cross-linked polyurethanes (Figure 4.14). These results indicate that the adsorption of polyurethanes at the water/oil interfaces does not alter significantly the balance of interaction energies at the water-oil interfaces that determine the optimum condition for demulsification and phase separation. As observed for the samples treated with phenolic resins only (Figure 4.14), a qualitative agreement was obtained in the trends for interfacial tension and $t_{50\%}$.

4.4.3. Synergistic action and overdosage effects

Figure 4.22 (a) shows bottle test results for emulsion samples treated with the phenolic resin PR_3, with the cross-linked polyurethane PU_3 and also with both chemicals



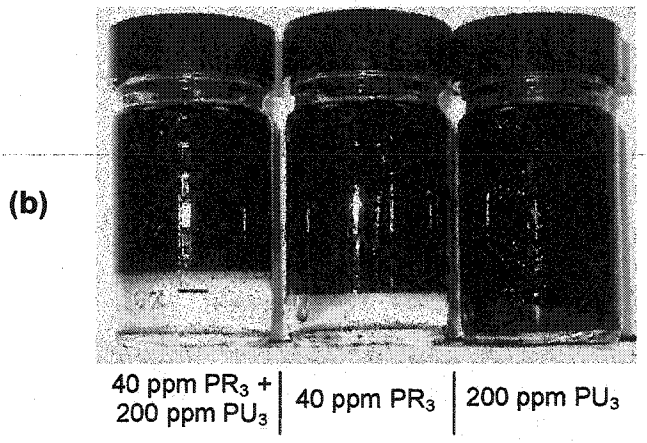
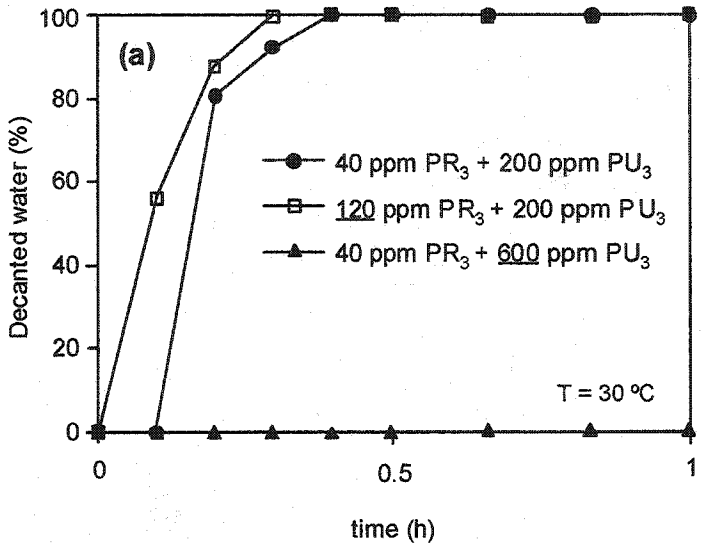


Figure 4.22. Results from a bottle test designed to screen the synergistic performance of phenolic resins and cross-linked polyurethanes; (b) appearance of the samples one day after the beginning of the test.

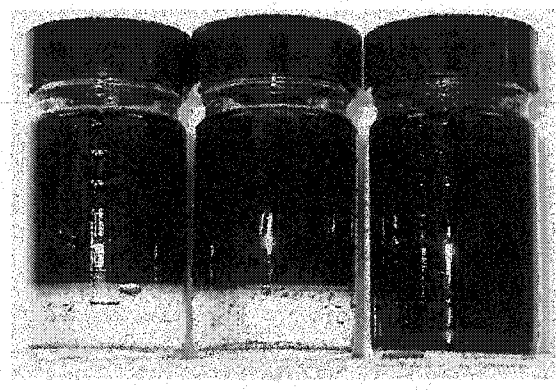
added simultaneously. It is seen that when both chemicals are added, complete separation occurs after 24 minutes. In contrast, no water separation was observed within the first hour when either chemical was added individually. Figure 4.22 (b) shows a picture of the emulsion samples 24 hours after the beginning of the test. It is seen that the phenolic resin does lead to water separation at a slower rate. Therefore, the cross-linked polyurethane seems to increase the rate at which the phenolic resin acts when promoting coalescence. A molecular mechanism is proposed to explain the synergistic action of these chemicals in section 4.5.

Figure 4.23(a) (previous page) shows results from bottle tests designed to evaluate the effect of overdosage on the performance of these chemicals. The reference system is the emulsion sample treated with 40 ppm of phenolic resin PR_3 and 200 ppm of polyurethane PU_3 that was reported in Figure 4.22(a). Two additional samples, one containing three times the former concentration of PR_3 (120 ppm) and equal concentration of PU_3 (200 ppm), and another treated with the same concentration of PR_3 (40 ppm) but thrice the reference concentration of PU_3 (600 ppm) were also tested. Results indicate that an increase in the concentration of PR_3 led to an increase in the rate of water separation, since the time needed to achieve complete separation was reduced from 24 min to 18 min. In contrast, separation of water was not observed for the sample treated with 600 ppm of PU_3. This result demonstrates that an excess of cross-linked polyurethane inhibits the occurrence of coalescence in the system.

Synergistic and inhibiting effects were also observed in experiments performed with other phenolic resins. Figure 4.24 shows measurements from bottle tests in which the performances of the resin PR_4 alone (diamonds) and in combination with the polyurethane PU_3 (filled circles) were tested. Firstly, it is seen that the addition of PU_3



(b)



40 ppm PR_3 + 200 ppm PU_3 | 120 ppm PR_3+ 200 ppm PU_3 | 40 ppm PR_3+ 600 ppm PU_3

Figure 4.23. Results from a bottle test designed to screen overdosage effects when using phenolic resins and cross-linked polyurethanes; (b) appearance of the samples one day after the beginning of the test.

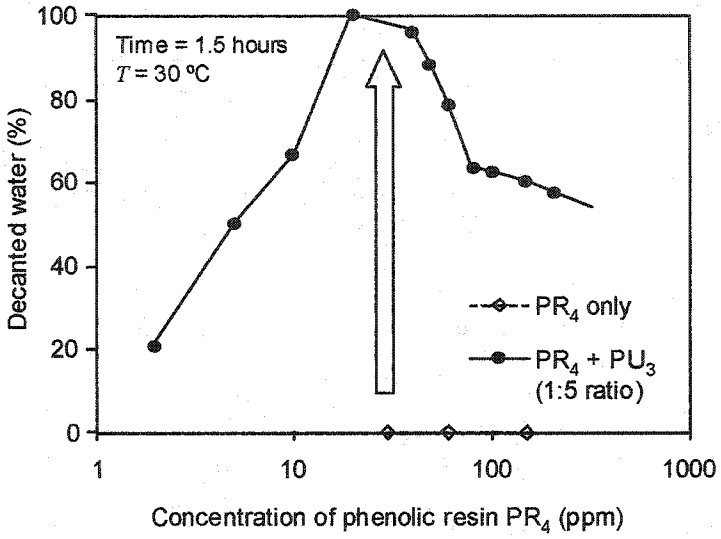


Figure 4.24. Results from bottle tests for emulsions treated with the phenolic resin PR_4 with (filled circles) and without (open circles) polyurethane PU_3. The arrows illustrate synergistic and inhibiting effects on the performance.

favored water separation. It is seen that none of the water phase would have separated in absence of the polyurethane within 1.5 hours, whereas complete separation can be obtained in that timeframe in the presence of such polymer (up arrow). This illustrates that, when added at an adequate dosage, crosslinked polyurethanes significantly enhance the performance of phenolic resins. However, an excessive dosage of polyurethane results in a significant reduction of the amount of water that coalesces to form a separate layer. For example, it is seen that the addition of PU_3 to emulsions treated with 240 ppm of PR_4, resulted in a reduction of the amount of water that is separated after 1.5 hours from nearly 100 % to approx. 50% (down arrow). This inhibiting effect is discussed further in section 4.5.

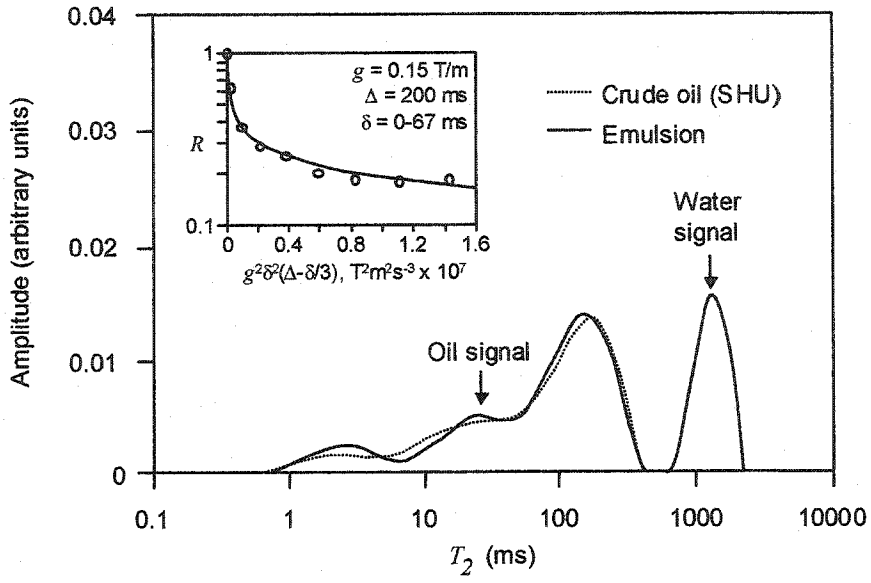


Figure 4.25. T_2 distribution of the emulsion used to follow-up the performance of demulsifiers via NMR. The inserted plot shows results from NMR-PGSE experiments for the same emulsion.

4.4.4. NMR characterization of emulsions undergoing phase separation

The nuclear magnetic resonance (NMR) techniques that were developed as part of this investigation (Chapter 3) were applied to evaluate how phenolic resins and cross-linked polyurethanes affect the drop size distribution of emulsions undergoing chemical demulsification.

Figure 4.25 shows a representative T_2 distribution of the emulsions that were used in these studies before the addition of demulsifier. Such distribution was obtained by performing a CPMG test as explained in Sections 3.2 and 3.5. In the CPMG experiments that are described in this section, 16 stacks were accumulated in all cases and an average noise level of 0.48% was obtained. It took approx. 4 minutes to complete each of these tests. For the particular test reported in Figure 4.25, two separate peaks were

obtained, one at short relaxation times that corresponds to the oil phase and another at long relaxation times corresponding to the water phase. The T_2 distribution did not change after 6 hours for emulsions that were not treated, thus indicating that coalescence and changes in drop sizes were negligible within such time frame in absence of demulsifiers. The inserted graphic in Figure 4.25 shows the attenuation profile that is obtained from PGSE test (Sections 3.3 and 3.5) performed on the same emulsion, plotted in the usual way of R vs. $g^2\delta^2(\Delta-\delta/3)$ (circles). Data from the CPMG and PGSE tests were combined as explained in section 3.4.3 to determine the drop size distribution of this emulsion, and the surface relaxivity ρ. The drop size distribution that is obtained by applying such procedure to the data reported in Figure 4.25 is shown later in Figure 4.30 (t = 0). The distribution exhibits a log-normal shape with geometric mean diameter d_{gV} = 11.5 μm and geometric standard deviation σ_g = 0.48. A surface relaxivity ρ = 0.85 μm/s was obtained in this case. This value is consistent with the surface relaxivities reported for emulsions of brine in SHU crude oil that were reported in Table 3.2. In what follows, this surface relaxivity is assumed constant when interpreting CPMG data for emulsions undergoing phase separation.

Figure 4.26 shows the T_2 distributions of the water phase for an emulsion treated with 240 ppm of phenolic resin PR_3. Since all the structural information for the determination of the drop size distribution is contained within the signal of the water phase, the relaxation times of the oil phase are omitted in this plot for the sake of simplicity. It is seen in Figure 4.26 that the addition of PR_3 led to a monotonic displacement of the T_2 distribution toward longer relaxation times. This trend suggests a reduction in the contribution of surface relaxativity to the relaxation of transverse magnetization and therefore to a reduction in the surface-to-volume ratio of the

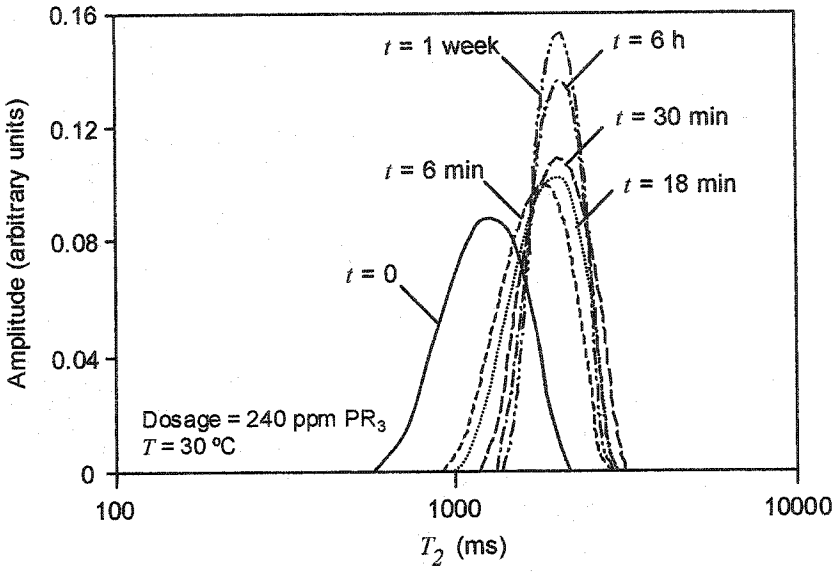


Figure 4.26. Evolution of the T_2 distribution of the water phase for an emulsion treated with 240 ppm of the phenolic resin PR_3. The distribution of the oil phase has been omitted to simplify the interpretation of the plot.

emulsion, provided that ρ remains relatively constant. Such reduction occurs as coalescence of water droplets takes place and large droplets form.

Figure 4.27(a) reports estimates for the transient drop size distribution of the emulsion treated with PR_3. These distributions were calculated from the T_2 distributions shown in Figure 4.26 using Eq. [3.4] and a surface relaxivity of 0.85 μm/s. Figure 4.27(b) shows essentially the same information, but plotting this time the Sauter mean diameter of the distribution d_{AV} (filled circles), which is calculated via Eq. [3.44], and the drop sizes that correspond to T_2 values for which $f_i = f_{i,MAX}/2$ (open circles), where $f_{i,MAX}$ is the volume fraction of protons with $T_2 = T_{2,LM}$ (see Eq. [3.45]). The range of drop sizes in between open circles is indicative of the dispersity of drop sizes present in the emulsion. The drop diameters that can be resolved for the set of conditions used in

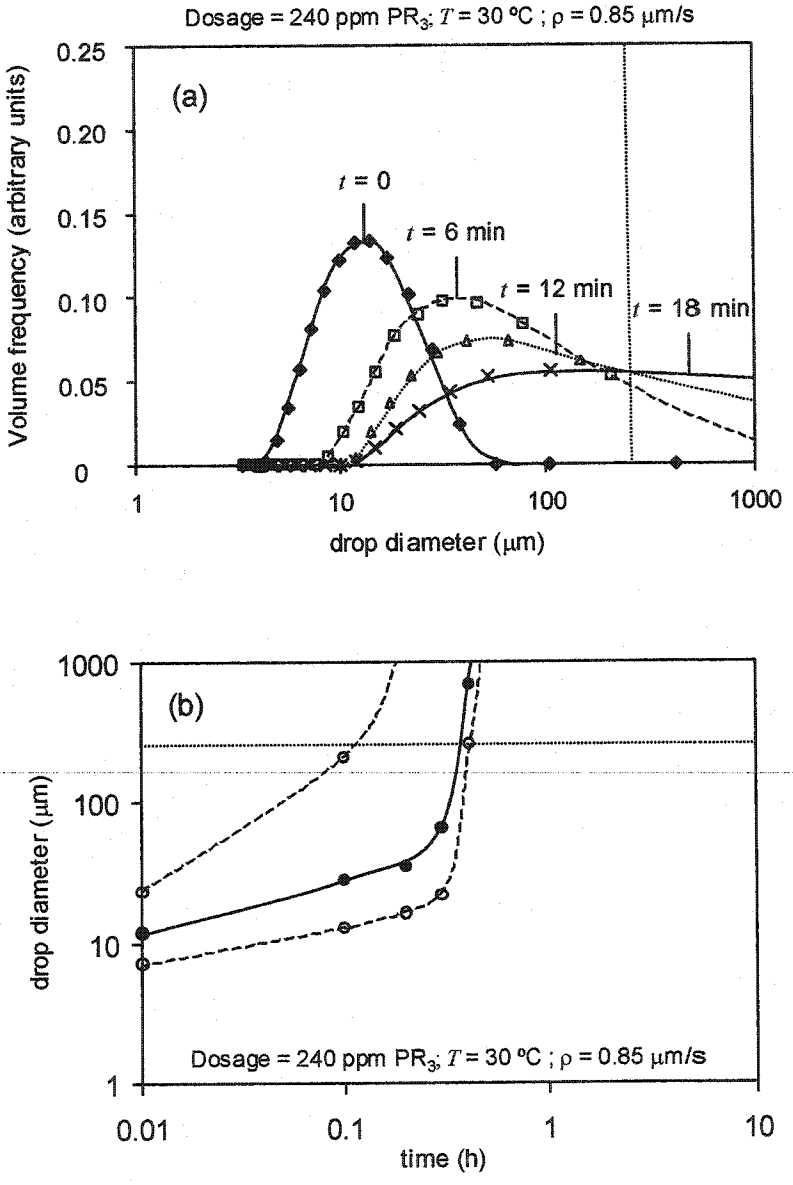


Figure 4.27. (a) Time-dependent drop size distribution of the emulsion treated with 240 ppm of phenolic resin PR_3; (b) transient behavior of the Sauter mean diameter d_{AV} (filled circles) and polydispersity (open circles) of the emulsion. The convention used to calculate the lower and upper limits shown in open circles is provided in the text.

these experiments range between 30 nm and 250 μm according to Eqs. [3.15] and [3.12], respectively. The maximum limit is indicated in Figure 4.27 with dotted lines.

Figure 4.27 indicates that the phenolic resin PR_3 promotes rapid and monotonic growth of the mean and polydispersity of droplet sizes. The marked widening of the drop size distribution is indicative of a separation process in which droplets coalesce against a layer of bulk fluid. In this case, a single coalescence event increases the radius of curvature of the drop from any given finite value to infinite. The ability of a drop to reach such layer is proportional to its initial position and sedimentation rate. Since the latter is proportional to d^2 (Eq. [1.8]), coalescence of large droplets is favored. This fact also influences the number of successful collision leading to coalescence, since larger drops travel faster throughout the bulk and therefore collide with a larger number of droplets per unit time. The fact that the drop size distribution shifts toward very large values in a very short time frame suggest that the phenolic resin acts mainly by reducing the energy barrier associated with the rupture of the thin films that form between approaching droplets, as discussed later.

The decanted water layer was separated from the oil phase one week after the beginning of the test and the phases were analyzed individually via NMR-CPMG. Figure 4.28 shows the T_2 distributions of the oil and water phases that were obtained from such analysis. The transverse relaxation of the water phase could be described with a single relaxation time of 2.0 s, which is moderately smaller than the one that is obtained for the brine before emulsification (2.7 s). A sample of brine containing 240 ppm of the phenolic resin PR_3 also rendered a bulk relaxation time of 2.7 seconds, thus indicating that the demulsifier does not contribute by itself to the observed reduction in $(T_{2,bulk})_w$. Therefore, it might be expected that some paramagnetic materials initially present in the crude oil

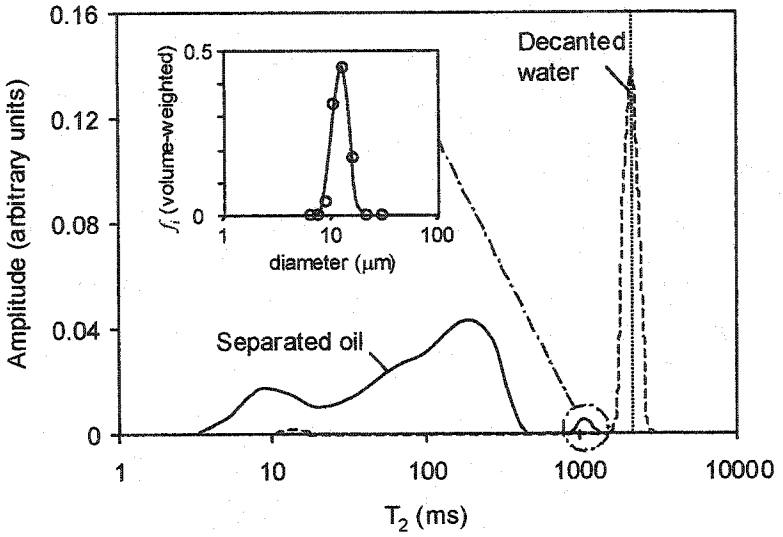


Figure 4.28. T_2 distributions of the oil and water phases that were separated by decantation from the emulsion treated with 240 ppm of phenolic resin PR_3, one week after the beginning of the experiment. The inserted plot shows the estimated drop size distribution for the droplets that remained dispersed in the oil phase.

were transferred to the aqueous phase while phase separation took place. This fact was considered when estimating the transient drop size distributions reported in Figure 4.27.

The T_2 distribution of the crude oil indicates that some water still remained dispersed after one week. The water signal that was detected is highlighted with a circle in Figure 4.28. The relative areas of the oil and water peak can be used to estimate the volume fraction of each of the phases (Eq. [3.17]). By doing so, it was found that the amount of water remaining in the oil (grind-out) is 0.7 % of the total volume of the initial emulsion, while the decanted water accounts for 28.7 %. The total water content is therefore 29.4 vol.%, which is very close to the actual value (30 %). This indicates that the phenolic resin is able to separate most, but not all the water present in the emulsion, as was noted earlier via viscosity measurements (Figure 4.15(b)).

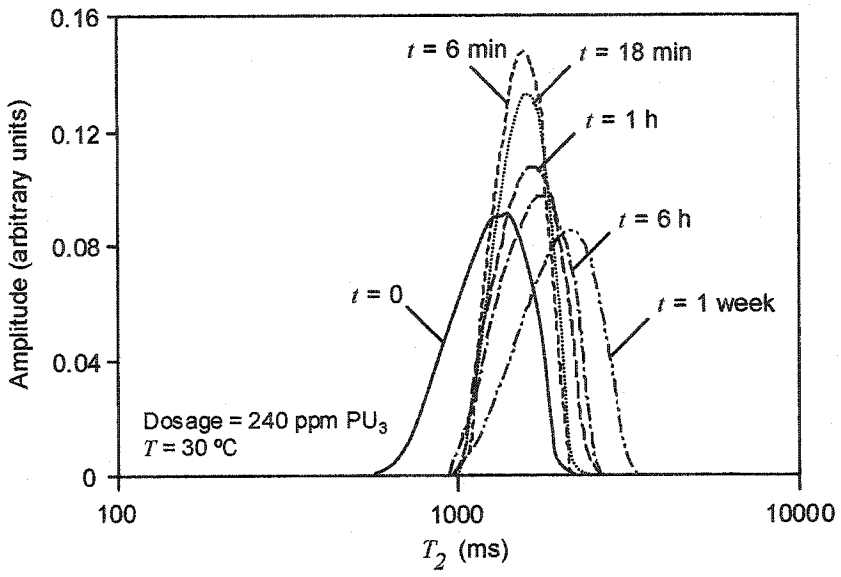


Figure 4.29. Evolution of the T_2 distribution of the water phase for an emulsion treated with 240 ppm of the cross-linked polyurethane PU_3. The distribution of the oil phase has been omitted to simplify the interpretation of the plot.

Figure 4.29 shows the T_2 distributions of the water phase for an emulsion treated with 240 ppm of cross-linked polyurethane PU_3. As in Figure 4.26, the relaxation times of the oil phase are omitted in this plot for the sake of simplicity. The T_2 distributions also exhibit in this case a monotonic displacement toward longer relaxation times. Nevertheless, the transient behavior of the T_2 distribution is different in this case. Within the first six minutes, the distribution becomes narrower as the fractions of the long relaxation times grow at the expense of the fractions of the short relaxation times. Afterwards, the distribution widens as the fractions of the long relaxation times grow and the fractions of the short relaxation times diminish.

An analogous trend is observed in the drop size distributions that are reported in Figure 4.30(a), which were estimated with the T_2 data summarized in Figure 4.29 using a surface relaxivity of 0.85 μm/s. In this case, it is seen that within the first 6 minutes after

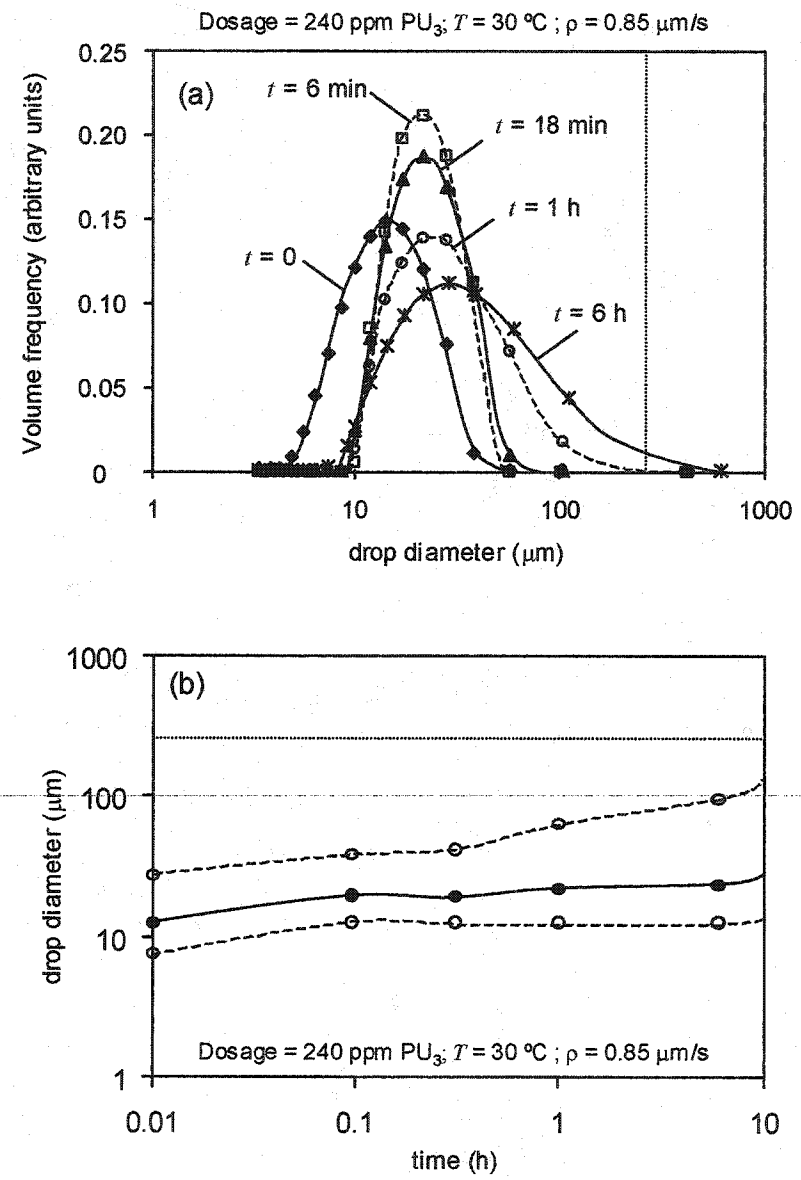


Figure 4.30. (a) Time-dependent drop size distribution of the emulsion treated with 240 ppm of cross-linked polyurethane PU_3; (b) transient behavior of the Sauter mean diameter d_{4V} (filled circles) and polydispersity (open circles) of the emulsion. The convention used to calculate the lower and upper limits shown in open circles is provided in the text.

dosage, small droplets had been removed from the emulsion. In consequence, the width of the distribution diminished. Afterwards, a slow but steady growth of the large droplets is observed along with an increase in the polydispersity of drop sizes. It becomes clear from the data reported in Figure 4.30 (b) that the growth in mean size and polydispersity is much slower in this case when compared with the corresponding trends that were obtained for the emulsion treated with the phenolic resin (Figure 4.27).

Since a water layer is not collected at the bottom of the container when the emulsion is treated with a cross-linked polyurethane alone (see Figure 4.17), CPMG experiments were performed in the presence of a magnetic field gradient in order to resolve the water/oil composition in different regions of the sample. When a gradient of strength g is imposed, the steady magnetic field is not uniform in space and the Larmor frequency depends on the position of the nuclei [$\omega(r) = \gamma B(r)$]. Two spins at positions r_1 and r_2, such that $B(r_1) \neq B(r_2)$, precess at different Larmor frequencies. The coil ("antenna") of the spectrometer is tuned to measure the response of the region where spins precess at a specific Larmor frequency ω_0. Therefore, only those spins are sensed by the spectrometer. This principle, which is pervasively applied in petrophysical and logging applications [48] and other fields, allows characterizing "slices" of the sample of interest. In this case, an additional contribution to the relaxation time T_2 is caused by the diffusion of the spins in the field gradient and Eq. [3.2] becomes [48]:

$$\frac{1}{T_{2,i}} = \frac{1}{T_{2,bulk}} + \rho\left(\frac{S}{V}\right)_i + \frac{(\gamma g t_E)^2 D}{12} \qquad [4.6]$$

where $t_E = 2\tau$ is the time between consecutive echoes (see Figure 3.1).

Figure 4.31 shows the T_2 distributions that were obtained after applying the above-mentioned technique on three regions (top, middle and bottom) of the sample treated

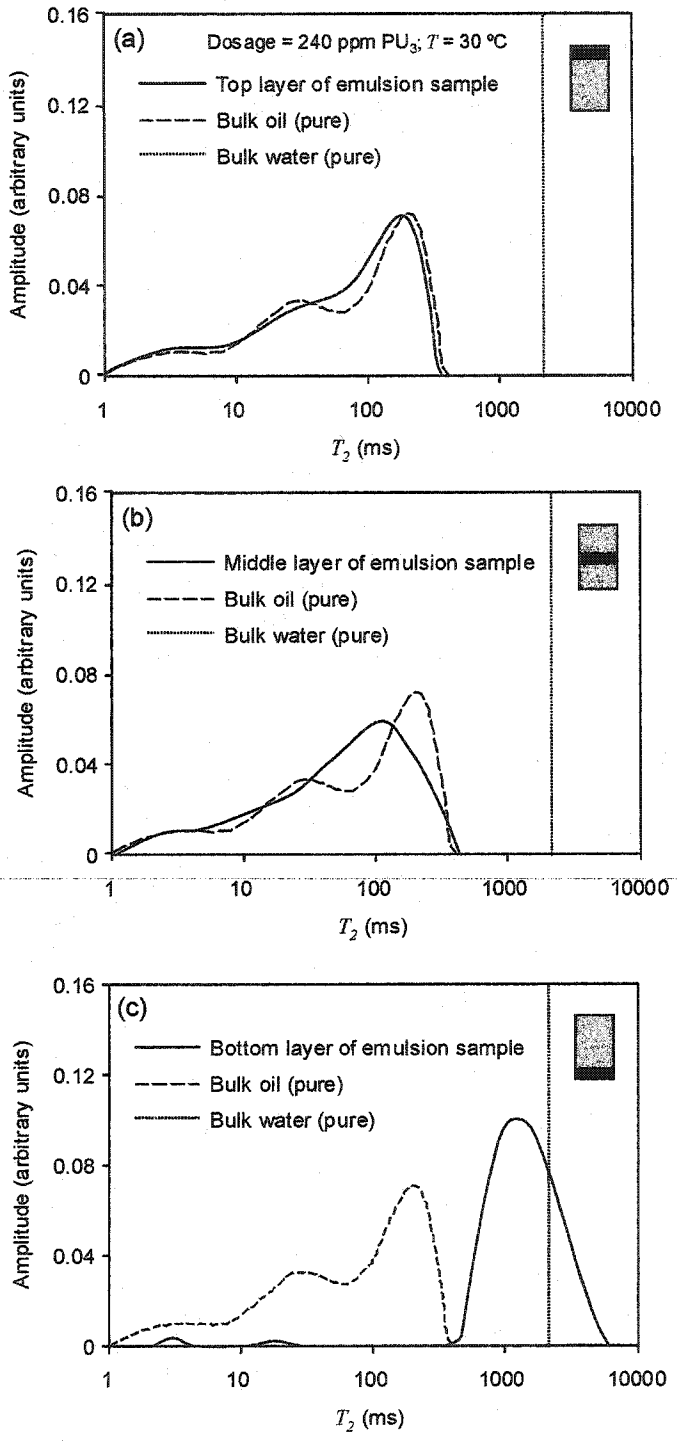


Figure 4.31. T_2 distributions of selected regions of the emulsion treated with 240 ppm of cross-linked polyurethane PU_3, one week after the beginning of the experiment.

with the polyurethane PU_3 one week after the beginning of the test. The T_2 distributions of the crude oil (dashed line) and of the brine (dotted line) are also shown as reference. The relaxation of the brine was well described with a single relaxation time T_2 = 2.2 s. This value agrees well with the T_2 that is calculated from Eq. [4.6] in the limit $S/V \rightarrow 0$ (T_2 = 2.3 s). The experiments were performed using t_E = 400 μs and g = 0.132 T/m. 16 stacks were accumulated in all cases and an average noise level of 2.3 % was obtained. The volume fraction of the sample that was analyzed using this technique was 0.125. This value was determined from the ratio of the initial magnetization in presence and in absence of a magnetic field gradient using a pure fluid as reference (water in this case). Therefore, the "slices" that were characterized out of a sample of 38 mm in height had a thickness of 4.8 mm. Figure 4.31 indicates that only oil was present in the top and middle regions of the sample, while the water phase was collected at the bottom. This assessment agrees with previous observations in bottle and viscosity tests which indicated that the cross-linked polyurethane promotes sedimentation of water droplets, even though a clear layer of decanted water is not observed at the bottom of the container. The observations on Figure 4.30 regarding the ability of PU_3 to collect small droplets in a short timeframe and the absence of water droplets in most of the sample (Figure 4.31) indicate that this chemical can be used to remove small drops that otherwise would be 'left behind' when using chemicals that promote fast coalescence, such as the phenolic resins tested here.

Finally, an experiment with samples treated with a mixture of a phenolic resin (PR_3, 40 ppm) and a cross-linked polyurethane (PU_3, 200 ppm) was also performed. When both components were added, drop sizes grew beyond the resolution limit of the

technique (d_{MAX} = 250 μm) within the time that takes to complete a CPMG test (4 minutes). This fact demonstrates that both components act synergistically as was demonstrated in Section 4.4.3.

4.5. ON THE MECHANISM OF CHEMICAL DEMULSIFICATION

The results shown in preceding sections for emulsions treated with alkylphenolformaldehyde indicate that performance was optimum with a resin exhibiting an intermediate content of polar (polyoxyethylene/polyoxypropylene) groups. At such composition: (1) the maximum water separation rate was observed; (2) the decay in shear viscosity was also more pronounced; (3) the equilibrium interfacial tension was minimal; (4) performance was affected by temperature in a manner consistent with conventional knowledge for the behavior of polyalkoxylated surfactants at the optimum formulation condition for microemulsion formation; (5) NMR measurements indicated that the mean size and the polydispersity of drop sizes grew monotonically in time, in a relatively short timescale (minutes to a few hours). These results suggest that, at the optimum condition for phase separation, phenolic resins promote *fast coalescence without significant aggregation*.

In contrast, the cross-linked polyurethanes promoted *aggregation* of droplets. It was found that that the performance of these chemicals improved as their molecular weight increased. Interfacial tension data suggest that these compounds do not alter significantly the condition for optimum formulation referred to above when they are dosed along with phenolic resins. NMR measurements indicated that the mean size grew monotonically in time, but at a significantly slower pace than the one observed for phenolic resins (hours to days). Interestingly, during the first minutes of the test, the drop size distribution exhibited a reduction in polydispersity at the expense of the removal of

small drops. These results show that high molecular weight molecules such as the polyurethanes used in this study can remove small droplets from the bulk oil very efficiently, as mentioned by Breen *et al.* [27]. It was also demonstrated via NMR that these polymers removed droplets from the oil phase, but did not promote their coalescence once they were collected at the bottom of the sample. The data reported in this chapter suggest that cross-linked polyurethanes lead to phase separation via *fast aggregation and slow coalescence*.

When a phenolic resin and a cross-linked polyurethane are dosed concomitantly, water separation takes place at a much faster rate (seconds to a few minutes). In this case, both types of molecules play synergistic roles. Firstly, the phenolic resins may displace the indigenous materials (asphaltenes/resins) adsorbed at the water-oil interfaces, thus disrupting the rigid network of colloidal asphaltenes that otherwise would stabilize the drops against coalescence [Figures 4.32(a.1) and 4.32(a.2)]. This would lead to the formation of "patches" of adsorbed asphatenes surrounded by continuous regions depleted of these materials (see Figure 4.8). Kilpatrick [18] has coined the term "islands of aromaticity" to refer to these isolated asphaltene domains. Depleted regions of two nearby droplets may get in contact while the film that separates them is drained. Following the ideas of Vrij [49], varicose capillary waves may develop in these regions and a hole can be formed when two waves at opposite interfaces touch each other [Figures 4.32(a.3)]. The fact that the trends for water separation performance and interfacial tension were in qualitative agreement (Figure 4.14) supports the notion that the formation of holes dictates the onset of coalescence (see Section 1.2.4.3, Eq. [1.22]). Coalescence will take place if the hole that is formed is able to overcome the energy penalty that is involved in the reversion of the interfacial curvature and the expansion of the film against the film of adsorbed materials [Figure 4.32(a.4)].

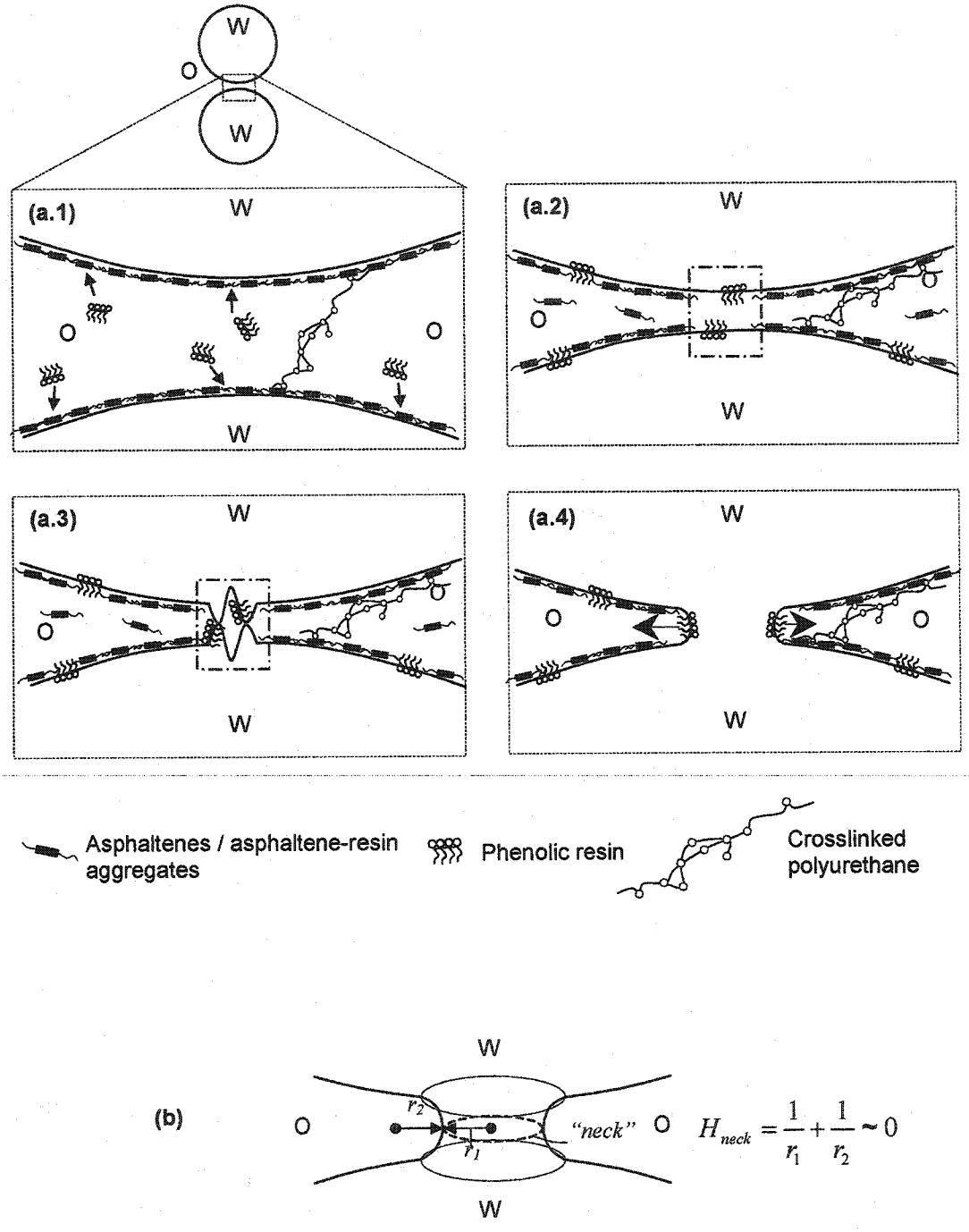


Figure 4.32. (a) Plausible conformation of indigenous materials (asphaltenes/asphaltene-resin aggregates), phenolic resin and cross-linked polyurethane molecules at the water-oil interface when two water drops approach each other and the formation of a "hole" takes place; (b) schematic representation of the hole, showing the region of near-zero interfacial curvature.

According to Kabalnov and Wennerström [50], the attainment of the optimum formulation notably increases the rate of phase separation in emulsions because at this physicochemical condition, the spontaneous curvature of the interfacial film is zero. Near-zero curvature can be attained locally at the neck of the hole (Figure 4.32 (b)). Therefore, the phenolic resin with balanced affinity for both phases minimizes the energy penalty that is involved in the onset and expansion of a region with local reverse curvature (hole) that precedes coalescence.

Following Kabalnov and Wennerström's ideas, the onset of reverse curvature and coalescence in W/O emulsions should be favored as more hydrophilic phenolic resins are used as demulsifiers. However, the water separation rate diminished when the EO/PO content of the phenolic resins was increased beyond the optimum value (Figure 4.12). This can be explained by considering that as more hydrophilic phenolic resins were dosed, the interfacial tension increased (Figure 4.14). The referred increase in interfacial tension would have led to a reduction of the probability of hole formation via overlapping of varicose capillary waves in opposite interfaces, as mentioned above. If this interpretation is correct, the kinetics of coalescence are dictated primarily by the probability of forming new holes, and secondarily by the ability to overcome the energy penalty involved in the expansion of such holes.

Secondly, it is plausible to think that polyurethanes acted as "bridges" between drops, thus increasing the average time in which two nearby drops remain close to each other and therefore the probability for collisions leading to a successful coalescence event (Figure 4.32 (a.2)). Coalescence events would also be favored by the fact that polyurethane molecules promoted group sedimentation (Figure 4.19), since both the rate

of sedimentation and the cross-sectional area of the flocculate undergoing sedimentation increase (see section 1.2.4.1).

Finally, it was observed that when an excess of cross-linked polyurethane was added, coalescence was retarded probably due to significant changes in the composition of the interfacial film leading to steric stabilization (see discussion for Figure 1.5). It can be concluded that when both components are added concomitantly and at the right dosage, *fast aggregation* (promoted mainly by a cross-linked polyurethane) *and fast coalescence* (aided by the presence of a phenolic resin) occur.

4.6. REFERENCES

1. S.E. Friberg, Emulsion stability, in "Emulsions - a fundamental and practical approach", J. Sjöblom, Editor. Kluwer Academic Publishers, Dordretch, 1991, pp. 1-24.
2. P. Walstra, Emulsion stability, in "Encyclopedia of Emulsion Technology", P. Becher, Editor. Vol. 4. Marcel Dekker, Inc., New York, 1990, pp. 1-62.
3. P. Becher, "Emulsions. Theory and Practice", Oxford University Press, New York, 2001.
4. D. Espinat, E. Rosemberg, M. Scarsella, L. Barre, D. Fenistein, and D. Broseta, Colloidal structural evolution from stable to flocculated state of asphaltene solutions and heavy crudes, in "Structure and dynamics of asphaltenes", O. Mullins and E. Sheu, Editors, Plenum Press, New York, 1998.
5. J.G. Speight and S.E. Moschopedis, On the molecular nature of petroleum asphaltenes, in "Chemistry of asphaltenes", J.W. Bunger and N.C. Li, Editors, Surfactant Science Series, Vol. 195. American Chemical Society, Washington, D. C., 1981.
6. O.P. Strausz, T.W. Mojelski, and E.M. Lown, The molecular structure of asphaltene - an unfolding story, *Fuel*, **71** (1992) *1355-1363*
7. K.L. Gawrys, P.M. Spiecker, and P.K. Kilpatrick, The role of asphaltene solubility and chemical composition on asphaltene aggregation, *Petr. Sci. Technol.*, **21** (2003) *461-489*
8. K.A. Ferworn and W.Y. Svrcek, Characterization and phase behavior of asphaltenic crude oils, in "Structure and dynamics of asphaltenes", O. Mullins and E. Sheu, Editors. Plenum press, New York, 1998.
9. J. McLean, P.M. Spiecker, A. Sullivan, and P.K. Kilpatrick, The role of petroleum asphaltenes in the stabilization of water-in-oil emulsions, in "Structure and dynamics of asphaltenes", O. Mullins and E. Sheu, Editors, Plenum Press, New York, 1998.
10. T.F. Yen, J.G. Erdman, and S.S. Pollack, Investigation of the structure of petroleum asphaltenes by X-ray diffraction, *Analyt. Chem.*, **33** (1961) *1587-1594*

11. J.P. Dickie and T.F. Yen, Macrostructures of the asphaltic fractions by various instrumental methods, *Analyt. Chem.*, **39** (1967) *1847-1852*

12. J. Czarnecki and J. Masliyah, Emulsion studies associated with bitumen recovery from Canadian oil sands: Part II. "Proceedings of the 3rd International Conference on Petroleum Phase Behavior and Fouling", New Orleans, USA, 2002, pp. 323-328

13. A. Goldszal, M. Bourrel, C. Hurtevent, and J.-L. Volle, Stability of water in acidic crude oil emulsions, "Proceedings of the 3rd International Conference on Petroleum Phase Behavior and Fouling", New Orleans, USA, 2002, pp. 386-400

14. Y.H. Kim, A.D. Nikolov, D. Wasan, H. Díaz-Arauzo, and C.S. Shetty, Demulsification of water-in-crude oil emulsions: effects of film tension, elasticity, diffusivity and interfacial activity of demulsifier individual components and their blends, *J. Disp. Sci. Technol.*, **17** (1996) *33-53*

15. J.E. Strassner, Effect of pH on interfacial films and stability of crude oil-water emulsions, *J. Petrol. Tech.*, March (1968) *303-312*

16. S.E. Taylor, Resolving crude oil emulsions, *Chemistry & Industry*, **20** (1992) *770-773*

17. J. Masliyah, Z. Xu, K. Nandakumar, A. Yeung, and J. Czarnecki, Emulsion studies associated with bitumen recovery from Canadian oil sands: Part I, "Proceedings of the 3rd International Conference on Petroleum Phase Behavior and Fouling", New Orleans, USA, 2002, pp. 316-322

18. P.K. Kilpatrick, Water-in-oil emulsion stabilization in petroleum-water mixtures by asphaltenes and naphthenates, "Proceedings of the 3rd World Congress on Emulsions" (CD), Lyon, France, September 24-27, 2002.

19. M.v.d. Waarden, Stability of emulsions of water in mineral oils containing asphaltenes, *Kolloid Z.*, **156** (1958) *116-122*

20. D.D. Eley, M.J. Hey, and J.D. Symonds, Emulsions of water in asphaltene-containing oils. 1. droplet size distribution and emulsification rates, *Colloids Surf.*, **32** (1988) *87-101*

21. J. McLean and P.K. Kilpatrick, Effect of asphaltene aggregation in model heptane-toluene mixtures on stability of water-in-oil emulsions, *J. Colloid Interface Sci.*, **196** (1997) *23-34*

22. D.T. Wasan and A.D. Nikolov, Structure and stability of emulsions, in "Encyclopedic Handbook of Emulsion Technology", J. Sjöblom, Editor, Marcel Dekker, Inc., New York, 2001, pp. 59-70.

23. K. Khristov, S.D. Taylor, J. Czarnecki, and J. Masliyah, Thin Liquid Film Technique - applications to water-oil-water bitumen emulsion films, *Colloids Surf. A.: Phys. Chem. Eng. Aspects*, **174** (2000) *183-196*

24. K. Lissant, "Demulsification", Surfactant Science Series, Vol. 13. Marcel Dekker, Inc., New York, 1983.

25. C.W. Angle, Chemical demulsification of stable crude oil and bitumen emulsions in petroleum recovery - a review, in "Encyclopedic handbook of emulsion technology", J. Sjöblom, Editor. Marcel Dekker, Inc., New York, 2001, pp. 541-594.

26. F. Staiss, R. Bohm, and R. Kupfer, Improved demulsifier chemistry: a novel approach in the dehydration of crude oil, *SPE Prod. Eng.*, (1991) *334-338*

27. P.J. Breen, A. Yen, and J. Tapp, Demulsification of asphaltene-stabilized emulsions - correlation of demulsifier performance with crude oil composition, "Proceedings of the 3rd International Conference on Petroleum Phase Behavior and Fouling", New Orleans, USA, 2002, pp. 359-366

28. J. Sjöblom, E.E. Johnsen, A. Westvik, M.-H. Ese, J. Djuve, I.H. Auflem, and H. Kallevik, Demulsifiers in the oil industry, in "Encyclopedic handbook of emulsion technology", J. Sjöblom, Editor, Marcel Dekker, New York, 2001, pp. 595-619.

29. P.J. Breen, in *Surfactant adsorption and surface solubilization*, R. Sharma, Editor, ACS Symposium Series. Vol. 615. American Chemical Society, Washington, D. C., 1995, pp. 268-279.

30. S. Mukherjee and A.P. Kushnick, Effect of demulsifiers on interfacial properties governing crude oil demulsification, in "Oil field chemistry: enhanced recovery and production stimulation", T.F. Borchardt and T.F. Yen, Editors. ACS Symposium Series. Vol. 396, American Chemical Society, Washington, D. C., 1989. pp. 364-374

31. M.-H. Ese, L. Galet, D. Clausse, and J. Sjöblom, Properties of Langmuir surface and interfacial films built up by asphaltenes and resins: influence of chemical demulsifiers, *J. Colloid Interface Sci.*, **220** (1999) *293-301*

32. M. Li, B. Peng, X. Zheng, and Z. Wu, Interfacial rheology of crude oil emulsions, in "Encyclopedic handbook of emulsion technology", J. Sjöblom (Eds.), Marcel Dekker, Inc., New York, 2001, pp. 515-524.

33. A.K. Malhotra and D.T. Wasan, Interfacial rheological properties of adsorbed surfactant films with applications to emulsion and foam stability, in "Thin liquid films", I. Ivanov, Editor. Surfactant Science Series, Vol. 29. Marcel Dekker, Inc., New York, 1988, pp. 829-890.

34. M.A. Krawczyk, D.T. Wasan, and S.S. Chandrashekar, Chemical demulsification of petroleum emulsions using oil-soluble demulsifiers, *Ind. Eng. Chem. Res.*, **30** (1991) *367-375*

35. T.F. Tadros, Rheological properties of emulsion systems, in "Emulsions - a fundamental and practical approach", J. Sjöblom, Editor. Kluwer Academic Publishers, Dordretch, 1991.

36. X. Yang, W. Lu, M.-H. Ese, and J. Sjöblom, Film properties of asphaltenes and resins, in "Encyclopedic Handbook of Emulsion Technology", J. Sjöblom, Editor. Marcel Dekker, Inc., New York, 2001, pp. 525-540.

37. R.J. Hunter, "Foundations of colloidal science", Oxford University Press, Oxford, UK, 2001.

38. A.-A. Abdel-Azim, N.N. Zaki, and N.E.S. Maysour, Polyalkoxylated amines for breaking water-in-oil emulsions: effect of structural variations on the demulsification efficiency, *Polym. Adv. Technol.*, **9** (1998) *159-166*

39. M. Amaravathi and B.P. Pandey, Ethylene oxide-propylene oxide copolymers as demulsifiers for petroleum emulsions, *Research and Industry*, **36** (1991) *198-202*

40. K.J. Saunders, "Organic polymer chemistry", Chapman and Hall, London, 1973.

41. G. Odian, "Principles of polimerization", John Wiley & Sons, Inc., New York, 1991.

42. A. Goldszal and M. Bourrel, Demulsification of crude oil emulsions: correlation to microemulsion phase behavior, *Ind. Eng. Chem. Res.*, **39** (2000) *2746-2751*

43. P.D. Berger, C. Hsu, and J.P. Arendell, Designing and selecting demulsifiers for optimum field performance on the basis of production fluid characteristics, *SPE Prod. Eng.*, November (1988) *522-526*

44. P. Winsor, "Solvent properties of amphiphilic compounds", Butterworths, London, 1954.

45. J.L. Salager, Guidelines for the formulation, composition and stirring to attain desired emulsion properties (type, droplet size, viscosity and stability), in "Surfactants in Solution", A.K. Chattopadhyay and K.L. Mittal, Surfactant Science Series, Vol. 64. Marcel Dekker, New York, 1996, pp. 261-295.

46. R. Antón and J.L. Salager, Emulsion instability in the three-phase behavior region of surfactant-alcohol-oil-brine systems, *J. Colloid Interface Sci.*, **111** (1986) *54-59*

47. D.J. McClements, Theoretical prediction of emulsion color, *Adv. Colloid Interface Sci.*, **97** (2002) *63-89*

48. K.-J. Dunn, D.J. Bergmann, and G.A. Latorraca, "Nuclear magnetic resonance. Petrophysical and logging applications", Pergamon Press, Oxford, UK, 2002.

49. A. Vrij, Posible mechanism for the spontaneous rupture of thin free liquid films, *Disc. Faraday Soc.*, **42** (1966) *23-33*

50. A.S. Kabalnov and H. Wennerström, Macroemulsion stability: The oriented wedge theory revisited, *Langmuir*, **12** (1996) *276-292*

Chapter 5
Conclusions and Future Work

5.1. Conclusions

5.1.1. Destabilization of emulsions via mass transfer (Chapter 2)

The solubilization rates of individual drops of linear alkanes (n-octane, n-nonane, n-decane and n-undecane) and n-octane/n-undecane, n-decane/n-undecane, n-octane/squalane and n-decane/squalane mixtures in aqueous $C_{12}E_8$ solutions (2.5 wt. %) were limited by interfacial resistance to mass transport, not by diffusion in the surfactant solution. Numerical results from models built on plausible assumptions correlated well with the data obtained in solubilization tests. In particular, data consistently showed that the partitioning of squalane between the oil drop and the micelles was negligible, a fact that eased considerably the mathematical treatment of mass transport and vindicated the proposed modeling.

A model was proposed to evaluate mass transfer in polydisperse emulsions, limited to the case in which one solute is transferred from drop to bulk solution and vice versa. This model assumes transport rates dictated by interfacial resistance, and not by molecular or micellar diffusion in the surfactant solution. It was satisfactorily used to simulate results from three experiments reported in literature for mass transfer in emulsions of hydrocarbons dispersed in aqueous nonionic surfactant solutions, namely, the solubilization of drops in an undersaturated surfactant solution, the Ostwald ripening of a single emulsion and the compositional ripening of a mixed emulsion.

Simulations for tests in which mass transport took place at a bulk concentration below the solubility limit (solubilization, compositional ripening) showed that considering

the polydispersity in drop sizes significantly improved the agreement between predicted and experimental transient characteristics such as the mean drop size or the concentration of solute in the surfactant solution. Also, it was demonstrated that the trends that are observed for the transient drop size distribution or the mean size of drops undergoing solubilization are heavily influenced by the basis (number, area or volume of droplets) on which these properties are reported.

Calculations for the Ostwald ripening experiment indicated that mass transfer was not limited by diffusion. They strongly suggest that mass transfer was controlled by events taking place at the interfaces and that the experimental ripening rate is somewhat higher than its corresponding theoretical value due to phenomena not included in the model such as enhanced transport between drops that have flocculated and are nearly in contact. The extension of the LSW theory presented in this work for interface-controlled Ostwald ripening of emulsions was validated via numerical simulations.

The surfactant concentration had a complex influence on solubilization kinetics. Solubilization experiments for single drops of n-octane in aqueous solutions indicated that, in the absence of surfactant, mass transport is limited by the molecular diffusion of the alkane in water. For drops of n-octane in surfactant solutions at concentrations above the *cmc*, incorporation of oil in micelles and further transport of such micelles across the aqueous phase dictated the rates of solubilization. At low surfactant concentrations, both interfacial resistance and diffusional resistance to micellar transport were significant. As the surfactant concentration was increased, spontaneously-generated convection was observed. The characteristic velocities of the convective currents were found to increase with surfactant concentration and to decrease with drop size. Convection reduced the diffusional resistance to mass transport, leaving interfacial

resistance as the rate-controlling mechanism for moderate and large surfactant concentrations. The analysis of the solubilization data with a model that considers mixed kinetics in the presence of convection suggests that the mass transfer coefficient at the water-oil interfaces is nearly proportional to the first power of the surfactant concentration. This finding supports the hypothesis that adsorption/fusion of micelles at the interface, followed by desorption/emission of swollen micelles carrying the solute, are the events at the molecular scale that determine the onset of an interfacial resistance to mass transport. Finally, it was found that the reduction in density of the aqueous phase that occurs near the drop when solubilization takes place could have acted concomitantly with minute interfacial tension gradients that develop along the water/oil interface to induce convective currents as the surfactant concentration was increased.

5.1.2. NMR Characterization of emulsions (Chapter 3)

A novel approach to process experimental data from classic NMR experiments for the characterization of water-in-oil emulsions has been proposed and tested in emulsions of water in crude oils. The method combines results from the PGSE and CPMG tests to render the drop size distribution of the emulsion, the water/oil ratio and the average surface relaxivity. To our knowledge, this is the first experimental procedure that is proposed in the general literature to determine the surface relaxivity at liquid-liquid interfaces. Obviously, ρ can be determined by combining CPMG data with any independent measurement of the drop size distribution, not necessarily PGSE, but there is an evident benefit in performing such measurement with the same instrument and practically at the same time at which the CPMG test is done. For the systems tested in this investigation, the surface relaxations varied between 0.5 μm/s and 2.1 μm/s and

they increased with the content of asphaltenes and paramagnetic materials in the crude oil.

As part of the development of such method, the theoretical framework to calculate drop size distributions from CPMG data has been reviewed and expanded, and the classic theory for PGSE has been extended to take into account the general case in which the amplitude of the spin-echo is influenced by the transverse magnetization of the continuous and drop phases.

5.1.3. Destabilization of emulsions via aggregation, sedimentation and coalescence (Chapter 4)

The effect of alkylphenol polyalkoxylated (EO/PO) resins and cross-linked polyurethanes of known structure and composition on the stability and properties of brine-in-crude-oil emulsions was assessed experimentally via bottle tests, interfacial tension experiments, viscosity measurements and nuclear magnetic resonance relaxometry. The phenolic resins promoted coalescence of droplets. The fastest rate for water separation was obtained when the emulsions were treated with resins exhibiting intermediate EO/PO content, in a fashion consistent with the optimum formulation for microemulsion formation in oil-water-surfactant systems. In contrast, cross-linked polyurethanes promoted aggregation and slow coalescence, and they were more effective with increase of molecular weight. When both types of molecules were added concomitantly, water separation rates were significantly higher than those observed when they were used individually. In this case, it seems that polyurethanes contributed to increase the water separation rate, but they retarded coalescence when added at high concentrations. These findings can be explained qualitatively in terms of a molecular

mechanism that involves the displacement of asphaltenes adsorbed at the water/oil interfaces by the phenolic resins, and the formation and expansion of holes between approaching droplets in regions depleted of asphaltenes. The action of the phenolic resins is supplemented by the cross-linked polyurethanes, which may act as "bridges" between droplets, thus increasing the probability for collisions leading to successful coalescence events.

5.2. FUTURE WORK

The analysis of the kinetics of dissolution of droplets of mixed oils presented in Chapter 2 was limited to solubilization experiments of binary alkane mixtures. However, the model that was proposed in section 2.2.1 (Eqs. [2.15]-[2.29]) can be used to account for the solubilization of multicomponent systems. It is suggested to explore the behavior of systems containing three solutes with measurable solubility in the continuous phase. The analysis would require either calculating or measuring the activities of each component in the mixture as a function of the composition of the rest of the components.

The evaluation of the rate-limiting mechanism for micellar solubilization of individual droplets in aqueous solutions of the nonionic surfactant $C_{12}E_8$ was shown to depend significantly on the onset of convection as the surfactant concentration was increased. It is suggested to carry out a more detailed analysis of the causes of convection beyond the preliminary analysis presented in Section 2.5.4 for this phenomenon. It is required to solve the equations of continuity and motion for the configuration shown in Figure 2.32, taking into account changes in density in the bulk fluid that surrounds the droplets due to mass transfer, and internal circulation in the droplet. The analysis should result in an expression for the Sherwood number as a function of the Rayleigh number similar to Eq.

[2.48], which would be more representative of the actual solubilization process. The initial analysis should consider the case of constant interfacial tension. Further refinements of the model should consider interfacial tension gradients along the water-oil interface to evaluate the concomitant occurrence of buoyancy-driven convection and Marangoni flow.

Also, further insight is required on the applicability of the model reported in Section 2.2.3 for Ostwald ripening, because the agreement between experiments and theory was adequate but not exact as discussed in Section 2.5.3.2. Since the kinetics of solubilization of drops of several alkanes in solutions of $C_{12}E_8$ was well characterized in this investigation, Ostwald ripening experiments on emulsions of n-octane, n-decane or n-undecane in 2.5 wt.% solutions of $C_{12}E_8$ would be adequate for this regard.

The improvements to the theory for the interpretation of NMR restricted diffusion experiments reported in Chapter 3 are valid for the classic PGSE sequence shown in Figure 3.2, but not for the modifications of the sequence that have appeared subsequently and that are commonly used nowadays, such as the stimulated spin-echo (SSE) and the flow-compensated PGSE sequences referred to in section 3.3.2 (p. 130). It is foreseen that Eq. [3.32] would still hold for these sequences, but with expressions for κ (the relative contribution of the attenuation ratio of the continuous phase to the overall attenuation ratio) different from Eq. [3.33]. Therefore, it is suggested to extend the theoretical considerations that are made in Section 3.3.3 to the above-mentioned sequences.

In addition, this investigation provided for the first time a method to measure surface relaxation rates at the water-oil interfaces, and a few values of ρ were reported in

Chapters 3 and 4. The combined CPMG-PGSE method provides the means to perform systematic investigations on the factors that affect surface relaxation in emulsions.

Also, it is suggested to study the applicability of the CPMG-PGSE method to systems different from water-in-crude oil emulsions, such as emulsions of water in light oils, emulsions of oil in water and multiple emulsions.

Finally, it is suggested to continue the investigation on the mechanism of chemical demulsification of oilfield emulsions, in order to establish the extent to which the elementary steps suggested in section 4.5 are representative of the phenomena reported in Chapter 4. Future experiments could include thin film drainage experiments to elucidate effect of the demulsifiers on drainage rates and kinetics of film rupture, and interfacial viscosity measurements to assess the effect of the demulsifiers on the mechanical properties of the network of colloidal asphaltenes that can be expected to form at the interfaces.

Appendix A

Usage of the log-normal p.d.f. to describe drop size distributions in emulsions

The log-normal probability distribution function, as applied to emulsions, can be written as:

$$p_{gN} = \frac{1}{N_0}\frac{\mathbf{d}N}{\mathbf{d}d} = \frac{1}{d\sqrt{2\pi}\sigma_g} e^{\frac{(\ln d - \ln d_{gN})^2}{2\sigma_g^2}} \quad ; \quad \sigma_g > 0 \qquad [A.1]$$

and its cumulative form is given by:

$$P_{gN} = \int_0^d p(d)\,\mathbf{d}d = \frac{1}{2}\left[1 + erf\left(\frac{\ln d - \ln d_{gN}}{\sqrt{2}\sigma_g}\right)\right] \qquad [A.2]$$

Here, N is the number of droplets with diameter d, N_0 is the overall number of drops in the emulsion and d_{gN} is the geometric mean size, which is sometimes noted d_0. The parameter σ_g is a measure of the width of the size distribution as shown later. It can be demonstrated that p_{gN} is normalized, i.e.,

$$\int \frac{1}{N_0}\mathbf{d}N = \lim_{a\to 0^+}\int_a^\infty p_{gN}\,\mathbf{d}d = \int_{-\infty}^{\infty} p_{\ln}\,\mathbf{d}(\ln d) = \int_{-\infty}^{\infty} p_{\log}\,\mathbf{d}(\log d) = 1 \qquad [A.3]$$

with

$$p_{\ln} = p_{gN}d = \frac{1}{\sqrt{2\pi}\sigma_g} e^{\frac{(\ln d - \ln d_{gN})^2}{2\sigma_g^2}} \quad ; \quad p_{\log} = (\ln 10)p_{\ln} = \frac{1}{\sqrt{2\pi}\sigma_{\log}} e^{\frac{(\log d - \log d_{gN})^2}{2\sigma_{\log}}} \qquad [A.4]$$

and $\sigma_{\log} = \sigma_g/\ln 10$. Figure A.1 shows in solid lines plots of p_{gN}, $p_{\ln}$ and $p_{\log}$ vs. d, ln$d$ (base-e logarithm) and log$d$ (base-10 logarithm) respectively, using d_{gN} = 10 μm and σ = 1. The

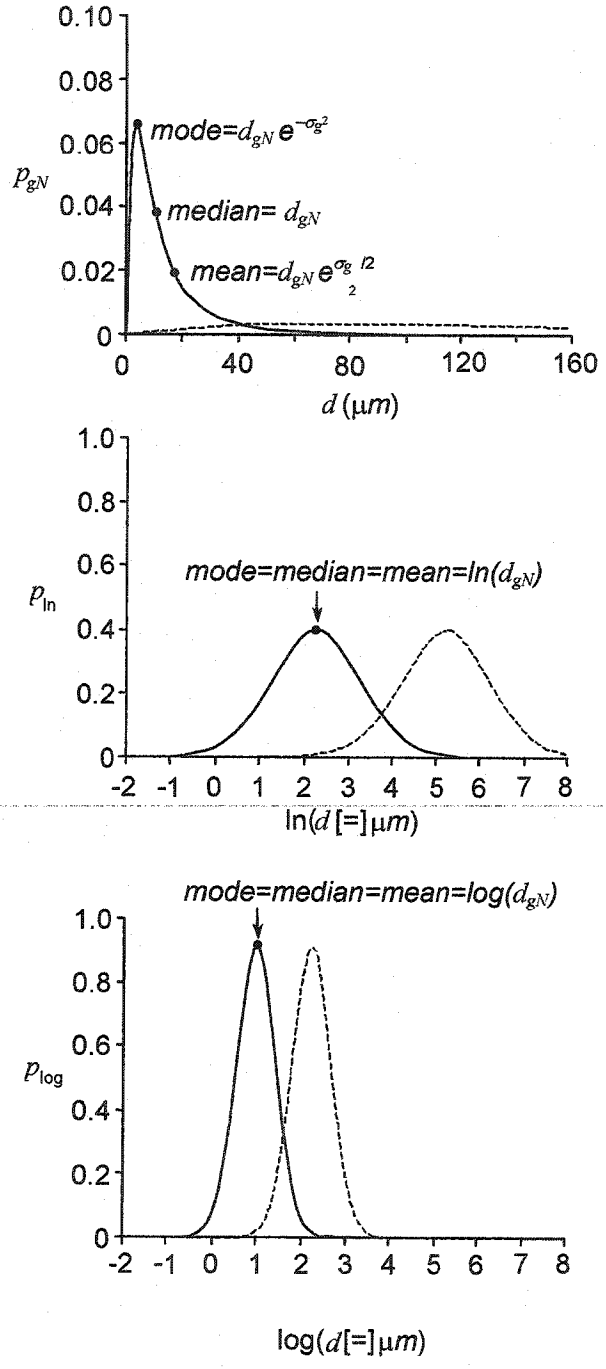


Figure A.1. Calculated log-normal size distributions as a function of the scale used to plot particle size, using d_{gN} = 10 μm and σ_g = 1. Solid lines: number-based distributions. Dashed lines: corresponding volume-weighted distributions.

area below any of these plots is unity if integration is carried on as indicated in Eq. [A.3]. Shown are also the mode (size with maximum probability), the median (value under which 50% of the sizes are found) and the statistical mean (expectation) of the distribution, which are given by [1]:

$$mode: \ \frac{\mathrm{d}\, p_k}{\mathrm{d}\, x}(x_{mode}) = 0; \quad median: \ \int^{x_{median}} p_k dx = 0.50; \quad mean: \ x_{mean} = \int x p_k dx \qquad [A.5]$$

with $x = d$, $\ln d$ or $\log d$ when $p_k = p_{gN}$, $p_{\ln}$ or $p_{\log}$, respectively.

Figure A.1 is useful to identify two common pitfalls in the usage of this p.d.f. for emulsions. First, it is seen that the size distribution function must be redefined when changing the scale at which the drop size is plotted. Otherwise, the resulting distribution is not normalized. Second, it is seen that the mode, median and mean are different in each case. The latter also applies to the variance of the distribution, which reports the square of the deviation of the abscissas from their mean value:

$$variance = \int (x - x_{mean})^2 p_k dx \qquad [A.6]$$

and that is equal to $e^{2\ln d_{gN} + \sigma_g^2}\left(e^{\sigma_g^2} - 1\right)$, σ_g^2 or $\sigma_{\log}^2$ for p_{gN}, $p_{\ln}$ or $p_{\log}$ respectively.

Importantly, the product of the log-normal distribution p_{gN} (or $p_{\ln}$, $p_{\log}$) times the drop size d powered to a real number n, equals another log-normal distribution with identical σ_g but shifted abscissa [2]. For p_{gN}, this is:

$$p^* = \alpha d^n p_{gN} = \frac{1}{d\sqrt{2\pi}\sigma_g} e^{-\frac{(\ln d - \ln d^*)^2}{2\sigma_g^2}} \qquad [A.7]$$

$$d^* = d_{gN} e^{n\sigma_g^2}; \ \alpha = e^{-n\left(\ln d_{gN} + \frac{n\sigma_g^2}{2}\right)} \qquad [A.8]$$

α is a normalization factor, which assures that $\int p^* \mathrm{d}d = 1$. Eqs. [A.7] and [A.8] can be proved easily by noting that $d^n = e^{n\ln d}$. Hence,

$$p^* = \alpha e^{n\ln d}\left[\frac{1}{d\sqrt{2\pi}\sigma_g} e^{-\frac{(\ln d - \ln d_{gN})^2}{2\sigma_g^2}}\right] =$$

$$= \frac{\alpha}{d\sqrt{2\pi}\sigma_g} e^{\frac{-(\ln d - \ln d_{gN})^2 + 2n\sigma_g^2 \ln d}{2\sigma_g^2}} = \frac{\alpha}{d\sqrt{2\pi}\sigma_g} e^{\frac{-\left[\ln^2 d - 2\ln d\left(\ln d_{gN} + n\sigma_g^2\right) + \ln^2 d_{gN}\right]}{2\sigma_g^2}} =$$

$$= \frac{\alpha}{d\sqrt{2\pi}\sigma_g} e^{\frac{-\left[\ln d - \left(\ln d_{gN} + n\sigma_g^2\right)\right]^2 + 2n\sigma_g^2 \ln d_{gN} + n^2\sigma_g^4}{2\sigma_g^2}} = \frac{\alpha e^{n\left(\ln d_{gN} + \frac{n\sigma_g^2}{2}\right)}}{d\sqrt{2\pi}\sigma_g} e^{\frac{\left[\ln d - \left(\ln d_{gN} + n\sigma_g^2\right)\right]^2}{2\sigma_g^2}} \qquad \text{[A.9]}$$

whence the expressions for d^* and α given in [A.8] are readily obtained.

The distribution of sizes in emulsions is often reported based on the volume of the droplets or the interfacial area. In such cases, the size distribution functions are given by:

$$p_{gV} = \frac{1}{V_0}\frac{\mathrm{d}V}{\mathrm{d}d} = \alpha_{gN\to gV} d^3 p_{gN} \qquad \text{[A.10]}$$

$$p_{gA} = \frac{1}{A_0}\frac{\mathrm{d}A}{\mathrm{d}d} = \alpha_{gN\to gA} d^2 p_{gN} \qquad \text{[A.11]}$$

where V and A are the volume and area of a drop of diameter d, and V_0 and A_0 are the overall volume and surface area of the drops, respectively. The sub-indexes in the normalization constants $d_{gN\to gV}$ and $d_{gN\to gA}$ identify the change of reference used to report the distribution.

According to Eq. [A.7], both p_{gV} and p_{gA} are log-normal distributions if so is p_{gN}. Figure A.1 illustrates this feature for the volume-weighted distribution calculated using Eq.

[A.10] and plotted in dashed lines. It also shows that d remains unchanged as referred earlier. From Eq. [A.8], the volume-weighted geometric mean diameter d_{gV} and the constant $d_{gN\to gV}$ are given by:

$$d_{gV} = d_{gN} e^{3\sigma_g^2}; \qquad \alpha_{gN\to gV} = e^{-3\left(\ln d_{gN} + \frac{3}{2}\sigma_g^2\right)} \qquad \text{[A.12]}$$

Similarly, for the area-weighted distribution:

$$d_{gA} = d_{gN} e^{2\sigma_g^2}; \qquad \alpha_{gN\to gA} = e^{-2\left(\ln d_{gN} + \sigma_g^2\right)} \qquad \text{[A.13]}$$

The parameters d_{gV} and d_{gA} are sometimes referred as d_{33} and d_{22} respectively. In general, data of drop size distribution are fitted using a log-normal curve and the result for the geometric mean corresponds either to d_{gN}, d_{gA} or d_{gV} depending on the reference used to report the distribution.

The integrals shown in Table 1.1 (Chapter 1) for the several mean drop sizes that are commonly reported for emulsions can be solved for the log-normal p.d.f. with the aid of functional theory [2]. However, the properties of the log-normal distribution explained above provide a much simpler method to address this matter. For example, for the surface-volume (Sauter) mean diameter d_{AV}, Eqs. [A.1], [A.10], [A.11], [A.12] and [A.13] can be combined to obtain:

$$d_{AV} = \frac{\int d^3 \mathbf{d}N}{\int d^2 \mathbf{d}N} = \frac{\int d^3 p_{gN} \mathbf{d}d}{\int d^2 p_{gN} \mathbf{d}d} = \frac{\alpha_{gN\to gA}}{\alpha_{gN\to gV}} \frac{\int p_{gV} \mathbf{d}d}{\int p_{gA} \mathbf{d}d} = d_{gN} e^{\frac{5}{2}\sigma_g^2} \qquad \text{[A.14]}$$

The procedure can be applied to relate any average size with d_{gN}, and therefore with other mean diameters listed in Table 1.1. By doing so, the expression:

$$d_j = d_i e^{\beta_{ij}\sigma_g^2} \qquad \text{[A.15]}$$

is always obtained, where d_i and d_j are two any average sizes and β_{ij} is a corresponding constant, as given in Table A-1.

The usefulness of Table A.1 can be illustrated as follows: A 20-ml sample of an O/W emulsion with ϕ = 0.20 has a mean size d_{NL} = 10 μm and σ_g = 0.3. (a) What is the overall interfacial area of this emulsion? (b) What volume of a second emulsion with ϕ = 0.10, d_{NV} = 20 μm would have the same number of drops than the first emulsion sample?

Table A-1. Values of β_{ij} for the expression $d_j = d_i e^{\beta_{ij}\sigma_g^2}$.

d_j \ d_i	d_{gN}	d_{gA}	d_{gV}	d_{NL}	d_{NA}	d_{NV}	d_{LA}	d_{LV}	d_{AV}	d_{VM} or d_{WM}
d_{gN}	0	-2	-3	-½	-1	-3/2	-3/2	-2	-5/2	-7/2
d_{gA}	2	0	-1	3/2	1	½	½	0	-½	-3/2
d_{gV}	3	1	0	5/2	2	3/2	3/2	1	½	-½
d_{NL}	½	-3/2	-5/2	0	-½	-1	-1	-3/2	-2	-3
d_{NA}	1	-1	-2	½	0	-½	-½	-1	-3/2	-5/2
d_{NV}	3/2	-½	-3/2	1	½	0	0	-½	-1	-2
d_{LA}	3/2	-½	-3/2	1	½	0	0	-½	-1	-2
d_{LV}	2	0	-1	3/2	1	½	½	0	-½	-3/2
d_{AV}	5/2	½	-½	2	3/2	1	1	½	0	-1
d_{VM} or d_{WM}	7/2	3/2	½	3	5/2	2	2	3/2	1	0

(a) The surface-to-volume ratio of the drops in an emulsion is given by Eq. [1.3]:

$$\frac{A_0}{V_0} = \frac{6}{d_{AV}} \text{ whence } A_0 = \frac{6V_{emul}\phi}{d_{AV}} \qquad [A.16]$$

where V_{emul} is the volume of emulsion sample. Also, from Table A.1 we have:

$$d_{AV} = d_{NL}\,\mathbf{exp}(2\sigma_g^2) \qquad [A.17]$$

By replacing Eq. [A.17] in Eq. [A.16] and substituting values we obtain:

$$S = \frac{6V_{emul}\phi}{d_{NL}\,\mathbf{exp}(2\sigma_g^2)} = \frac{6\cdot(2\cdot10^{-5}m^3)\cdot 0.20}{1\cdot10^{-5}m\cdot\mathbf{exp}(2\cdot0.3^2)} = 2m^2$$

(b) The number-to-volume ratio of droplets in an emulsion is given by Eq. [1.2]:

$$\frac{N_0}{V_0} = \frac{6}{\pi d_{NV}^3} \quad \text{whence } N_0 = \frac{6V_{emul}\phi}{\pi d_{NV}^3} \qquad [A.18]$$

From Table A.1:

$$d_{NV} = d_{NL}\,\mathbf{exp}(\sigma_g^2) \qquad [A.19]$$

Since the number of drops in the two emulsion samples is the same, from Eqs. [A.18]-[A.19] we have:

$$\frac{(N_0)_1}{(N_0)_2} = \frac{(V_{emul})_1}{(V_{emul})_2}\frac{\phi_1}{\phi_2}\left[\frac{(d_{NV})_2}{(d_{NV})_1}\right]^3 = 1 \quad \text{whence}$$

$$(V_{emul})_2 = (V_{emul})_1\frac{\phi_1}{\phi_2}\left[\frac{(d_{NV})_2}{(d_{NL}\,\mathbf{exp}(\sigma_g^2))_1}\right]^3 = 20cm^3\,\frac{0.20}{0.10}\left[\frac{2\cdot10^{-5}m}{1\cdot10^{-5}m\,\mathbf{exp}(0.3^2)}\right]^3 = 244cm^3$$

REFERENCES

1. R.V. Hogg and A. Craig, "Introduction to mathematical statistics", Macmillan Publishing Co., Inc., New York, 1978
2. C. Orr, Emulsion droplet size data, in "Encyclopedia of Emulsion Technology", P. Becher, Editor, Volume 1. Marcel Dekker, New York, 1983, Chapter 6

Appendix B

Analyses of crude oils

Table B.1. Analyses of crude oils

Property/Component	Units	Crude oil		
		MP6	SHU	PBB
°API		28.5	28.7	20.5
Shear viscosity [a]	mPa.s	19	22	207
Relaxation time ($T_{2,bulk}$)	ms	91	57	8.7
Hydrogen index		0.986	0.928	0.906
Self-diffusion coefficients				
D_{LM}	m^2/s	$1.78.10^{-10}$	$1.75.10^{-10}$	$7.3.10^{-12}$
σ_D		0.27	0.75	---
SARA Analysis [b]				
Saturates	wt. %	51.82	32.48	30.8
Aromatics	wt. %	37.67	50.90	20.5
Resins	wt. %	7.53 (4.67)	14.28 (9.19)	31.6 (29.2)
Asphaltenes	wt. %	2.97 (1.84)	2.34 (1.50)	17.1 (15.8)
% loss in evaporation	wt. %	38.0	35.7	7.7
Element Analysis [c]				
Aluminum (Al)	ppm	< 0.2	0.5	0.3
Barium (Ba)	ppm	< 0.02	0.05	0.04
Calcium (Ca)	ppm	1.2	4.40	51
Chromium (Cr)	ppm	0.07	0.05	0.04
Cobalt (Co)	ppm	0.10	0.40	0.04
Copper (Cu)	ppm	< 0.02	0.16	0.13
Iron (Fe)	ppm	2.4	7.9	51
Magnesium (Mg)	ppm	0.4	0.40	4.4
Manganese (Mn)	ppm	< 0.02	< 0.02	1.9
Molybdenum (Mo)	ppm	< 0.20	< 0.2	< 0.2
Nickel (Ni)	ppm	1.0	13	2.9
Potassium (K)	ppm	< 0.2	2.1	1.7
Sodium (Na)	ppm	1.8	3.5	6.4
Strontium (Sr)	ppm	< 0.02	< 0.02	< 0.02
Vanadium (V)	ppm	0.14	33	0.11
Zinc (Zn)	ppm	0.36	1.2	40

a Shear viscosity measured at 30°C and shear rate of 66 s^{-1}.

b Composition of oil topped at 60°C with N_2 stream. Numbers in parenthesis stand for composition of oil as received (before topping). For example, in the composition of the crude oil Rice-1, 1.84 = 2.97*(1-38.0/100). Tests performed by Baseline DGSI – Analytical Laboratories

c Element analyses performed by OndeoNalco Energy Services, L.P.

Appendix C
Equations for NMR characterization of emulsions

C.1. THE "FAST-DIFFUSION" LIMIT IN PRACTICE

Brownstein and Tarr [1] showed that the relaxation of the proton magnetization $M(t)$ of a pure, isotropic fluid confined in a sphere of radius a is given by the sum of decreasing exponential functions with positive intensity I_n:

$$M(t) = M(0)\sum_{n=0}^{\infty} I_n \cdot e^{-t/T_n} \quad . \qquad [C.1]$$

where

$$I_n = \frac{12(\sin\lambda_n - \lambda_n \cos\lambda_n)^2}{\lambda_n^3[2\lambda_n - \sin(2\lambda_n)]}; \quad \sum_{n=0}^{\infty} I_n = 1 \ , \qquad [C.2]$$

$$\frac{1}{T_n} = \frac{1}{T_{bulk}} + \frac{\lambda_n^2 D}{a^2} \ , \qquad [C.3]$$

and the eigenvalues λ_n are determined from:

$$\lambda \cot\lambda = 1 - \rho a/D \ . \qquad [C.4]$$

Figure C.1 shows a plot of the first three intensities I_0, I_1 and I_2 as a function of $\rho a/D$. In the limit of "fast-diffusion" ($\rho a/D$ << 1, see Eq. [3.5]), the first mode (n = 0) dominates ($I_0 \rightarrow 1$; $\{I_1, I_2, \ldots, I_n\} \rightarrow 0$) and the transient magnetization can be modeled using one exponential:

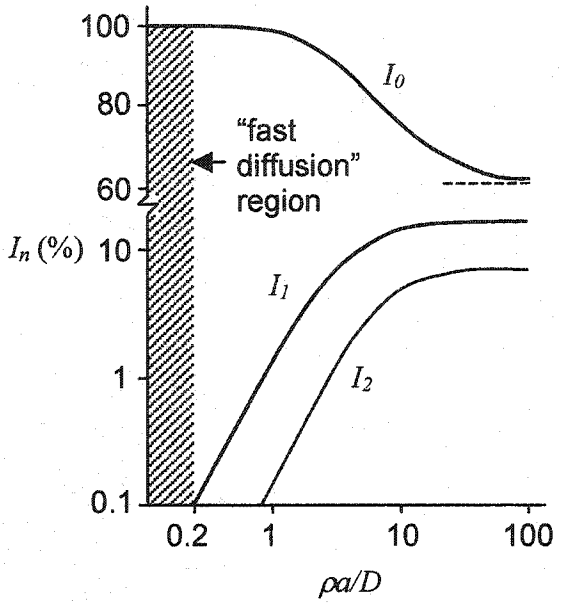


Figure C.1. Plot of the three first intensities I_0, I_1 and I_2 of the magnetization of an isotropic fluid confined in a sphere. In the "fast diffusion" mode, the first intensity I_0 dominates. Adapted from Ref. [1]

$$M_{FDL}(t) = M(0)e^{-t/T_0} . \qquad [C.5]$$

Also, it can be shown from Eq. [C.4] that when $\rho a/D$ << 1, the first eigenvalue is given by:

$$\lambda^2_{0,FDL} = 3\rho a/D - \tfrac{3}{5}(\rho a/D)^2 + O\left[(\rho a/D)^3\right] . \qquad [C.6]$$

Eq. [3.3] and [3.4] are obtained by replacing the first term in the right hand side of Eq. [C.6] in Eq. [C.3]. The sub-index "2" is added to denote transverse relaxation times:

$$\frac{1}{(T_0)_{FDL}} \equiv \frac{1}{T_2} = \frac{1}{T_{2,bulk}} + \rho\frac{3}{a} \quad \text{whence} \quad a = 3\rho\left(\frac{1}{T_2} - \frac{1}{T_{2,bulk}}\right)^{-1}$$

When $\rho a/D$ = 0.24582... ~ ¼ the intensity I_0 accounts for 99.9 % of the initial magnetization (Figure C.1). We adopt this value for $\rho a/D$ as the threshold for the fast-diffusion regime.

Finally, it can be shown that the error that is made in the determination of drop sizes by neglecting the second and higher order term of Eq. [C.6] is $e(\%) \cong 20(\rho a/D)$. Therefore, Eq. [3.4] is exact for $\rho a/D \rightarrow 0$, and it overestimates the drop size by 5% when $\rho a/D$ = ¼.

C.2. DERIVATION OF EQ. [3.32] AND PARTICULAR CASES:

The amplitudes of the spin-echoes that are acquired in a PGSE experiment on emulsions in presence ($g > 0$) or absence ($g = 0$) of magnetic field gradient pulses are, respectively:

$$M_{EMUL}(2\tau, g>0) = M_{DP}(2\tau, g>0) + M_{CP}(2\tau, g>0), \text{ and} \qquad [C.7]$$

$$M_{EMUL}(2\tau, g=0) = M_{DP}(2\tau, g=0) + M_{CP}(2\tau, g=0), \qquad [C.8]$$

whence:

$$R_{EMUL} = \frac{M_{DP}(2\tau, g>0) + M_{CP}(2\tau, g>0)}{M_{DP}(2\tau, g=0) + M_{CP}(2\tau, g=0)} . \qquad [C.9]$$

It is straightforward to show from Eq. [C.9] that:

$$R_{EMUL} = (1-\kappa)R_{DP} + \kappa R_{CP} . \qquad [C.10]$$

where R_{DP} and R_{CP} are the time-resolved attenuation ratios of the drop and continuous phases, respectively:

$$R_{DP} = \frac{M_{DP}(2\tau, g>0)}{M_{DP}(2\tau, g=0)};\ R_{CP} = \frac{M_{CP}(2\tau, g>0)}{M_{CP}(2\tau, g=0)}. \qquad [C.11]$$

The parameter κ ($0 \leq \kappa \leq 1$),

$$\kappa = \left[1 + \frac{M_{DP}(2\tau, g=0)}{M_{CP}(2\tau, g=0)}\right]^{-1}, \qquad [C.12]$$

weights the relative contribution of R_{DP} and R_{CP} to the overall attenuation ratio of the emulsion.

Once the distribution of relaxation times of each phase are resolved from the T_2 distribution of the emulsion, κ can be calculated as follows,

$$\kappa = \left[1 + \frac{\sum (f_i)_{DP}\ \mathbf{exp}\left[-2\tau/(T_{2,i})_{DP}\right]}{\sum (f_i)_{CP}\ \mathbf{exp}\left[-2\tau/(T_{2,i})_{CP}\right]}\right]^{-1}, \qquad [C.13]$$

After substituting Eqs. [3.3] and [3.16] in Eq. [C.13], we obtain:

$$\kappa = \left[1 + \frac{\phi_{DP}}{\phi_{CP}}\frac{HI_{DP}}{HI_{CP}}\frac{\mathbf{exp}\left[-2\tau/(T_{2,bulk})_{DP}\right]}{\sum (x_i)_{CP}\ \mathbf{exp}\left[-2\tau/(T_{2,i})_{CP}\right]}\sum (x_i)_{DP}\ \mathbf{exp}\left[-6\tau\rho/a_i\right]\right]^{-1};\ (x_i)_k = \frac{(f_i)_k}{\sum_j (f_j)_k}.$$

[C.14]

Eq. [C.14] can be simplified and κ computed from transverse relaxation data determined independently for each phase if the effect surface relaxation on the PGSE spin-echo is negligible. This is:

$$\kappa = \left[1 + \frac{\phi_{DP}}{\phi_{CP}} \frac{HI_{DP}}{HI_{CP}} \frac{\exp\left[-2\tau/\left(T_{2,bulk}\right)_{DP}\right]}{\sum \left(x_i\right)^*_{CP} \exp\left[-2\tau/\left(T_{2,i}\right)^*_{CP}\right]}\right]^{-1} \qquad [C.15]$$

Eq. [C.15] is valid if a_m >~ $2\tau\rho$, where a_m is the minimum drop size that can be determined from the T_2 distribution of the emulsion for which f_i > 0. In a typical PGSE experiment on emulsions, 2τ = 100 ms, ρ = 0.5 μm/s and therefore a_m > 0.05 μm. For this reason, Eq. [C.15] provides a satisfactory value of κ in most practical cases. Furthermore, the natural relaxation of the continuous phase can be computed approximately in terms of its logarithmic-mean T_2, $(T_{2,bulk})_{CP}$. If so, Eq. [C.15] becomes:

$$\kappa \cong \left[1 + \frac{\phi_{DP}}{\phi_{CP}} \frac{HI_{DP}}{HI_{CP}} \frac{\exp\left[-2\tau/\left(T_{2,bulk}\right)_{DP}\right]}{\exp\left[-2\tau/\left(T_{2,bulk}\right)_{CP}\right]}\right]^{-1} \qquad [C.16]$$

Eq. [C.16] is useful to illustrate the two limiting cases for κ. Firstly, $\kappa \rightarrow 0$ for highly concentrated emulsions ($\phi_{CP} \rightarrow 0$), or for mixtures in which the continuous phase has relaxed completely at the time the spin-echo is acquired, because $\exp\left[-2\tau/\left(T_{2,bulk}\right)_{CP}\right] \rightarrow 0$. In this case, Eq. [3.32] correctly reduces to Eq. [3.26], i.e., R_{EMUL} is determined only by the attenuation ratio of the drop phase. Conversely, $\kappa \rightarrow 1$ (and $R_{EMUL} = R_{CP}$ according to Eq. [3.32]) for very dilute emulsions ($\phi_{DP} \rightarrow 0$), or for mixtures in which the drop phase has relaxed completely at the time the spin-echo is acquired since $\exp\left[-2\tau/\left(T_{2,bulk}\right)_{DP}\right] \rightarrow 0$.

C.3. REFERENCES

1. K.R. Brownstein and C.E. Tarr, Importance of classical diffusion in NMR studies of water in biological cells, *Phys. Rev. A*, **19** (1979) *2446-2453*

Appendix D

MATLAB codes used to process NMR CPMG/PGSE data

D.1. Files and Installation

Original software was developed to process NMR CPMG/PGSE data. It consists of 14 Matlab (.m) files and two data (.dat) files. The .m files were developed in Matlab, Student Version, Release 12 (The MathWorks, Inc.). Figure D.1 shows the names of these files and the way they must be stored in a memory device so they can be executed.

D.2. Execution and Structure of Input Files

To execute the code, all files must be copied in the same directory (arbitrarily named CMPG_PGSE in Fig. D.1). Also, two subdirectories must be created: INPUT and

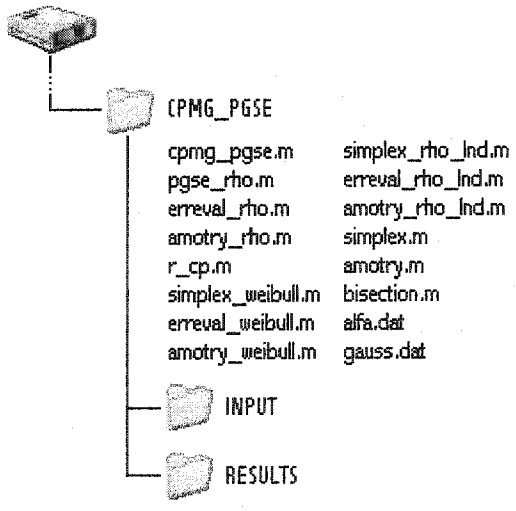


Figure D.1. Files required to process NMR CPMG/PGSE data with Matlab and tree organization of files and sub-directories, as required for execution.

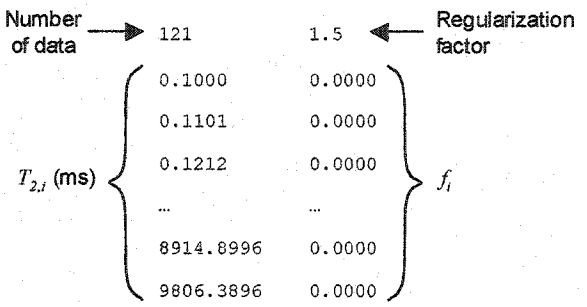


Figure D.2. Schematic representation of the ordering required for input files containing CPMG data.

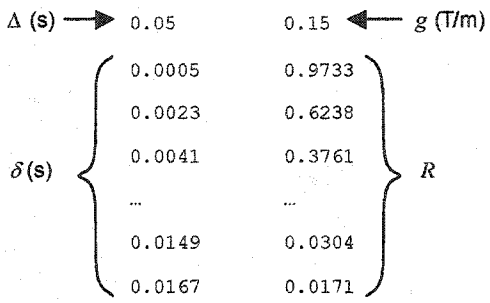


Figure D.3. Schematic representation of the ordering required for input files containing PGSE data.

RESULTS. Source CPMG and PGSE datafiles must be stored in the directory INPUT. Reports summarizing results are automatically stored in the directory RESULTS.

The main file of the code is *cpmg_pgse.m*. The rest of the files are accessed as subroutines of such file. The code is executed by simply typing *cpmg_pgse* in the prompt symbol (>>) of Matlab as shown later.

It is important to clarify how the CPMG and PGSE data must be organized in the input files to successfully run the code. Figure D.2 shows the arrangement that must be observed in the source files for CPMG data. The first datum corresponds to the number m of $T_{2,i}$-f_i values that will be considered ($1 \leq i \leq m$). The second datum in the first line is the regularization factor used to invert transverse relaxation data into T_2 distribution, according to the method described by Huang [1]. The code described in this Appendix does not use the regularization factor when processing the data, so an arbitrary number can be assigned for this datum if such information is unknown. The remaining elements in the first column are the $T_{2,i}$ values (in ms) and the remaining data in the second column are the corresponding f_i values. This code works for water/oil mixtures exhibiting

two separate peaks in the T_2 distribution, with the peak at short T_2 values corresponding to the oil signal and the peak at long T_2 values corresponding to the water signal.

Figure D.3 indicates how the PGSE data must be organized in the corresponding source file. The first datum corresponds to the diffusion time Δ, in seconds. The second datum in the first line is the strength of the magnetic field gradient g, in T/m. The remaining elements of the first column are the chosen durations of the pulsed gradient (δ, in s) and the remaining data in the second column are the corresponding attenuation ratios R. The code is valid for diffusion measurements performed following the sequence shown in Figure 3.2, with $\tau = \Delta$. Once the data are organized as indicated in Figures D.2 and D.3, they must be saved in the directory INPUT (see Figure D.1), preferably in text (.txt) or data (.dat) files.

D.3. ALGORITHM

Figure D.4 shows the algorithm of the code that was developed to process CPMG/PGSE data. The flowchart is self-explanatory, and the nomenclature is fully consistent with the one adopted for Chapter 3.

D.4. EXAMPLES

In this section we illustrate the usage of the Matlab codes with two sets of synthetic data. These data were created superimposing artificial T_2 distributions for the water phase to the T_2 distribution of the crude oil MP6 shown in Figure 3.3. The T_2 distributions for the water phase were generated with ϕ_W = 0.30, $(T_{2,bulk})_W$ = 2.8 s in all cases. The properties of the oil phase are listed in Appendix B.

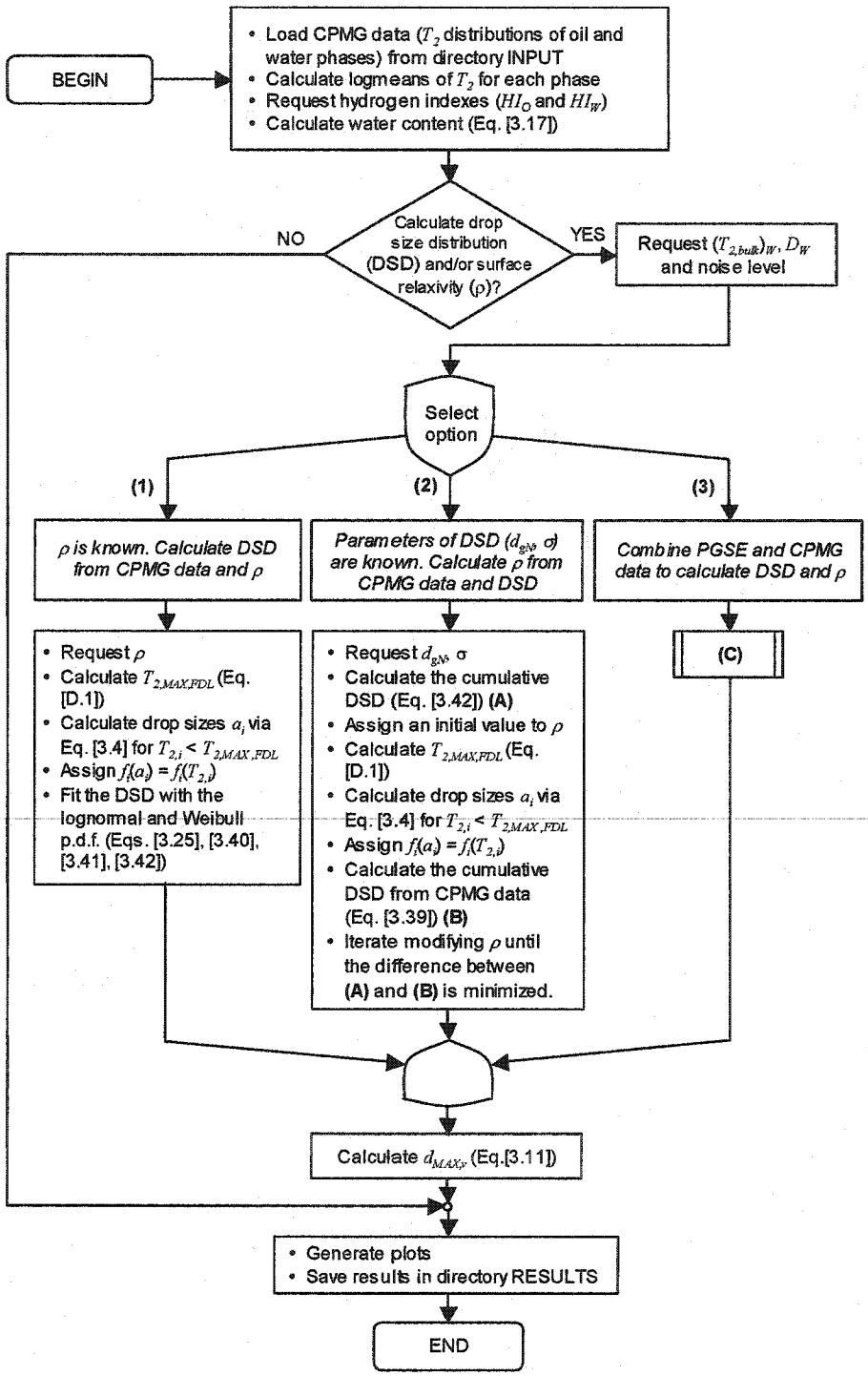


Figure D.4. Flowchart summarizing the algorithm of the Matlab code.

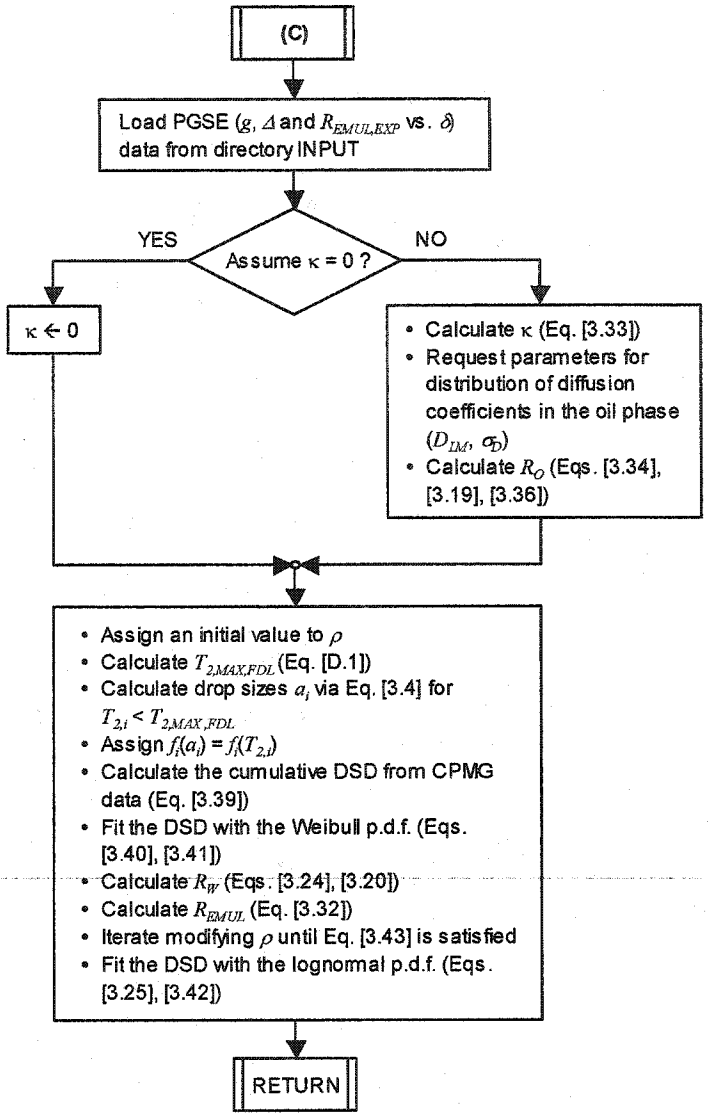


Figure D.4 (cont.) Flowchart summarizing the algorithm of the Matlab codes.

D.4.1. Example 1: Water and oil in contact as bulk fluids, not emulsified

Figure D.5 shows the key to process CPMG data from a mixture of oil and water when the fluids are in contact, i.e., not emulsified, as it would appear in the Matlab screen. The file *cpmg_demo1.dat* was previously stored in the directory INPUT. The texts shown highlighted and in bold characters are the input information provided by the

```
EDU>> cpmg_pgse

Characterization of Emulsions via NMR-CPMG/PGSE
***********************************************

 Name of file (with extension) where CPMG data are saved ? : cpmg_demo1.dat
 File where results will be stored [ Default (press Enter) = results.dat ] ? : ↙
 res_demo1.dat

 Regularization factor (alpha) = 1

Pre-processing
--------------

 Please check following results with Figure 1

 Number of peaks = 2

 Peak 1 : From T2 = 3.481 ms to T2 = 464.2 ms.
    This peak has 2 maxima at T2 = 9.085, and T2 = 195.7 ms.

 Peak 2 : From T2 = 2134.1561 ms to T2 = 3780.7877 ms.
    This peak has 1 maximum at T2 = 2840.5618 ms.

 Oil Signal    : Peak 1. T2 average = 90.5577 ms.
 Water signal : Peak 2. T2 average = 2800.0027 ms.

Parameters
----------

 Hydrogen Index - Oil phase     [Default (press Enter) = 1.0] ? : 0.984
 Hydrogen Index - Aqueous phase [Default (press Enter) = 1.0] ? : 1

 Water content (vol.%) = 30.0011

 Calculate (1) Average properties of the phases as bulk fluids
           (2) Drop size distribution (DSD) and/or surface relaxivity
           [ Default (press Enter) = 2 ]                              ? : 1

 Results
 -------

 Oil phase    : T2 bulk = 90.5577 ms.
 Water phase : T2 bulk = 2800.0027 ms.

 Results are stored in file res_demo1.dat
```

Figure D.5. Key to run the Matlab code for Example 1.

user. The symbol (↙) indicates that the text in the following line would appear in the screen at the end of the line where such symbol is inserted. The code generates the plot shown in Figure D.6 and the file *res_demo1.dat* shown in Figure D.7, which is stored in the directory RESULTS.

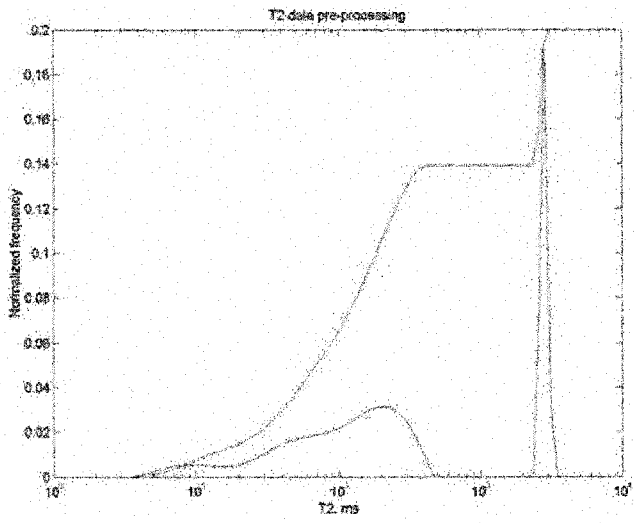


Figure D.6. Plot generated by the code for the T_2 distribution (blue) and the corresponding cumulative curve (red) for Example 1.

```
Analysis CPMG data
------------------

 Input file: cpmg_demo1.dat
 Regularization factor (alpha) = 1

Preprocessing
-------------
 Number of peaks = 2

 Peak 1 : From T2 = 3.481 ms to T2 = 464.2 ms.
    This peak has 2 maxima at T2 = 9.085, and T2 = 195.7 ms.

 Peak 2 : From T2 = 2134.1561 ms to T2 = 3780.7877 ms.
    This peak has 1 maximum at T2 = 2840.5618 ms.

 Oil Signal   : Peak 1. T2 average = 90.5577 ms.
 Water signal : Peak 2. T2 average = 2800.0027 ms.

Parameters
----------
 Hydrogen Index - Oil phase     = 0.984
 Hydrogen Index - Aqueous phase = 1

 Requested calculation : T2 bulk

 Results
 -------

 Oil phase   : T2 bulk = 90.5577 ms.
 Water phase : T2 bulk = 2800.0027 ms.
 Water content (vol.%) = 30.0011
```

Figure D.7. Report generated for the code for Example 1.

If the user attempts to calculate a drop size distribution from the dataset of this example, the code generates the following message:

```
MORE THAN 10 % OF THE SIGNAL OF THE WATER PHASE IS ORIGINATED FROM BULK WATER
AND/OR FROM DROPLETS WITH SIZES LARGER THAN THE MAXIMUM SIZE FOR WHICH THE
FAST DIFFUSION APPROXIMATION IS VALID. IT IS STRONGLY SUGGESTED TO REMOVE
BULK WATER FROM THE SAMPLE AND PERFORM NEW CPMG/PGSE TESTS IN THE REMAINING
EMULSION, SO THE DROP SIZE DISTRIBUTION CAN BE DETERMINED.
```

In general, this message appears whenever the T_2 values below $T_{2,max,FDL}$ account for 10% or less of the cumulative T_2 distribution of the water phase. $T_{2,max,FDL}$ is given by:

$$T_{2,\mathbf{max},FDL} = \left[\frac{1}{(T_{2,bulk})_W} + \rho \frac{6}{d_{MAX,FDL}} \right]^{-1} \qquad [D.1]$$

and $d_{MAX,FDL}$ is given by Eq. [3.7].

D.4.2. Example 2: Emulsion of small droplets

This example aims to illustrate the performance of the code when the assumption of fast diffusion is valid for all droplets. In this case, the T_2 distribution of the water phase was generated assuming that the emulsion exhibits a lognormal distribution of sizes with d_{gV} = 15 μm and σ = 0.30. Also, surface relaxation ρ = 0.46 μm/s was assumed to generate the synthetic data. The synthetic data is noise-free, but a noise level of 0.5 % was input to the code to illustrate results from Eq. [3.11] for $d_{MAX,V}$.

Figure D.8 shows the key to run this second example, as it would appear in the Matlab screen. Figures D.9, D.10 and D.11 show the plots generated by the code for the T_2 distribution, the attenuation profile and the volume-weighted drop size distribution,

```
EDU>> cpmg_pgse

Characterization of Emulsions via NMR-CPMG/PGSE
***********************************************

 Name of file (with extension) where CPMG data are saved ? : cpmg_demo2.dat
 File where results will be stored [ Default (press Enter) = results.dat ] ? : ↙
 res_demo2.dat

 Regularization factor (alpha) = 1

Pre-processing
--------------

 Please check following results with Figure 1

 Number of peaks = 2

 Peak 1 : From T2 = 3.481 ms to T2 = 464.2 ms.
    This peak has 2 maxima at T2 = 9.085, and T2 = 195.7 ms.

 Peak 2 : From T2 = 1095.1595 ms to T2 = 2840.5618 ms.
    This peak has 1 maximum at T2 = 1940.1419 ms.

 Oil Signal    : Peak 1. T2 average = 90.5577 ms.
 Water signal : Peak 2. T2 average = 1918.9377 ms.

Parameters
----------

 Hydrogen Index - Oil phase     [Default (press Enter) = 1.0] ? : 0.984
 Hydrogen Index - Aqueous phase [Default (press Enter) = 1.0] ? : 1

 Water content (vol.%) = 29.9988

 Calculate (1) Average properties of the phases as bulk fluids
           (2) Drop size distribution (DSD) and/or surface relaxivity
           [ Default (press Enter) = 2 ]                              ? : 2

 T2 bulk (ms) [ Default (press Enter) = 2800 ] ? : 2800

 Diffusion coefficient water (m2/s) [Default (press Enter) = 2.3E-9] ? : 2.3e-9

 Noise level (%) [Default (press Enter) = 0 for unknown] ? : 0.5

 Please indicate your choice:
 ----------------------------
 (1) Surface relaxivity is known. Calculate DSD.
 (2) Parameters of DSD are known. Calculate surface relaxivity
 (3) PGSE data are available. Calculate surface relaxivity and DSD
     [ Default (press Enter) = 3 ]                                  ? : 3

 Name of file (with extension) where PGSE data are saved ? : pgse_demo2.dat

 Time between gradient pulses (s) = 0.05

 Strength of magnetic field gradient (T/m) = 0.15

 Fractional contribution of continuous phase to R in PGSE tests (kappa):
 -----------------------------------------------------------------------
  Calculate kappa from (1) T2 distribution emulsion
                       (2) Data for pure components
                       (3) Assume kappa = 0
                       [ Default (press Enter) = 1 ] ? : 1
  kappa = 0.48027
```

Figure D.8. Key to run the Matlab code for Example 2.

```
 Mean Diffusion coef. continuous phase (m2/s) [Default (press Enter)= 1E-10] ? : 1.78e-10

 Standard deviation Diff. coef. continuous phase  [Default (press Enter)= 0] ? : 0.27

 Iteration # 2
 . . .
 Iteration # 30

 Results
```

```
-------
Log-normal distribution fit of cumulative probability P(d), d = drop diameter :
       /d
P(d)= | p(x)*dx;  p(x) = {1/[(2*pi)^.5*sigma*x]}*exp{-[ln(x)-ln(dgV)]^2/(2*sigma^2)}
       /0
dgV (micron) = 14.9682    [ dgN (micron) = 11.4254; d32 (micron) = 13.0774 ]
sigma        = 0.30005

Water content (WC, vol.%)                = 29.9988

Water in droplets (d =< d_max_FDL) (% of WC) = 100
Bulk water  (% of WC)                        = 0

Surface relaxivity (micron/s)            = 0.45869

Contribution of oil phase to R (kappa)   = 0.48027

Cutoff drop diameter for fast diffusion limit (d_max_FDL, microns) = 2507.133
Maximum drop size dictated by T2,bulk and SNR (d_max_SNR, microns) = 188.0473

Parameters of the bimodal Weibull distribution
-----------------------------------------------
sigma1       = 1.0473
sigma2       = 1.2447
m1           = 5.9157
m2           = 4.1505
omega        = 0.1522
a0 (microns) = 2.4751

Results are stored in file res_demo2.dat
```

Figure D.8. (cont.) Key to run the Matlab code for Example 2.

respectively. The report for this test is omitted for the sake of brevity, but in any case, the same results are also displayed in Figure D.8.

It is seen in Figure D.8 that the code correctly calculated d_{gV}, σ and ρ. Figures D.10 and D.11 show that excellent fits to the synthetic data were achieved. Interestingly, figure D.11 also shows that the bimodal Weibull distribution overlaps the lognormal distribution when a suitable set of parameters for the latter is chosen. Therefore, emulsions exhibiting lognormality in drop sizes can be considered as particular cases of those for which the bimodal Weibull distribution is valid.

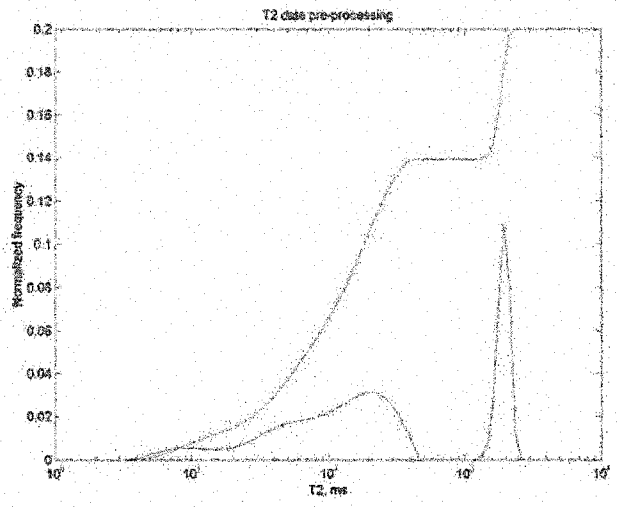


Figure D.9. Plot generated by the code for the T_2 distribution (blue) and the corresponding cumulative curve (red) for Example 2.

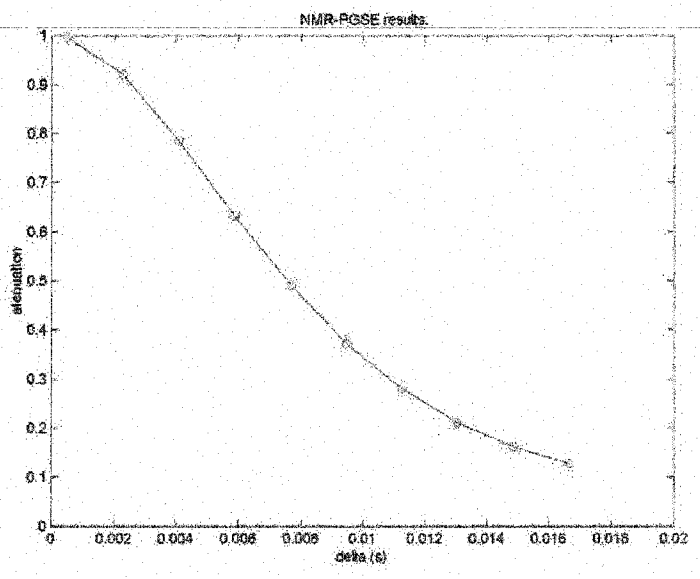


Figure D.10. Plot generated by the code for the attenuation profile for Example 2. Circles, synthetic data; solid line, best fit to the data using the model reported in Chapter 3.

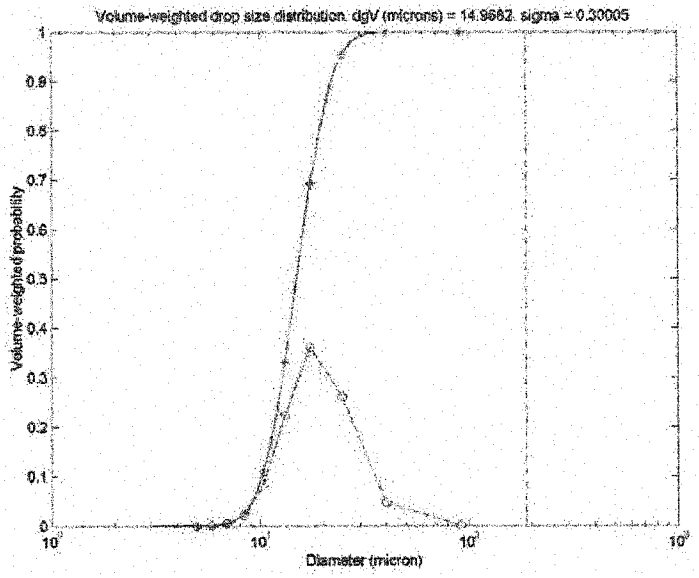


Figure D.11. Plot generated by the code for the volume-weighted drop size distribution for Example 2. Circles, synthetic data from CPMG; stars, cumulative distribution for the synthetic data; red dashed line, best fit using the bimodal Weibull distribution; blue dashed line, best fit using the lognormal distribution; red solid line; best fit to the cumulative distribution using the bimodal Weibull distribution; blue solid line; best fit to the cumulative distribution using the lognormal distribution; dash-dot line, $d_{MAX,}$ as calculated from Eq. [3.12].

Figure D.11 also shows the position of $d_{MAX} = d_{MAX,v}$ relative to the drop size distribution. Since all drop sizes are below $d_{MAX,}$ the NMR-based distribution can be considered fully representative of the actual drop size distribution of the tested emulsion, as was demonstrated in Chapter 3 when comparing NMR and microphotography data.

D.4.3. Example 3: Emulsion containing a small volume of bulk water

This example aims to illustrate the case in which coalescence has taken place in the emulsion to a significant extent and in consequence, very large drops are and/or a small amount of decanted bulk water is in contact with the emulsion. In these cases, the T_2 distribution typically shows T_2 values beyond $T_{2MAX,FDL}$ and even beyond $T_{2,bulk}$ in some cases, due to the inability of the regularization methods to resolve for the T_2 distribution of bulk water with a single T_2 value, but instead with a narrow distribution of T_2 values

around $T_{2,bulk}$. When $T_{2,i} \rightarrow T_{2,bulk}$, Eq. [3.4] predicts that $a_i \rightarrow \infty$. For this reason, the results that are generated by the code in these cases should be interpreted as an approximate estimate for the drop size distribution of the drops that remain dispersed in the emulsion. The ability of NMR-based methods to accurately resolve for the drop size distribution in these cases can be improved, for example, by separating the bulk water from the emulsion sample before performing the tests.

The T_2 distribution of this example was generated by shifting the water peak of the former example to higher relaxation times. The distribution is resolved assuming that the surface relaxation ρ = 0.46 μm/s is known a priori, and that the noise level is 0.5 % as before.

Figure D.12 summarizes the key to run this example, as it would appear in the Matlab window. Results of the analysis are also summarized in this Figure. The program estimates that 95.3 % of the water phase is dispersed as droplet with sizes below $d_{MAX,FDL}$ = 2500 μm (also below d_{MAX} = $d_{MAX,v}$ = 189 μm, as shown in Figure D.14), whereas 4.7 % can be considered bulk water. Figure D.13 shows (solid lines) the T_2 distribution for this example and Figure D.14 the corresponding drop size distribution. The cumulative distribution shown in Figure D.14 is truncated to the last drop size for which the fast-diffusion approximation is valid.

The Matlab code allows reprocessing the CPMG data to discard the signal from droplet with sizes greater than $d_{MAX,FDL}$ and correlate only sizes of drops for which the fast-diffusion approximation is valid. It is seen in Figure D.12 that the user is given this option, and if desired, a new file is created with the edited CPMG data. An estimate of the drop size distribution of drops with $d < d_{MAX,FDL}$ is obtained by re-running the code as shown in the Example 1 and specifying the edited file as the source of CPMG data.

```
EDU>> cpmg_pgse

Characterization of Emulsions via NMR-CPMG/PGSE
***********************************************

 Name of file (with extension) where CPMG data are saved ? : cpmg_demo1.dat
 File where results will be stored [ Default (press Enter) = results.dat ] ? :
 res_demo1.dat

 Regularization factor (alpha) = 1

Pre-processing
--------------
 Please check following results with Figure 1

 Number of peaks = 2

 Peak 1 : From T2 = 3.481 ms to T2 = 464.2 ms.
    This peak has 2 maxima at T2 = 9.085, and T2 = 195.7 ms.

 Peak 2 : From T2 = 1325.143 ms to T2 = 3437.0797 ms.
    This peak has 1 maximum at T2 = 2347.5717 ms.

 Oil Signal   : Peak 1. T2 average = 90.5577 ms.
 Water signal : Peak 2. T2 average = 2321.9137 ms.

Parameters
----------

 Hydrogen Index - Oil phase     [Default (press Enter) = 1.0] ? : 0.984
 Hydrogen Index - Aqueous phase [Default (press Enter) = 1.0] ? : 1

 Water content (vol.%) = 29.9988

 Calculate (1) Average properties of the phases as bulk fluids
           (2) Drop size distribution (DSD) and/or surface relaxivity
           [ Default (press Enter) = 2 ]                          ? : 2

 T2 bulk (ms) [ Default (press Enter) = 2800 ] ? : 2800

 Diffusion coefficient water (m2/s) [Default (press Enter) = 2.3E-9] ? : 2.3E-9

 Noise level (%) [Default (press Enter) = 0 for unknown] ? : 0.5

 Please indicate your choice:
 ----------------------------
 (1) Surface relaxivity is known. Calculate DSD.
 (2) Parameters of DSD are known. Calculate surface relaxivity
 (3) PGSE data are available. Calculate surface relaxivity and DSD
     [ Default (press Enter) = 3 ]                              ? : 1

 Surface relaxivity (micron/s) ? : 0.46

 IMPORTANT: T2 distribution surpassed T2_max. Excess computed as bulk water.

 4.7277 % of the signal from the water phase is originated in bulk
 and/or in droplets with sizes larger than the maximum size for which the
 fast diffusion limit is valid. Would you like to discard the signal from
 such droplets and reprocess the CPMG data, taking into account the signal
 from drops with size d < d_MAX,FDL only ?

 (1) YES     (2) NO      [Defaults (press Enter) = 1] ?                : 1
```

Figure D.12. Key to run the Matlab code for Example 3.

```
File where modified CPMG data will be stored
[ Default (press Enter) = reprocess.dat ] ? : reprocess.dat

Results
-------
Log-normal distribution fit of cumulative probability P(d), d = drop diameter :
       /d
P(d)= | p(x)*dx;  p(x) = {1/[(2*pi)^.5*sigma*x]}*exp{-[ln(x)-ln(dgV)]^2/(2*sigma^2)}
       /0
dgV (micron) = 31.2151    [ dgN (micron) = 15.3084; d32 (micron) = 21.8599 ]
sigma        = 0.48734

Water content (WC, vol.%)                = 29.9988

Water in droplets (d =< d_max_FDL) (% of WC) = 95.2723
Bulk water  (% of WC)                        = 4.7277

Surface relaxivity (micron/s)            = 0.46

Cutoff drop diameter for fast diffusion limit (d_max_FDL, microns) = 2500
Maximum drop size dictated by T2,bulk and SNR (d_max_SNR, microns) = 188.5838

Parameters of the bimodal Weibull distribution
----------------------------------------------
sigma1       = 2.1827        sigma2       = 1.4303
m1           = 4.2096        m2           = 4.0617
omega        = 0.36338       a0 (microns) = 3.4718

Results are stored in file res_demo3.dat

Data for reprocessing are stored in file reprocess.dat
```

Figure D.12 (cont.) Key to run the Matlab code for Example 3.

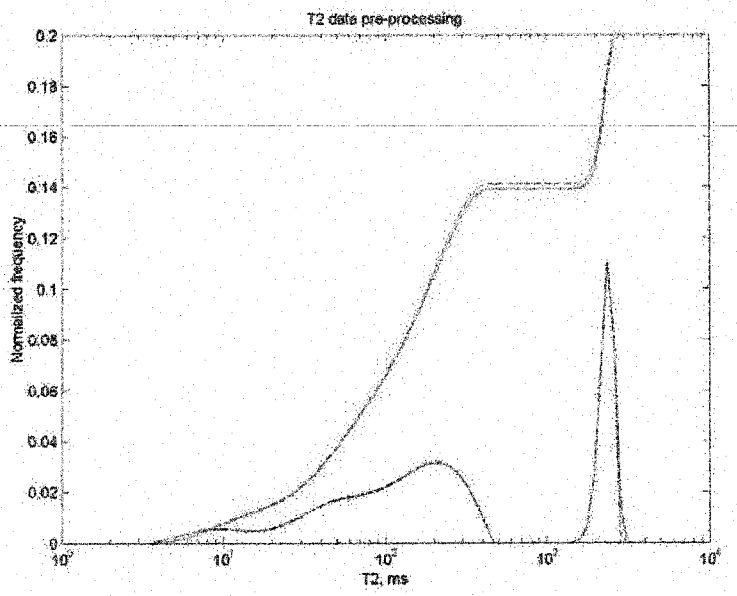


Figure D.13. Plot generated by the code for the T_2 distribution (blue) and the corresponding cumulative curve (red) for Example 3. Solid lines, original dataset; dashed lines, edited CPMG dataset after discarding the contribution of bulk water.

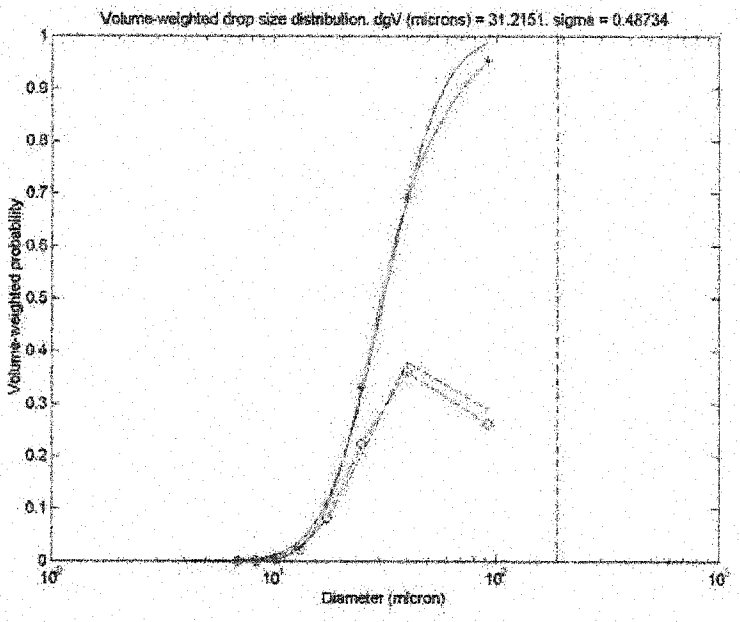


Figure D.14. Plot generated by the code for the volume-weighted drop size distribution for Example 3, without reprocessing. The description of the features of Figure D.9 given in the caption of such also applies in this case.

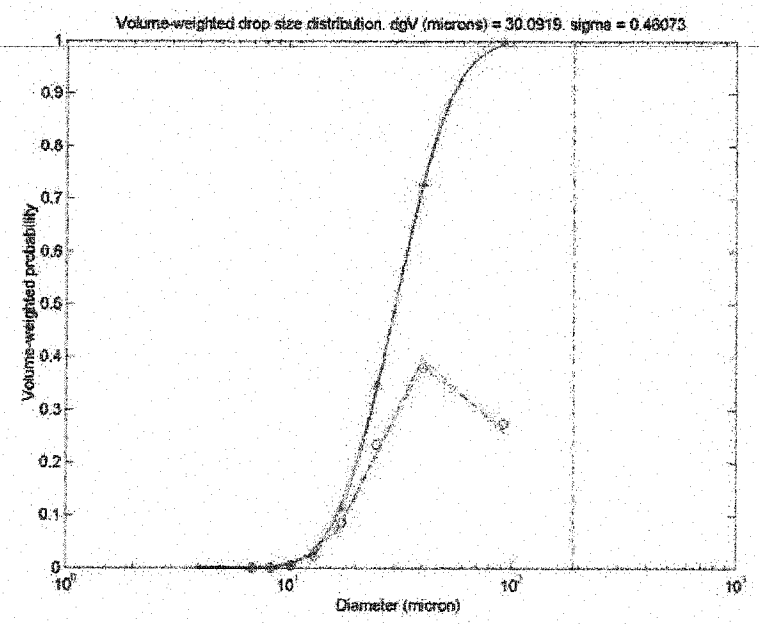


Figure D.15. Plot generated by the code for the volume-weighted drop size distribution for Example 3, after reprocessing.

The reprocessed T_2 distribution is shown in dashed lines in Figure D.13. Figure D.15 shows the corresponding drop size distribution, which differ slightly from the one shown in Figure D.14 as might be expected. The water content that is calculated from the reprocessed dataset is slightly below 30 vol.%, i.e.,

$$29.0\ vol.\% = \frac{30\left(1-4.7/100\right)}{70+30\left(1-4.7/100\right)} x100\,,$$

since the contribution of bulk water to the T_2 distribution has been discarded.

D.5. MATLAB CODES

The contents of the files listed in Figure D.1 are provided below. A brief description of the operations performed by such file is provided in each case.

File cpmg_pgse.m

```
% ------------------------------------------------------------------------
%     Characterization of O/W Emulsions via NMR-CPMG/PGSE - File CPMG_PGSE.m
% ------------------------------------------------------------------------
%   Copyright (C) 2001-2003 Alejandro Pena, Clarence Miller and George Hirasaki
%
% This software is provided pursuant to a license agreement containing restrictions
% on its disclosure, duplication and use. This software contains confidential and
% proprietary information, and may not be extracted or distributed, in whole or in
% part, for any purpose whatsoever, without the express written permission of the
% authors. This notice, and the associated author list, must be attached to all
% copies, or extracts, of this software. Any additional restrictions set forth in
% the license agreement also apply to this software.
%
% File CPMG_PGSE.m: Main program for processing of CPMG/PGSE data.
%
% References:
% * Equations for CPMG/PGSE data processing are presented in:
%   Pena AA and Hirasaki GJ. Enhanced Characterization of Oilfield Emulsions via
%   NMR Diffusion and Transverse Relaxation Experiments. Advances in Colloids and
%   Interface Science. In press.
% * This program uses the Simplex method to carry on least square minimization.
%   The code for Simplex method has been adapted from:
%   Press et. al. Numerical recipes in FORTRAN 77. Cambridge Univ. Press (1992)
%
% ------------------------------------------------------------------------
```

```
clear data erro P psum Ptry x erro2 P2 psum2 Ptry2 x2 T2_water_old;
clear cumul calc_cumul diam freq freq_oil freq_water T2 T2_oil T2_water tempmax;
clear prob calc_prob_lnd calc_prob_bwd peak_max tempmax ini_peak end_peak pos_max;
clear calc_cumul_lnd calc_cumul_bwd cumul_water cumul_water_old freq_water_old;
clear T2_temp freq_temp cumul_temp;
close all;
minval = 1E-4;
kappa = 0;
flag_end = 0;
flag_reprocess = 0;
resp_rep = 0;

disp(' ');
disp('Characterization of Emulsions via NMR-CPMG/PGSE');
disp('*********************************************');
disp(' ');

% Pre-processing of T2 distribution

nombre = input(' Name of file (with extension) where CPMG data are saved ? : ','s');
cd input;
data = load(nombre);
cd ..;
temp = ' File where results will be stored [ Default (press Enter) = results.dat ] ? : ';
nombre2 = input(temp,'s');
if isempty(nombre2)==1
   nombre2 = 'results.dat';
end
cd results;
fid = fopen(nombre2,'w');
disp(' ');
fprintf(fid,'Analysis CPMG data \n');
fprintf(fid,'------------------ \n');
fprintf(fid,'\n');
fprintf(fid,' Input file: %s \n',nombre);

% Regularization parameter (alpha)
alpha = data(1,2);
temp = [' Regularization factor (alpha) = ',num2str(alpha)];
disp(temp);
fprintf(fid,'%s \n',temp);
disp(' ');
fprintf(fid,'\n');

T2 = data(2:max(size(data)),1);
freq = data (2:max(size(data)),2);
npeaks = 0;
nmax = 0;
flag = 0;
flag2 = 0;
for i=1:(max(size(T2)));
   if freq(i) < minval
      freq(i) = 0;
   end
   cumul(i)=sum(freq(1:i));
   if ((i==1)+(i==max(size(T2))))== 0; % i <> 1 and i <> max(size(T2))
      if ((freq(i) < minval) + (freq(i+1) >= minval)) == 2 ;
         npeaks = npeaks + 1;
         ini_peak(npeaks) = i;
         flag = 1;
      end
      if ((freq(i)>= freq(i-1)) + (flag == 1)) == 2;
         flag2 = 0;
         pos_max_temp = i;
      else
         if ((flag == 1) + (flag2 == 0)) == 2;
            nmax = nmax + 1;
```

```
            pos_max(nmax) = pos_max_temp;
            peak_max(nmax) = npeaks;
            flag2 = 1;
         end
      end
      if ((freq(i) < minval) + (freq(i-1) >= minval) + (flag == 1)) == 3;
         end_peak(npeaks) = i;
         flag = 0;
      end
   end
end
freq = freq./max(cumul);
cumul = cumul./max(cumul);
if max(freq)>1
   ymax = (fix(max(freq)/10)+1)*10;
else
   ymax = (fix(max(freq)*10)+1)/10;
end
xmin = 10^(fix(log10(T2(ini_peak(1)))-1));
xmax = 10^(fix(log10(T2(end_peak(npeaks)))+1));
figure(1);
semilogx(T2,freq,'-b');
hold on;
semilogx(T2,cumul.*ymax,'-r');
axis([xmin xmax 0 ymax]);
xlabel('T2, ms');
ylabel('Normalized frequency');
title('T2 data pre-processing');
disp('Pre-processing');
disp('--------------');
disp(' ');
disp(' Please check following results with Figure 1 ');
disp(' ');
temp = [' Number of peaks = ',num2str(npeaks)];
disp(temp);
disp(' ');
fprintf(fid,'Preprocessing \n');
fprintf(fid,'-------------- \n');
fprintf(fid,' Number of peaks = %d \n',npeaks);
fprintf(fid,'\n');

for i = 1:npeaks
    temp = [' Peak ',num2str(i),' : From T2 = ',num2str(T2(ini_peak(i))),' ms to T2 = ↙
    ',num2str(T2(end_peak(i))),' ms.'];
    disp(temp);
    fprintf(fid,'%s \n',temp);
    temp2 = 0;
    for j = 1:nmax
       if peak_max(j) == i
          temp2 = temp2 + 1;
          tempmax(temp2) = pos_max(j);
       end
    end
    if temp2 == 1
       temp = ['    This peak has 1 maximum at T2 = ',num2str(T2(tempmax(1))),' ms.'];
       disp(temp);
       fprintf(fid,'%s \n',temp);
       disp(' ');
       fprintf(fid,'\n');
    else
       temp = ['    This peak has ',num2str(temp2),' maxima at'];
       for j = 1:(temp2-1)
           temp = [temp,' T2 = ',num2str(T2(tempmax(j))),','];
       end
       temp = [temp,' and T2 = ',num2str(T2(tempmax(temp2))),' ms.'];
       disp(temp);
       fprintf(fid,'%s \n',temp);
       disp(' ');
       fprintf(fid,'\n');
```

```
    end
end

% Average T2 value - oil peak

T2_oil = T2(ini_peak(1):end_peak(1));
freq_oil = freq(ini_peak(1):end_peak(1));
freq_oil = freq_oil / sum(freq_oil);
temp = size(T2_oil);
if temp(1) == 1
    T2_oil = T2_oil';
end
temp = size(freq_oil);
if temp(1) == 1
    freq_oil = freq_oil';
end
T2_avg_o = 10^(freq_oil'*log10(T2_oil));
temp = [' Oil Signal   : Peak 1. T2 average = ',num2str(T2_avg_o),' ms.'];
disp(temp);
fprintf(fid,'%s \n',temp);

% Average T2 value - water peak

T2_water = T2(ini_peak(npeaks):end_peak(npeaks));
freq_water = freq(ini_peak(npeaks):end_peak(npeaks));
cumul_water = cumul(ini_peak(npeaks):end_peak(npeaks))-cumul(ini_peak(npeaks));
cumul_water = cumul_water./max(cumul_water);
freq_water = freq_water / sum(freq_water);
temp = size(T2_water);
if temp(1) == 1
    T2_water = T2_water';
end
temp = size(freq_water);
if temp(1) == 1
    freq_water = freq_water';
end
temp = size(cumul_water);
if temp(1) == 1
   cumul_water = cumul_water';
end
fid2 = fopen('waterpeak.dat','w');

for i = 1 : max(size(T2_water))
   fprintf(fid2,' %6.4e  %6.4e \n ',T2_water(i), freq_water(i));
end
fclose(fid2);

clear data;
data = load('waterpeak.dat');
P0 = [1 1 1 1 .5];
cd ..;
Simplex_weibull;          % Routine to fit T2_water data to the bimodal Weibull ↙
distribution
omega_old = omega;
sigma1_old = sigma1;
sigma2_old = sigma2;
m1_old = m1;
m2_old = m2;
cd results;

T2_avg_w = 10^(freq_water'*log10(T2_water));
temp = [' Water signal : Peak ',num2str(npeaks),'. T2 average = ',num2str(T2_avg_w),' ↙
ms.'];
disp(temp);
fprintf(fid,'%s \n',temp);
disp(' ');
fprintf(fid,'\n');

T2_min = T2_water(1);
```

```
% PROCESSING

disp('Parameters');
disp('----------');
disp(' ');
fprintf(fid,'Parameters \n');
fprintf(fid,'---------- \n');

% Water cut

Area_w = (cumul(end_peak(npeaks))-cumul(ini_peak(npeaks)));
Area_o = cumul(ini_peak(npeaks));
HI_o = input(' Hydrogen Index - Oil phase     [Default (press Enter) = 1.0] ? : ');
if isempty(HI_o)==1
   HI_o = 1;
end
HI_w = input(' Hydrogen Index - Aqueous phase [Default (press Enter) = 1.0] ? : ');
if isempty(HI_w)==1
   HI_w = 1;
end
Water_cut = (Area_w/HI_w)/(Area_w/HI_w + Area_o/HI_o)*100;
temp = [' Hydrogen Index - Oil phase     = ',num2str(HI_o)];
fprintf(fid,'%s \n',temp);
temp = [' Hydrogen Index - Aqueous phase = ',num2str(HI_w)];
fprintf(fid,'%s \n',temp);
disp(' ');
fprintf(fid,'\n',temp);
disp([' Water content (vol.%) = ' num2str(Water_cut)]);
disp(' ');
temp = [' Calculate (1) Average properties of the phases as bulk fluids        ';
        '           (2) Drop size distribution (DSD) and/or surface relaxivity '];
disp(temp);
ans = input('           [ Default (press Enter) = 2 ]                          ? : ');
if isempty(ans)==1
      ans = 2;
end

if ans == 1 % Calculates T2 bulk as the weighted average from each peak

   fprintf(fid,' Requested calculation : T2 bulk \n');
   fprintf(fid,'\n');
   disp(' ');
   temp = [' Results';' -------'];
   disp(temp)
   disp(' ');
   fprintf(fid,' Results\n',temp(1));
   fprintf(fid,' -------\n');
   fprintf(fid,'\n');
   temp = [' Oil phase   : T2 bulk = ',num2str(T2_avg_o),' ms.'];
   disp(temp);
   fprintf(fid,'%s \n',temp);
   temp = [' Water phase : T2 bulk = ',num2str(T2_avg_w),' ms.'];
   disp(temp);
   fprintf(fid,'%1s \n',temp);
   temp = [' Water content (vol.%) = ',num2str(Water_cut)];
   fprintf(fid,'%s \n',temp);

else % Calculates drop size distribution

   fprintf(fid,' Requested calculation : Drop size distribution \n');
   fprintf(fid,'\n');
   disp(' ');
   T2_bulk = input(' T2 bulk (ms) [ Default (press Enter) = 2800 ] ? : ');
   if isempty(T2_bulk)==1
       T2_bulk = 2800;
   end
   temp = [' T2 bulk (ms) = ',num2str(T2_bulk)];
   fprintf(fid,'%s \n',temp);
```

```
disp(' ');
DC = input (' Diffusion coefficient water (m2/s) [Default (press Enter) = 2.3E-9] ? ↙
 : ');
if isempty(DC)==1
    DC = 2.3E-9;
end
temp = [' Diffusion coefficient water phase (m2/s) = ',num2str(DC)];
fprintf(fid,'%s \n',temp);
disp(' ');
SNR = input(' Noise level (%) [Default (press Enter) = 0 for unknown] ? : ');
if isempty(SNR)==1
    SNR = 0;
end
temp = [' Noise level (%) = ',num2str(SNR)];
fprintf(fid,'%s \n',temp);
disp(' ');
if SNR > 0
   SNR = (100-SNR)/SNR;
end
temp = [' Please indicate your choice:                                          ';
        ' --------------------------                                            ';
        ' (1) Surface relaxivity is known. Calculate DSD.                       ';
        ' (2) Parameters of DSD are known. Calculate surface relaxivity         ';
        ' (3) PGSE data are available. Calculate surface relaxivity and DSD'];
disp(temp);
ans = input('     [ Default (press Enter) = 3 ]                                  ? : ');
if isempty(ans)==1
    ans = 3;
end

if ans == 1 % Calculates parameters dgN and sigma
   disp(' ');
   rho = input(' Surface relaxivity (micron/s) ? : ');
   disp(' ');
   T2_max = 1/(1/T2_bulk + 12*(rho*1e-6)^2/(DC*1000));

   for i = 1:max(size(T2_water))

      if T2_water(i) >= T2_max
         temp = ' IMPORTANT: T2 distribution surpassed T2_max. Excess computed as ↙
        bulk water.';
         flag_reprocess = 1;
         disp(temp);
         disp(' ');
         fprintf(fid,'%s \n',temp);
         fprintf(fid,'\n');
         clear tempx tempy tempz T2_water_old cumul_water_old freq_water_old;
         T2_water_old = T2_water;
         cumul_water_old = cumul_water;
         freq_water_old = freq_water;
         tempx = T2_water(1:i-1);
         tempy = cumul_water(1:i-1);
         tempz = freq_water(1:i-1);
         clear T2_water cumul_water freq_water;
         T2_water = tempx;
         cumul_water = tempy;
         freq_water = tempz;

         if ((cumul_water(i-1) < (1 - eps)) + (cumul_water(i-1) > 0.9)) == 2

            temp1 = [ ' ' num2str(100-max(cumul_water)*100)...
                 ' % of the signal from the water phase is originated in bulk'];
            temp2 =   ' and/or in droplets with sizes larger than the maximum size ↙
            for which the ';
            temp3 =   ' fast diffusion limit is valid. Would you like to discard ↙
            the signal from   ';
            temp4 =   ' such droplets and reprocess the CPMG data, taking into ↙
            account the signal  ';
            temp5 =   ' from drops with size d < d_MAX,FDL only ?  ';
```

```
            disp(temp1);
            disp(temp2);
            disp(temp3);
            disp(temp4);
            disp(temp5);
            disp(' ');

            resp_rep =...
            input(' (1) YES     (2) NO      [Defaults (press Enter) = 1] ?
            : ');
            if isempty(resp_rep) == 1
               resp_rep = 1;
            end

            if resp_rep == 1
               disp(' ')
               temp = ' File where modified CPMG data will be stored ';
               disp(temp);
               nombre3 = input(' [ Default (press Enter) = reprocess.dat ] ? : ','s');
               if isempty(nombre3)==1
                  nombre3 = 'reprocess.dat';
               end
               disp(' ');
            end
         end

         break;
      end

   end
   if max(cumul_water) < 0.9
      flag_end = 1;
   else
      diam = 6E-3*rho./(1./T2_water - 1/T2_bulk);
      temp = size(diam);
      if temp(1) == 1
         diam = diam';
      end
      data = [diam cumul_water];
      cd ..;
      bisection;
      simplex;
      temp = size(data);
      temp2 = size(freq_water);
      if temp(1) ~= temp2(1)
         freq_water = freq_water'
      end
      data = [diam./2 freq_water];
      P0 = [t1 t2 t3 t4 t5];
      Simplex_weibull;
      cd results;
   end

else
   if ans == 3
       cd ..;
       t1 = 1;
       t2 = 1;
       t3 = 1;
       t4 = 1;
       t5 = 0.1;
       PGSE_rho;
       if max(T2_water) >= T2_max
          T2_water_old = T2_water;
          cumul_water_old = cumul_water;
          freq_water_old = freq_water;
          T2_water = T2_temp;
          cumul_water = cumul_temp;
```

```
            freq_water = freq_temp;
        end
        if max(cumul_water) < 0.5
            flag_end = 1;
        else
            clear data;
            diam = 6E-3*rho./(1./T2_water - 1/T2_bulk);
            temp = size(diam);
            if temp(1) == 1
               diam = diam';
            end
            data = [diam cumul_water];
            bisection;
            simplex;
        end

    else
        disp(' ');
        dgN   = input(' Number-based geometric mean diameter (dgN, microns) ? : ');
        sigma = input(' Geometric standard deviation (sigma) ?                : ');
        disp(' ');
        fprintf(fid,'\n');
        cd ..;
        simplex_rho_lnd;
        if max(T2_water) >= T2_max
            T2_water_old = T2_water;
            cumul_water_old = cumul_water;
            freq_water_old = freq_water;
            T2_water = T2_temp;
            cumul_water = cumul_temp;
            freq_water = freq_temp;
        end
        if max(cumul_water) < 0.5
            flag_end = 1;
        else
            clear data;
            diam = 6E-3*rho./(1./T2_water - 1/T2_bulk);
            temp = size(diam);
            if temp(1) == 1
               diam = diam';
            end
            data = [diam./2 freq_water];
            P0 = [t1 t2 t3 t4 t5];
            Simplex_weibull;
        end
    end
    cd results;
end

diam_max = DC*1E12/(2*rho);
if SNR > 0
    diam_max_SNR = 2*rho*SNR*(T2_bulk/1000)/exp(1);
end

if flag_end == 0

    if kappa > 0
       temp = [' Logmean diffusion coefficient oil phase (m2/s) = ' num2str(DC_CP)];
       fprintf(fid,'%s \n',temp);
       temp = [' St. dev. diffusion coeffs. oil phase           = ' num2str(SD_CP)];
       fprintf(fid,'%s \n',temp);
    end
    fprintf(fid,'\n');
    temp = [' Results';' -------'];
    disp(temp)
    disp(' ');
    fprintf(fid,'\n');
    fprintf(fid,' Results \n',temp(1));
    fprintf(fid,' ------- \n',temp(1));
```

```
fprintf(fid,'\n');

figure(4)
calc_prob_lnd(1) = 0;
calc_prob_bwd(1) = 0;
for i = 2:max(size(diam))
   xtempi = log(diam(i)/diam(1));
   xtempi_1 = log(diam(i-1)/diam(1));
   calc_prob_lnd(i) = 0.5*(erf(log(diam(i)/dgV)/(2^.5*sigma))- erf(log(diam(i-
  1)/dgV)/(2^.5*sigma)));
   calc_prob_bwd(i) = (omega*(exp(-1*(xtempi_1/sigma1)^m1)-exp(-
   1*(xtempi/sigma1)^m1)) + ...
    (1-omega)*(exp(-1*(xtempi_1/sigma2)^m2)-exp(-1*(xtempi/sigma2)^m2)));
end
semilogx(diam,freq_water,'ok');
hold on;
semilogx(diam,calc_prob_lnd,'--b');
semilogx(diam,calc_prob_bwd,'--r');
semilogx([diam_max diam_max],[0 1],'-.g');
if SNR > 0
      semilogx([diam_max_SNR diam_max_SNR],[0 1],'-.k');
end
ymax = 1;
clear u_lnd u_bwd T2_temp calc_cumul_lnd calc_cumul_bwd diam_temp;
temp1 = 0.7*min(log10(diam));
temp2 = max(log10(diam));
temp3 = (temp2-temp1)/100;
x = temp1:temp3:temp2;
x = 10.^x;
u_lnd = (log(x./dgV))./(2^.5*sigma);
calc_cumul_lnd = .5.*(1 + erf(u_lnd));
T2_temp = log(T2_min):(log(T2_max/T2_min)/100):log(max(T2_water));
T2_temp = exp(T2_temp);
diam_temp = 6E-3*rho./(1./T2_temp - 1/T2_bulk);
u_bwd = log(diam_temp./diam_temp(1));
calc_cumul_bwd = (omega.*(1-exp(-1.*(u_bwd./sigma1).^m1)) + ...
                  (1-omega).*(1-exp(-1.*(u_bwd./sigma2).^m2)));
semilogx(diam,cumul_water.*ymax,'*k');
semilogx(x,calc_cumul_lnd.*ymax,'-b');
semilogx(diam_temp,calc_cumul_bwd.*ymax,'-r');
xlabel('Diameter (micron)');
ylabel('Volume-weighted probability');
title(['Volume-weighted drop size distribution. dgV (microns) = ',...
      num2str(dgV),'. sigma = ',num2str(sigma)]);
xmin = 10^(fix(log10(diam(1))-1));
if SNR > 0
   xmax = 10^(fix(log10(diam_max_SNR))+1);
else
   xmax = 10^(fix(log10(diam(max(size(diam)))))+1);
end
axis([xmin xmax 0 ymax]);
fprintf(fid,' Volume-weighted drop size distribution \n');
fprintf(fid,' \n');
fprintf(fid,' d (microns)  Prob. (vol. frac.) Cumul. Prob \n');
for i = 1:max(size(diam))
   fprintf(fid,' %6.4e     %6.4e     %6.4e \n',diam(i), freq_water(i),
cumul_water(i));
end
fprintf(fid,' \n');
temp1 = ' Log-normal distribution fit of cumulative probability P(d), d = drop
diameter : ';
temp2 = '       /d';
temp3 = ' P(d)= | p(x)*dx;  p(x) = {1/[(2*pi)^.5*sigma*x]}*exp{-[ln(x)-
ln(dgV)]^2/(2*sigma^2)}';
temp4 = '       /0';
disp(temp1);
disp(temp2);
disp(temp3);
disp(temp4);
```

```
disp(' ');
fprintf(fid,' %s \n',temp1);
fprintf(fid,' %s \n',temp2);
fprintf(fid,' %s \n',temp3);
fprintf(fid,' %s \n',temp4);
fprintf(fid,'\n');

dgN = dgV / exp(3*sigma^2);
d32 = dgN * exp(1.5*sigma^2);

temp = [' dgV (micron) = ' num2str(dgV) '    [ dgN (micron) = ' ...
       num2str(dgN) '; d32 (micron) = ' num2str(d32) ' ]'];

disp(temp)
fprintf(fid,' %s \n',temp);
temp = [' sigma        = ' num2str(sigma)];
disp(temp)
disp(' ');
fprintf(fid,' %s \n',temp);
fprintf(fid,'\n');
temp = [' Water content (WC, vol.%)               = ',num2str(Water_cut)];
disp(temp);
fprintf(fid,'%s \n',temp);
disp(' ');
fprintf(fid,'\n');
temp = [' Water in droplets (d =< d_max_FDL) (% of WC) = ' ↙
 num2str(100*max(cumul_water))];
disp(temp)
fprintf(fid,' %s \n',temp);
temp = [' Bulk water  (% of WC)                        = ' num2str(100- ↙
 max(cumul_water)*100)];
disp(temp);
fprintf(fid,' %s \n',temp);
disp(' ');
fprintf(fid,'\n');
temp = [' Surface relaxivity (micron/s)           = ',num2str(rho)];
disp(temp);
fprintf(fid,'%s \n',temp);
disp(' ');
fprintf(fid,'\n');
if kappa > 0
   temp = [' Contribution of oil phase to R (kappa)  = ',num2str(kappa)];
   disp(temp);
   fprintf(fid,'%s \n',temp);
   disp(' ');
   fprintf(fid,'\n');
end

temp = [' Cutoff drop diameter for fast diffusion limit (d_max_FDL, microns) = ↙
       ',...
       num2str(diam_max)];
disp(temp);
fprintf(fid,'%s \n',temp);

if SNR > 0

   temp = [' Maximum drop size dictated by T2,bulk and SNR (d_max_SNR, microns) = ↙
          ',...
          num2str(diam_max_SNR)];
   disp(temp);
   disp(' ');
   fprintf(fid,'%s \n',temp);
   fprintf(fid,'\n');

end

temp1 = ' Parameters of the bimodal Weibull distribution ';
temp2 = ' ------------------------------------------- ';
temp3 = [' sigma1       = ' num2str(sigma1)];
```

```
      temp4 = [' sigma2       = ' num2str(sigma2)];
      temp5 = [' m1           = ' num2str(m1)];
      temp6 = [' m2           = ' num2str(m2)];
      temp7 = [' omega        = ' num2str(omega)];
      temp8 = [' a0 (microns) = ' num2str(diam(1)/2)];
      disp(' ');
      disp(temp1);
      disp(temp2);
      disp(temp3);
      disp(temp4);
      disp(temp5);
      disp(temp6);
      disp(temp7);
      disp(temp8);
      fprintf(fid,' %s \n',temp1);
      fprintf(fid,' %s \n',temp2);
      fprintf(fid,' %s \n',temp3);
      fprintf(fid,' %s \n',temp4);
      fprintf(fid,' %s \n',temp5);
      fprintf(fid,' %s \n',temp6);
      fprintf(fid,' %s \n',temp7);
      fprintf(fid,' %s \n',temp8);

   else

      fprintf(fid,'\n');
      temp = [' Water content (WC, vol.%) = ',num2str(Water_cut)];
      fprintf(fid,'%s \n',temp);
      fprintf(fid,'\n');

      temp = [' MORE THAN 10 % OF THE SIGNAL OF THE WATER PHASE IS ORIGINATED FROM BULK ↙
      WATER  ';
     ' AND/OR FROM DROPLETS WITH SIZES LARGER THAN THE MAXIMUM SIZE FOR WHICH THE     ';
     ' FAST DIFFUSION APPROXIMATION IS VALID. IT IS STRONGLY SUGGESTED TO REMOVE      ';
     ' BULK WATER FROM THE SAMPLE AND PERFORM NEW CPMG/PGSE TESTS IN THE REMAINING    ';
     ' EMULSION, SO THE DROP SIZE DISTRIBUTION CAN BE DETERMINED.                     '];
      disp(' ');
      disp(temp);
      temp = temp';
      fprintf(fid,'%s \n',temp(1:80));
      fprintf(fid,'%s \n',temp(81:160));
      fprintf(fid,'%s \n',temp(161:240));
      fprintf(fid,'%s \n',temp(241:320));
      fprintf(fid,'%s \n',temp(321:400));
      disp(' ');
      fprintf(fid,'\n');
      temp = [' Cutoff drop diameter for fast diffusion limit (d_max_FDL, microns) = ↙
      ',...
               num2str(diam_max)];
      disp(temp);
      fprintf(fid,'%s \n',temp);

   end

end

disp(' ');
disp([' Results are stored in file ' nombre2]);
disp(' ');
cd ..;

if ((flag_reprocess == 1) + (resp_rep == 1)) == 2

   cd input;
   data = load(nombre);
   fid3 = fopen(nombre3,'w');
   fprintf(fid3,' %6.4e  %6.4e \n ',data(1,1), data(1,2));
   for i = 2 : max(size(data))
      if data(i,1) > T2_max
```

```
         fprintf(fid3,' %6.4e  %6.4e \n ',data(i,1), 0);
      else
         fprintf(fid3,' %6.4e  %6.4e \n ',data(i,1), data(i,2));
      end
   end
   fclose(fid3);
   cd ..;
   cd results;
   temp = ([' Data for reprocessing are stored in file ', nombre3]);
   disp(temp);
   disp(' ');
   fprintf(fid,'\n');
   fprintf(fid,' %s \n',temp);
   cd ..;

end

fclose(fid);
```

File pgse_rho.m

```
% ------------------------------------------------------------------------------
%      Characterization of W/O Emulsions via NMR-CPMG/PGSE - File PGSE_rho.m
% ------------------------------------------------------------------------------
% Copyright (C) 2001-2003 Alejandro Pena, Clarence Miller and George Hirasaki
%
% File PGSE_rho.m: Generates attenuation profile for a PGSE experiment using the
%                  drop size distribution that is calculated from the T2 distri-
%                  bution of the water phase for a given surface relaxivity.
%
% ------------------------------------------------------------------------------

clear alfa2 alfaR data erro Ldelta P psum Ptry R a x y kappa;
disp(' ');
nombre = input(' Name of file (with extension) where PGSE data are saved ? : ','s');
cd input;
data_PGSE = load(nombre);
cd ..;

Udelta = data_PGSE(1,1);
G = data_PGSE(1,2);
disp(' ');
disp([' Time between gradient pulses (s) = ' num2str(Udelta)]);
disp(' ');
disp([' Strength of magnetic field gradient (T/m) = ' num2str(G)]);
disp(' ');
disp(' Fractional contribution of continuous phase to R in PGSE tests (kappa): ');
disp(' ------------------------------------------------------------------------  ');
disp(' ');
disp([' Calculate kappa from (1) T2 distribution emulsion    ';
      '                      (2) Data for pure components    ';
      '                      (3) Assume kappa = 0            ']);
Calckappa = input('                          [ Default (press Enter) = 1 ] ? : ');
if isempty(Calckappa)==1
   Calckappa = 1;
end
disp(' ');
if Calckappa == 1
   temp = size(freq);
   if temp(1) == 1
       freq = freq';
   end
   temp1 =  freq(ini_peak(npeaks):end_peak(npeaks))'*exp(-2*(Udelta*1000)./T2_water);
   temp2 =  freq(ini_peak(1):end_peak(1))'*exp(-2*(Udelta*1000)./T2_oil);
else
   if Calckappa == 2
      temp = [' Water content (vol.%) [ Default (press Enter) = '  num2str(Water_cut) '↙
```

```
      ] : '];
      fwx = input(temp);
      if isempty(fwx)==1
         fwx = Water_cut/100;
      else
         fwx = fwx/100;
      end
      temp = [' Mean T2 water phase [ Default (press Enter) = '  num2str(T2_avg_w) ' ms ↙
      ] : '];
      T2wx = input(temp);
      if isempty(T2wx)==1
         T2wx = T2_avg_w;
      end
      temp = [' Mean T2 oil phase   [ Default (press Enter) = '  num2str(T2_avg_o) ' ms ↙
      ] : '];
      T2ox = input(temp);
      if isempty(T2ox)==1
         T2ox = T2_avg_o;
      end
      temp1 =  fwx*HI_w*exp(-2*(Udelta*1000)/T2wx);
      temp2 =  (1-fwx)*HI_o*exp(-2*(Udelta*1000)./T2ox);
   end
end
if Calckappa ~= 3
    kappa = 1/(1+temp1/temp2);
    disp(' ');
    disp([' kappa = ' num2str(kappa)]);
    disp(' ');
else
    kappa = 0;
end

gamma = 2.675e8;          % Magnetogyric ratio of the proton, rad/s.T

n = 20;                   % First n roots of the equation u * J(5/2,u) - J(3/2,u) = 0
temp = load('alfa.dat'); % (to be used in erreval_rho.m)
alfaR = temp(1:n);        %
```

```
temp = load('gauss.dat');                % Gaussian quadrature points
u =    [-1*temp(:,1) ; temp(:,1) ];
w_gc = [   temp(:,2) ; temp(:,2) ];

if (kappa > 0)
   R_CP;                  % Attenuation profile for continuous phase
end

ndim = 1;                 % Number of variables: 1 (rho)
ftol = 1e-4;              % Permitted tolerance (control)
rtol = 1 + ftol;          % Tolerance factor (to be calculated)
ITMAX = 150;              % Maximum number of iterations

% Definition of the simplex

P0 = -0.6931; % ln0.50

lambda = P0/2;

P = [P0 ; P0 + lambda];

% Evaluation of errors at the corners of the Simplex

for w = 1:(ndim + 1)
    lnrho = P(w);
    erreval_rho;
    erro(w) = sumerr;
end

% Minimization of error
```

```
iter = 0;
psum = sum(P,1);
disp(' ');

while rtol >= ftol    % Beginning of while loop

   ilo = 1;
   if erro(1) > erro(2)
      ihi = 1;
      inhi = 2;
   else
      ihi = 2;
      inhi = 1;
   end
   for i = 1:(ndim + 1)
      if erro(i) <= erro(ilo)
         ilo = i;
      end
      if erro(i) > erro(ihi)
         inhi = ihi;
         ihi = i;
      else
         if erro(i) > erro(inhi)
            if i ~= ihi
                inhi = i;
            end
         end
      end
   end

   iter = iter + 2;
   disp([' Iteration # ' num2str(iter)]);
   fac = -1;
   amotry_rho;
   if errotry <= erro(ilo)
      fac = 2;
      amotry_rho;
   elseif errotry >= erro(inhi)
      errosave = erro(ihi);
      fac = 0.5;
      amotry_rho;
      if errotry >= errosave
         for w = 1:(ndim + 1)
            if w ~= ilo
               for j = 1:ndim
                  psum(j) = 0.5*(P(w,j)+P(ilo,j));
                  P(w,j) = psum(j);
               end
               lnrho = psum(1);
               erreval_rho;
               erro(w) = sumerr;
            end
         end
         iter = iter + ndim;
         psum = sum(P,1);
      end
   else
      iter = iter - 1;
   end
   rtol = 2*abs(erro(ihi)-erro(ilo))/(abs(erro(ihi))+abs(erro(ilo))+eps);
   if iter >= ITMAX
      disp('WARNING: ITMAX for PGSE_rho exceeded');
      rtol
      rtol = 0;
   end
end %end of while loop

disp(' ');
temp = erro(1);
```

```
erro(1) = erro(ilo);
erro(ilo) = temp;
for i = 1:ndim
   temp = P(1,i);
   P(1,i) = P(ilo,i);
   P(ilo,i) = temp;
end

rho = exp(P(1));

% Averaging  and plotting results

figure(3);
plot(data_PGSE(2:max(size(data_PGSE)),1),data_PGSE(2:max(size(data_PGSE)),2),'or');
hold on;
plot(data_PGSE(2:max(size(data_PGSE)),1),R,'-k');
xlabel('delta (s)');
ylabel('atenuation');
temp = 10^fix(log10(max(data_PGSE(2:max(size(data_PGSE)),1))) - 1);
xmax = (fix(max(data_PGSE(2:max(size(data_PGSE)),1))/temp) + 1)*temp;
axis([0 xmax 0 1]);
title([' NMR-PGSE results.']);
```

File r_cp.m

```
% ------------------------------------------------------------------------------
%         Characterization of W/O Emulsions via NMR-CPMG/PGSE - R_CP.m
% ------------------------------------------------------------------------------
% Copyright (C) 2001-2003 Alejandro Pena, Clarence Miller and George Hirasaki
%
% File R_CP.m: Calculates the PGSE attenuation profile for the continuous phase
%              of the emulsion. It is assumed that the continuous phase exhibits
%              a lognormal distribution of diffusion coefficients.
%
% ------------------------------------------------------------------------------

clear Diff temp1 temp2 R_CPh DC_CP SD_CP

DC_CP = input(...
' Mean Diffusion coef. continuous phase (m2/s) [Default (press Enter) = 1E-10] ? : ');
if isempty(DC_CP)==1
    DC_CP = 1E-10;
end
SD_CP = input(...
' Standard deviation Diff. coef. continuous phase  [Default (press Enter) = 0] ? : ');
if isempty(SD_CP)==1
    SD_CP = 0;
end
SD_CP = SD_CP + eps;

% Correction for restricted diffusion in continuous phase

eta = 1/(1+ Water_cut/200 + (1/4) * (Water_cut/74.02)^9);

% Attenuation profile. Integration is carried

R_CPh = zeros(1,(max(size(data_PGSE))-1));

for k = 1:(max(size(data_PGSE))-1)
   Ldelta = data_PGSE(k + 1, 1);
   for i = 1:max(size(u))
      Diff = eta*DC_CP*((1+u(i))/(1-u(i)))^SD_CP;
      temp1 = exp(-1*gamma^2*Ldelta^2*G^2*(Udelta-Ldelta/3)*Diff);
      temp2 = 2*temp1*exp(-1*(log((Diff/(eta*DC_CP))))^2/(2*SD_CP^2))/((8*atan(1))...
              ^.5*(1-u(i)^2));
      R_CPh(k) = R_CPh(k) + temp2 * w_gc(i);
   end
end
```

File erreval_rho.m

```
% ------------------------------------------------------------------------------
%     Characterization of O/W Emulsions via NMR-CPMG/PGSE - File erreval_rho.m
% ------------------------------------------------------------------------------
% Copyright (C) 2001-2003 Alejandro Pena, Clarence Miller and George Hirasaki
%
% File erreval_rho.m: Calculates the error in the fit of the PGSE data. Numerical
%                     integration of the theoretical expression for attenuation
%                     profile is performed via Gaussian quadrature (24 points)
%
% ------------------------------------------------------------------------------

clear T2_temp cumul_temp freq_temp xr x_exp y z a a_exp R;
rho = exp(lnrho);
d_min = 6E-9*rho./(1./T2_min - 1/T2_bulk);
d_max = DC/(2*rho*1e-6);
T2_max = 1/(1/T2_bulk + rho*6E-9/d_max);

if max(T2_water) >= T2_max
   for i = 1:max(size(T2_water))
      if T2_water(i) >= T2_max
         clear tempx tempy tempz;
         tempx = T2_water(1:i-1);
         tempy = cumul_water(1:i-1);
         tempz = freq_water(1:i-1);
         clear freq_temp T2_temp cumul_temp;
         T2_temp = tempx;
         cumul_temp = tempy;
         freq_temp = tempz;
         break;
      end
   end
else
   T2_temp = T2_water;
   cumul_temp = cumul_water;
   freq_temp = freq_water;
end

a_exp = 3E-9*rho./(1./T2_temp-1/T2_bulk);
temp = size(a_exp);
if temp(1) == 1
    a_exp = a_exp';
end
data = [a_exp freq_temp];
P0 = [t1 t2 t3 t4 t5];
Simplex_weibull;
ndim = 1;

if 2*max(a_exp) > d_max
   xmax = log(d_max/d_min);    % xmax is ksi' in theoretical development
else
   xmax = log(2*max(a_exp)/d_min);
end

xr = (xmax/2).*(u + 1);        % Transforming Gaussian points into drop radii a
a = (d_min/2).*exp(xr);

sumerr = 0;

for k = 1:(max(size(data_PGSE)-1))

   Numerator = 0;
   Denominator = 0;
   Ldelta = data_PGSE(k+1,1);   % Duration of gradient, s (from experimental data)
   for i = 1:max(size(a))
      clear alfa2;
```

```
      alfa2 = (alfaR / a(i)).^2;
      alfa2 = alfa2 + eps;
      coef = 1./(alfa2.*(alfaR.^2 - 2));
      suma = 0;
      for j = 2:n
         temp = 2 + exp(-1*alfa2(j)*DC*(Udelta - Ldelta))-2*exp(-1*alfa2(j)*DC*Udelta);
         temp = temp - 2*exp(-1*alfa2(j)*DC*Ldelta) + exp(-1*alfa2(j)*DC*(Udelta + ↙
         Ldelta));
         temp = 2*Ldelta/(alfa2(j)*DC)- temp/(alfa2(j)*DC)^2;
         suma = suma + coef(j)*temp;
      end
      y(i) = exp(-2*G^2*gamma^2*suma);
      z(i) = ((omega*m1/sigma1^m1)*xr(i)^(m1-1)*exp(-1*(xr(i)/sigma1)^m1)+ ...
           ((1-omega)*m2/sigma2^m2)*xr(i)^(m2-1)*exp(-1*(xr(i)/sigma2)^m2));
      y(i) = y(i) * z(i);
      y(i) = y(i) * xmax / 2 ;
      z(i) = z(i) * xmax / 2 ;
      Numerator   = Numerator   + y(i)*w_gc(i);
      Denominator = Denominator + z(i)*w_gc(i);
   end

   R(k) = Numerator/Denominator;
   if kappa > 0
       R(k) = R(k) * (1 - kappa) + R_CPh(k) * kappa;
   end
   sumerr = sumerr + (data_PGSE(k+1,2) - R(k))^2;

end

lastrho = rho;
figure(5);
hold on;
plot(data_PGSE(2:max(size(data_PGSE)),1),data_PGSE(2:max(size(data_PGSE)),2),'or');
hold on;
plot(data_PGSE(2:max(size(data_PGSE)),1),R,'-g');
xlabel('delta (s)');
ylabel('atenuation');
temp = 10^fix(log10(max(data_PGSE(2:max(size(data_PGSE)),1)))) - 1);
xmax = (fix(max(data_PGSE(2:max(size(data_PGSE)),1))/temp) + 1)*temp;
axis([0 xmax 0 1]);
title([' NMR-PGSE results.']);
```

File amotry_rho.m

```
% ------------------------------------------------------------------------------
%       Characterization of O/W Emulsions via NMR-CPMG/PGSE - amotry_rho.m
% ------------------------------------------------------------------------------
% Copyright (C) 2001-2003 Alejandro Pena, Clarence Miller and George Hirasaki
%
% File amotry_rho.m: Extrapolates by a factor fac through the face of the Simplex
%                    across from the high point, tries it and replaces the high
%                    point if the new point is better.
%
% ------------------------------------------------------------------------------

fac1 = (1-fac)/ndim;
fac2 = fac1 - fac;
for j = 1:ndim
    Ptry(j) = psum(j)*fac1-P(ihi,j)*fac2;
end
lnrho = Ptry(1);
erreval_rho;
errotry = sumerr;
if errotry < erro(ihi)
    erro(ihi) = errotry;
    for j = 1:ndim
        psum(j) = psum(j) - P(ihi,j) + Ptry(j);
        P(ihi,j) = Ptry(j);
```

```
    end
end
```

File simplex_weibull.m

```
% ------------------------------------------------------------------------------
%   Characterization of O/W Emulsions via NMR-CPMG/PGSE - File Simplex_weibull.m
% ------------------------------------------------------------------------------
% Copyright (C) 2001-2003 Alejandro Pena, Clarence Miller and George Hirasaki
%
% File Simplex_weibull.m: Applies the downhill Simplex method to determine the
%                         numerical values of the parameters of the bimodal
%                         Weibull distribution that render the best fit of the
%                         drop size distribution calculated from CPMG data
%                         with a given surface relaxivity.
%
% ------------------------------------------------------------------------------

clear x2 y yobs erro2 P2 psum2;

x2 = log(data(:,1)./data(1,1));

ndim2 = 5;                  % Number of variables: dgN and sigma
ftol2 = 1e-8;               % Permitted tolerance (control)
rtol2 = 1 + ftol2;          % Tolerance factor (to be calculated)
ITMAX2 = 100000;            % Maximum number of iterations

% Definition of the simplex

%P0 = [1 1 1 1 .5];

lambda = P0/2;
e1 = [1 0 0 0 0];
e2 = [0 1 0 0 0];
e3 = [0 0 1 0 0];
e4 = [0 0 0 1 0];
e5 = [0 0 0 0 1];

P2 = [P0 ; P0 + lambda(1)*e1; P0 + lambda(2)*e2; P0 + lambda(3)*e3; P0 + lambda(4)*e4; ↙
P0 + lambda(5)*e5];

% Evaluation of errors at the corners of the Simplex

for w2 = 1:(ndim2 + 1)
    t1 = P2(w2,1);
    t2 = P2(w2,2);
    t3 = P2(w2,3);
    t4 = P2(w2,4);
    t5 = P2(w2,5);
    erreval_weibull;
    erro2(w2) = sumerr2;
end

% Minimization of error
iter2 = 0;
psum2 = sum(P2,1);

while rtol2 >= ftol2    %beginning of while loop

ilo2 = 1;
if erro2(1) > erro2(2)
    ihi2 = 1;
    inhi2 = 2;
else
    ihi2 = 2;
    inhi2 = 1;
end
for i = 1:(ndim2 + 1)
```

```
    if erro2(i) <= erro2(ilo2)
        ilo2 = i;
    end
    if erro2(i) > erro2(ihi2)
        inhi2 = ihi2;
        ihi2 = i;
    else
        if erro2(i) > erro2(inhi2)
            if i ~= ihi2
                inhi2 = i;
            end
        end
    end
end

if iter2 >= ITMAX2
   ans = 'ITMAX in Simplex_Weibull.m exceeded'
end

iter2 = iter2 + 2;
fac2 = -1;
amotry_weibull;
if errotry2 <= erro2(ilo2)
   fac2 = 2;
   amotry_weibull;
elseif errotry2 >= erro2(inhi2)
   errosave2 = erro2(ihi2);
   fac2 = 0.5;
   amotry_weibull;
   if errotry2 >= errosave2
      for w2 = 1:(ndim2 + 1)
          if w2 ~= ilo2
              for j = 1:ndim2
                  psum2(j) = 0.5*(P2(w2,j)+P2(ilo2,j));
                  P2(w2,j) = psum2(j);
              end
              t1 = P2(w2,1);
              t2 = P2(w2,2);
              t3 = P2(w2,3);
              t4 = P2(w2,4);
              t5 = P2(w2,5);
              erreval_weibull;
              erro2(w2) = sumerr2;
          end
      end
      iter2 = iter2 + ndim2;
      psum2 = sum(P2,1);
   end
else
   iter2 = iter2 - 1;
end
rtol2 = 2*abs(erro2(ihi2)-erro2(ilo2))/(abs(erro2(ihi2))+abs(erro2(ilo2))+eps);

end %end of while loop

temp = erro2(1);
erro2(1) = erro2(ilo2);
erro2(ilo2) = temp;
for i = 1:ndim2
   temp = P2(1,i);
   P2(1,i) = P2(ilo2,i);
   P2(ilo2,i) = temp;
end

% Averaging  and plotting results
t1 = P2(1,1);
t2 = P2(1,2);
t3 = P2(1,3);
t4 = P2(1,4);
```

```
t5 = P2(1,5);

%Plot drop size distribution
sigma1 = t1^2;
sigma2 = t2^2;
m1 =     t3^2;
m2 =     t4^2;
omega =  1/(1+exp(-1*t5));

erreval_weibull;
y(1) = cum(1);
yobs(1) = data(1,2);
for i = 2:max(size(x2));
    yobs(i) = data(i,2);
end
```

File erreval_weibull.m

```
% ------------------------------------------------------------------------------
%    Characterization of Emulsions via NMR-CPMG/PGSE - File erreval_weibull.m
% ------------------------------------------------------------------------------
% Copyright (C) 2001-2003 Alejandro Pena, Clarence Miller and George Hirasaki
%
% File erreval_weibull.m: Calculates the error in the fit of the drop size distri-
%                         bution data with the bimodal Weibull p.d.f.
%
% ------------------------------------------------------------------------------

clear cum;
sumerr2 = 0;
sigma1 = t1^2;
sigma2 = t2^2;
m1 =     t3^2;
m2 =     t4^2;
omega =  1/(1+exp(-1*t5));
for k = 1:max(size(x2))
   cum(k) = omega*(1-exp(-1*(x2(k)/sigma1)^m1)) + (1-omega)*(1-exp(- ↙
   1*(x2(k)/sigma2)^m2));
   if k == 1
       y(k) = cum(k);
   else
       y(k) = cum(k) - cum(k-1);
   end
   sumerr2 = sumerr2 + (data(k,2) - y(k))^2;
end
```

File amotry_weibull.m

```
% ------------------------------------------------------------------------------
%     Characterization of O/W Emulsions via NMR-CPMG/PGSE - amotry_weibull.m
% ------------------------------------------------------------------------------
% Copyright (C) 2001-2003 Alejandro Pena, Clarence Miller and George Hirasaki
%
% File amotry_weibull.m: Extrapolates by a factor fac2 through the face of the
%                        Simplex across from the high point, tries it and
%                        replaces the high point if the new point is better.
%
% ------------------------------------------------------------------------------

fac12 = (1-fac2)/ndim2;
fac22 = fac12 - fac2;
for j = 1:ndim2
    Ptry2(j) = psum2(j)*fac12-P2(ihi2,j)*fac22;
end
```

```
t1 = Ptry2(1);
t2 = Ptry2(2);
t3 = Ptry2(3);
t4 = Ptry2(4);
t5 = Ptry2(5);
erreval_weibull;
errotry2 = sumerr2;
if errotry2 < erro2(ihi2)
    erro2(ihi2) = errotry2;
    for j = 1:ndim2
        psum2(j) = psum2(j) - P2(ihi2,j) + Ptry2(j);
        P2(ihi2,j) = Ptry2(j);
    end
end
```

File simplex_rho_lnd.m

```
% ------------------------------------------------------------------------------
%     Characterization of W/O Emulsions via NMR-CPMG/PGSE - simplex_rho_lnd.m
% ------------------------------------------------------------------------------
% Copyright (C) 2001-2003 Alejandro Pena, Clarence Miller and George Hirasaki
%
% File simplex_rho_lnd.m: Applies downhill Simplex method to determine surface
%                         relaxivity when the parameters of the drop size distri-
%                         bution are known
% ------------------------------------------------------------------------------

clear u_lnd;
dgV = dgN*exp(3*sigma^2);

ndim = 1;                % Number of variables: 1 (rho)
ftol = 1e-8;             % Permitted tolerance (control)
rtol = 1 + ftol;         % Tolerance factor (to be calculated)
ITMAX = 150;             % Maximum number of iterations

% Definition of the simplex

P0 = -0.6931; % ln(0.5)

lambda = P0/2;

P = [P0 ; P0 + lambda];

% Evaluation of errors at the corners of the Simplex

for w = 1:(ndim + 1)
    lnrho = P(w);
    erreval_rho_lnd;
    erro(w) = sumerr;
end

% Minimization of error

iter = 0;
psum = sum(P,1);
disp(' ');

while rtol >= ftol    %beginning of while loop

   ilo = 1;
   if erro(1) > erro(2)
      ihi = 1;
      inhi = 2;
   else
      ihi = 2;
```

```
      inhi = 1;
   end
   for i = 1:(ndim + 1)
      if erro(i) <= erro(ilo)
         ilo = i;
      end
      if erro(i) > erro(ihi)
         inhi = ihi;
         ihi = i;
      else
         if erro(i) > erro(inhi)
            if i ~= ihi
                inhi = i;
            end
         end
      end
   end

   iter = iter + 2;
   disp([' Iteration # ' num2str(iter)]);
   fac = -1;
   amotry_rho_lnd;
   if errotry <= erro(ilo)
      fac = 2;
      amotry_rho_lnd;
   elseif errotry >= erro(inhi)
      errosave = erro(ihi);
      fac = 0.5;
      amotry_rho_lnd;
      if errotry >= errosave
         for w = 1:(ndim + 1)
            if w ~= ilo
               for j = 1:ndim
                  psum(j) = 0.5*(P(w,j)+P(ilo,j));
                  P(w,j) = psum(j);
               end
               lnrho = psum(1);
               erreval_rho_lnd;
               erro(w) = sumerr;
            end
         end
         iter = iter + ndim;
         psum = sum(P,1);
      end
   else
      iter = iter - 1;
   end
   rtol = 2*abs(erro(ihi)-erro(ilo))/(abs(erro(ihi))+abs(erro(ilo))+eps);
   if iter >= ITMAX
      disp('Warning: ITMAX for PGSE_rho exceeded');
      rtol
      rtol = 0;
   end
end %end of while loop

disp(' ');
temp = erro(1);
erro(1) = erro(ilo);
erro(ilo) = temp;
for i = 1:ndim
   temp = P(1,i);
   P(1,i) = P(ilo,i);
   P(ilo,i) = temp;
end

rho = exp(P(1));
```

File erreval_rho_lnd.m

```
% ------------------------------------------------------------------------------
%    Characterization of W/O Emulsions via NMR-CPMG/PGSE - erreval_rho_lnd.m
% ------------------------------------------------------------------------------
% Copyright (C) 2001-2003 Alejandro Pena, Clarence Miller and George Hirasaki
%
% File erreval_rho_lnd.m: Calculates the error between the cumulative CPMG data for
%                         the water phase and the cumulative lognormal distribution
%                         for a given surface relaxivity
% ------------------------------------------------------------------------------

clear T2_temp cumul_temp freq_temp x a R;
rho = exp(lnrho);
T2_max = 1/(1/T2_bulk + 12*(rho*1e-6)^2/(DC*1000));

T2_temp = T2_water;
cumul_temp = cumul_water;
freq_temp = freq_water;

if max(T2_water) >= T2_max
   for i = 1:max(size(T2_water))
      if T2_water(i) >= T2_max
         clear tempx tempy tempz;
         tempx = T2_water(1:i-1);
         tempy = cumul_water(1:i-1);
         tempz = freq_water(1:i-1);
         clear freq_temp T2_temp cumul_temp;
         T2_temp = tempx;
         cumul_temp = tempy;
         freq_temp = tempz;
         break;
      end
   end
end

sumerr = 0;
clear diam u_lnd cal_cumul;

diam = 6E-3*rho./(1./T2_temp - 1/T2_bulk);
u_lnd = (log(diam./dgV))./(2^.5*sigma);
calc_cumul = .5.*(1 + erf(u_lnd));
sumerr = sum((cumul_temp-calc_cumul).^2);
```

File amotry_rho_lnd.m

```
% ------------------------------------------------------------------------------
%     Characterization of O/W Emulsions via NMR-CPMG/PGSE - amotry_rho_lnd.m
% ------------------------------------------------------------------------------
% Copyright (C) 2001-2003 Alejandro Pena, Clarence Miller and George Hirasaki
%
% File amotry_rho_lnd.m: Extrapolates by a factor fac through the face of the
%                        Simplex across from the high point, tries it and
%                        replaces the high point if the new point is better.
%
% ------------------------------------------------------------------------------

fac1 = (1-fac)/ndim;
fac2 = fac1 - fac;
for j = 1:ndim
    Ptry(j) = psum(j)*fac1-P(ihi,j)*fac2;
end
lnrho = Ptry(1);
```

```
erreval_rho_lnd;
errotry = sumerr;
if errotry < erro(ihi)
    erro(ihi) = errotry;
    for j = 1:ndim
        psum(j) = psum(j) - P(ihi,j) + Ptry(j);
        P(ihi,j) = Ptry(j);
    End
end
```

File simplex.m

```
% ------------------------------------------------------------------------------
%       Characterization of O/W Emulsions via NMR-CPMG/PGSE - File Simplex.m
% ------------------------------------------------------------------------------
% Copyright (C) 2001-2003 Alejandro Pena, Clarence Miller and George Hirasaki
%
% File Simplex.m: Applies the downhill Simplex method to determine the
%                 numerical values of the parameters of the lognormal
%                 distribution that render the best fit of the
%                 drop size distribution calculated from CPMG data
%                 with a given surface relaxivity.
%
% ------------------------------------------------------------------------------

clear u_lnd;

ndim = 2;                % Number of variables for simplex : dgV and sigma
ftol = 1e-5;             % Permitted tolerance (control)
rtol = 1 + ftol;         % Tolerance factor (to be calculated)
ITMAX = 150;             % Maximum number of iterations

% Definition of the simplex
dgV_aprox = davg;
sigma_aprox = sigma;
P0 = [davg sigma];

lambda = P0/2;
e1 = [1 0];
e2 = [0 1];
if ndim == 1
   e1 = [0 0]
   e2 = e1;
end

P = [P0 ; P0 + lambda(1) * e1 ; P0 + lambda(2) * e2];

% Evaluation of errors at the corners of the Simplex

for z = 1:(ndim + 1)
   dgV = P(z,1);
   sigma = P(z,2);
   u_lnd = (log(data(:,1)./dgV))./(2^.5*sigma);
   calc_cumul = .5.*(1 + erf(u_lnd));
   erro(z) = sum((data(:,2)-calc_cumul).^2);
end

% Minimization of error

iter = 0;
psum = sum(P,1);

while rtol >= ftol    % beginning of while loop

ilo = 1;
if erro(1) > erro(2)
```

```
   ihi = 1;
   inhi = 2;
else
   ihi = 2;
   inhi = 1;
end
for i = 1:(ndim + 1)
   if erro(i) <= erro(ilo)
      ilo = i;
   end
   if erro(i) > erro(ihi)
      inhi = ihi;
      ihi = i;
   else
      if erro(i) > erro(inhi)
         if i ~= ihi
            inhi = i;
         end
      end
   end
end

iter = iter + 2;
fac = -1;
amotry;
if errotry <= erro(ilo)
   fac = 2;
   amotry;
   elseif errotry >= erro(inhi)
      errosave = erro(ihi);
      fac = 0.5;
      amotry;
      if errotry >= errosave
         for z = 1:(ndim + 1)
            if z ~= ilo
               for j = 1:ndim
                  psum(j) = 0.5*(P(z,j)+P(ilo,j));
                  P(z,j) = psum(j);
               end
               dgV = psum(1);
               sigma = psum(2);
               u_lnd = (log(data(:,1)./dgV))./(2^.5*sigma);
               calc_cumul = .5.*(1 + erf(u_lnd));
               erro(z) = sum((data(:,2)-calc_cumul).^2);
            end
         end
         iter = iter + ndim;
         psum = sum(P,1);
      end
   else
      iter = iter - 1;
   end
   rtol = 2*abs(erro(ihi)-erro(ilo))/(abs(erro(ihi))+abs(erro(ilo))+eps);
   if iter >= ITMAX
      ans = 'ITMAX exceeded'
      rtol
      rtol = 0;
   end
end %end of while loop

temp = erro(1);
erro(1) = erro(ilo);
erro(ilo) = temp;
for i = 1:ndim
   temp = P(1,i);
   P(1,i) = P(ilo,i);
   P(ilo,i) = temp;
end
```

File amotry.m

```
% ------------------------------------------------------------------------------
%         Characterization of O/W Emulsions via NMR-CPMG/PGSE - amotry.m
% ------------------------------------------------------------------------------
% Copyright (C) 2001-2003 Alejandro Pena, Clarence Miller and George Hirasaki
%
% File amotry.m: Extrapolates by a factor fac through the face of the Simplex
%                across from the high point, tries it and replaces the high point
%                if the new point is better.
%
% ------------------------------------------------------------------------------

fac1 = (1-fac)/ndim;
fac2 = fac1 - fac;
for j = 1:ndim
    Ptry(j) = psum(j)*fac1-P(ihi,j)*fac2;
end
dgV = Ptry(1);
if ndim == 2
   sigma = Ptry(2);
end
u_lnd = (log(data(:,1)./dgV))./(2^.5*sigma);
calc_cumul = .5.*(1 + erf(u_lnd));
errotry = sum(abs(data(:,2)-calc_cumul));
if errotry < erro(ihi)
    erro(ihi) = errotry;
    for j = 1:ndim
        psum(j) = psum(j) - P(ihi,j) + Ptry(j);
        P(ihi,j) = Ptry(j);
    end
end
```

File bisection.m

```
% ------------------------------------------------------------------------------
%     Characterization of O/W Emulsions via NMR-CPMG/PGSE - File bisection.m
% ------------------------------------------------------------------------------
% Copyright (C) 2001-2003 Alejandro Pena, Clarence Miller and George Hirasaki
%
% File bisection.m: Applies the bisection method to determine the
%                   numerical values of the parameters of the lognormal
%                   distribution that render the best fit of the
%                   drop size distribution calculated from CPMG data
%                   with a given surface relaxivity.
%
% ------------------------------------------------------------------------------

clear u_lnd c;
k = 1;
while data(k,2) <= 0.5
   k = k + 1;
end

tempy = log10(data((k-1:k),1));
tempx = data((k-1:k),2);
c = polyfit(tempx,tempy,1);
temp = c(1)*0.5 + c(2);

davg = 10^temp;

% Calculating sigma {PgV = .5 * [1 + erf(u)]; u = ln(d/dgV)/2^.5*sigma}
% with bisection method

difer = 1;
```

```
sigma = 10;
delt  = -0.045 + eps;
u_lnd = (log(data(:,1)./davg))./(2^.5*sigma);
calc_cumul = .5.*(1 + erf(u_lnd));
sumerr = sum((cumul_water-calc_cumul).^2);

while abs(difer) > 1e-8

   sigma = sigma + delt;
   u_lnd = (log(data(:,1)./davg))./(2^.5*sigma);
   calc_cumul = .5.*(1 + erf(u_lnd));
   sumerr_n = sum((data(:,2)-calc_cumul).^2);
   difer = sumerr_n - sumerr;
   if difer > 0
      sigma  = sigma - delt;
      delt   = delt / 2;
   else
      sumerr = sumerr_n;
   end
end
```

File alfa.dat (First 20 roots of the equation $xJ_{5/2}(x) - J_{3/2}(x) = 0$)

```
    0.00000000
  2.08157597
  5.94036999
  9.20584014
 12.40444502
 15.57923641
 18.74264558
 21.89969648
 25.05282528
 28.20336100
 31.35209173
 34.49951492
 37.64596032
 40.79165523
 43.93676147
 47.08139741
 50.22565165
 53.36959182
 56.51327046
 59.65672900
 62.80000056
```

File gauss.dat (values for 24-point Gaussian quadrature)

```
0.06405689286260562608   0.12793819534675215697
0.19111886747361630916   0.12583745634682829612
0.31504267969616337438   0.12167047292780339120
0.43379350762604513848   0.11555066805372560135
0.54542147138883953566   0.10744427011596563478
0.64809365193697556925   0.09761865210411388827
0.74012419157855434624   0.08619016153195327591
0.82000198597390292195   0.07334648141108030573
0.88641552700440103421   0.05929858491543678074
0.93827455200273275852   0.04427743881741980616
0.97472855597130949819   0.02853138862893366318
0.99518721999702136018   0.01234122979998719954
```

D.6. References

1. C.C. Huang, "Estimation of rock properties by NMR relaxation methods", MSc Thesis, Rice University, Houston, USA, 1997.